THE HONG KONG
POLYTECHNIC UNIVERSITY
香港理工大學
Pao Yue-kong Library
包玉剛圖書館

Copyright Undertaking

This thesis is protected by copyright, with all rights reserved.

By reading and using the thesis, the reader understands and agrees to the following terms:

1. The reader will abide by the rules and legal ordinances governing copyright regarding the use of the thesis.
2. The reader will use the thesis for the purpose of research or private study only and not for distribution or further reproduction or any other purpose.
3. The reader agrees to indemnify and hold the University harmless from and against any loss, damage, cost, liability or expenses arising from copyright infringement or unauthorized usage.

IMPORTANT

If you have reasons to believe that any materials in this thesis are deemed not suitable to be distributed in this form, or a copyright owner having difficulty with the material being included in our database, please contact lbsys@polyu.edu.hk providing details. The Library will look into your claim and consider taking remedial action upon receipt of the written requests.

Pao Yue-kong Library, The Hong Kong Polytechnic University, Hung Hom, Kowloon, Hong Kong

http://www.lib.polyu.edu.hk

APPLICATIONS OF DIELECTRIC BARRIER DISCHARGE PLASMA ACTUATOR FOR FLOW CONTROL

ZONGNAN CHEN

PhD

The Hong Kong Polytechnic University

2023

The Hong Kong Polytechnic University

Department of Mechanical Engineering

Applications of Dielectric Barrier Discharge Plasma Actuator for Flow Control

Zongnan Chen

A thesis submitted in partial fulfilment of the requirements
for the degree of Doctor of Philosophy

Sept. 2022

CERTIFICATE OF ORIGINALITY

I hereby declare that this thesis is my own work and that, to the best of my knowledge and belief, it reproduces no material previously published or written, nor material that has been accepted for the award of any other degree or diploma, except where due acknowledgement has been made in the text.

_____(Signed)

Zongnan Chen (Name of student)

Abstract

Active flow control using dielectric barrier discharge (DBD) plasma actuators has become a promising technology to promote aerodynamic performance. This thesis presents the investigation of the application of AC-driven DBD plasma actuators and plasma streamwise vortex generators (PSVGs) on a D-shaped bluff body in low Reynolds number and a pulsed nanosecond dielectric barrier discharge plasma actuator (NSDBD) on a supersonic compression corner.

First, the characteristics of different ACDBD and NSDBD plasma actuators and PSVGs on the flat plate model have been studied experimentally. As one of the most interested in a flow control field, the thermal effects of the NSDBD with varying pulse voltages and pulse repetitive frequencies (PRFs) under different air pressures ranging from 0.1 to 1 bar are studied experimentally. The results will provide references for the mechanism detection of icing mitigation and flow control based on NSDBD plasma actuators.

The control performance of a streamwise-oriented DBD plasma actuator, a set of PSVGs, and a hybrid actuator on the reduction in bluff body flow separation, vortex-induced vibration (VIV), and wake fluctuation is experimentally investigated. Particle image velocimetry (PIV) is used to obtain details on the flow fields over a short D-shaped bluff body. Force measurement is conducted to compare the reduction in drag and vibration oscillations using these three types of plasma actuators. The PIV flow fields show that all of the plasma actuators suppress the flow separation on the bluff body, narrow the size of the wake, and decrease the turbulence kinetic energy (TKE) level in the wake. This stable controlled vortex shedding system can reduce the effect of the natural frequency of the bending stiffness-dominated cylinder structure system, thus avoiding the occurrence of resonance in advance. The reduction in drag and lateral lift oscillation are studied by mapping the changes in force coefficients and fluctuations as a function of Reynolds number. A comparison of these plasma actuators shows that the hybrid actuator achieves best drag reduction, suppression of lift oscillation, and Kármán vortex shedding in the wake at low speed, because three-dimensional flow structures are generated on the surface of the bluff body that consequently enhance the mixing.

The control performance of a pulsed NSDBD plasma actuator with varying pulse voltages and locations for a laminar flow separation on a supersonic compression corner is studied using experiments and numerical simulations under a unit Reynolds number of 7.8×10^6 m^{-1} and Mach number of 4. The plasma actuators are placed either upstream or downstream of the separation point, extending in the spanwise direction. The Schlieren technique is used to visualize the shock wave interaction and estimate the propagation speed of the induced shock by the plasma actuator. The results indicate that the high-speed external fluid is entrained into the original separation region after NSDBD activation upstream of the separation point, resulting in flow reattachment upstream of the corner. The entrained fluid with high momentum compels the main separation to move downstream,

accompanied by the fragmentation of the original shear layer. For a supersonic compression corner, excitation near the separation point achieves a higher efficiency in suppressing the separation bubble.

List of Publications

Journal articles:

[1] L. Shen, **Z. Chen**, and C.-Y. Wen, "Experimental Investigation of the Flow Structure over a Delta Wing Via Flow Visualization Methods," *J Vis Exp,* no. 134, Apr 23 2018.

[2] **Z. Chen**, L. Shen, and C.-Y. Wen, "Flow Control on a Bluff Body Using Dielectric Barrier Discharge Plasma Actuators," *AIAA Journal*, vol. 57, no. 7, pp. 2670-2674, 2019.

[3] L. Shen, **Z. Chen**, and C.-Y. Wen, "Thermal Effect on the Performance of an Alternating-Current Dielectric-Barrier-Discharge Plasma Actuator," *AIAA Journal,* vol. 58, no. 8, pp. 3368-3377, 2020.

[4] **Z. Chen** and C.-Y. Wen, "Flow Control of a D-Shaped Bluff Body Using Different Dbd Plasma Actuators," *Journal of Fluids and Structures*, vol. 103, Art. no. 103292, 2021.

[5] **Z. Chen**, J. Hao, and C.-Y. Wen, "Control of Supersonic Compression Corner Flow Using a Plasma Actuator," *Physics of Fluids,* vol. 34, no. 7, 2022.

[6] **Z. Chen**, C. Wong, and C.-Y. Wen, " Thermal Effects on the Performance of a Nanosecond Dielectric Barrier Discharge Plasma Actuator in Low Air Pressure," *Physics of Fluids,* vol. 35, 017110, 2023.

[7] **Z. Chen**, J. Hao, and C.-Y. Wen, "Periodic Control of Supersonic Compression Corner Flow Using a Nanosecond Dielectric Barrier Discharge Plasma Actuators," (in preparation)

Conferences:

[1] **Z. Chen** and C.-Y. Wen, "Flow Control of a D-Shaped Bluff Body Using Plasma Streamwise Vortex Generators," *The 24th Annual Conference of HKSTAM 2020 in conjunction with The 16th Shanghai – Hong Kong Forum on Mechanics and Its Application*, December 5, 2020, HK.

[2] **Z. Chen**, J. Hao, and C.-Y. Wen, "Flow Control on a Supersonic Compression Corner with the Nanosecond Surface Dielectric Barrier Discharge Plasma Actuators," *The 7th International Conference on Jets, Wakes and Separated Flows*, March 15-17, 2022, Nihon Univ., Tokyo, Japan.

Acknowledgements

Firstly, I would like to express my sincere gratitude to my supervisor Prof. Chih-yung Wen for the continuous support of my Ph.D. study and life. Prof. Wen is rigorous in research and noble in character and is a model for my whole life. His careful guidance helped me in all the time of research. I am fortunate to have such a mentor who can take the trouble to instruct and encourage me. In particular, Prof. Wen provided me with a relaxed and free research environment and encouraged me to conduct research according to my interests, which greatly benefited me.

I also want to thank Dr. Jiaao Hao and Dr. Lu Shen for their illuminating and consistent instruction in my research. Besides, I would like to deeply thank the staff at the Department of Mechanical Engineering. In particular, I want to thank Jack, Billy, and Chiu for their kind help in my experiments and Zijian and Jeremy for their precious suggestions. Also, I have greatly indebted my friends, roommates, and group members in GH034 for their friendship and kindness.

Finally, I would like to thank my parents and family for their love and support. Without their selfless affection, I could not finish this research reassuringly.

Table of Contents

List of Figures

List of Tables

Nomenclature

General

a_i	ith POD coefficient
C	Chord length [mm]
C_D	Drag coefficient
C_f	Surface friction coefficient
C_p	Surface pressure coefficient
C_p	Specific heat capacity [$Jkg^{-1}K^{-1}$]
C'_D	Drag coefficient oscillation
C'_L	Lateral lift coefficient oscillation
D	Bluff body diameter [mm]
E_{ac}	Alternating current power supply voltage [V]
E_A	Discharge energy [J]
E_G	Heat transfer from plasma to gas [J]
E_{heat}	Surface heating energy [J]
E_{in}	Input energy [J]
E_S	Heat convection from gas to surface [J]
E_{Th}	Thermal energy [J]
f_{ac}	Frequency of alternating current power supply [Hz]
f_m	Modulation frequency [Hz]
f_n	First natural frequency in the y direction in air [Hz]
f_o	Dominant oscillating frequency in the y direction [Hz]
f_{st}	Strouhal frequency [Hz]
f_x^*	Normalized drag force frequency
f_y^*	Normalized transverse lift frequency
F_D	Drag force [N]
F^+	Dimensionless periodic frequency, $(PRF \cdot L_0)/U_\infty$
H	Pressure sensor height [mm]
I	Turbulence intensity
I_{ac}	Alternating current power supply current [A]
k	Thermal conductivity [$Wm^{-1}K^{-1}$]
l	Plasma actuator discharge length [mm]
L	Total cylinder length in the z direction [mm]
L_0	Flat plate length [mm]
L_b	Bubble length [mm]

L_e	Exposed electrode width [mm]
L_r	Ramp length [mm]
L_p	Plasma location [mm]
M_∞	Freestream Mach number
p_∞	Freestream pressure [Pa]
P	Air pressure [Pa]
P_E	Electrical power consumption [Wm^{-1}]
$\dot{q}$	Heat flux [Wm^{-2}]
Re	Reynolds number
Re_∞	Freestream Reynolds number [m^{-1}]
Re_D	Reynolds number based on the round nose diameter
Re_o	Roshko number based on the dominant oscillating frequency
St	Strouhal number
St_o	Strouhal number based on the dominant oscillating frequency
t	Time [s]
t_0	Characteristic time, $t_0 = L_0/U_\infty$
t^*	Nondemensional time, $t^* = t/t_0$
T	Temperature [K]
T_∞	Freestream temperature [K]
T^*	Nondimensional temperature, $T^* = T/T_w$
T_w	Wall temperature [K]
Th	Thrust [N]
u,v,w	Flow velocity in the x, y, and z directions [ms^{-1}]
U_∞	Freestream velocity [ms^{-1}]
U_r	Reduced velocity, $U_r = U_\infty/f_n D$
V_{pp}	Peak to peak voltage of AC [kV]
x,y,z	Coordinate based on the model [mm]

Greek Letters

θ	Ramp angle [°]
η	Actuator efficiency
η_E	Electrical efficiency
η_G	Gas heating efficiency
η_{heat}	Surface heating efficiency
η_K	Kinetic efficiency
η_{Th}	Thermal efficiency

η_S	Heating convection efficiency
λ_i	Eigenvalue of the *i*th POD mode
λ_z	Spanwise distance between two adjacent electrodes [mm]
ω	Vorticity [s^{-1}]
ρ_∞	Freestream density [kg m^{-3}]
φ_i	*i*th POD mode

Special symbols

–	Averaged quantity
*	Dimensionless quantity
’	Fluctuant quantity

Abbreviations

AC	Alternating current
AOA	Angle of attack
CCD	Charge coupled device
DBD	Dielectric barrier discharge
DC	Duty cycle
EMI	Electro-Magnetic interference
EW	Expansion wave
FFT	Fast Fourier transform
IS	Induced shock
ISS	Induced separation shock
LES	Leading edge shock
NS	Nanosecond
PIV	Particle image velocimetry
PMMA	Polymethyl methacrylate
POD	Proper orthogonal Decomposition
PSD	Power spectral density
PRF	Pulse repetition frequency
PSVGs	Plasma streamwise vortex generators
RP	Reattachment point
RS	Reattachment shock
SL	Separated shear layer
SP	Separation point
SS	Separation shock
TKE	Turbulence kinetic energy

TP	Triple point
TTL	Transistor-transistor logic
VIV	Vortex induced vibration

CHAPTER 1 Introduction

1.1. Background

Flow control has always been one of the important topics in aerodynamics since it was firstly presented as a modern concept by Prandtl[1], which is of significant interest for industrial and academic research. Generally, it can be divided into passive flow control and active flow control (AFC). To date, considerable research has been devoted to passive flow control to improve aerodynamics, such as wing blades, vortex generators, etc. Passive control is using a passive device to change the flow state, accompanied by a defect that can not achieve the best control effect when the actual flow field deviates from the predetermined state. The active flow control directly applies the appropriate disturbance to couple with the object flow field. It can appear at the required time and place to obtain local or global effective flow changes through local energy input, so as to significantly improve the flight performance of air vehicles.

There are various types of actuators applied in active flow control. The classification of actuators was proposed by Cattafesta and Sheplak[2], including fluidic, moving object/surface, plasma, and others (e.g., electromagnetic, magnetohydrodynamic). For fluidic classification, the typical devices are zero-net mass-flux (ZNMF) or synthetic jet actuators[3]. Previous studies have shown that synthetic jets[4, 5] have great application potential in flow control. Another class with a moving object/surface induces a local fluid motion, such as the electrodynamic ribbon oscillator, vibrating flaps, oscillating wires, etc. More recently, plasma actuators are popular in active flow control as their lightweight and fast time response. Moreau has reviewed their classifications and applications[6]. It can be divided into corona discharge, dielectric barrier discharge, local arc discharge, spark jet, etc. The most popular variant is the dielectric barrier discharge (DBD) plasma actuator, which is detailedly investigated in this study.

The interest in technologies that broaden the roles and capabilities of unmanned aerial vehicles (UAVs)/micro aerial vehicles (MAVs) and robotic airships has increased rapidly over the last decade[7, 8]. These air vehicles, generally operated at various freestream conditions, are potential platforms for aerial exploration, monitoring, and surveillance. Active flow control based on dielectric barrier discharge (DBD) plasma actuators is one of the promising technologies in advancing the aerodynamic performance and maneuvering of aerial vehicles, because plasma actuators are fully electronic with no moving parts such as flaps or ailerons; they have an extremely fast response, very low mass, and low input power. Particularly, they are flexible, so that they can be formed to various shapes and located on the air vehicles with relative ease.

Even though flow control using a DBD plasma actuator has been studied for decades, the mechanisms that are responsible for a specific flow authority are still unclear, especially in compressible flow control. The shedding wake over a bluff body and laminar separation on a supersonic compression corner are two typical flow regimes in the incompressible and compressible

flow. Therefore, this thesis aims to gain a relatively comprehensive investigation of these two kinds of flows, determine their control mechanisms using DBD plasma actuators, and explore an effective control strategy for this potential technique.

1.2. Literature review

This section is intended to provide a comprehensive literature survey of investigations on flow control using DBD plasma actuators, especially on the unsteady vortex shedding phenomena over a bluff body and the laminar separation over a supersonic compression corner. The development of DBD plasma actuators is presented first.

1.2.1. DDB plasma actuators

1.2.1.1. Alternating-current single DBD plasma actuator (ACDBD)

The single dielectric barrier discharge plasma actuator has gained great popularity in active fluid control in the past decade due to its distinguish proprieties: it is fully electrical without any moving mechanical parts; it can respond in an extremely short time; it is easy to be controlled; it is light and flexible such that it can be installed on an irregular surface; the power consumption is relatively low[9]. A traditional dielectric barrier discharge plasma actuator can be divided into four main parts: an electrode exposed in the air, an electrode insulated in the model, the dielectric barrier between these two electrodes, and a high voltage and high-frequency ac power supply[10], as shown in Figure 1-1 (a). Under the effects of the high-voltage ac power, the air around the exposed electrode is ionized. This continuous ionization can be observed directly with the naked eye and is known as plasma. The ions in the plasma are forced by the electrical field and move from the exposed electrode to the insulated electrode and vice versa with less ion/electron movement. The collision of ions, electron and the neutral gas molecules induces a relatively large-scale local flow motion in the plasma region, which is also known as the ionic wind[11, 12]. The strength of the induced flow is strongly dependent on the applied voltage and its frequency, as well as the geometry of the actuator. Corke *et al.*[9, 13] and Moreau *et al.*[14] gave more details about the mechanism of DBD plasma actuators.

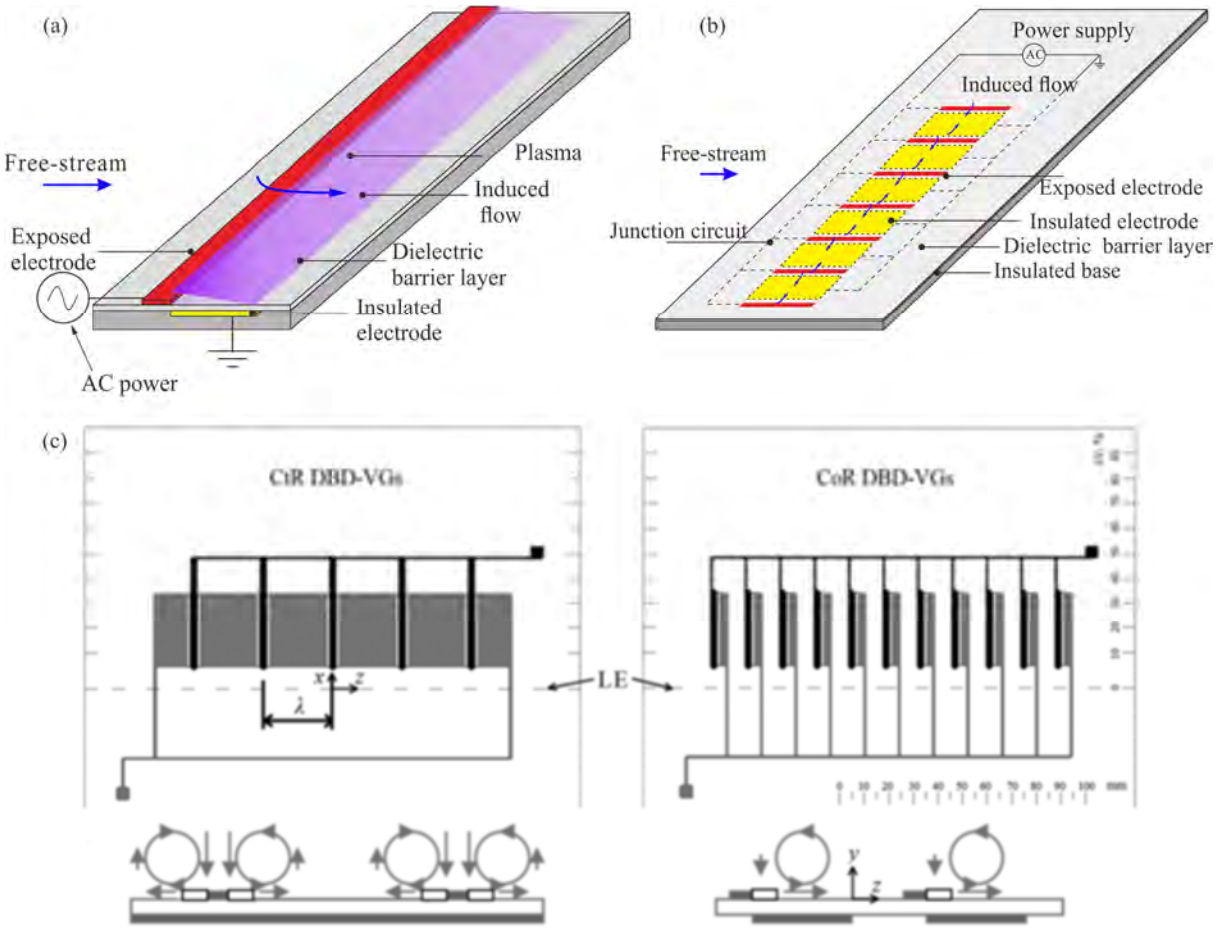

Figure 1-1. Schematics showing the configurations of (a) a traditional DBD plasma actuator; (b) PSVGs; (c) schematics of PSVGs by Jukes *et al.*(2013)[15].

1.2.1.2. Plasma streamwise vortex generators (PSVGs)

In the past decade, a novel plasma actuator called plasma streamwise vortex generators (PSVGs) has been reported. The typical configuration is shown in Figure 1-1(b). Because of the common covered electrode, plasma forms on both sides of each surface electrode. It has been shown that the resulting body force gives rise to a series of opposing wall jets in the spanwise direction that collide and interact with the external flow, thereby generating pairs of counter-rotating streamwise vortices which is related to the size between exposed electrodes[16]. These become the basis for enhanced cross-stream mixing of momentum within the boundary layer for separation control. Jukes (2013) *et al.*[15] compared two streamwise oriented DBD plasma actuators on a NACA 4418 airfoil for flow separation control, which created counterrotating and corotating vortex arrays, shown as Figure 1-1 (c). The counterrotating vortex actuator was found performing slightly better than the other one.

Wicks *et al.*[16] experimentally studied the influences of parameters, such as freestream velocity, applied peak-to-peak voltage, length of the active electrode, and spanwise interelectrode spacing on streamwise vorticity generation and provided the guidance for optimizing the PSVGs design based on the vorticity transport equation. The guidance was also experimentally validated. Kelley *et al.*[17]

presented the design and scaling of PSVGs in a variable pressure gradient environment and conducted measurements in the boundary layer on the suction surface of a V-22 wing model for separation control. The PSVGs have been applied to control the various flow due to the better performance than a straight DBD. However, the control performance on a short D-shaped bluff body is still unclear, which is highly dependent on the local flow authority.

1.2.1.3. Nanosecond surface DBD plasma actuator (NSDBD)

Typically, the working principle of plasma actuators is based on forming a low-temperature plasma through ionizing gas molecules between a pair of electrodes under a high voltage. Various plasma actuators are used based on different discharge types, such as corona, dielectric barrier, and spark discharges. A corona discharge is an electrical discharge caused by the ionization of a fluid such as air surrounding a high-voltage conductor. An ionized wind will be generated when a pair of strip electrodes is set oppositely[18]. A spark discharge is applied in different actuators, such as plasma synthetic jet actuators (PSJAs)[19] and localized arc filament plasma actuators (LAFPAs)[20]. A surface dielectric barrier discharge (DBD) plasma actuator, which is typically composed of four primary parts (a high voltage power, an exposed electrode, an insulated electrode, and a dielectric barrier between these two electrodes) has been applied to a variety of flow control problems[21]. For a DBD plasma actuator, the discharge features heavily depend on the input waveform. As a widely used flow control method, a high-frequency alternative current voltage-driven DBD plasma actuator (ACDBD) is characterized by a relatively large-scale local flow motion known as ionic wind[10, 22]. Compared to ACDBD, NSDBD discharge supplied with a nanosecond scale pulse duration has a much higher power density, leading to a fast-heating process. After each discharge pulse, energy deposition occurs quickly in the vicinity of the discharge streamers to form a strong thermalized area. This fast-heating process is essentially a direct excitation of molecules by electron impacts followed by fast quenching or decomposition with “hot” atom formation[23], which will be discussed in detail in Chapter 4.3.3. Then, an induced shock wave originates at each discharge streamer and propagates to the surrounding air[24]. Figure 1-2 shows typical schlieren images of the side view for four sequent time delays after discharge[25]. Therefore, the residual heat stemming from the energy deposition and the baroclinic vorticity caused by the interaction between the induced shock wave and the mainstream are the two fundamental characteristics of NSDBD plasma actuators, which have been regarded as control mechanisms. An ACDBD also releases thermal energy to the surrounding air[26, 27]. A series of ultrasounds was observed when an ACDBD was excited at a few kHz frequencies by Zhang *et al.*[28]. They hypothesized that the streamer discharge in the positive-going cycle plays an important role in generating the induced ultrasound.

The aforementioned studies indicate that NSDBD is a novel and potential technology for subsonic and supersonic flow control. Thus, comprehensive investigations of the NSDBD’s characteristics in the induced shock and energy deposition have attracted the attention of many researchers, which is of both fundamental and practical importance. Zhao *et al.*[29] investigated the

induced shock waves and subsequent flow dynamics of an NSDBD plasma actuator and attributed the shock wave to a microblast. The time evolution of the shock pressure profile follows the Friedlander equation well. Zhang *et al.*[30] studied the induced shock wave and starting vortex features and found that the velocity of a starting vortex markedly increases with a short pulse rise time due to an increased reduced electric field *E*/*N*. For residual heat accumulation, Correale *et al.*[24] measured the energy deposition region in different dielectric materials with various dielectric constants, volume resistivities, and thermal conductivities. They found that a high dielectric strength and a low volumetric resistivity are preferred for a barrier, together with a high heat capacitance and a low thermal conductivity coefficient, to maximize the efficiency of the thermal energy deposition induced by an NSDBD plasma actuator. Ndong *et al.*[31] indicated that geometric parameters, such as the electrode length and gap, drastically modify the plasma behavior. According to the fast-heating process, the application of icing mitigation on aircraft was investigated[32-34]. Liu *et al.*[35] investigated the unsteady heat transfer process over the airfoil/wing model exposed in frozen-cold airflows and found that the thermal characteristics are closely coupled with the boundary layer airflow. The anti-/deicing performance can be dramatically improved by increasing the pulse repetition frequency (PRF).

Table 1-1. Parameters given in the literature for the NSDBD plasma actuators' characteristics.

Authors	Voltage (kV)	PRF (kHz)	Air pressure (atm)	Energy input (mJ/cm per pulse)
Starikovskii *et al.*[36, 37], 2009	12, 25, 50	One pulse	0.3~1.8	0.2~0.6
Takashima *et al.*[38], 2011	10~20	0.1~1	1	0.3
Little *et al.*[39], 2012	15	0.01~1	1	0.3
Ndong *et al.*[31], 2013	5,10	0.01	1	0.2
Correale *et al.*[24, 40], 2015	10	0.1, 1	1	0.08
Nudnova *et al.*[41], 2015	17.5, 20.5	One pulse	0.4~1	0.5 mJ/mm^3
Liu *et al.*[35],2019	10	1~6	1	0.2
Wei *et al.*[34], 2019	8	6	1	0.4
Zhang *et al.*[30], 2019	13.5	0.5,1	1	0.5
Current study	25, 35	1,2,3	0.1~1	0.75~2

Table 1-1 shows the voltage, PRF, air pressure, and energy input involved in the current research on the NSDBD plasma actuator's characteristics. Thereinto, for the thermal effects, Starikovskii et al.[37] estimated the gas temperature using emission spectra of 0 to 0 transition of the 2^+ system of the nitrogen molecule with an unresolved rotational structure. They found that the temperature increase is 40 K during the discharge phase and additional 100 K after 1μs in the first pulse on the discharge gap (energy input 11 mJ). Correale et al.[40] measured the surface temperature increase with different

dielectric layer thicknesses and materials and quantified the heating efficiency of the NSDBD plasma actuator. Besides, for the low air pressure, Nudnova et al.[41] indicated fast gas heating is almost independent of pressure in the range 450–760 Torr (~0.6 atm to 1 atm) under a low applied voltage between 17.5 kV to 20.5 kV. But the temperature increase for 1μs reduces to 50–70 K at 300 Torr (~0.4 atm) from 140–180 K at 1 atm. This change may be highly related to the discharge mode transition, which is a function of the applied high voltage and the gas pressure[42]. However, to date, the thermal performance of an NSDBD plasma actuator is still unclear, which is considered a dominant mechanism, particularly under a wide range of air pressures from 0.1 to 1 atm in the troposphere where the air vehicles travel and with a high PRF. Therefore, the investigation of NSDBD thermal performance at low air pressure has practical importance in the field of active flow control. As a first step, this paper aims to systematically investigate the discharge characteristics of an NSDBD plasma actuator under different air pressures in the quiescent air with experiments and the corresponding efficiencies, as well as the effects of residual heat stemming from the energy deposition on the flow. Meanwhile, to compare with other research, extremely high applied voltages and frequencies are used to explore the application feasibility of NSDBD plasma actuators in the aeronautical industry.

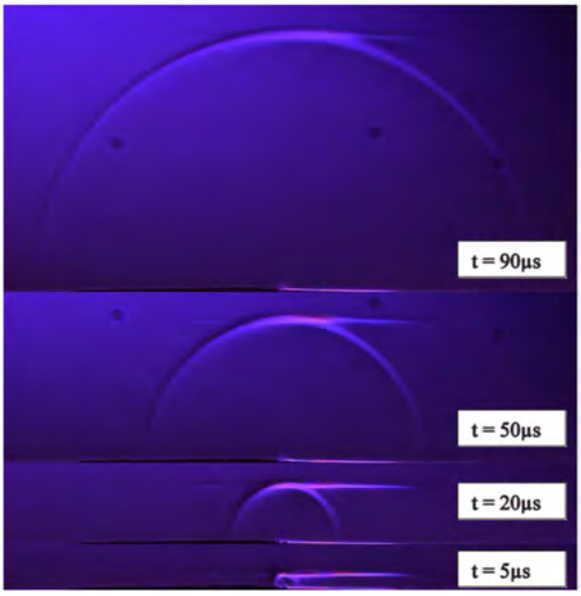

Figure 1-2. Phase-locked schlieren images of the shock wave generated by nanosecond pulse discharge with a straight DBD actuator[25].

1.2.2. Vortex shedding over a bluff body

1.2.2.1. Shedding wake of a bluff body

Vortex shedding from a bluff body induces structural vibration and acoustic noise when the body is subjected to crossflow. The flow unsteadiness increases in the wake due to the existence of periodic oscillations, which results in adverse effects on the flow/structure interaction. Figure 1-3(a) shows typical vortex shedding from a cylinder. Harmful effects of periodic oscillations can be reduced by the suppression of the vortex shedding. Therefore, flow control of vortex shedding behind a bluff body is

important for engineering problems, which aims at successfully reducing the drag, delaying the separation, and suppressing the vibration and noise. The vortex shedding process is affected strongly by the flow separation from a short bluff body with a round nose; meanwhile, the geometry of the trailing edges is also an important inducement[43, 44].

Vortex shedding is commonly observed when fluids flow past a bluff body. In 1966, Gerrard has given a useful vortex formation model[43]. The interaction between the two separating shear layers is a key element in the formation of vortex shedding. The vortex streets are formed through the interaction of the two separated shear layers via entrainment. The growing vortex is ultimately cut off by the entrainment of the vorticity and shed from the bluff body. Figure 1-3(b) illustrates the typical sketch of it. Entrained fluid (a) is engulfed into the growing vortex while (b) finds its way into the developing shear layer[45]. The near-wake flow between the base of the body and the growing vortex oscillates in size, and some further fluid, (c), is temporarily entrained into it. Entrained flow (a), which contains some fluid with oppositely signed vorticity to that in the growing vortex, is the largest of the three flows.

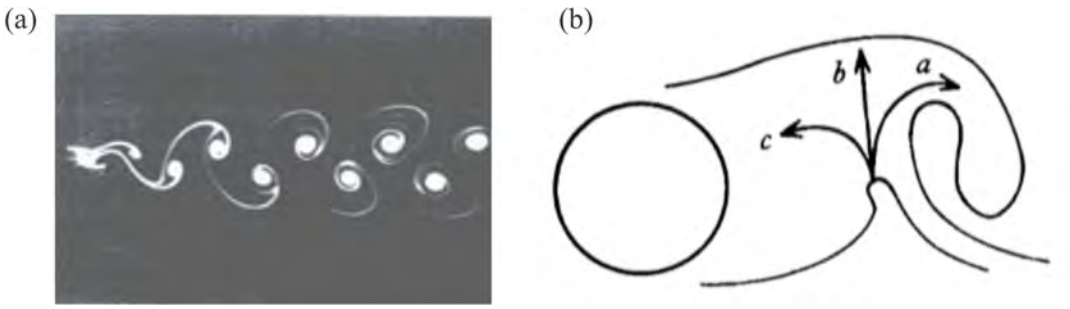

Figure 1-3. (a) Vortex shedding from a cylinder (*Re* = 105). (b) Filament-line sketch of the formation region[43]. (From Gerrard 1966)

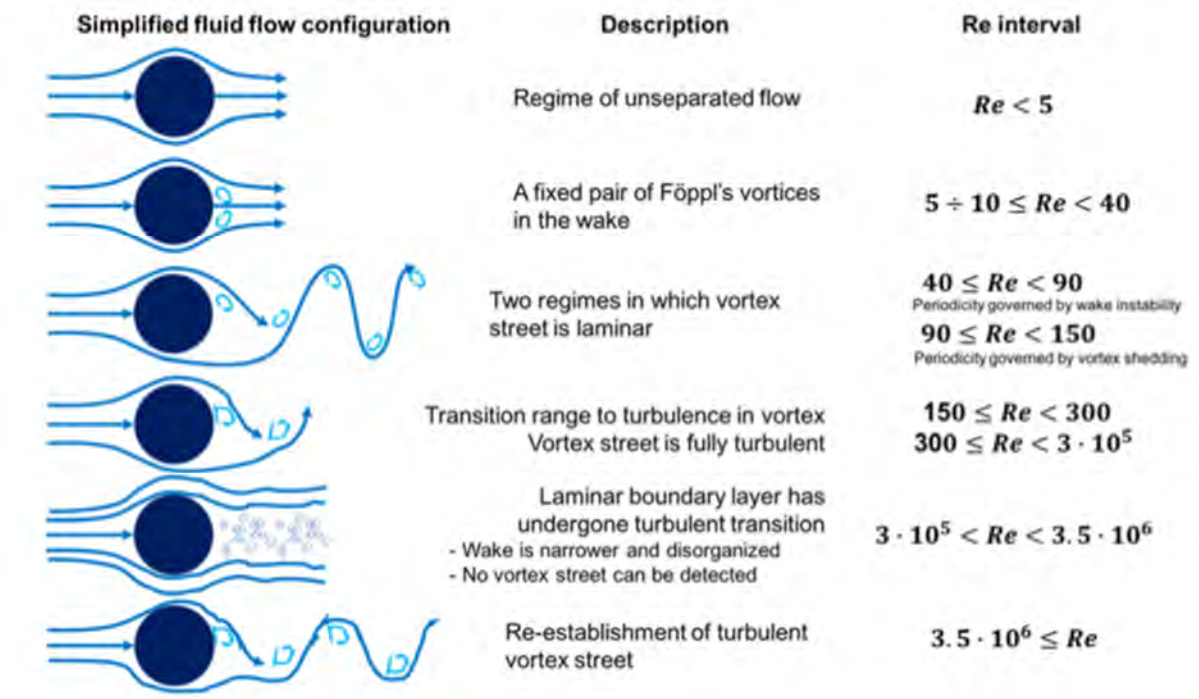

Figure 1-4. Regimes of fluid flow across a smooth circular[46]. (From Lienhard 1966)

Marris (1964) summarized the development of the wake of a cylinder with increasing Reynolds numbers on the basis of others' earlier work[47]. Lienhard (1966) gave the regimes of fluid flow under different Reynolds numbers shown in Figure 1-4. For Reynolds number values less than 5, the fluid passes around the cylinder without vortex formation. By increasing the velocity of the stream ($5 < Re < 40$), the fluid separates forming two stationary vortices at the rear of the cylinder in an unstable configuration. For *Re* values between 40 and 150, there is an alternating evolution of the vortex. Above $Re = 150$ the vortex wake is laminar until $Re = 300$ where the wake becomes turbulent. For the 300 to 3×10^5 range of *Re*, the wake is completely turbulent. In this region, the vortex shedding occurs with a well-defined frequency. When the Reynolds number is between 3×10^5 and 3×10^6 the wake becomes narrower and disorganized and the vortex shedding occurs non-harmonic. Finally for $Re > 3 \times 10^6$ the vortex evolution is reestablished in a harmonic but turbulent way[46].

In 1997, Zdravkovich[48] subdivided a flow regime over a circular cylinder into 15 typical states based on the boundary layer characteristics on the cylinder surface and the separated shear layer as shown in Table 1-2. In a global flow structure of a short bluff body, the flow properties may share the same features as a circular cylinder. Nevertheless, the shape of the afterbody and the near wake region of a short bluff body downstream from its separation points strongly affect the flow structures[49]. To illustrate the control mechanism on the separated shear layers, the Reynolds numbers in this study include the TrSL (transition in shear layers) properties listed in Table 1-2, where the formation of transition vortices occurs in free shear layers.

Table 1-2. Classification of flow regimes in a circular cylinder wake by Zdravkovich[48].

State		*Re* ranges	Properties
Laminar (L)	L1	0 to 4-5	Creeping flow or non-separation region
	L2	4-5 to 30-48	Steady separation or closed near-wake regime
	L3	30-48 180-200	Periodic laminar regime
Transition in wake (TrW)	TrW1	180-200 to 220-250	Transition of laminar eddies in the wake
	TrW2	220-250 to 350-400	Transition of irregular eddies in the wake
Transition in shear layers (TrSL)	TrSL1	350-400 to 1 K-2 K	Development of transition waves
	TrSL2	1 K-2 K to 20 K-40 K	Formation of transition eddies
	TrSL3	20 K-40 K to 100 K-200 K	Burst to turbulent
Transition in boundary layers (TrBL)	TrBL0	100 K-200 K to 300 K-340 K	Pre-critical regime
	TrBL1	300 K-340 K to 380 K-400 K	One-bubble regime
	TrBL2	380 K-400 K to 0.5 M-1 M	Two-bubble regime
	TrBL3	0.5 M-1 M to 3.4 M-6 M	Supercritical regime
	TrBL4	3.4 M-6 M to 6 M-8 M	Post-critical regime
Fully turbulent (T)	T1	6-8 M to 20-50M	Quasi-turbulent flow regime
	T2	*Re* - ∞	Complete transition

Other than the bluff nose facing upstream, which strongly affects the near wake flow, the geometry of the trailing edges is also an important inducement. A D-shaped short bluff body that combines a round nose with a square trailing afterbody is a common geometry in trucks, trains, blunt airfoils, gondolas in airships, and so on. Note that "short" herein means the limitations of the streamwise length compared to its cross-stream dimension, where the ratio of the chord length to the thickness (C/D) is small. Yamagata *et al.*[50] experimentally and numerically studied flows over D-shaped cylinders at various C/D ratios and found that the C/D ratios strongly affected the fluctuations in the near wake at a fixed freestream velocity. When the C/D ratio is large enough, "elongated" bluff bodies have leading edge flow separation, followed by reattachment along the body and subsequent separation at the trailing edge (Taylor *et al.* [51]). Vortex-induced vibration (VIV) of bluff bodies is also an important problem, but few studies focused on D-shaped geometry. Zhao *et al.*[49] found that the

afterbody plays an important role in affecting the wake characteristics and may even change the nature of a structure's VIV. Their results indicated that a D-shaped body exhibits different frequency responses dominated by VIV and galloping; the wake modes associated with response systems were also investigated. The flow unsteadiness increases in the wake due to the presence of periodic oscillations, which results in adverse effects on the flow and structural interactions. The harmful effects of periodic oscillations can be reduced by suppressing vortex shedding. Therefore, flow control of vortex shedding behind a bluff body is important for engineering applications and may successfully reduce the drag, delay the separation, and suppress the vibration and noise.

1.2.2.2. Applications of DBD on the bluff body

To date, considerable research has been devoted to passive flow control to improve aerodynamics, which is of significant interest for industrial and academic research. Thiria *et al.*[52] experimentally investigated turbulent drag reduction of a blunt trailing edge cylinder using a smaller cylinder located behind a D-shaped body. Parezanovic and Cadot[53] investigated the sensitivity of the global properties of this passive flow control method and discussed the corresponding physical mechanisms. Dielectric barrier discharge (DBD) plasma actuators and plasma streamwise vortex generators (PSVGs) have recently attracted considerable attention in the flow control field for their flexibility, high efficiency, and fast response[26].

In recent years, active flow control over a blunt body using this technology has been investigated by many researchers. Do *et al.*[54] used DBD actuators to delay flow separation at the round-cornered trailing edge of a bluff body. Skewed electrodes and reversed electrodes relative to the flow direction are utilized as two different electrode configurations. It is seen that the skewed electrode provides a positive effect on separation delay while the reversed electrode induces earlier flow separation. Figure 1-5 shows the flow separation control.

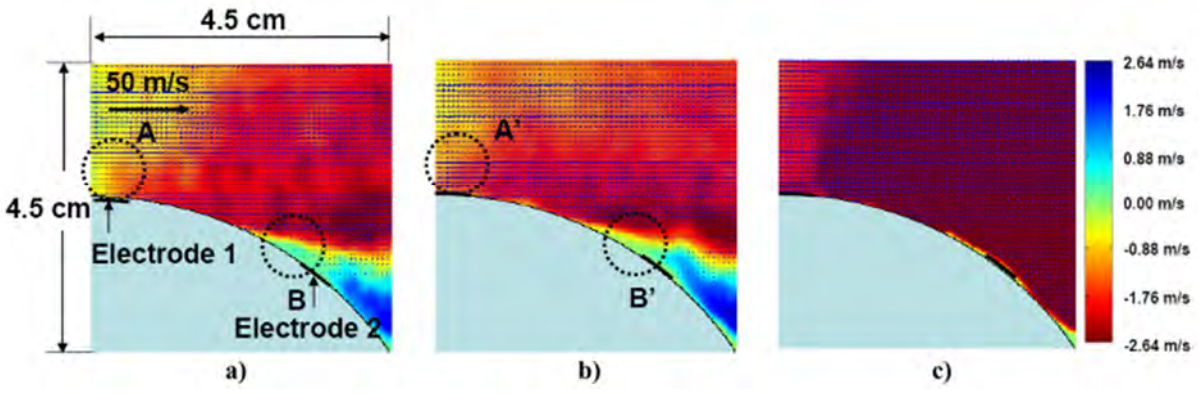

Figure 1-5. PIV images obtained from an average of 100 instantaneous PIV images near Electrode 1 and 2. The flow speed is 7.5 m/s. The color map illustrates the vertical velocity. (a) no discharge, (b) 6 kV, 40 kHz NSDBD, (c) 12 kV, 25 kHz ACDBD[54].

Bhattacharya *et al.*[55] conducted experiments to optimize the spatial-forcing-wavelength of a DBD actuator array which generated three-dimensional flows to control the wake of a circular

cylinder. Three-dimensional forcing of the wake of a circular cylinder was studied experimentally to determine the optimal spatial-forcing-wavelength for drag reduction. Dielectric-barrier-discharge plasma actuators were mounted on a cylinder in a square-wave pattern to create the three-dimensional forcing. For most spatial wavelengths and blowing ratios, the segmented plasma actuators produced streamwise vorticity that altered the wake development, formation length, and drag.

More recently, PSVGs applications for the control of cylinder wake flows[56], airfoil aerodynamics[17], and boundary layer characteristics on flat plates[16] have increased considerably. For a shedding wake flow, Naghib-Lahouti *et al.*[57] and Ayad[58] investigated the wake flow control of a blunt trailing edge-profiled body using PSVGs. The significant attenuation of large-amplitude geometric perturbations generated by vortex shedding in the wake after control was observed. Notably, in their studies, the leading edge flow separation was completely reattached to the body surface. In 2017, Julie *et al.*[59] arranged PSVGs to control flow separation on a cylindrical bump on a flat plate that is approached by a turbulent boundary layer by. The lock-on shifts sometimes, i.e., the large streamwise vortices center switch spanwise location, explaining the bi-modality in the flow. The details of the bi-modality are further investigated by conditional averaging and proper orthogonal decomposition.

Although many efforts have been put into flow control using DBD actuators, the control mechanism of PSVGs is still not clear. Besides, the potential of PSVGs for drag reduction and suppression of the periodic oscillations in bluff body wakes has not been sufficiently explored. This study is dedicated to extending the understanding of PSVGs for flow control of a bluff body: firstly, to compare impacts of applying DBD plasma actuators in different configurations on a bluff body; secondly, to compare the controlling effects on the bluff body wake flow and to understand the corresponding control mechanisms.

1.2.3. Laminar flow over a supersonic compression corner

1.2.3.1. Laminar separation on a supersonic compression corner

Shock-wave/boundary-layer interaction (SWBLI) is a common phenomenon that occurs in supersonic flow under different conditions. A compression corner, as the basic geometry, has been applied in many supersonic/hypersonic vehicles, including wings, engine inlets, junctions, etc. The flow physics of SWBLIs over a compression corner depends on whether the state of the incoming boundary layer upstream of the separation is laminar or turbulent. For a laminar interaction, the shock-induced separated flow is highly sensitive to upstream disturbances and can support self-sustained global instabilities[60, 61]. Streamwise streaks in heat transfer have been extensively observed, which are essentially the footprints of counterrotating streamwise vortices on the model surface and can cause significantly elevated peak heating with strong spanwise variations and promote boundary-layer transition downstream of the reattachment. Additionally, the laminar separation bubble can oscillate at a low frequency[62, 63]. On the other hand, for a turbulent interaction, the separation shock usually undergoes a back-and-forth motion with a dominant frequency much lower than that of the energetic eddies in the incoming boundary layer, typically by a factor of 0.1 to 0.01. The low-frequency, large-

scale unsteadiness can induce an adverse response of the vehicle structure and a degradation of the aircraft performance. Similar flow phenomena have also been observed in many other canonical configurations. Therefore, it is of interest to reduce the size of the separation region, the strength of the separation shock, and the pressure and heat flux peaks to suppress the generation of counterrotating streamwise vortices and to control the low-frequency unsteady motion of the shock system.

1.2.3.2. Applications of DBD on a supersonic compression corner

Active flow control via plasma actuators has attracted significant attention because of its flexibility, high efficiency, and fast response[64]. It has been widely used to improve the aerodynamic performance, including the elimination of flow separation on an airfoil, drag reduction, and suppression of the vortex-induced vibration of structures[65]. To effectively control supersonic flow, three types of plasma actuators have been developed in the literature, including plasma synthetic jet actuators (PSJAs)[19], localized arc filament plasma actuators (LAFPAs)[20], and nanosecond surface dielectric barrier discharge (NSDBD) plasma actuators[66]. Compared with NSDBD plasma actuators, PSJAs have a larger volume occupancy, which increases the actuator mass and limits the spatial arrangement[67]. Furthermore, both PSJAs and LAFPAs[68] can barely maintain uniformity, leading to strong three-dimensional (3-D) effects. Therefore, NSDBD plasma actuators have unique superiority and potential in active flow control.

The application of NSDBD plasma actuators in active flow control has been extensively investigated both experimentally and numerically[34, 35], such as the control of flow separation over an airfoil[36] and a backward-facing step[69] and control of the boundary-layer transition over a flat plate[70]. However, only a few studies have addressed supersonic flow control. An early attempt was made by Nishihara *et al.*[71], who used an NSDBD plasma actuator to control a Mach 5 flow over a cylinder. The induced shock wave propagated upstream toward the bow shock and increased the shock stand-off distance by up to 25%. However, the changes in aerodynamic characteristics were not measured. Subsequently, Bisek *et al.*[72] and Zheng *et al.*[73] numerically reproduced the flow phenomenon observed by Nishihara *et al.*[71] using a phenomenological and a self-similar plasma model, respectively. They found that NSDBD plasma actuators were very effective at moving the standing bow shock with a minimal energy budget and that the drag of the cylinder was appreciably reduced. It is indicated that a supersonic maneuver can be achieved by changing the normal force and pitching moment using NSDBD plasma actuators. Kinefuchi *et al.* experimentally[74] and numerically[75] investigated the control effects of NSDBD on flow separation induced by an impinging oblique shock over a flat plate, shown in Figure 1-6. Compared to parallel electrodes, the canted electrodes resulting in vorticity production successfully suppressed the boundary-layer separation, which was attributed to momentum transfer from the main flow to the boundary layer.

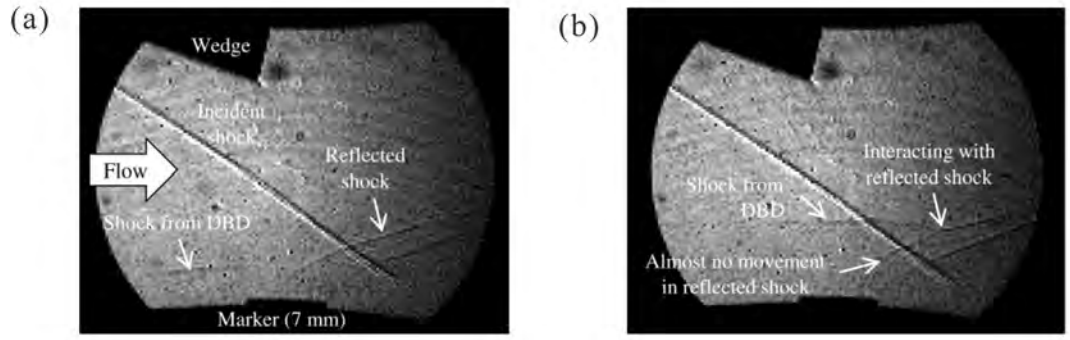

Figure 1-6. Shock propagation from baseline plasma actuator: (a) 12 μs and (b) 32 μs after pulse interact with shock-wave/boundary-layer (Kinefuchi *et al.*, 2018[74])

The aforementioned studies indicate that NSDBD is a novel and potential technology for supersonic flow control. To date, there are only limited studies addressing supersonic SWBLI control using plasma actuators and even fewer using NSDBD plasma actuators. As mentioned before, the flow physics of supersonic SWBLIs depend heavily on the state of the incoming boundary layer. For both laminar and turbulent interactions, the control effects and mechanisms of NSDBD plasma actuators remain unclear. Therefore, as a first step, this study aims to systematically investigate the understanding of supersonic laminar interaction control. To achieve this objective, experiments are conducted to visualize the shock wave interaction and measure the discharge properties, and numerical analyses are executed to ascertain key information, including the shock systems, skin friction and surface pressure distribution, and temperature evolution of separated flow fields. Moreover, the effect of different locations of plasma actuators is studied to provide an optimized configuration under the given conditions.

1.3. Objectives

The objective of this research is to conduct an experimental and simulation study about the applications of DBD plasma actuators for active flow control. Although many efforts have been put into this field, the underlying control mechanisms are still unclear. The relative research gap has shown in the literature review section. The compressible and incompressible flow control applications of DBD plasma actuators are studied, as shown in Figure 1-7. The D-shaped bluff body and a ramp are selected as the geometry. The basic characteristics of DBD plasma actuators in static air were studied first in each aspect.

The main objectives of this study are divided into three main parts, which are listed as below:

A. The basic characteristics of DBD plasma actuators.
   i. To investigate the fundamentals of a straight ACDBD plasma actuator and find out the relations between the electrical parameters and induced flows.
   ii. To study the basics of AC-driven PSVGs and ascertain how the geometry and electrical parameters influence the induced contour rotating vortex.

iii. To explore the thermal effects of a NSDBD plasma actuator at low air pressure and figure out the potential applications, especially in supersonic flow control.

B. Control effects on a short D-shaped bluff body.

i. To apply different DBD configurations using the optimized DBD plasma actuators on the semi-circle-square (D-shaped) body to compare the control authority and their impacts on the flow structure.

ii. To measure the unsteady flow phenomena, aerodynamic performance, and periodic vibrations, and find out the underlying control mechanisms.

iii. To optimize the control strategy based on the underlying flow control mechanisms of DBD plasma actuators on the bluff body.

C. Control effects on a supersonic compression corner.

i. To conduct experiments and observe the shock wave/boundary layer interactions on a supersonic compression corner with/without NSDBD plasma actuators.

ii. To apply plasma models in a CFD code called parallel hypersonic aerothermodynamics and radiation optimized solver (PHAROS) and validate the models and basic flows.

iii. To simulate the control effects and compare them with the experimental results.

iv. To understand the evolution of the flow structure over the compression corner under the DBD control based on the numerical simulation, to find the underlying flow control mechanisms.

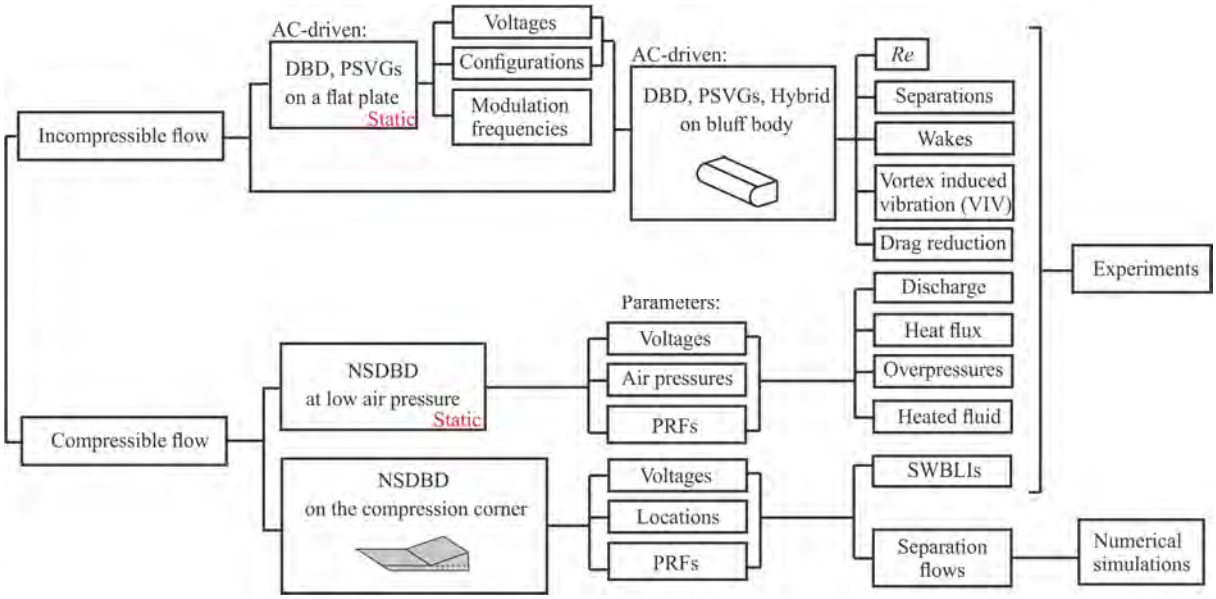

Figure 1-7. Schematics of objectives and methodology in this study.

1.4. Outline

In Chapter 1, the background of this research is introduced. First, a literature survey of DBD plasma actuators is provided. Then, based on the specific flow authority, the literature review of

vortex shedding phenomena behind a bluff body and a laminar separation on the supersonic compression corner are presented. Applications of DBD actuators of these two flow structures are reviewed. Also, the problems that should be solved in this research are stated.

In Chapter 2, the detailed experimental procedure is presented. The wind tunnel setup and models used for experiments are explained. The involved techniques are introduced and the corresponding data processing is demonstrated, including voltage, current, capacitance, particle image velocimetry, force, hot-wire, pitot tube and overpressure measurement, and infrared, Schlieren visualizations.

In Chapter 3, the details of the numerical simulations are presented. The CFD code is developed in a multi-block parallel finite-volume CFD solver RHAROS. The plasma models, governing equations, flux schemes and time marching methods are introduced. Also, the plasma model is validated with experimental results. The mesh used and the independence are introduced. Moreover, a supersonic flow over a flat plate with an NSDBD plasma actuator switch-on is discussed.

In Chapter 4, the characteristics of DBD plasma actuators in the quiescence air on a flat plate model are explored. First, the electrical properties and induced flows of ACDBD and PSVGs were studied. Then, as the most interested in a flow control field, the thermal effects of the NSDBD with varying pulse voltages and pulse repetitive frequencies (PRFs) under different air pressures ranging from 0.1 to 1 bar are studied experimentally. The underlying mechanism is discussed.

In Chapter 5, the flow structures around a bluff body using different configurations of DBD actuators are investigated. The flow separation and average wake structures are studied to verify the control mechanism. Based on the PIV results, the three-dimensional flow that takes momentum into the boundary layer in the PSVGs case is observed. Also, the reduction of vortex-induced vibration (VIV) is observed. At last, the POD analysis is conducted and the control mechanism is discussed.

In Chapter 6, the control performance of a pulsed NSDBD plasma actuator with varying pulse voltages and locations on a supersonic compression corner is studied using experiments and numerical simulations. The effects of the suppression of separation bubble are examined and the underlying control mechanism is detailly analyzed. Also, the periodic control effects are simulated.

In Chapter 7, the content of this study is concluded. Suggested directions for future work are introduced.

CHAPTER 2 Experimental details

Experiments were conducted in this study to investigate the application of DBD plasma actuators for flow control. The measurements were produced in a closed-loop wind tunnel for low-speed flow control. For the flow control over a supersonic compression corner, the experiments were conducted in a Ludwieg tube. Various techniques were used to demonstrate the flow characteristics qualitatively and quantitively. This chapter introduces the involved techniques, including particle image velocimetry (PIV), hot wire measurement, pitot tube measurement, force measurement, pressure measurement, Schlieren visualization, and infrared thermography. Meanwhile, the setup of models, configurations and control circuits of DBD plasma actuators are presented in detail.

2.1. Wind tunnel and test models

2.1.1. Low-speed wind tunnel

The experiments were conducted in the test section of a closed-loop low-speed wind tunnel at the Hong Kong Polytechnic University. The size of the test section was 1.2 m (length) × 0.6 m (width) × 0.6 m (height), as shown in Figure 2-1(a). In the experiments, the freestream velocity U_∞ was 1.67 m/s to 6.67 m/s, with the corresponding Reynolds numbers based on the half circular cylinder's diameter (Re_D) ranging from 3×10^3 to 1.2×10^4. The corresponding turbulence intensity of the freestream was less than 0.4%.

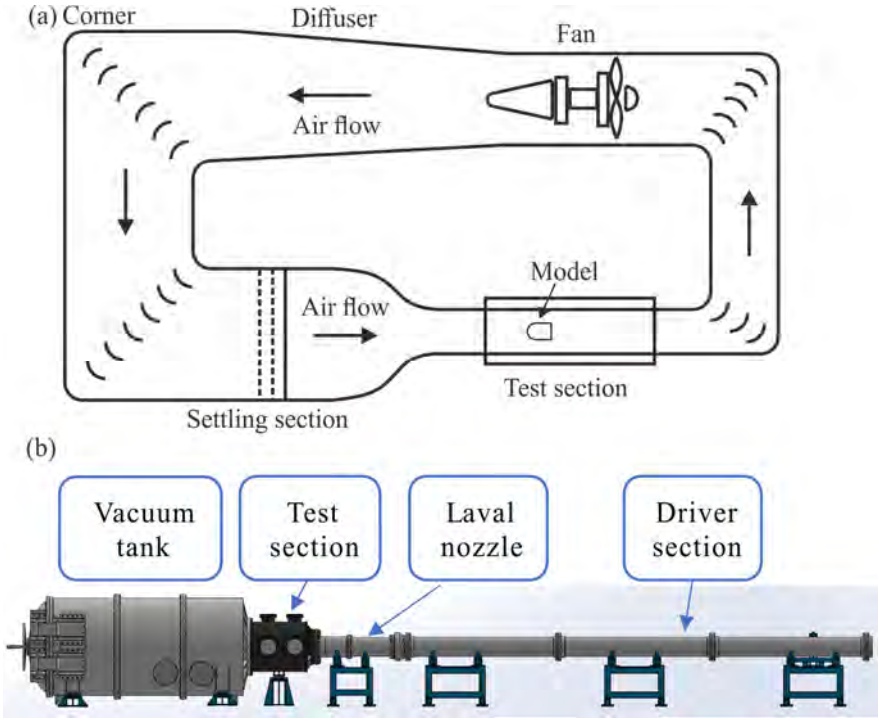

Figure 2-1. (a) The side view of the low-speed close loop wind tunnel; (b) the schematic of the Ludwieg tube.

2.1.2. Ludwieg tube

The supersonic experiments were conducted in a supersonic Ludwieg tube at the high-speed thermofluid laboratory of the Hong Kong Polytechnic University with a flow Mach number of 4. The diameter of the nozzle is 300 mm, and the test section has a length of 1000 mm, as shown in Figure 2-1(b). The quasi-steady test time is at least 40ms. Table 2-1 lists the free stream conditions used in the experimental and numerical studies. The incoming flow has a total pressure of 1710 ± 10 kPa and a total temperature of 297 ± 2 K with a unit Reynolds number of 7.8 $\times 10^6$. Until now, we did not observe the clear liquefaction of air may be due to the low pressure of the freestream even though the temperature is quite low. In the future, we could focus on this with more technologies developed.

Table 2-1. Free stream conditions.

M_∞	Re_∞ (1 m^{-1})	p_∞ (Pa)	U_∞ (ms^{-1})	ρ_∞ ($kg \cdot m^{-3}$)	T_∞ (K)
4.0	7.8× 10^6	1126	674	0.055	70.7

2.1.3. Test models

2.1.3.1. The D-shaped model

The bluff body model used in this study was a half-cylindrical-head cylinder (see Figure 2-2(a)) composed of acrylic. The spanwise length of the entire model was 600 mm. The diameter D of the round nose was 30 mm (thickness of the model) with a streamwise cord length C = 45 mm. Plasma actuators 100 mm long were installed symmetrically on the upper and lower surfaces of the central part of the model. Electrodes of actuators were composed of 0.025 mm thick copper films and the dielectric layer was comprised of 1 mm thick acrylic. The upper and lower surfaces of the model were milled 1 mm down to indent the actuators to be as flush with the surfaces as possible. Because of the negligible thickness of the exposed electrodes compared to D, the difference between the control-off cases and various electrode configurations was considered rather limited. The control-off case is called the baseline case hereinafter.

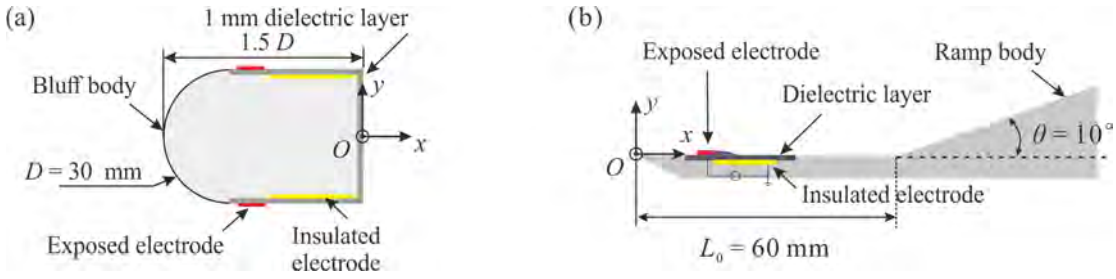

Figure 2-2. (a) Schematic of the half-cylindrical head cylinder and (b) schematic of the ramp model with a sharp leading edge and an NSDBD actuator installed.

2.1.3.1. The compression corner

The compression corner model comprises a flat plate with a sharp leading edge followed by a ramp. Figure 2-2(b) depicts the main details of the compression corner. The lengths of the flat plate L_0

and the ramp L_r are 60 mm and 150 mm, respectively. The width of the model is 200 mm. A sharp front with a radius of 0.05 mm is adjoined to the flat plate with an adjustable ramp between 0° and 20° (± 0.01°). In the current experimental and numerical studies, a moderate deflection angle of 10° was considered to have a large separation region but without the formation of secondary vortices under the given free-stream conditions. Due to the short running time of the shock tunnel, the surface was assumed to be an isothermal wall with a fixed temperature (T_w) of 297 K. The NSDBD plasma actuator was placed at different locations above the flat plate. The distance L_P is from the leading edge to the starting location of plasma, which is usually considered the downstream edge of the exposed electrode. The coordinate system is constructed with the origin located at the leading edge of the flat plate, as shown in Figure 2-2(b). The *x*-axis is coincident with the flow direction, and the *y*-axis points in the vertical direction.

2.2. DBD plasma actuators

2.2.1. Layouts

2.2.1.1. Configurations on a flat plate test

A DBD plasma actuator, which is typically composed of four main parts: a high voltage power supply, an exposed electrode, an insulated electrode, and a dielectric barrier between these two electrodes, has been applied to a variety of flow control problems. Figure 2-3 shows a typical layout of a DBD plasma actuator driven by a nano-second pulse. The DBD plasma actuator comprises two electrodes (0.01 mm thick copper) mounted on both sides of a dielectric layer. This dielectric layer was made of four layers of Kapton films with a total thickness of 0.02 mm. The spanwise length of the actuator was 100 mm, and the widths of the exposed (L_e) and insulated electrodes were 5 and 20 mm, respectively. Here, the long insulated electrode is selected to keep the sufficient extension of discharge streamers. There was no gap or overlap between the two electrodes. The actuator was flush placed on a 10-mm-thick acrylic flat plate as an insulated plane to prevent plasma formation below the dielectric layer. The insulated plane was placed on a thick foam plate to insulate the heat transfer from the bottom surface. The coordinate system was constructed with the junction between two electrodes' edges. The *x*-axis coincides with the plasma streamer direction, and the *y*-axis points in the vertical direction.

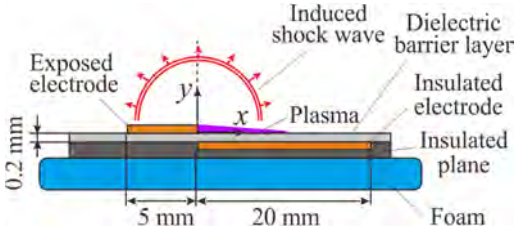

Figure 2-3. Schematic of the DBD plasma actuator on the flat plate driven by a nano-second pulse.

2.2.1.2. Configurations on the D-shaped body

According to the study of characteristics of plasma actuators on the flat plate, three configurations of plasma actuators were selected to investigate on a D-shaped bluff body: a typical DBD plasma actuator (DBD; see Figure 2-4(a)), plasma streamwise vortex generators (PSVGs; see Figure 2-4(b)), and a combination of DBD actuators and PSVGs (hybrid; see Figure 2-4(c)). The exposed and insulated electrodes' widths were 3.2 mm and 16 mm, respectively. In the DBD and hybrid actuators, the gap between the exposed (the exposed electrodes in the traditional DBD actuator part) and insulated electrodes along the spanwise direction was set at 2 mm for optimal performance[76] (Figure 2-4(a) and Figure 2-4(c)). In the PSVGs and hybrid actuator, according to Wicks' study[16, 17], the optimal value of the spanwise distance between two adjacent PSVG electrodes was set at 25.4 mm (λ_z). Along the spanwise direction, a 2-mm interval was left between the exposed and insulated electrodes. In addition, before installing the PSVGs on the bluff body, the characteristics were studied on the flat plate, which was presented detailedly in Chapter 4.2.

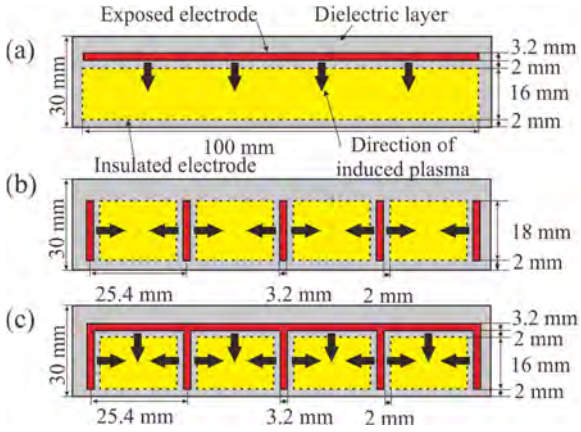

Figure 2-4. Configurations of (a) a traditional DBD plasma actuator, (b) PSVGs, and (c) the hybrid DBD plasma actuator on the D-shaped bluff body. The black arrows mark the directions of plasma.

2.2.1.3. Configurations on the compression corner

The NSDBD plasma actuator comprises two electrodes (0.01mm-thick copper) mounted on both sides of a dielectric layer (0.2mm-thick acrylic). The spanwise length of the actuator is 200mm, and the widths of the exposed and insulated electrodes are 2 and 10mm, respectively. There is no gap or overlap between the two electrodes which is the same as the layout on the flat plate model. The actuator was flush placed on an acrylic flat plate to indent the actuator to be as flush as possible with the top surface. The model surface was carefully disposed of to minimize the unevenness due to the exposed electrode and the gaps between different model parts.

The NSDBD plasma actuator was placed at different locations above the flat plate section on the ramp model. The distance L_P is from the leading edge to the starting location of plasma, which is usually considered the downstream edge of the exposed electrode. The coordinate system is

constructed with the origin located at the leading edge of the flat plate, as shown in Figure 2-2(b). The *x* axis is coincident with the flow direction, and the *y* axis points in the vertical direction.

2.2.2. Control circuits

Based on different experiments, different circuits were used. Figure 2-5 shows the schematics of control circuits and operation devices used in AC-driven DBD plasma actuators. The actuators were driven by a 20 kHz sine waveform AC power supply. The applied voltage was measured using a high voltage probe (Tektronix P6015A), and a 100 Ω resistor was connected in series for current measurement. The voltages were acquired by the oscilloscope and saved on a computer at last. The modulation wave generator was used to provide a low-frequency square modulation wave to the power supply which works with a continuous sinusoidal wave. Two AC power supplies were used in this study: a high voltage power supply, and a PVM/DDR plasma driver with a constant alternating frequency of 20 kHz. Notably, a class I ceramic capacitor C_c = 33 nF was connected in series with the resistor on the grounded side to measure the power consumption of the circuit[77].

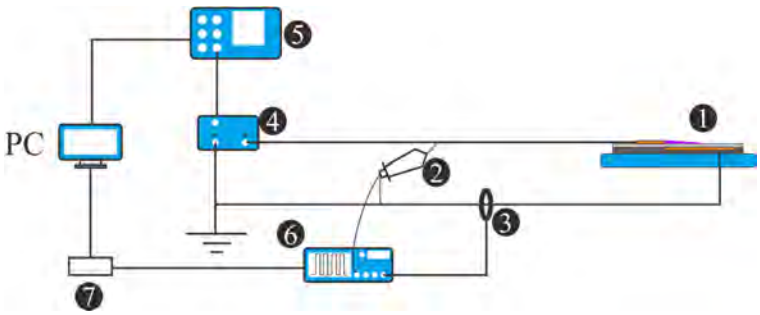

Figure 2-5. Schematics of the control circuit used in AC-driven DBD plasma actuators. 1. DBD plasma actuator; 2. high voltage probe; 3. current shunt; 4. power supplier; 5. modulation wave generator; 6. oscilloscope; 7. data acquisition system (DAQ).

Because the NSDBD plasma actuator was applied for supersonic flow control, a different trigger logic was required to synchronize the activation of the Ludwieg tube. Figure 2-6 presents the schematics of the control circuits. First, the wind tunnel's rupture signal and the high-speed camera's synchronization signal were chosen as the input of an AND-gate. The falling edge of the TTL signal from the AND-gate was used as the edge trigger for the synchronizer. Here, the rupture signal is a TTL signal at 5 V, given by the LabView. When the pressure in the gas storage section reaches a designed value, the control circuit will get in a waiting stage. Once the pressure suddenly drops, a rupture signal will be given. At the same time, the high-speed camera's synchronization signal was given as a chosen frequency. Then, the synchronizer will be edge triggered. Subsequently, the synchronizer will trigger the camera to record and touch off the pulse generator. The time delays of different channels were adjusted carefully to ensure the exposure time was locked in the expected time instantaneously. It is worth noting that the time delay between the discharge and the external trigger signal was fixed at 1 μs due to internal circuits. Figure 2-6(b) also presents the equipment that used the two power supply systems.

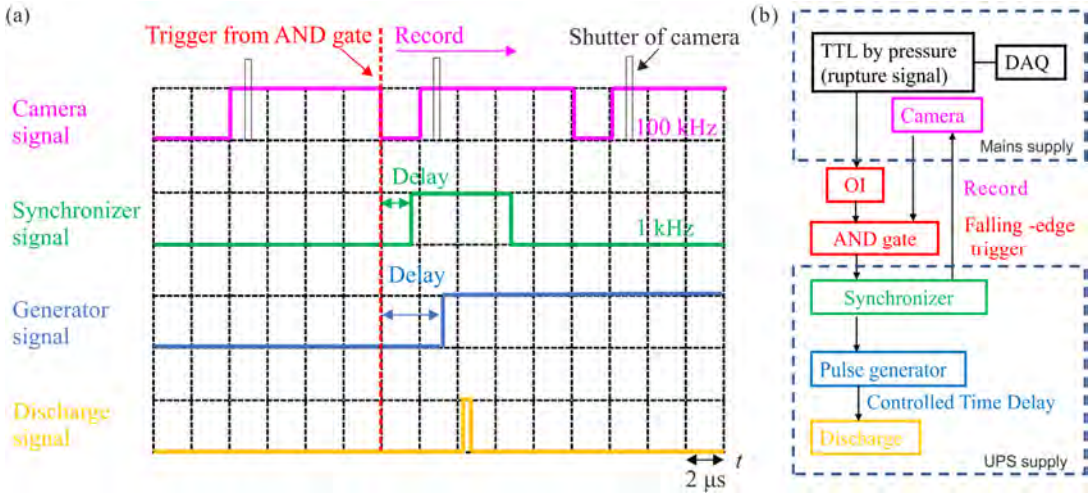

Figure 2-6. Schematics of signals in the control circuit of an NSDBD plasma actuator; and (b) schematics of the control circuit.

The optoelectronic isolator(OI) was designed in the control circuits to escape the electromagnetic interference (EMI) noise on the ground coming from the pulse generator which will heavily disturb the rapture signal of the Ludwieg tube. The electronic components in the OI circuit, such as resistors and diode, were carefully selected, and the circuits were firstly simulated in the Simulink, shown in Figure 2-7(a). The optocoupler contains a source of light, almost always a near-infrared light-emitting diode, that converts the electrical input signal into light, a closed optical channel, and a photosensor, which detects incoming light and either generates electric energy according to the diode situation. Thus, the input and output terminals of the optocoupler possess different ground, realizing the ground isolation. The large EMI noise on the ground caused by the pulse generator won't transfer to the trigger end and disturb the rupture signal. It is worth noting that the saturation region of the triode coordinated with a NOT gate to realize the identical polarity of transistor-transistor logic (TTL) signal real-time transmission.

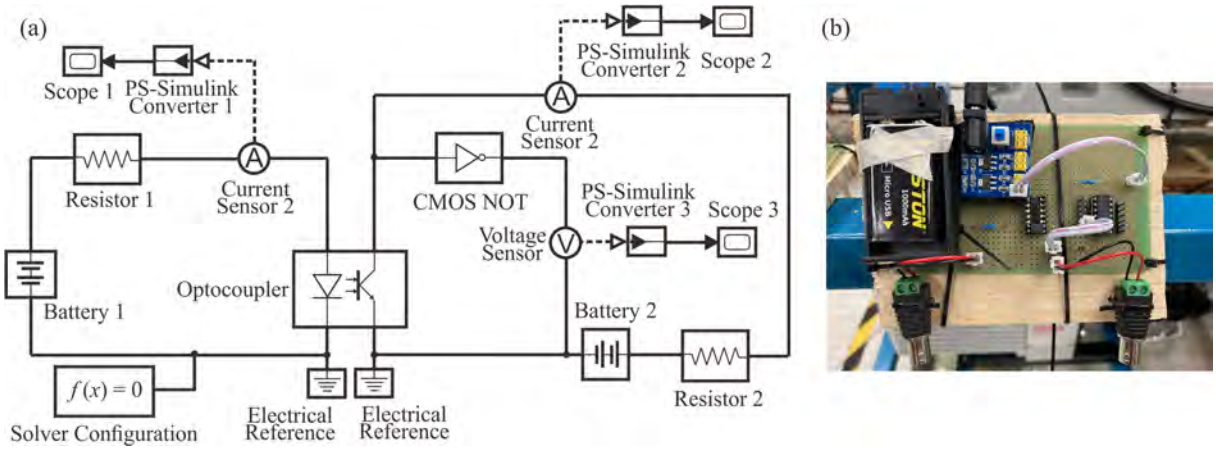

Figure 2-7. (a) The artificial circuit of the optoelectronic isolator in the control loop in Simulink; (b) the physical circuit board of the optoelectronic isolator.

2.3. Experimental measurements and setups

2.3.1. The voltage, current, and capacitance measurement

The applied voltage and current were measured using a high voltage probe (Tektronix P6015A) and a current shunt probe (Megaimpulse CS-10/500), respectively. The connecting circuit has shown in the last section. For the operational condition of the plasma actuators, an AC power supply in a sinusoidal waveform with a frequency of 20 kHz and a peak-to-peak voltage of 8 to 14 kV was applied. Note that, for the control on the bluff body, the controls were considered continuous because the active sine wave frequency was much higher than natural vortex shedding frequencies[10]. For the NSDBD, the voltage of 25 kV and 35 kV were applied by a nanosecond pulse generator (NPG 18/3500) with a pulse repetition frequency of 1000 Hz, 2000 Hz, and 3000 Hz. Both electrical signals are recorded by an oscilloscope(Agilent DSO-2014A) with a bandwidth of 100 MHz and a sampling rate of 2 GSa/s. In addition, a synchronization system was set up using a synchronizer (BNC Delay Pulse Generator 575-8C). Note that a photocoupled circuit was applied in the trigger system to reduce the EMI in the data acquisition system. The system was connected using high voltage coaxial cables(RG 217) with four shielding layers. To avoid the large EMI, a single uninterrupted power supply(EcoFlow Delta) was used for the pulse generator. The voltage and current measurements were involved in all experiments using DBD plasma actuators, and capacitance measurement was only used in AC-driven plasma actuators currently.

2.3.2. PIV measurement

To investigate the details of the control mechanics of the DBD actuators, the qualitative information of the flow field is significant. Therefore, in this study, 2D particle image velocimetry (PIV) measurement was used to measure the flow field. Figure 2-8(a) shows the schematics of the setup for PIV measurement. The laser beam came from a dual-pulse laser (EverGreen, 600 mJ of each pulse) and went through the convex lens, which was used to adjust the thickness of the laser sheet. The cylindrical lens was used to refract the laser beam to be a laser sheet. The silver mirror was used to reflect the laser sheet to the test section. Therefore, the laser sheet position can be set by adjusting the cylindrical lens location and the direction of the sliver mirror.

The control circuit of the PIV system is shown in Figure 2-8(b). The original trigger signal was from the modulation wave generator worked in the DBD circuit (see Figure 2-5). A delay generator (Stanford DG535) was used additionally to adjust the time gap between the event trigger and the first frame. Thus, the phase-lock PIV could be obtained in the periodic control cases. A CCD camera (HiSense 4M) with a resolution of 2080 × 2080 pixels and a 532 nm dual-pulse laser (EverGreen, with each pulse of 600 mJ) were triggered by a synchronizer (BNC 575). In PIV experiments, the entire wind tunnel was seeded by a TSI 9307-6 aerosol generator with olive oil droplets, and the diameter of typical oil particles was about 1 μm. The oil particle density concentration in the wind tunnel was approximately 650 $\mu g/m^3$. Thus, the overall flow density changed less than 0.1%. An adaptive PIV

correlation (Dantec DynamicStudio) was used for the data analysis. At the present stage, the PIV measurement was used to establish the velocity field sequence over a D-shaped bluff body in incompressible flow.

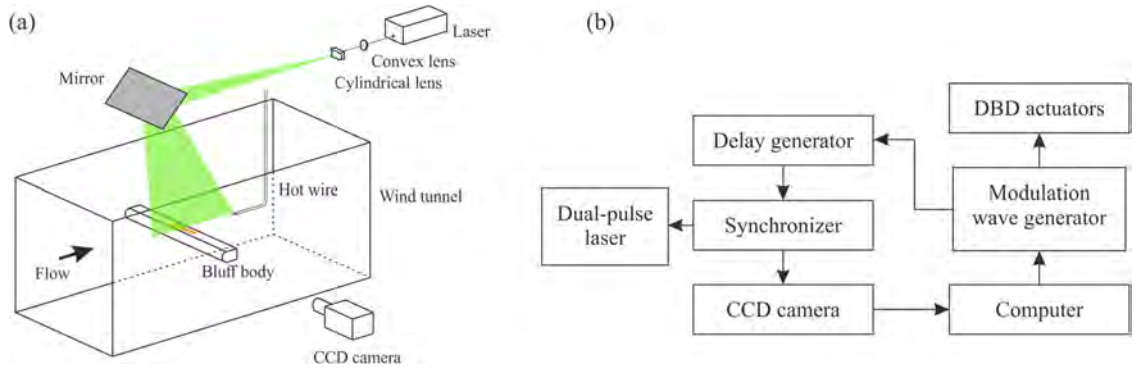

Figure 2-8. (a) Schematics of setup for PIV and hot wire measurement. (b) The control circuit of the PIV system.

To obtain the flow field around the bluff body, appropriate observation planes were selected for the PIV measurement, as shown in Figure 2-9(a). Along the streamwise direction, five *y*-*z* observation planes were used from x = -20 mm to x = 20 mm with an interval of 10 mm. (x = 0 mm was at the trailing edge of the model.) Along the spanwise direction, two *x*-*y* observation planes were also used, at z = 0 (called section A) and z = -12.7 mm (called section B), corresponding to the symmetric plane between the two central exposed electrodes and the plane over the central adjacent exposed electrode, respectively. For each case, the experiments were repeated three times. An adaptive PIV correlation was used for the data analysis. The data used were presented in the forms of: (a) the mean velocity field with an uncertainty of less than 1.25%[78], (b) the mean vorticity field with an estimated uncertainty (defined in Eq. (2-1)) of less than 0.25%[79], (c) the Reynolds stress components $\overline{v'^2}(x,y)$ and $\overline{u'v'}(x,y)$, and (d) spatial proper orthogonal decomposition (POD) modes.

$$\overline{\omega_x} \equiv \frac{\partial v_z}{\partial y} - \frac{\partial v_y}{\partial z} \tag{2-1}$$

The POD method was used to extract the spatiotemporal characteristic of the flow field, which can use $\boldsymbol{a}_n(t)$ and $\boldsymbol{\varphi}_n(x)$ to establish the velocity function $\boldsymbol{u}(\boldsymbol{x},t)$ with the form[80, 81]:

$$\boldsymbol{u}(\boldsymbol{x},t) = \sum_{n=1}^{\infty} \boldsymbol{a}_n(t)\boldsymbol{\varphi}_n(\boldsymbol{x}) \tag{2-2}$$

In this study, an algorithm (Eq. (2-2) to Eq. (2-9)) proposed by Meyer *et al.*[82] was used to solve this problem. First, 1000 instantaneous PIV measurements were considered as the snapshots of the flow, and the time-averaged velocity field was calculated as the 0th mode of the POD. The rest N snapshots with the two dimension fluctuating components from $\boldsymbol{u}(u,v)$ are arranged in a matrix $\boldsymbol{U}$ as

$$\boldsymbol{U} = [\boldsymbol{u}_1\ \boldsymbol{u}_2\ \ldots \boldsymbol{u}_N] \tag{2-3}$$

Then the autocovariance matrix is set by

$$\boldsymbol{C} = \boldsymbol{U}^T\boldsymbol{U} \tag{2-4}$$

and the corresponding eigenvalue problem

$$\boldsymbol{C}\boldsymbol{A}_i = \lambda_i\boldsymbol{A}_i \tag{2-5}$$

will be solved. Note that the solutions are ordered according to eigenvalues size to ensure the first few modes have the most energy. Then, the POD modes $\boldsymbol{\varphi}_i$ can be established by

$$\boldsymbol{\varphi}_i = \frac{\sum_{n=1}^{N}\boldsymbol{A}_{i,n}\boldsymbol{u}_n}{||\sum_{n=1}^{N}\boldsymbol{A}_{i,n}\boldsymbol{u}_n||}, i = 1, \dots, N, \tag{2-6}$$

where $\boldsymbol{A}_{i,n}$ is nth component of the eigenvector corresponding to λ_i in Eq. (2-5) and the discrete 2-norm is defined as

$$||y|| = \sqrt{y_1^2 + y_2^2 + \cdots + y_M^2} \tag{2-7}$$

The POD coefficients are determined by projecting the fluctuating part of the velocity field on to the POD modes

$$\boldsymbol{a}_n = \boldsymbol{\psi}^T\boldsymbol{u}_n \tag{2-8}$$

where $\boldsymbol{\psi} = [\boldsymbol{\varphi}_1\ \boldsymbol{\varphi}_2 \dots \boldsymbol{\varphi}_N]$. At last, the original flow field can be reconstructed using the expansion of the fluctuating part of a snapshot n.

$$\boldsymbol{u}_n = \boldsymbol{\psi}\boldsymbol{a}_n \tag{2-9}$$

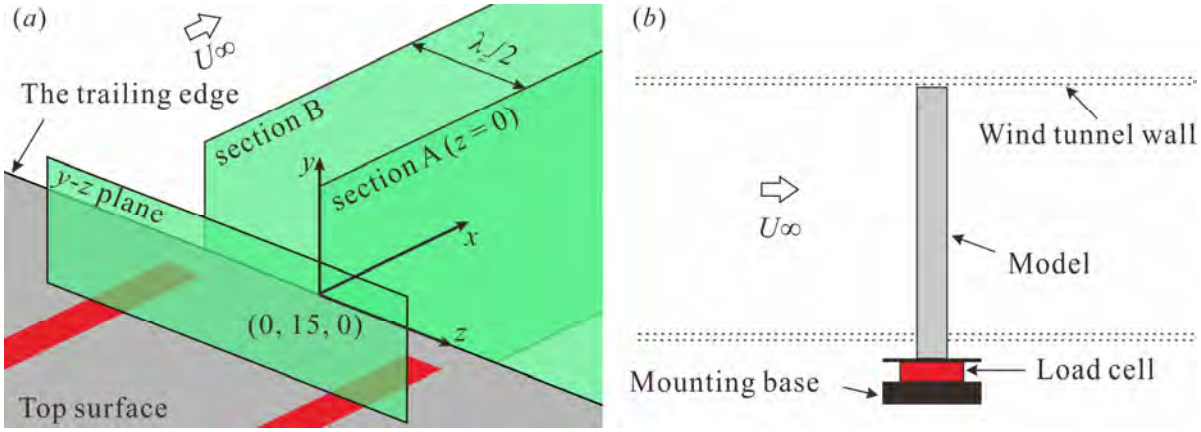

Figure 2-9. (a) Schematics of the bluff body model and observation planes in the PIV measurement and (b) the model's installation and force measurement's load cell.

2.3.3. Hot-wire and pitot tube measurement

Single hot wire was used to measure the fluctuating velocity to detect the vortex shedding frequencies in the flow. The probe was fixed on a three-dimensional traverse system (model Mitutoyo 192-616), as shown in Figure 2-8(a). The probe head was a tungsten wire with a length of 1 mm and a diameter of 5 μm (Dantec miniature wire probe, straight (55P11)). A constant temperature circuit (Dantex Streamline) was used to operate the whole system. Data was acquired by a DAQ board (NI PCI-6143) with a sampling frequency of 2000 Hz. The duration was 1 minute, producing a total of 1.2 × 10^5 data for each record. The fluctuations of the streamwise velocity component were acquired at a

location of x = 120 mm, y = 30 mm, and z = 0 mm, with a sampling frequency of 2000 Hz and the uncertainty was less than 2%. For the measurement, at least three records were collected for further processing. In this study, the velocity fluctuations after the bluff body were measured by the hot wire. A pitot tube was used to measure the freestream velocity, and signals were monitored by the pressure calibrator (FCO560).

2.3.4. Force measurement

The force on the bluff body was measured using a six-component load cell (ATI Nano43 transducer) with a maximum load of 9 N. Figure 2-9(b) schematically shows the arrangement of the load cell, mounting base, and cylinder model. To isolate the low-frequency vibration of the wind tunnel, the mounting base was clamped on a frame fixed on the ground floor. The load cell was connected between the mounting base and cylinder. Before the experiment, the load cell was statically calibrated using hanging standard masses ranging from 1 to 200 g. The force measurement for each case was repeated 5 times to satisfy the experimental repeatability with a sampling rate of 2000 Hz, and the uncertainty was less than 1.25%.

To acquire the natural frequency of the bending stiffness-dominated structure (same as in Figure 2-9(b)), an automatic model hammer (vlmpact-61) was used to precisely and reproducibly excite the structures and measure the excitation forces. A non-contact laser Doppler vibrometer (Ploytec PSV-400) was used to capture the frequency shift of backscattered laser light from the vibrating structure to determine its instantaneous velocity and displacement. At the present stage, the force measurement was used to acquire the dynamics of the D-shaped bluff body with/without DBD plasma actuators in incompressible flow.

2.3.5. Infrared thermography and discharge visualization

The surface temperature of the NSDBD plasma actuator was measured using a mid-wave infrared camera (FLIR A6751sc) with a 25 mm lens. Two calibrated temperature intervals ranging from 10 to 90 °C and 35 to 150 °C were used, and the measurement accuracy was 0.018 °C. In this study, the change in temperature ($\Delta T = T_t - T_{initial}$) is presented rather than the absolute temperature. The initial temperature $T_{initial}$ of the dielectric layer was measured before each experiment. The sampling frequency of the infrared camera was set at 100 Hz with a frame resolution of 4.2 pixels/mm. It was installed above a silicon window mounted on the discharge chamber, which has a 95% of transmitivity on the infrared wave. A one-dimensional semi-infinite model was used to calculate the heat flux by the temperature-time series[83]. The equation is shown as,

$$\dot{q_n} = 2\sqrt{\frac{\rho C_p k}{\pi}} \sum_{j=1}^{n} \frac{T_j - T_{j-1}}{\sqrt{t_n - t_j} + \sqrt{t_n - t_{j-1}}} \quad \textbf{(2-10)}$$

where $\dot{q_n}$, T_j and t_n are the heat flux, surface temperature and time of the n step; ρ, C_p and k are the density, specific heat capacity and thermal conductivity of the model surface material. In the current

study, ρ, C_p and k are equal to 1420 kg/m^3,1090 J/kg·K, 0.12 W/m·K for the Kapton tape used in the experiment.

In addition, a CCD camera (PCO.pixelfly) with a Nikon AF Microlens (60 mm $f1:2.8D$) was used to visualize the plasma generated by the NSDBD plasma actuator. The camera exposure time was varied with the PRF to keep the same numbers of pulses covered during one exposure time. The sampling frequency was set at 10 Hz with a resolution of 1392 × 1040 pixels. The frame resolution was 14.35 pixels/mm.

The plasma actuator was mounted into a constant volume low-pressure chamber with three optical windows 200 mm in diameter (see Figure 2-10(a)). The top optical window was made of silicon with a 95% transmitivity on the infrared wave as an observation window for the infrared camera. The discharge images and schlieren diagnostics were acquired through the two side windows made of quartz. When performing a specific optical experiment, the irrelevant windows were covered with lids to avoid light getting inside the discharge chamber. The discharge chamber was pumped down to 0.1 to 1.0 bar in the experiments, and the pressure was monitored by a pressure transductor (Kulite XT-190SM-250A) mounted on the chamber bottom.

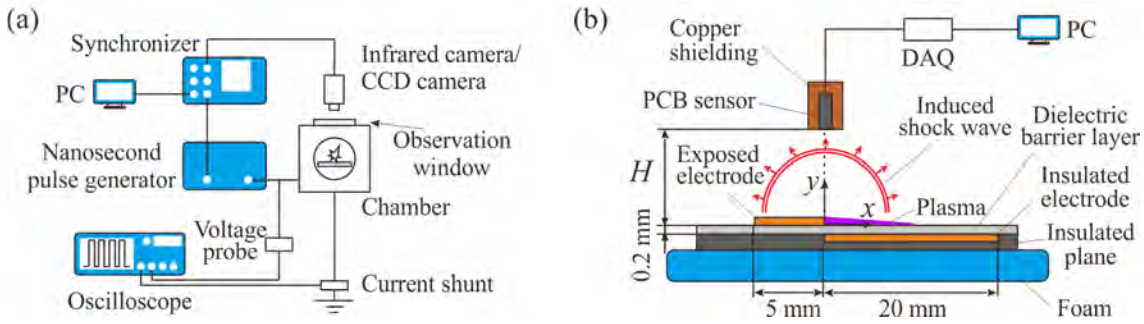

Figure 2-10. (a) Schematic of the infrared camera visualization setup; (b) schematics of the NSDBD plasma actuator and setup of the pressure sensor.

At the present stage, infrared thermography was used to measure the thermal effects of DBD plasma actuators and discharge visualization was used to measure the discharge properties of NSDBD under various low air pressures.

2.3.6. Overpressure measurement

A fast response dynamic pressure transducer (model PCB 132A31) was used to record the pressure profiles of induced shock waves. The pressure sensor was protected with copper shielding to weaken the electromagnetic interference and mounted facing normal to the actuator surface at the origin point, as shown in Figure 2-10(b). The rise time of the sensor was less than 0.5 μs, and the resolution is 7 Pa. The data were acquired by the DAQ device (Model NI Pxle-6368) at a sampling frequency of 2 MHz. A height gauge (model Mitutoyo192-616) with a 0.05-mm resolution was used to measure the distance from the sensor center to the actuator surface. The overpressure measurement

was used to establish the induced shock propagate characteristics after different air pressures by the NSDBD plasma actuator.

2.3.7. Schlieren setup

A Schlieren technique was used to capture the shock structures and estimate their propagation velocities. This optical diagnostic technique is based on the variation of the medium refractive index caused by the changes of the gas density[29]. Our Schlieren system (WCL250G) is composed of a collimation and viewing system, shown in Figure 2-11. A xenon lamp with an intensity of 80-300 mW/cm^2 was used as a light source. To obtain a high-resolution Schlieren image, a Nikon Nikkor microlens (105 mm *f*1:2.8*D*) was used, thereby giving rise to a spatial image resolution of approximately 0.11 mm/pixel. Shock structures were recorded using a high-speed camera (FASTCAM SA-Z type 2100K-M-32GB) with a resolution of 640 × 280 pixels. In order to record the propagation of the induced shock, the frame rate and shutter of the high-speed camera were set as 100 kHz and 0.25 μs. The Schlieren images were used to get the induced shock structures generated by NSDBD and the shock systems over the compression corner in the supersonic flow field.

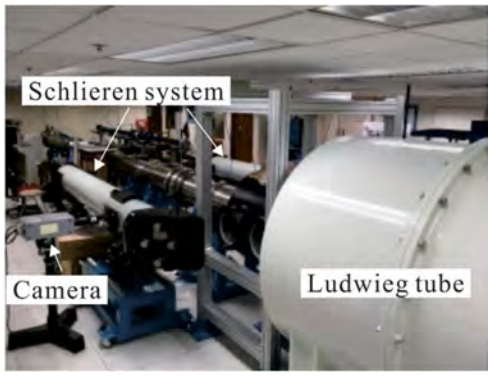

Figure 2-11. Schematic of Schlieren system.

2.4. Remark

In this chapter, details of the experimental setup were presented. The DBD plasma actuators' layouts, control circuits, wind tunnel, and experimental models were illustrated. Experimental techniques involved in this thesis were briefly introduced, including voltage, current, capacitance, PIV, force, hot-wire, pitot tube and overpressure measurement, and infrared, Schlieren visualization.

CHAPTER 3 Numerical details

The numerical simulations were adopted to provide more details of the flowfields with and without control and to reveal the control mechanisms. In this study, the NSDBD model was established first in a multi-block parallel finite-volume CFD solver RHAROS[84] developed by Dr. Hao. Then, the simulation results over a supersonic compression corner were compared with experimental studies, which will be analyzed in chapter 6 in detail. In this chapter, the details of plasma models and governing equations are presented first. Then, the plasma model is validated with experimental results. The mesh used and its independence are introduced. Moreover, a supersonic flow over a flat plate with an NSDBD plasma actuator switch-on is discussed. Note that, in this study, the numerical simulation only focuses on the supersonic flow control using an NSDBD plasma actuator.

3.1. Plasma models

As the discharge process is so complicated that there are only simplified models, there is no detailed model based on the discharge physics[85]. Because the plasma dynamic is essentially multiscale both in space and time, establishing an exact physics model is still challenging. For an NSDBD plasma actuator flow control, the time scale is from nanosecond for the discharge to millisecond for the fluid flow. The spatial scale is from the local discharge region in the order of millimeters to the perturbed flow in tens of centimeters. These obstacles bring large difficulties in numerical simulations of NSDBD[86].

In the current research, the residual heat stemming from the energy deposition and the baroclinic vorticity caused by the interaction between the induced shock wave and the mainstream are the two fundamental characteristics of NSDBD plasma actuators, which have been regarded as the control mechanisms. Therefore, the estimation of residual heat plays a crucial role in an NSDBD model. Due to the particularly short discharge time of NSDBD, the body force is tended to be ignored. The inhomogeneous phenomenological plasma model[86, 87] and a self-similar plasma model[73, 88] are widely used in numerical simulation of flow control. Both methods estimate the power density distribution of the NSDBD plasma actuator and are coupled with the unsteady Navier-Stokes equations as a heating source. Compared with other models, the inhomogeneous phenomenological plasma model has a trivial computational cost and can predict reliable results. The model is validated by comparing the experimental results of compression-expansion wave structures and wave speeds. The quasi-1D self-similar model of a surface nanosecond plasma discharge is derived from 2D drift-diffusion equations based on the analysis that some physical procedures such as ion motion, electron diffusion, and recombination are insignificant on a nanosecond time scale and thus can be neglected[88]. This model predicts the key plasma parameters from the physical derivation but needs a certain computational cost. In this study, as the first step, the one-zone inhomogeneous phenomenological plasma was used due to its low computational cost and accurate plasma parameter prediction. But this model still needs

to be perfected by a large amount of experimental data under complicated cases, such as complex air conditions and irregular electrode configurations. Moreover, the self-similar plasma model was also briefly introduced in this chapter.

3.1.1. One-zone inhomogeneous phenomenological plasma (OZIPP) model

A one-zone inhomogeneous phenomenological plasma (OZIPP) model[86] of surface NSDBD plasma actuator is adopted in this study to predict the key discharge parameters, such as the plasma length L_D, gas heating energy E_h for a single pulse per unit spanwise width, and its spatial distribution. By integrating the propagation velocity with the pulse rising time τ_r, the plasma length is estimated as a function of the peak voltage V and τ_r. Here, the propagation velocity is acquired by the curve fitting of the data. The energy input per unit spanwise width per pulse E_{in} is assumed to be a function of V and pulse repetition rate f obtained by curve fitting of the experimental data[38] as:

$$E_{in}(V,f) = \frac{\left(0.35215 - 0.14986 \times 0.99811^{f}\right)}{\left(0.35215 - 0.14986 \times 0.99811^{10}\right)} \left(0.18517V^{0} - 0.0610V^{1} + 0.00567V^{2}\right) \quad \textbf{(3-1)}$$

where E_{in} is in unit of mJ·cm^{-1} and V in kV. Therefore, E_h can be defined as:

$$E_h = \eta_h \cdot E_{in}(V,f) \quad \textbf{(3-2)}$$

where η_h is the efficiency of the energy input converted to gas heating. According to Maryia's work[23], η_h can be estimated as 35% during the discharge phase.

The spatial distribution of the gas heating energy density $ED_h(x, y)$, defined as Eq.**(3-3)**, can be obtained according to the averaged emission intensity ($EI(x/L_D, y/h)$) studied experimentally by Maryia *et al.*[23]. Note that it is assumed that the energy used to heat the gas is proportional to the intensity of the radiation.

$$ED_h(x,y) = E_h(V,f) \cdot \frac{EI(x/L_D, y/h)}{EI_T} \quad \textbf{(3-3)}$$

Here, EI_T is the integral value of the distribution function EI, and h is the thickness of plasma according to experiments. The emission intensity distribution EI/EI_T is shown equivalently in Figure 3-2(a). Therefore, the power density distribution is defined as

$$p_h(x,y) = ED_h(x,y)/\tau_h \quad \textbf{(3-4)}$$

where τ_h is a characteristic heating time. Unfer *et al.*[89] proposed a two-dimensional self-consistent numerical model of the discharge and gas dynamics to simulate the fast gas heating process, and a three-species physical model was presented by Wang[90] to predict the energy and forces. Montello *et al.*[91] indicated that the fast heating process in air occurs on a time scale (~100 ns) shorter than the characteristic acoustic time scale. Zheng *et al.*[88] found that a larger τ_h results in a delay of shock initiation and consequently a shock slightly lagging behind that with a smaller τ_h. In this study, τ_h is estimated to be 350 ns, which produces the best quantitative agreement with experiments[88].

3.1.2. Self-similar plasma model

A two-dimensional self-similar plasma model is established and developed by Takashima[92], using the surface ionization wave analysis[93]. The two-dimensional drift-diffusion equations can be reduced to a quasi-one-dimensional self-similar equation system, which is described as a parallel and perpendicular component of electric fields near the surface, defined as E_x and E_y. Meanwhile, the electron and ion density is defined as n_{ew} and n_{iw}. The plasma layer thickness parameter $\lambda = 1/\delta$, where δ is the plasma layer thickness. Therefore, the electron density can be written as:

$$n_e(x,y) = n_{ew}(x,y)e^{-y/\delta} \tag{3-5}$$

The equation system can be written:

$$\begin{gathered}
\frac{dE_x}{d\xi} = -\frac{3}{2}\frac{E_x^2}{\varphi} - \frac{e}{\varepsilon_0}(n_i - n_e) \\
\frac{dE_y}{d\xi} = \frac{dE_x}{dy} = \frac{\varepsilon}{h}E_x - \frac{en_e\mu_e E_y}{\varepsilon_0 V} \\
\frac{dE_y}{dy} = \frac{3}{2}\frac{E_x^2}{\varphi} \\
\frac{dn_e}{d\xi} = \frac{\nu n_e + n_e\mu_e\frac{dE_x}{d\xi} + n_e\mu_e\frac{3}{2}\frac{E_x^2}{\varphi} - n_e\mu_e\lambda E_y}{V - \mu_e E_x} \\
\frac{dn_i}{d\xi} = \frac{\nu n_e}{V} \\
\frac{d\lambda}{d\xi} = \frac{a}{V}\frac{d\nu}{dy}\frac{d(\ln\nu)}{d(\ln E)}
\end{gathered} \tag{3-6}$$

In this equation system, V is the wave speed, $\xi = x+Vt$ is the self-similar variable for the left-running wave, φ is the electric potential at the wall, $d\varphi/d\xi = -E_x$, h is the dielectric thickness, ε is the dielectric constant, $\mu_e = 300\cdot(760/\mathrm{P[torr]})$ cm^2/s is the electron mobility, $\nu = \alpha\mu_e E$ is the ionization frequency, α is the ionization coefficient, n_{e0} and $n_{e\infty}$ are initial electron density and asymptotic electron density behind the wave[73, 92]. The value of parameter a is determined from the current continuity relation across the ionization wavefront, whereas the ionization coefficient α is obtained by fitting the experimental Townsend ionization coefficient in nitrogen[73].

Given a combination of peak voltage V_p and τ_r, whose values are strongly load-dependent and known from a specific experiment, the above-mentioned discharge parameters like E_x, E_y, δ, and L_D can be predicted. The rate of coupled total energy per actuator length in the spanwise direction perpendicular to the page is given by:

$$\frac{dE_{in}}{d\xi} = \frac{\sigma^2(\xi)h}{2\varepsilon\varepsilon_0} + \int_0^{\xi}\frac{d\xi'}{V}\int_0^{\infty}\vec{j}\cdot\vec{E}\,dy \tag{3-7}$$

where $\sigma(\xi)$ is the charge density on the dielectric surface and $\vec{j}\cdot\overrightarrow{E}$ is the power coupled per unit volume. At last, the estimation of power density distribution is defined as:

$$p_h\,(x,y) = \frac{\eta_h \cdot E_{in}(V,f) \cdot f(x/L_D, y/\delta)}{\tau_h} \tag{3-8}$$

Here, the energy for gas heating is distributed in the plasma region also using a semi-empirical formula to obtain the energy density. And the η_h, τ_h are set the same as the OZIPP model at 35% and 350 ns, respectively.

3.2. Numerical method

The numerical simulations in this study are performed using a multiblock parallel finite-volume CFD code called PHAROS[84], which has been successfully applied to supersonic/hypersonic flows over capsule, double-cone, hollow-cylinder/flare[94], and double-wedge configurations[95]. The flow field variables are nondimensionalized by L_0, which is considered the characteristic length of the flow. The characteristic time of the flow t_0 is defined as L_0/U_∞, where U_∞ is the velocity of the free stream. Notably, only 2-D laminar simulations are considered in the present study.

3.2.1. Governing equations

The governing equations are the 2D compressible Navier-Stokes equations for a calorically perfect gas written in the following conservation form:

$$\frac{\partial \boldsymbol{U}}{\partial t} + \frac{\partial \boldsymbol{F}}{\partial x} + \frac{\partial \boldsymbol{G}}{\partial y} = \frac{\partial \boldsymbol{F_v}}{\partial x} + \frac{\partial \boldsymbol{G_v}}{\partial y} + \boldsymbol{S_h} \tag{3-9}$$

where

$$\boldsymbol{U} = \begin{pmatrix} \rho \\ \rho u \\ \rho v \\ \rho e \end{pmatrix}, \boldsymbol{F} = \begin{pmatrix} \rho u \\ \rho u^2 + p \\ \rho uv \\ (\rho e + p)u \end{pmatrix}, \boldsymbol{F_v} = \begin{pmatrix} 0 \\ \tau_{xx} \\ \tau_{xy} \\ u\tau_{xx} + v\tau_{xy} - q_x \end{pmatrix},$$
$$\boldsymbol{G} = \begin{pmatrix} \rho v \\ \rho uv \\ \rho v^2 + p \\ (\rho e + p)v \end{pmatrix}, \boldsymbol{G_v} = \begin{pmatrix} 0 \\ \tau_{xy} \\ \tau_{yy} \\ u\tau_{xy} + v\tau_{yy} - q_y \end{pmatrix}, \boldsymbol{S_h} = \begin{pmatrix} 0 \\ 0 \\ 0 \\ p_h \end{pmatrix} \tag{3-10}$$

In these expressions, ρ, p, u, and v are the density, pressure, and x and y velocity components, respectively. τ_{ij} is the shear stress tensor modeled under the assumption of a Newtonian fluid and Stokes' hypothesis, and q is the vector of heat conduction modeled according to Fourier's law. Sutherland's law is used to evaluate the dynamic viscosity. The specific heat ratio γ and Prandtl number Pr are set to 1.4 and 0.72, respectively. The effect of the discharge on flow is represented as a heating source in p_h of the energy equation predicted by the OZIPP model. Note that it is set to zero outside the heating time. In the current numerical study, the influence of the interaction of ionic wind is ignored because of the extremely short effective time of body force caused by plasma.

In the study, a finite volume method (FVM) was adopted to discrete the conservation equations. The integration in Eq.**(3-9)** is:

$$\frac{\partial \boldsymbol{U}}{\partial t} + \frac{1}{V}\int_S (\widehat{\boldsymbol{F}} - \widehat{\boldsymbol{F_v}}) \cdot \boldsymbol{n} dS = \boldsymbol{S_h} \tag{3-11}$$

where V is the control volume, $\boldsymbol{n}$ is the normal vector to the surface. The inviscid flux and viscid flux are defined as:

$$\widehat{\boldsymbol{F}} = \boldsymbol{F}\boldsymbol{i} + \boldsymbol{G}\boldsymbol{j} \tag{3-12}$$

$$\widehat{\boldsymbol{F_v}} = \boldsymbol{F_v}\boldsymbol{i} + \boldsymbol{G_v}\boldsymbol{j} \tag{3-13}$$

And further dispersing to:

$$\begin{aligned}
&\frac{\partial \boldsymbol{U}_{i,j}}{\partial t} = \\
&-\frac{1}{V_{i,j}}\left[\left(\boldsymbol{F}_{n,i+\frac{1}{2},j} - \boldsymbol{F}_{vn,i+\frac{1}{2},j}\right)S_{i+\frac{1}{2},j} - \left(\boldsymbol{F}_{n,i-\frac{1}{2},j} - \boldsymbol{F}_{vn,i-\frac{1}{2},j}\right)S_{i-\frac{1}{2},j}\right] \\
&-\frac{1}{V_{i,j}}\left[\left(\boldsymbol{G}_{n,i,j+\frac{1}{2}} - \boldsymbol{G}_{vn,i,j+\frac{1}{2}}\right)S_{i,j+\frac{1}{2}} - \left(\boldsymbol{G}_{n,i,j-\frac{1}{2}} - \boldsymbol{G}_{vn,i,j-\frac{1}{2}}\right)S_{i,j-\frac{1}{2}}\right] \\
&+\boldsymbol{S_h}_{\,i,j} \\
&= \boldsymbol{RHS^n}
\end{aligned} \tag{3-14}$$

Here, $\boldsymbol{F}_{\mathrm{n}}$, $\boldsymbol{G}_{\mathrm{n}}$ is the inviscid flux normal to the control volume surface, and $\boldsymbol{F}_{\mathrm{vn}}$, $\boldsymbol{G}_{\mathrm{vn}}$ is the viscid flux normal to the control volume surface.

3.2.2. Flux schemes

The inviscid fluxes are calculated using the modified Steger–Warming scheme, which can capture strong shocks stably while maintaining sufficient viscous resolution in the boundary layers[96]. The scheme is then extended to a higher order by the monotone upstream-centered schemes for conservation law reconstruction[97]. The viscous fluxes are calculated using a second-order central difference. An implicit line relaxation method[98] is utilized for time integration.

Based on the homogeneity of inviscid flux,

$$\boldsymbol{F}_n = \frac{\partial \boldsymbol{F}_n}{\partial \boldsymbol{U}}\boldsymbol{U} = \boldsymbol{A}\boldsymbol{U} \tag{3-15}$$

By characteristic decomposition for A matrix,

$$\boldsymbol{A} = \boldsymbol{L}\boldsymbol{\Lambda}\boldsymbol{R} \tag{3-16}$$

where $\boldsymbol{L}$ and $\boldsymbol{R}$ are the left and right characteristic vectors, respectively. By eigenvalue splitting of matrix $\boldsymbol{A}$:

$$\boldsymbol{A}^{+} = \boldsymbol{L}\boldsymbol{\Lambda}^{+}\boldsymbol{R},\ \boldsymbol{A}^{-} = \boldsymbol{L}\boldsymbol{\Lambda}^{-}\boldsymbol{R} \tag{3-17}$$

And inviscid flux can be rewritten as:

$$\boldsymbol{F}_{n,i+1/2,j} = \boldsymbol{A}^{+}_{i+1/2,j}\boldsymbol{U}_{i,j} + \boldsymbol{A}^{-}_{i+1/2,j}\boldsymbol{U}_{i+1,j} \tag{3-18}$$

The conservative variables can be written as:

$$\boldsymbol{U}^{+}_{i+1/2,j} = (1-\omega)\boldsymbol{U}_{i,j} + \omega\boldsymbol{U}_{i+1,j} \tag{3-19}$$

$$\boldsymbol{U}^{-}_{i+1/2,j} = \omega\boldsymbol{U}_{i,j} + (1-\omega)\boldsymbol{U}_{i+1,j} \tag{3-20}$$

where the weight factor ω is defined as:

$$\omega = \frac{1}{2}\frac{1}{(\alpha\nabla p)^2 + 1}$$
$$\nabla p = \frac{\left|p_{i,j} - p_{i+1,j}\right|}{\min\left(p_{i,j} - p_{i+1,j}\right)} \quad \textbf{(3-21)}$$

Here the parameter α was used to determine a weight factor ω. Normally, a larger α induces a more stable computation but with high numerical dissipation. It is obvious that this scheme will transfer to the original Steger–Warming scheme in the region where the pressure changes sharply, e.g., near the shock, to increase the numerical stability. Meanwhile, in the region of pressure changes gently, e.g., in the boundary layer, the modified scheme keeps the high viscid resolution. In this study, α = 6 was set to guarantee accuracy and numerical stability.

Although the modified Steger–Warming scheme has a 1st order numerical accuracy, to improve the numerical accuracy to higher-order, the MUSCL (Monotonic Upstreamcentered Scheme for Conservation Laws) Scheme was used to reconstruct the primitive values. $\boldsymbol{Q}_{\mathrm{L}}$ and $\boldsymbol{Q}_{\mathrm{R}}$ can be written as:

$$\boldsymbol{Q}_L = \boldsymbol{Q}_{i,j} + \frac{1}{2}\, limiter(\boldsymbol{Q}_{i+1,j} - \boldsymbol{Q}_{i,j}, \boldsymbol{Q}_{i,j} - \boldsymbol{Q}_{i-1,j}) \quad \textbf{(3-22)}$$

$$\boldsymbol{Q}_R = \boldsymbol{Q}_{i+1,j} - \frac{1}{2}\, limiter(\boldsymbol{Q}_{i+2,j} - \boldsymbol{Q}_{i,j}, \boldsymbol{Q}_{i+1,j} - \boldsymbol{Q}_{i,j}) \quad \textbf{(3-23)}$$

where $\boldsymbol{Q}$ is:

$$\boldsymbol{Q} = (\rho_s\ u\ v\ p\ e)^{\mathrm{T}} \quad \textbf{(3-24)}$$

The limiter function used in this study is van Leer.

3.2.3. Time marching methods

Conduct a backward Euler discretization from the Eq.**(3-14)**:

$$\begin{aligned}
&\frac{\Delta \boldsymbol{U}_{i,j}^{n}}{\Delta t} = \\
&-\frac{1}{V_{i,j}}\left[\left(\boldsymbol{F}_{n,i+\frac{1}{2},j} - \boldsymbol{F}_{vn,i+\frac{1}{2},j}\right)S_{i+\frac{1}{2},j} - \left(\boldsymbol{F}_{n,i-\frac{1}{2},j} - \boldsymbol{F}_{vn,i-\frac{1}{2},j}\right)S_{i-\frac{1}{2},j}\right]^{n+1} \\
&-\frac{1}{V_{i,j}}\left[\left(\boldsymbol{G}_{n,i,j+\frac{1}{2}} - \boldsymbol{G}_{vn,i,j+\frac{1}{2}}\right)S_{i,j+\frac{1}{2}} - \left(\boldsymbol{G}_{n,i,j-\frac{1}{2}} - \boldsymbol{G}_{vn,i,j-\frac{1}{2}}\right)S_{i,j-\frac{1}{2}}\right]^{n+1} \\
&+\boldsymbol{S}_{\boldsymbol{h}\,i,j}^{n+1}
\end{aligned} \quad \textbf{(3-25)}$$

By linearizing the fluxes and source term, the equation can be further rewritten as:

$$\begin{aligned}
&\frac{\Delta \boldsymbol{U}_{i,j}^{n}}{\Delta t} = \\
&-\frac{1}{V_{i,j}}\left\{\left[\left(\frac{\partial \boldsymbol{F}_n}{\partial \boldsymbol{U}}\Delta \boldsymbol{U}\right)_{i+\frac{1}{2},j} - \left(\frac{\partial \boldsymbol{F}_{vn}}{\partial \boldsymbol{U}}\Delta \boldsymbol{U}\right)_{i+\frac{1}{2},j}\right]S_{i+\frac{1}{2},j}\right\}^{n} \\
&+\frac{1}{V_{i,j}}\left\{\left[\left(\frac{\partial \boldsymbol{F}_n}{\partial \boldsymbol{U}}\Delta \boldsymbol{U}\right)_{i-\frac{1}{2},j} - \left(\frac{\partial \boldsymbol{F}_{vn}}{\partial \boldsymbol{U}}\Delta \boldsymbol{U}\right)_{i-\frac{1}{2},j}\right]S_{i-\frac{1}{2},j}\right\}^{n}
\end{aligned} \quad \textbf{(3-26)}$$

$$-\frac{1}{V_{i,j}}\left\{\left[\left(\frac{\partial \boldsymbol{G}_n}{\partial \boldsymbol{U}}\Delta \boldsymbol{U}\right)_{i,j+\frac{1}{2}}-\left(\frac{\partial \boldsymbol{G}_{vn}}{\partial \boldsymbol{U}}\Delta \boldsymbol{U}\right)_{i,j+\frac{1}{2}}\right]S_{i,j+\frac{1}{2}}\right\}^n$$
$$+\frac{1}{V_{i,j}}\left\{\left[\left(\frac{\partial \boldsymbol{G}_n}{\partial \boldsymbol{U}}\Delta \boldsymbol{U}\right)_{i,j-\frac{1}{2}}-\left(\frac{\partial \boldsymbol{G}_{vn}}{\partial \boldsymbol{U}}\Delta \boldsymbol{U}\right)_{i,j-\frac{1}{2}}\right]S_{i,j-\frac{1}{2}}\right\}^n$$
$$+\left(\frac{\partial \boldsymbol{S_h}}{\partial \boldsymbol{U}}\right)_{i,j}^n+\boldsymbol{RHS}_{i,j}^n$$

Then, vector split for the inviscid flux as:

$$\left(\frac{\partial \boldsymbol{F}_n}{\partial \boldsymbol{U}}\Delta \boldsymbol{U}\right)_{i+\frac{1}{2},j}=(\boldsymbol{A}\Delta \boldsymbol{U})_{i+\frac{1}{2},j}=(\boldsymbol{A}^+\Delta \boldsymbol{U})_{i+\frac{1}{2},j}+(\boldsymbol{A}^-\Delta \boldsymbol{U})_{i+\frac{1}{2},j}$$
$$=(\boldsymbol{A}^+\Delta \boldsymbol{U})_{i,j}+(\boldsymbol{A}^-\Delta \boldsymbol{U})_{i+1,j} \quad \textbf{(3-27)}$$

The viscid flux can be written as:

$$\left(\frac{\partial \boldsymbol{F}_v}{\partial \boldsymbol{U}}\Delta \boldsymbol{U}\right)_{i+\frac{1}{2},j}=(\boldsymbol{L}\Delta \boldsymbol{U})_{i+1,j}-(\boldsymbol{L}\Delta \boldsymbol{U})_{i,j} \quad \textbf{(3-28)}$$

Jacobian of source terms:

$$\left(\frac{\partial \boldsymbol{S_h}}{\partial \boldsymbol{U}}\right)_{i,j}^n=\boldsymbol{S}_{i,j}^n \quad \textbf{(3-29)}$$

Then, the equation can be written as:

$$\boldsymbol{M}_{i,j}\Delta \boldsymbol{U}_{i,j}^n+\boldsymbol{SUB1}_{i,j}\Delta \boldsymbol{U}_{i-1,j}^n+\boldsymbol{SUP1}_{i,j}\Delta \boldsymbol{U}_{i+1,j}^n$$
$$+\boldsymbol{SUB2}_{i,j}\Delta \boldsymbol{U}_{i,j-1}^n+\boldsymbol{SUP2}_{i,j}\Delta \boldsymbol{U}_{i,j+1}^n=\boldsymbol{DU}_{i,j}^n \quad \textbf{(3-30)}$$

Here, the coefficient matrixes are:

$$\boldsymbol{M}_{i,j}=\boldsymbol{I}+\frac{\Delta t}{V_{i,j}}\left[(\boldsymbol{A}^++\boldsymbol{L})_{i,j}S_{i+\frac{1}{2},j}-(\boldsymbol{A}^--\boldsymbol{L})_{i,j}S_{i-\frac{1}{2},j}\right]$$
$$+\frac{\Delta t}{V_{i,j}}\left[(\boldsymbol{B}^++\boldsymbol{M})_{i,j}S_{i,j+\frac{1}{2}}-(\boldsymbol{B}^--\boldsymbol{M})_{i,j}S_{i,j-\frac{1}{2}}\right]-\Delta t\boldsymbol{S}_{i,j}^n \quad \textbf{(3-31)}$$

$$\boldsymbol{SUB1}_{i,j}=-\frac{\Delta t}{V_{i,j}}(\boldsymbol{A}^++\boldsymbol{L})_{i-1,j}S_{i-\frac{1}{2},j}$$
$$\boldsymbol{SUP1}_{i,j}=\frac{\Delta t}{V_{i,j}}(\boldsymbol{A}^--\boldsymbol{L})_{i+1,j}S_{i+\frac{1}{2},j} \quad \textbf{(3-32)}$$

The method of solving this large sparse matrix highly affects the cost of computation. Although LU–SGS method is successfully used in many compressible fluid computations, this method still has defects. To maintain the predicted accuracy of heat flux, the small grid size normal to the surface is needed, which leads to a high cell aspect ratio in the same total grid number. It causes a low efficiency for a viscid hypersonic simulation. Thus, to improve computational performance, a Data Parallel Point Relaxation(DPPR) method was applied to solve the sparse matrices in the present study.

3.3. Validations

3.3.1. Validations of the plasma model

First, the formation of induced flow on a flat plate in quiescent air was studied. To validate the OZIPP model, the conditions based on Zheng's experiment[88] were selected for comparison with numerical simulations. The computational domain is 40 mm and 20 mm with a grid resolution of 1000 × 500 in the x and y directions, respectively. The plasma region starts at x = 0. The peak voltage, atmospheric pressure, and temperature are set at 40 kV, 101325 Pa, and 300 K, respectively.

The induced shock wavefront consists of two parts: a semispherical shock and a planar shock, as clearly shown in Figure 3-1. The semispherical shock spreads starting from the alignment line of the exposed electrode and insulated electrode, and it is observed to be significantly weaker on the cathode side. The planar shock propagates upward parallel to the discharge streamers, which corresponds to the most gas heating energy. Meanwhile, a rarefaction wave is formed and propagates toward the plate surface. This rarefaction wave is then reflected from the surface and catches up to the induced shock wavefront. Finally, the induced shock wave is weakened and decelerates to a sonic wave due to the interaction with the rarefaction wave. The good agreement between the experimental and numerical Schlieren images indicates that the OZIPP model can accurately reproduce the propagation of the induced shock and hence the distribution of the gas heating energy implicitly. The simulated distribution of the gas heating energy density is shown in Figure 3-2(a). It can be seen clearly that both the longitudinal and vertical energy deposition distributions are nonuniform. The gas heating energy density decreases with the distance from the downstream edge of the exposed electrode in the discharge streamers' direction. Notably, the air density strongly changes in this region due to the fast gas heating, indicated by the white area near the surface in the numerical Schlieren images (Figure 3-1). Figure 3-2(b) shows the simulated overpressure at the shock wavefront in the cases of 5, 10, 20, and 30 μs after a pulsed nanosecond discharge. It can be used to estimate the shock wave propagation velocity because the peak value indicates the induced shock wavefront location. The perturbation caused by the induced shock is distributed in a thin region and quickly disappears after the induced shock propagates, which exhibits a localized and transient nature[73].

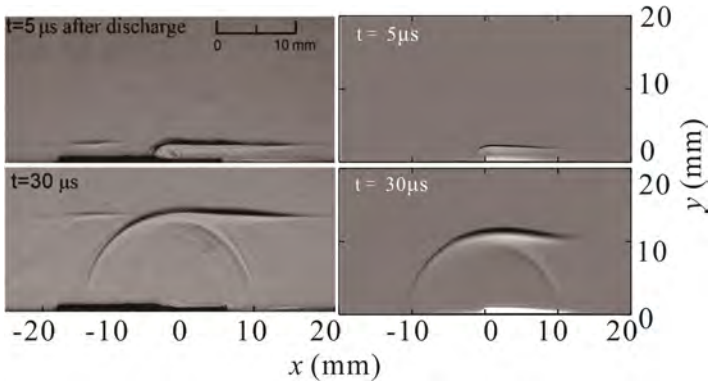

Figure 3-1. Comparison of experimental and numerical Schlieren images at different times after actuation under 40 kV (left column shows the experimental Schlieren images by Zheng *et al.*[88]; right column shows the numerical Schlieren images by the OZIPP model).

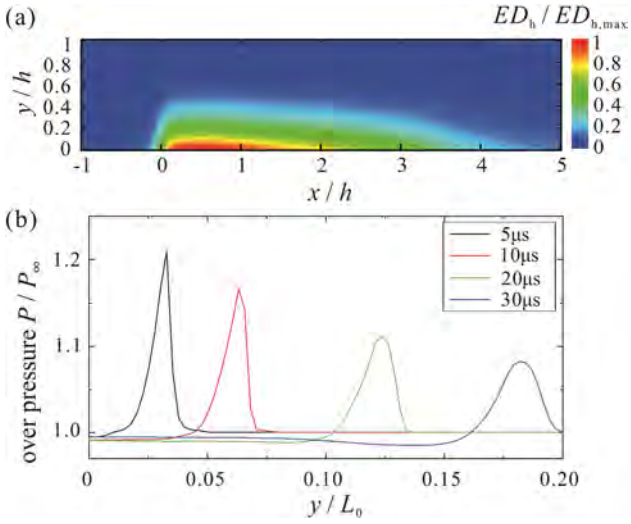

Figure 3-2. (a) Nondimensional gas heating energy density distribution and (b) overpressure distributions above the flat plate at x = 0 and t = 5, 10, 20, and 30 μs after a pulsed discharge.

3.3.2. Convergence study

The simulation comprised seven cases that were compared with each other to study the effects of NSDBD at different voltages and streamwise locations. The first case (C0) is the basic state without the actuator. The actuation voltages and actuator locations of other cases are listed in Table 3-1. Simulation cases with different parameters

Table 3-1. Simulation cases with different parameters.

Case	C0	C1	C2	C3	C4	C5	C6
V (kV)	-	25	25	25	50	50	50
L_p / L_0	-	0.33	0.50	0.67	0.33	0.50	0.67

To build the confidence of the simulations, the independence of time steps and grid numbers were investigated to maintain convergence and stability. Figure 3-3(a) shows the simulation domain. A $M_\infty = 4$ flow over a flat plate with the NSDBD plasma actuator installed at $L_p/L_0 = 0.67$ is simulated (case C6). The boundary conditions are specified as follows: the free-stream conditions are prescribed at the upper and left boundaries. A simple extrapolation outflow condition is used at the exit boundary. For the no-slip wall, isothermal conditions are specified with a wall temperature of 297 K. The distributions of dimensionless temperature T/T_w and overpressure P/P_∞ at $x/L_0 = 0.7$ (where the most gas heating energy is distributed at) and 2 μs after activation are shown in Figure 3-4. At this time and location, the plasma region will move but still keep enough high energy concentration. Thus, this time and location can be a characteristic of the thermal heat region of NSDBD in a given freestream condition to estimate the simulation convergence. Four different time steps of 0.1, 0.2, 0.5, and 1 ns under the same grid cells (total of 0.72×10^6) were used to validate the time step independence. It is noted that the maximum temperature along the wall-normal direction is quite susceptible to the time steps, and the temperature distribution shares a similar tendency. Notably, because the heating gas plays a dominant role in flow control, an accurate prediction of the heat input (consequently the temperature distribution) is particularly important. The temperature distribution result of 0.2 ns reaches time step independence. In contrast, the sensitivity of time steps to overpressure is relatively limited. The changes in temperature and pressure with grid refinement are shown in Figure 3-4(b). Three grid numbers of 0.18×10^6 (800 × 225), 0.36×10^6 (800 × 450), and 0.72×10^6 (1600 × 450) were used under the same time step (0.2 ns). The meshes are clustered near the leading edge, corner, and wall. Note that the mesh spacing at the wall is 1×10^{-6} m for all three cases(see Figure 3-3(b)), yielding a nondimensional wall distance of $y^+_{wall} \approx 0.3$. The present simulations show that the temperature distributions of grid schemes 0.36×10^6 and 0.72×10^6 are almost the same. The two-dimensional flow fields are almost identical for both cases. To ensure the convergence of the simulation, the mesh scheme with a total number of 0.72×10^6 grids and a time step of 0.2 ns are selected for all the simulations presented later in this study.

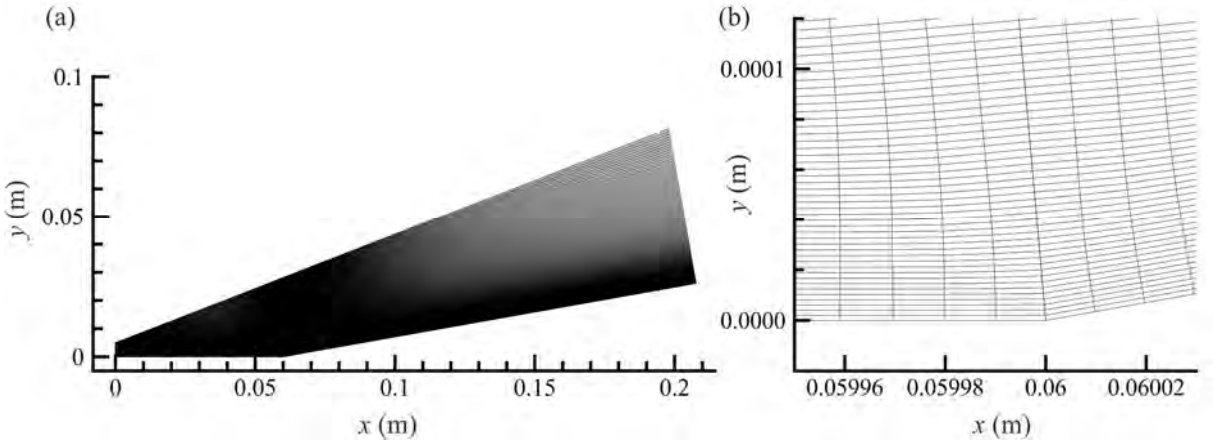

Figure 3-3. (a) Mesh domain of total simulation region for a compression corner; (b) the grid distribution at the corner (Grid 0.72×10^6 (1600×450)).

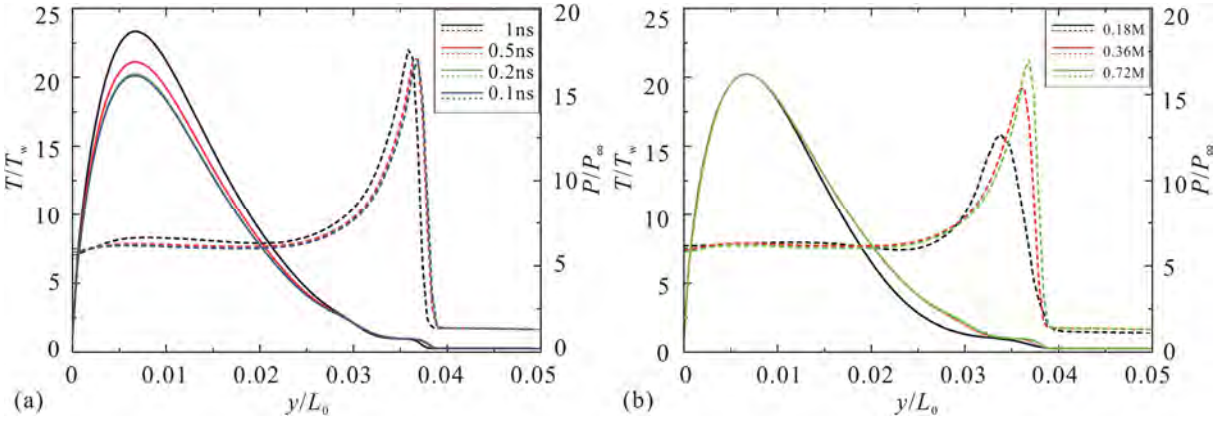

Figure 3-4. The distributions of dimensionless temperature (solid lines) and overpressure (dashed lines) for flow over a flat plate at x/L_0 = 0.7 and 2 μs after activation, with the change in (a) time steps and (b) grid cells. L_p/L_0 = 0.67 (case C6) and M_∞ = 4.

3.4. Case study

3.4.1. Flow structures over a flat plate

The control effects on a flat plate boundary layer flow at M_∞ = 4 are studied first. To compare with cases on the compression corner, the location and applied voltage of NSDBD of case C6 are selected at L_p/L_0 = 0.67 and 50 kV. The instantaneous vorticity contours at t^* = 0.1, 0.15, and 0.2 are shown in Figure 3-5(a)(b)(c), respectively. Here, the dimensional t^* is defined as t/t_0. At the beginning of the activation, the induced vortex can be observed clearly upstream of the heated gas, leading to a separation bubble with an induced separation shock (ISS, marked with a red solid line). The high momentum fluid is transported into the boundary layer under the entrainment of the induced vortex. Then, the separated flow reattaches to the surface and pushes the heated gas to move downstream. Meanwhile, the induced separation shock interacts with the induced semispherical shock (IS, marked with a blue solid line) by the NSDBD itself, forming a weak reflected expansion wave behind the

shock. The streamwise velocity profiles at three different locations (see Figure 3-6) become more plentiful in the boundary layer accompanied by a conspicuous decrease above the boundary layer, which indicates momentum exchange between the boundary layer and the upper flow. In the early stage of activation shown by the red dashed line in Figure 3-6, the velocity increment in the boundary layer is significant (Figure 3-6(b)), but there is a rare difference downstream compared to the baseline (Figure 3-6(c)) because the high-speed fluid has not yet propagated there. At the next moment at the same location (blue dashed-dotted line in Figure 3-6(c)), the velocity in the boundary layer increases, but this increment decreases at the subsequent moment (green-dotted line in Figure 3-6(c)). This indicates that the momentum exchange mainly exhibits a transient timeslot after excitation and a moving region around the heated gas depending on the freestream velocity. Notably, the ISS will decrease the velocity downstream. It can be seen that the velocity defect obtains the least influence of ISS at the location farthest away from it (x/L_0 = 1.0) at the same moment, e.g., the blue dashed-dotted lines in Figure 3-6(a)(b)(c). Figure 3-5(d)(e)(f) depict the early-stage development of heated gas. The residual heat is impelled downstream and dissipates very quickly. The maximum temperature decreases by approximately half within 10 μs. Notably, a perturbance occurs at the front edge of the residual heat, which is marked with an open circle in the left column of Figure 3-5. It seems to be generated by a pure thermal perturbance other than the propagation of the induced shock (IS). As shown in Figure 3-5(a), the shock-induced perturbance moves a distance away from the discharge region and is presented as a distortion of streamlines behind the shock front. This implies that the flow field can be disturbed by the propagation of IS, but the perturbance is transient and localized in the vicinity of the IS front. It has little contribution to the changes in the flow field when the IS has moved outside the plasma region.

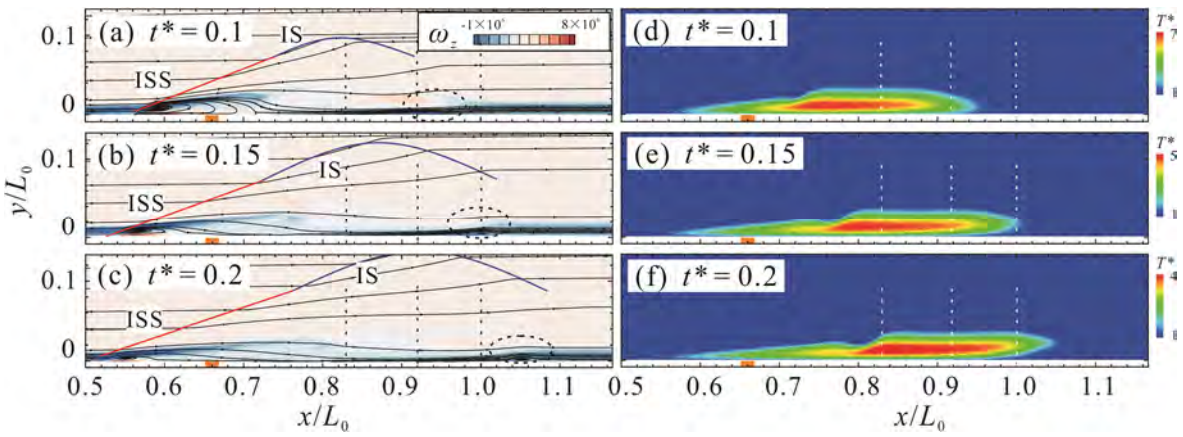

Figure 3-5. Contours of instantaneous vorticity ω_z (left column) with superimposed streamlines and nondimensional temperature $T^* = T/T_w$ (right column) at t^* = (a)(d) 0.1; (b)(e) 0.15; and (c)(f) 0.2. The actuator location is at L_p/L_0 = 0.67, and it is operated at 50 kV on a flat plate.

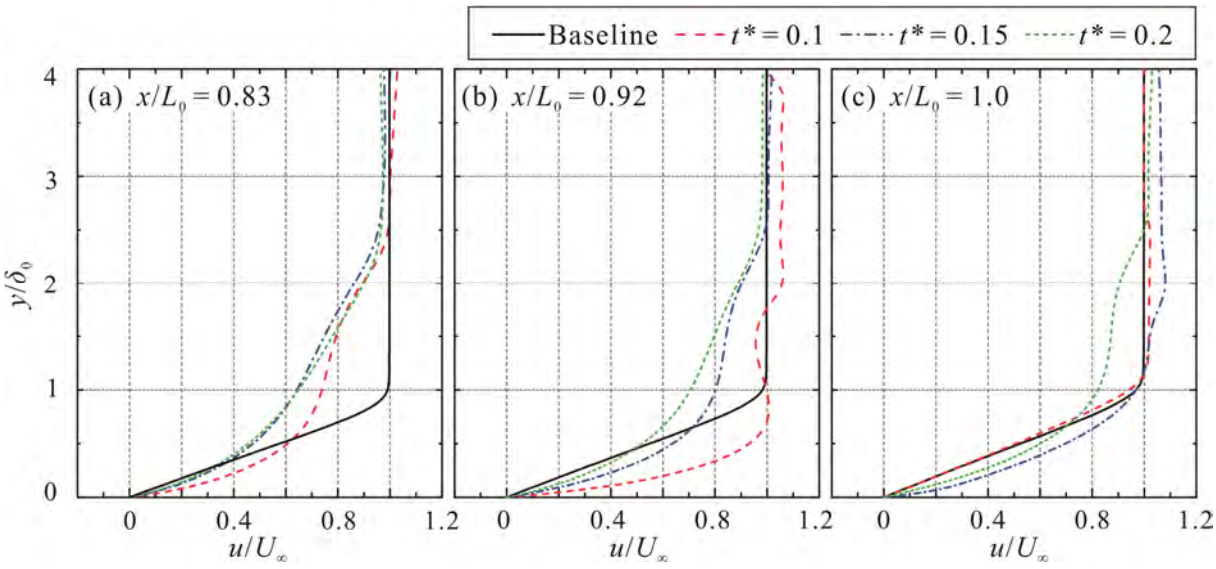

Figure 3-6. Streamwise velocity profiles in the vicinity of the boundary layer with and without control at (a) x/L_0 = 0.83, (b) x/L_0 = 0.92, and (c) x/L_0 = 1.0.

3.5. Remark

In this chapter, the NSDBD plasma models were introduced. The numerical methods of the multi-block parallel finite-volume CFD solver PHAROS are detailed presented. To build confidence in the simulations, the independence of time steps and grid numbers were investigated to maintain convergence and stability. The distributions of dimensionless temperature T/T_w and overpressure P/P_∞ at x/L_0 = 0.7 and 2 μs after activation on a flat plate boundary layer flow at M_∞ = 4 were selected to estimate the numerical simulation convergence. Meanwhile, its local control effects are studied, and it illustrates that the shock-induced perturbance has little contribution to the changes in the flow field, but a significant momentum exchange happens between the boundary layer and the upper flow after the activation.

CHAPTER 4 Characteristics of DBD plasma actuators

In this chapter, the characteristics of different DBD plasma actuators on the flat plate model have been studied. Even though the characteristics have been widely investigated[14-16, 76], the performance of DBD plasma actuators and PSVGs in the applications may be quite different from case to case due to the setups. Therefore, it is necessary to examine the same DBD plasma actuators before applying them on the specific model. Experiments were conducted with DBD plasma actuators on a flat plate with the same layout as those installed on the models. First, the electrical properties and induced flows of ACDBD and PSVGs were studied. As the most interested in a flow control field, the thermal effects of the NSDBD with varying pulse voltages and pulse repetitive frequencies (PRFs) under different air pressures ranging from 0.1 to 1 bar are studied experimentally.

4.1. Characteristic of a straight alternating-current DBD plasma actuator (ACDBD)

All the experiments of examination of actuators' performance were conducted in the wind tunnel in quiescent air. The voltage and current in the circuit (in Figure 2-5) were acquired by probes that are connected to the oscilloscope, and the data was recorded on the computer. The sampling frequency of the oscilloscope was 500 MHz, which was large enough to capture the discharge processing (usually with a duration of 10-20 ns)[99]. The current in the circuit was calculated from the voltage on the 100 Ω non-inductive resistor. Therefore, the power consumption was estimated.

4.1.1. Electrical characteristics

The voltages and currents of a traditional straight DBD plasma actuator are shown in Figure 4-1. The frequency of the AC power supply is 10 kHz from 12 kV to 18 kV. And all the voltages were acquired during 200 s. For Kriegseis's research, the currents of DBD plasma actuators can be divided into two parts, the conduction current and the displacement current[100]. The conduction current can be observed in Figure 4-1 as sharp pulses. The dominant discharges occurred during the positive-going cycle (the applied voltage from the minimum to the maximum). The change of applied peak-peak voltage affected the amplitude of the current peaks as well as the duration of discharging and the starting time. The maximum value of positive current peaks increased from 75 mA to 200 mA. The initial discharge advanced from 1.4×10^{-5} s to 0.2×10^{-5} s. Meanwhile, the duration extended about 1×10^{-5} s to 2×10^{-5} s. In the negative-going cycle, the tendency of amplitude and start time of the negative current pulses are similar, but it can be neglected compared to enormous positive current pulses.

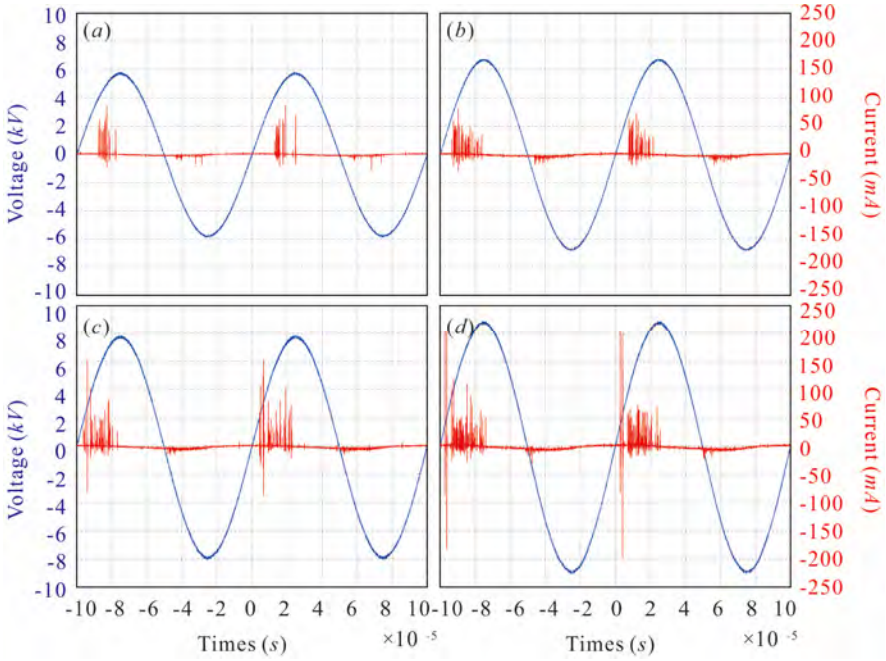

Figure 4-1. Voltages and currents of a traditional DBD plasma actuator with applied voltages (a) V_{pp} = 12 kV; (b) V_{pp} = 14 kV; (c) V_{pp} = 16 kV; (d) V_{pp} = 18 kV.

The accurate measurement of power consumption by DBD plasma actuators is a challenge due to the characteristics of the actuator current signal[77]. A *Q-V* diagram is the most common usage to determine the active power dissipated in the discharge using the area covered by the hysteresis loop[101]. In some of the available literature, the equations derived for the power calculation are based upon the geometric features of the *Q-V* diagram by assuming a perfect parallelogram[102].

Figure 4-2(a) shows a typical example of instant *Q-V* cyclograms (Lissajous figures) of the DBD plasma actuator with V_{pp} = 18 kV, which includes important details necessary to estimate the electric performance of the actuator[100]. It is obvious that the electric charge Q was increasing during the operation. At t = 20 s, the maximum electric charge in the circuit was Q = 63.4 nC; while at t = 200 s, it increased to Q = 68.9 nC. To better understand the temporal behavior of the DBD plasma actuator, two significant capacitance values C_{cold} for the non-ionization (cold) capacitance of the actuator and C_{eff} for the effective ionization capacitance are introduced (see dashed lines in Figure 4-2(a)). The local slopes dQ/dV were calculated within a quarter of the applied voltage cycle and then the averaged slope was obtained as the instant capacitance value. The result of this method was very close to that produced by the capacitance histogram analysis[100]. As can be seen from the inset graph in Figure 4-2(b), both the cold capacitance C_{cold} and the effective capacitance C_{eff} were maintained constant during the experiment with V_{pp} = 18 kV. Therefore, the capacitor properties of the DBD plasma actuator were unaffected by the operation duration in this experiment. As expected, the time-averaged cold capacitance was fixed at a constant value $C_{cold} \approx$ 4.2 pF in all cases. Meanwhile, the effective capacitance increased from C_{eff} = 7.8 pF at V_{pp} = 12 kV to C_{eff} = 14.0 pF at V_{pp} = 18 kV. The red dashed line indicated that the time-averaged effective capacitance was proportional to the applied

peak-to-peak voltage. Figure 4-2(c) shows temporal evolutions of the actuator power consumption with various V_{pp}, obtained using Eq.(4-3) based on the capacitor method. For instance, in the case of V_{pp} = 18 kV, the power consumption in per spanwise length is about $P_E \approx 65$ W/m at the beginning; it then increases exponentially to $P_E \approx 72$ W/m at t = 200 s. Similar exponential increases of the power consumption are also noted in the other cases. Thus, it can be known that the electric performance of the DBD plasma actuator was time-dependent and it varied a lot at the early time of the activation. In other words, the DBD plasma actuator needs a period of operation time to be steady. It is also obvious in Figure 4-2(c) that the power consumption increased greatly when the applied V_{pp} was increased. For comparison, the power consumptions at t = 200 s in these cases are plotted in Figure 4-2(d). One can see the power consumption of the actuator is almost proportional to the 3.5 power function of V_{pp} (as shown in Eq.(4-1)), which is consistent with the previous studies[103].

$$\frac{P_E}{f^{1.5} \cdot V_{pp}^{3.5}} = const. \tag{4-1}$$

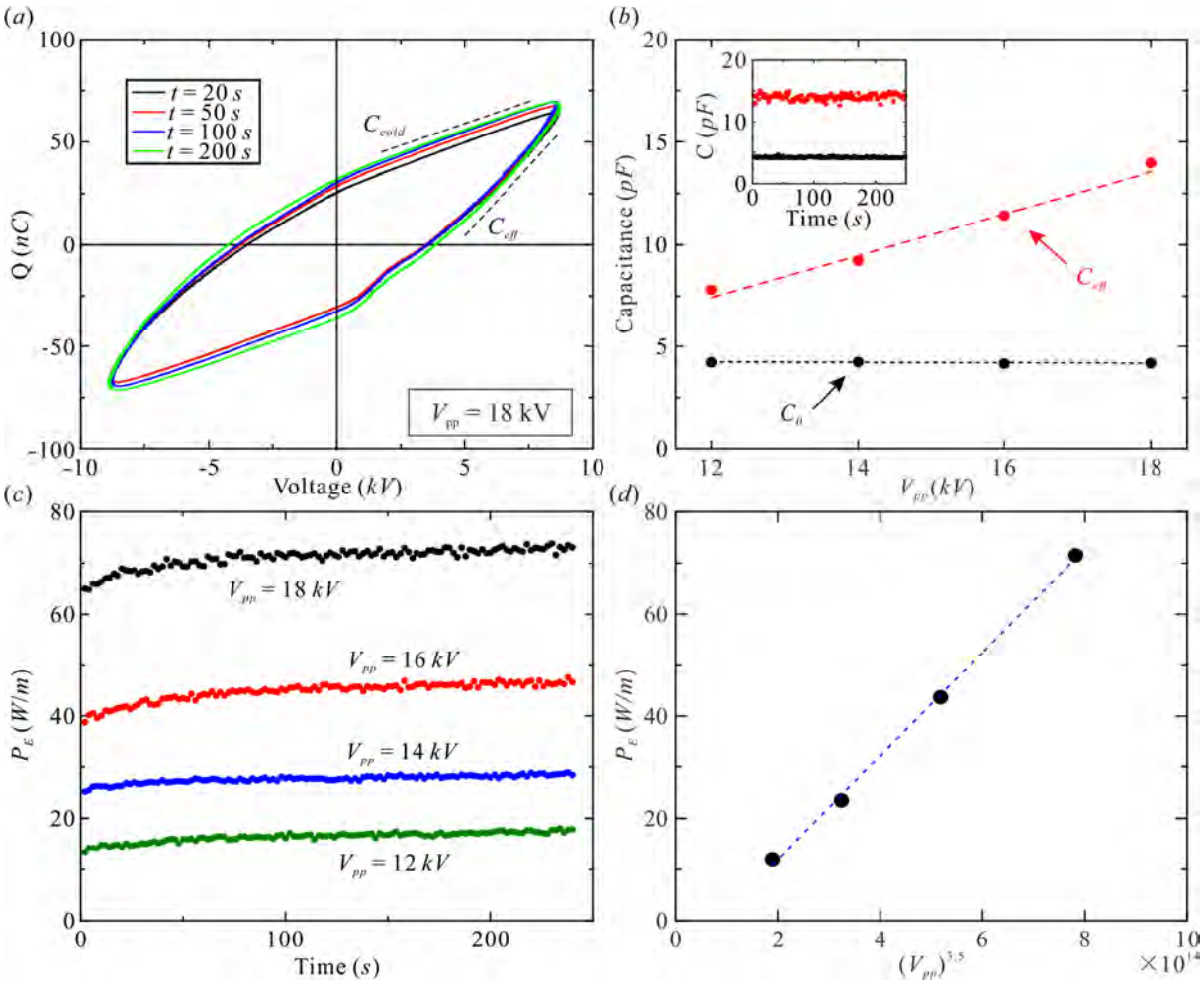

Figure 4-2. (a) The electric charge Q through the circuit against the applied voltage with V_{pp} = 18 kV (Lissajous figures); (b) the cold capacitance C_{cold} and the effective capacitance C_{eff} of the

DBD plasma actuator with different V_{pp}; (c) evolutions of the power consumption; and (d) the power consumption at t = 200 s with different V_{pp}.

In this study, two different methods were used to calculate power consumption. One is calculated by integrating the voltage and current (*V-I* method)[104], and the other uses a *Q-V* diagram. 100 cycles were used to acquire an average result for decreasing the error. For the *V-I* method, the electric power consumption of the DBD per unit length is defined as:

$$P_E = \frac{1}{TL}\int_0^T V_{DBD}(t) \times I(t)\, dt \tag{4-2}$$

For the *Q-V* method, the electric power consumption is given by:

$$P_E = \frac{1}{TL}\int_0^T V_{DBD}(t) \cdot C_m \frac{dV_m(t)}{dt}\, dt = \frac{1}{TL}\oint V_{DBD}(t) \cdot dQ(t) \tag{4-3}$$

where C_m is the capacitance of the monitor capacitor, V_m is the voltage of the monitor capacitor. Eq. (4-3) shows that the average power dissipated in a full discharge cycle is given by the area bounded by the *Q-V* diagram, multiplied by the frequency of the discharge cycle[105].

Figure 4-3 shows the temporal evolutions of the actuator power consumption with various V_{pp}, obtained using Eq.(4-2) and Eq.(4-3) based on the *V-I* and the *Q-V* method. The solid circles illustrate the results of the *V-I* method and the hollow circles show the data with the *Q-V* method. The two methods show a similar tendency, and in Ashpis's opinion[77], the *Q-V* method is more accurate. The superior performance is primarily due to the limited dynamic range and the adequate voltage level of the monitor capacitor signal, which allows the effect of the scope noise floor to be diminished and consequently improves the signal noise ratio enough for accurate power calculation[77]. It is also obvious in Figure 4-3(e) that the power consumption increased greatly when the applied V_{pp} was increased. For comparison, the power consumption at t = 200 s, in this case, is plotted in Figure 4-3(e). The power consumption difference calculated by the *V-I* method is more significant under a larger applied voltage.

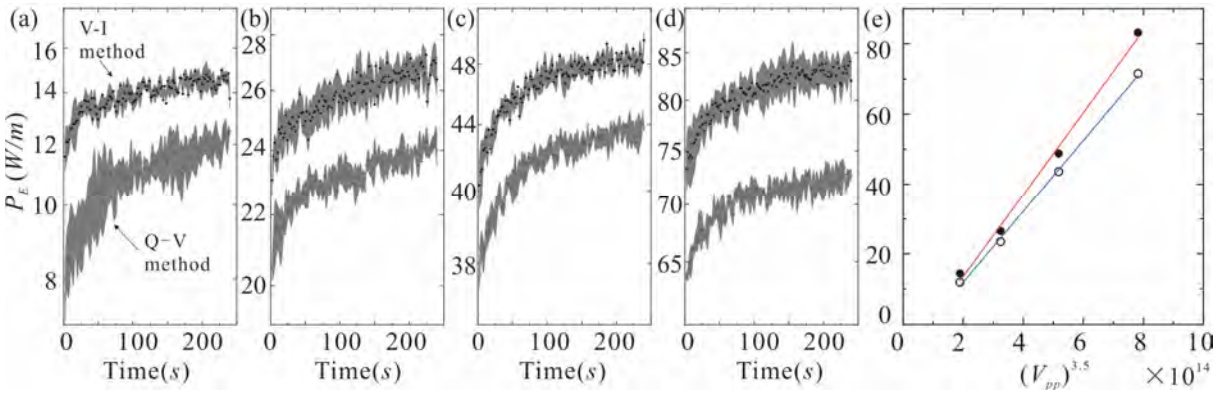

Figure 4-3. volutions of the power consumption with (a) V_{pp} = 12 kV; (b) V_{pp} = 14 kV; (c) V_{pp} = 16 kV; (d) V_{pp} = 18 kV; and (e) the power consumption at t = 200 s with different V_{pp} (solid circle: *V-I* method, hollow circle: *Q-V* method).

4.1.2. Induced flow

The PIV measurement was conducted in the *x-y* plane. The data acquisition duration was 200 seconds. In Figure 4-4, the time-averaged velocity contours with the velocity vectors in the case of V_{pp} = 18 kV are demonstrated from t = 40 s to t = 200 s, with an average time step of 40 seconds. In all of the frames, the DBD plasma actuator generates a wall-jet-like ionic wind on the surface. As the working time increases, the observed velocity magnitude of the induced flow increases gently. At the same time, the region with the large velocity magnitude is obviously stretched downstream, and the position where the highest velocity occurs also moves downstream. However, the time-averaged thickness of the induced flow changes little. In this measurement, the maximum time-averaged velocity reaches 3.75 m/s in 160 ~ 200 s. While, the instantaneous velocity map at t = 200 s shows that the maximum instantaneous velocity can even exceed 4 m/s. It means that the suction force over the exposed electrode enlarged since the ionic wind (blowing) velocity increased[106]. Note that, a fraction of 1 mm velocity data near the wall surface was not acquired because of the intense reflected light on the surface in PIV measurement, although the surface has been covered with a layer of mat paint which will not affect the surface roughness. But it will not affect the accuracy of the velocity field above the data deficiency region because of the adaptive algorithms in the PIV method for boundaries.

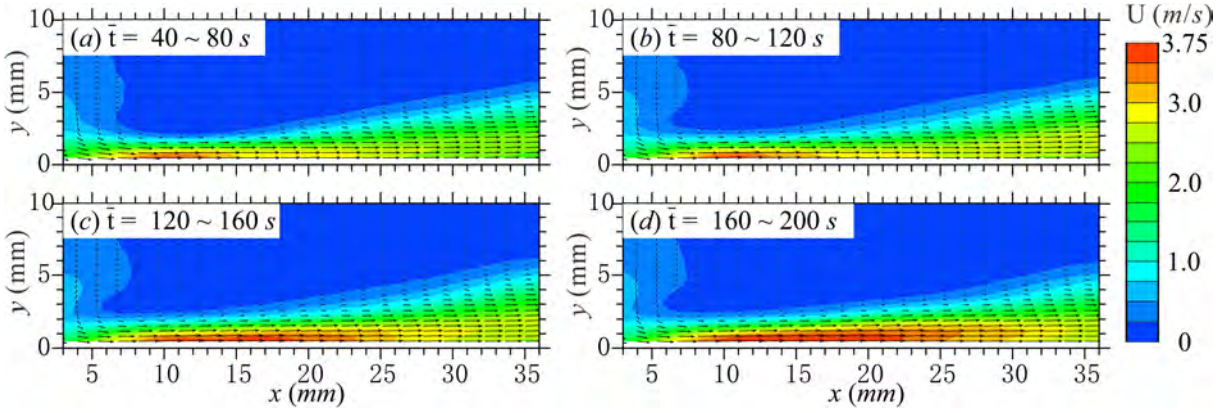

Figure 4-4. The velocity contours of the time-averaged PIV result in the *x-y* plane with the superimposed velocity vectors.(V_{pp} = 18 kV)

4.2. Characteristic of plasma streamwise vortex generators (PSVGs)

4.2.1. Electrical characteristics

To optimize the configuration of PSVGs, DBD plasma actuators with various geometries on the plate were studied. All the electrodes are made of a copper film with a thickness of 0.025 mm. For the DBD plasma actuator, the dielectric barrier layer is made of PMMA with a total thickness of 2 mm.

For the PSVGs 1-5, the dielectric barrier is made of aluminum oxide ceramics with a thickness of 1 mm. For PSVGs 6 and 7, the dielectric barrier is made of acrylic with a thickness of 1 mm. Detailed schematics of actuators are shown in Figure 4-5(a) is a traditional DBD layout; Figure 4-5(b) and (c) are PSVGs with saw teeth; and Figure 4-5(d), (e),(f),(g) and (h) are PSVGs with rectangular teeth. The critical parameters of these DBD plasma actuators are listed in Table 4-1. All the plasma actuators were driven by the AC power supply with 20 kHz.

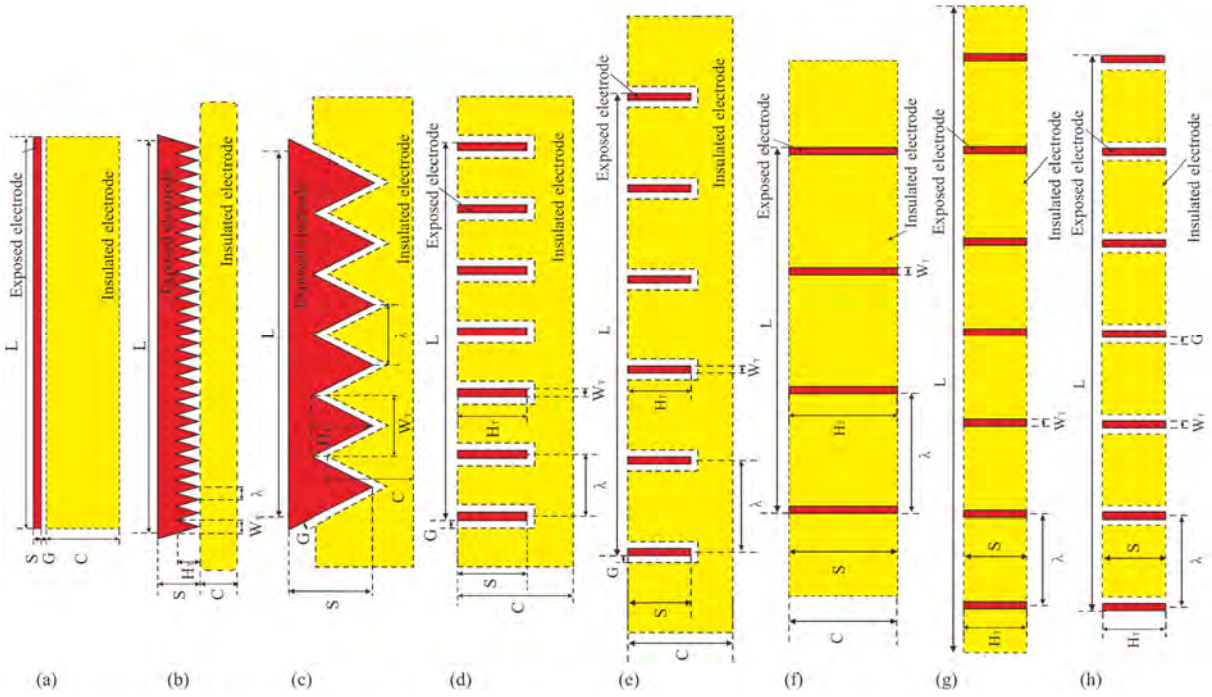

Figure 4-5. Schematics of the DBD plasma actuators. (a) tranditional DBD; (b) small saw tooth PSVGs (PSVGs-1); (c) large saw tooth PSVGs (PSVGs-2); (d) small gap PSVGs (PSVGs-3); and (e) large gap PSVGs (PSVGs-4); (f) no gap PSVGs(PSVGs-5) with large *C*; (g) no gap PSVGs (PSVGs-6) with small *C*; (h) small gap PSVGs(PSVGs-7) with small *C*.

Table 4-1. Key configuration parameters of plasma actuators.

Category	Electrode shape	L (mm)	S (mm)	C (mm)	W_T (mm)	H_T (mm)	G (mm)	λ (mm)
Meaning of parameters	/	Spanwise length of exposed electrode	Streamwise length of exposed electrode	Width of insulated electrode	Width of one tooth	Height of one tooth	An air gap between two electrodes	Exposed electrode wavelength
SDBD	Liner	100	2	20	/	/	2	/
PSVGs-1	Saw tooth	100	10	10	3.3	5	/	3.3
PSVGs-2	Saw tooth	96	18	26	16	16	2	16
PSVGs-3	Rectangular tooth	98	18	30	2	18	2	16

PSVGs-4	Rectangular tooth	132	18	30	2	18	2	25.4
PSVGs-5	Rectangular tooth	104.8	70	70	3.2	70	0	25.4
PSVGs-6	Rectangular tooth	155.2	18	18	3.2	18	0	25.4
PSVGs-7	Rectangular tooth	177.8	18	18	3.2	18	2	25.4

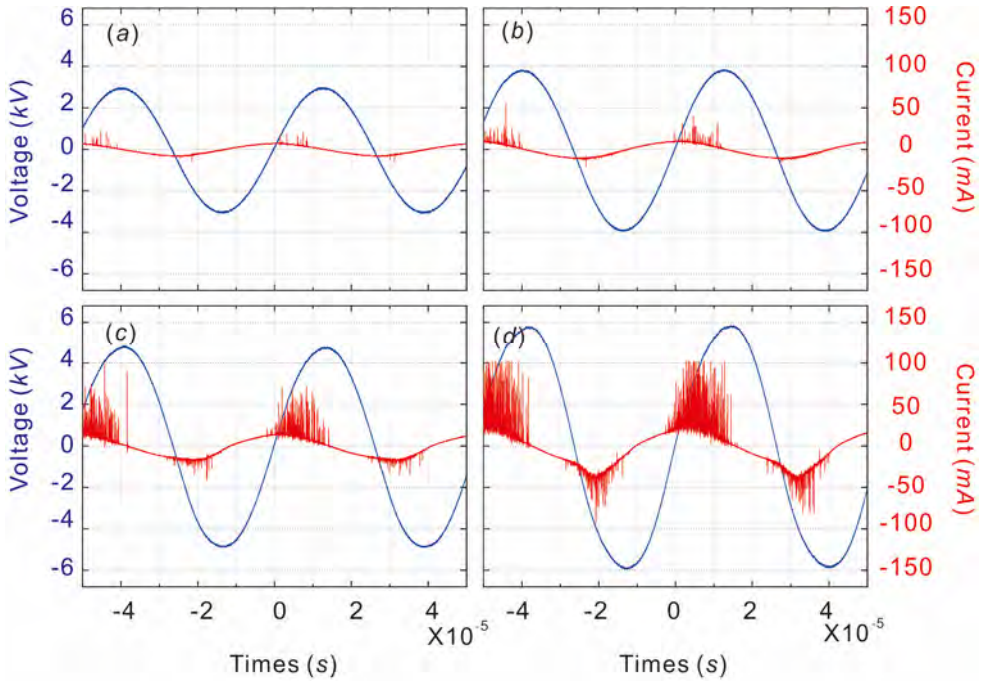

Figure 4-6. Voltages and currents of PSVG3(in Table 4-1) with applied voltages (a) V_{pp} = 6 kV; (b) V_{pp} = 8 kV; (c) V_{pp} = 10 kV; (d) V_{pp} = 12 kV with 20 kHz.

The voltages and currents of a PSVG with a rectangular configuration from 6 kV to 12 kV are shown in Figure 4-6. The tendency of current is similar to an ACDBD plasma actuator, independent of electrode layouts. It is worth noting that the discharge process is quite related to the applied voltage waveform. For a nano-second pulse voltage, the discharge is heavily different, which was investigated in detail in Chapter 4.3. The current pulse density is more intensive for a saw tooth configuration (not shown here) at the lower voltage at 6 kV to 8 kV, compared to the rectangular one (see Figure 4-6).

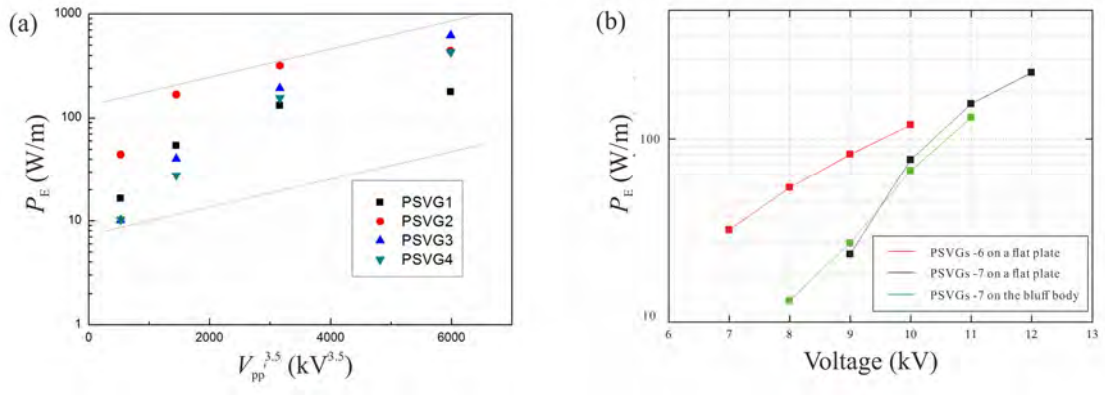

Figure 4-7. Power consumption of (a) PSVGs 1 to 4 and (b) PSVGs 6 and 7.

The power consumption of the PSVGs 1 to 4 on the flat plate is shown in Figure 4-7(a). In these cases, 80 cycles were acquired to obtain the average result. Similar to the DBD on the flat plate, the power consumption of PSVGs roughly fits the tendency of $P_E \sim V_{pp}^{3.5}$. Compared with the DBD, PSVGs have a much larger power consumption under the same peak-to-peak voltage due to their larger effective length. It is noted that the saw tooth layout (PSVGs 1 and 2) has a larger electric power at the same applied voltage compared to the rectangular ones (PSVGs 3 and 4). It may be caused by the point discharge on the tip of the tooth, which will enlarge the local discharge strength. Figure 4-7(b) shows the power consumption of PSVGs 6 and 7. Because the PSVGs were installed on the flat plate and the bluff body, the electric field is different. Thus, the P_E shares a little difference although under the same applied voltage. Note that, compared to the no gap case (PSVGs 6), the small gap case (PSVGs 7) has a smaller power consumption. It is because the local electrical field changes, directly decreasing the current vertically downward from the positive electrode. Benefiting from the gaps between two electrodes, the gap layout has a higher applied voltage with the same power consumption. Therefore, the PSVGs with gaps were applied over the D-shaped bluff body.

4.2.2. Induced flow

4.2.2.1. Continuous control

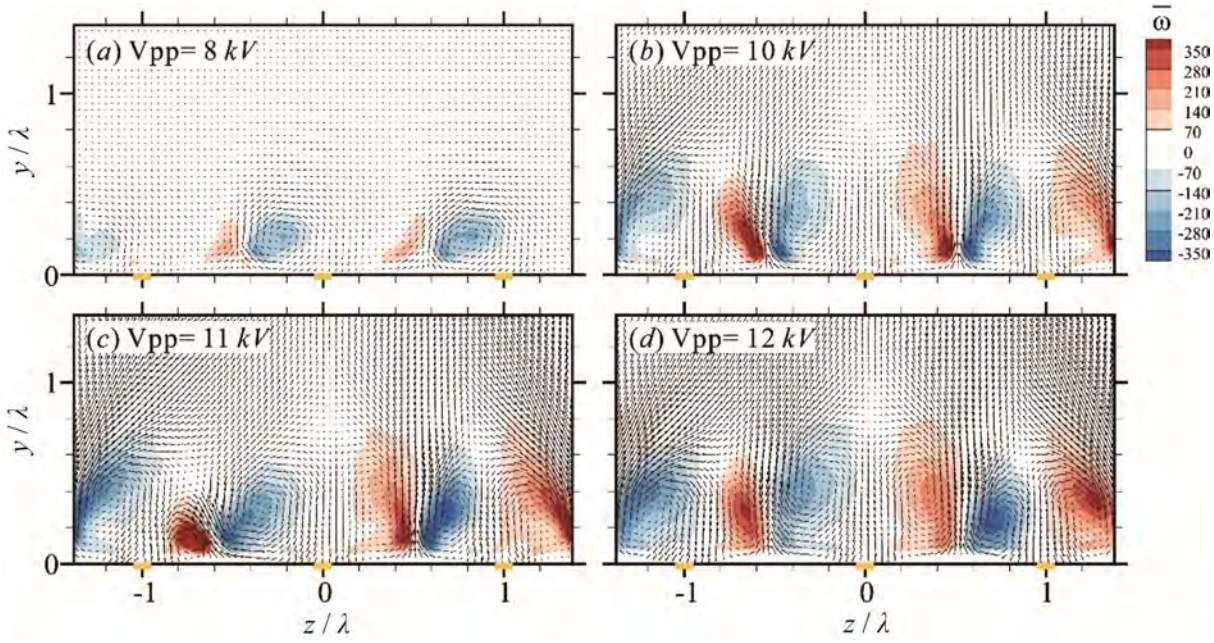

Figure 4-8. Time-averaged vorticity contour with velocity vectors of the induced flow caused by the PSVGs with V_{pp} = (a) 8kV; (b) 10kV; (c) 11kV; (d) 12kV.

Figure 4-8 shows the time-averaged induced flow structure generated by the PSVGs 5 shown in Figure 4-5(f). The PSVGs in these cases were driven by continuous power at 20 kHz. The observation plane was selected along spanwise (*y*-*z* plane). The coordinates were normalized by the spanwise interelectrode spacing. In the case with V_{pp} = 8 kV, the ionic wind was very small and ununiform. Therefore, few vorticities were generated and the induced counter-rotating vortex pair was relatively weak. At V_{pp} = 10 kV, the discharging became stronger and more uniform. Thus, pairs of the induced counter-rotating vortices were clearly observed between the electrodes. This result well agreed with others' work[16]. At the higher applied voltage, more vorticity was generated by the PSVGs. To further investigated the induced flow by PSVGs, streamwise flow structures were acquired by PIV measurement. Figure 4-9 shows the time-averaged induced flow structure generated by the PSVGs 7 at section A (1/2 λ). The PSVGs 7 in these cases were driven by continuous power. The coordinates were normalized by the spanwise interelectrode spacing. $\bar{V}$ is the average velocity in the *x*-*y* cross-section. In the case with V_{pp} = 9 kV, the induced wind was very small and ununiform. And at V_{pp} = 10 kV, the flow structure can be observed clearly in this section. The particles close to the middle part of the exposed electrode were accelerated along the *y* direction and up to the maximum speed at about *y* = 3 mm. Due to the larger electric field intensity at the downstream region, particles were accelerated downstream (a positive velocity component in *x* direction). Therefore, in the upstream region, some particles were attracted to compensate for the imbalance of flow quantity.

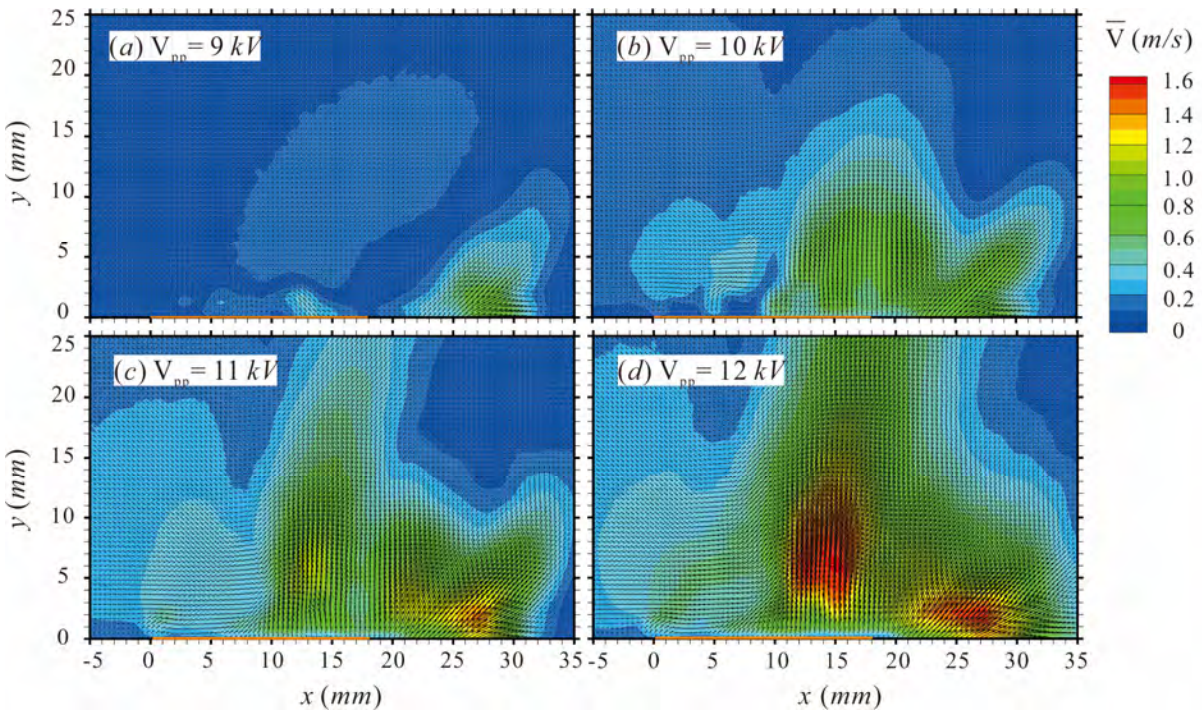

Figure 4-9. Time-averaged velocity contour with velocity vectors of the induced flow caused by the PSVGs 7 with V_{pp} = (a) 9 kV; (b) 10 kV; (c) 11 kV; (d) 12 kV at section A.

Figure 4-10 shows the time-averaged induced flow structure generated by the PSVGs 7 at section B. In the case with V_{pp} = 9 kV, the ionic wind was very small and ununiform. The particles near the downstream side of the exposed electrode (x = 18 mm) were attracted first. Because the upstream side (x = 0) was covered with tape, the electric field intensity on the downstream side was larger than the upstream side, and the downstream side was more affected by the tip discharge. Therefore, the particles were attracted to the downstream side firstly and the plasma also can be excited and detected on this side. At V_{pp} = 10 kV, it can be shown clearly that the velocity near two ends was larger than other areas. With a higher applied voltage, the phenomenon was more noticeable. At last, the PSVGs 7 was selected to fix on the bluff body because of its better performance considering the power consumption and induced flow.

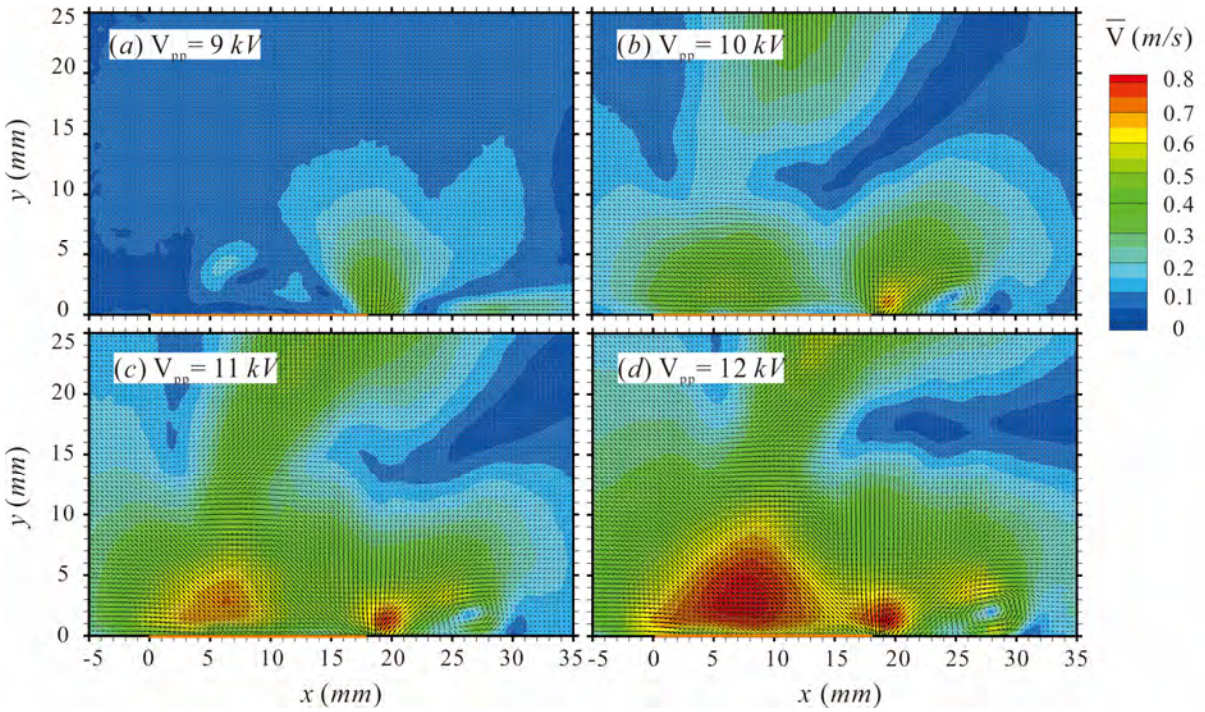

Figure 4-10. Time-averaged velocity contour with velocity vectors of the induced flow caused by the PSVGs 7 with V_{pp} = (a) 9 kV; (b) 10 kV; (c) 11 kV; (d) 12 kV at section B.

4.2.2.2. Periodic control

The modulation wave generator was used to provide a low-frequency square periodic wave to the power supply which works with a continuous sinusoidal wave of 20 kHz, shown in Figure 4-11 first line. The duty cycle (DC) can be defined as $t/T\times100\%$, where t is the active time of one cycle, and T is the total time of one cycle, as shown in Figure 4-11. And modulation frequency f_m is defined as $1/T$. Two f_m of 10 and 50 Hz were studied here and DC was set as a constant of 50%.

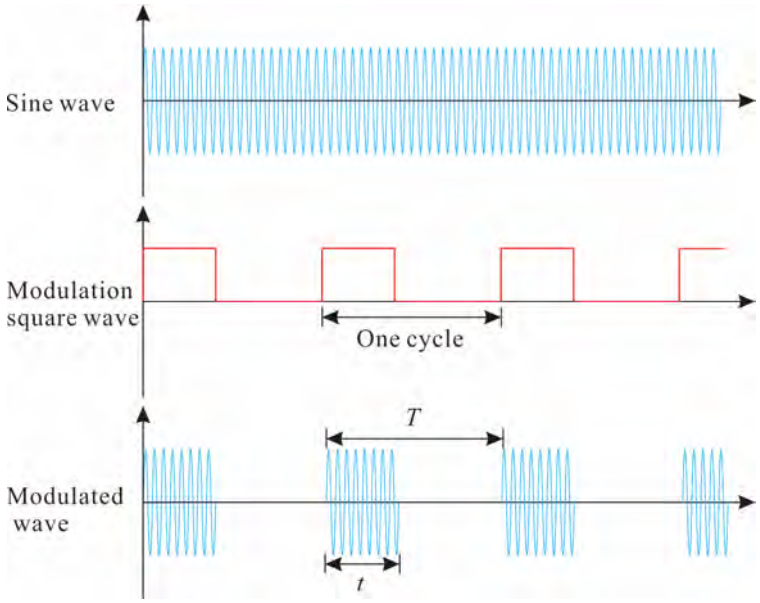

Figure 4-11. Schematics of signal modulation.

Figure 4-12 shows the phase-averaged vorticity contour with the velocity vector for the case with f_m = 10 Hz. Once the actuator was powered, strong shear flows were induced near the exposed electrodes and formed the starting vortices, as seen in Figure 4-12(b). This vortex forming process was similar with the case shown in Figure 4-12. Soon, because of the entrainment from the plasma actuator, the counter-rotating induced vortices met each other at the symmetric plane ($x/\lambda = \pm 0.5$), as seen in Figure 4-12(c). Then the vortex pairs detached from the wall due to the following induced flow and moved away vertically, as seen in Figure 4-12(d). Between the vortex pair, a strong jet-like shear flow was formed. Since the vortices detached from the wall, they were losing the vorticity feeding. This is because the dominant momentum was injected into the jet-like shear flow. Meanwhile, because of the suction above the exposed electrodes, the induced vorticity was locked in circulation zones, as marked by the dash circles in Figure 4-12(f). Once the PSVGs was switched off, the strength of the induced shear flow reduced significantly, so did the induced vortices.

Figure 4-13 shows the flow structure evolution under the effect of the PSVGs with a modulation frequency of f_m = 50 Hz. Accompanied by the increased modulation frequency, PSVGs generated more stable vortices pairs. However, the comparison between the low-frequency case (Figure 4-12) and the high-frequency case (Figure 4-13) shows that both the size and the strength of the induced vortices became smaller when the number increased. This is a result of the shorten active-duration of the PSVGs. From Figure 4-13(a) to (f), starting vortices were generated and entrained to the symmetric plane. Even though the PSVGs was turned off, the induced vortices were continuously transferred along the jet-like shear flow in the symmetric plane, seen in Figure 4-13(g) to (j). In the coming period, these vortices still existed and interacted with the newly-induced vortices. Therefore, there was a much more stable jet-like shear flow in the symmetric plane in this case than that in the low-frequency case. This indicates that using a high modulation frequency control can realize the stable vortex pairs but with less energy input.

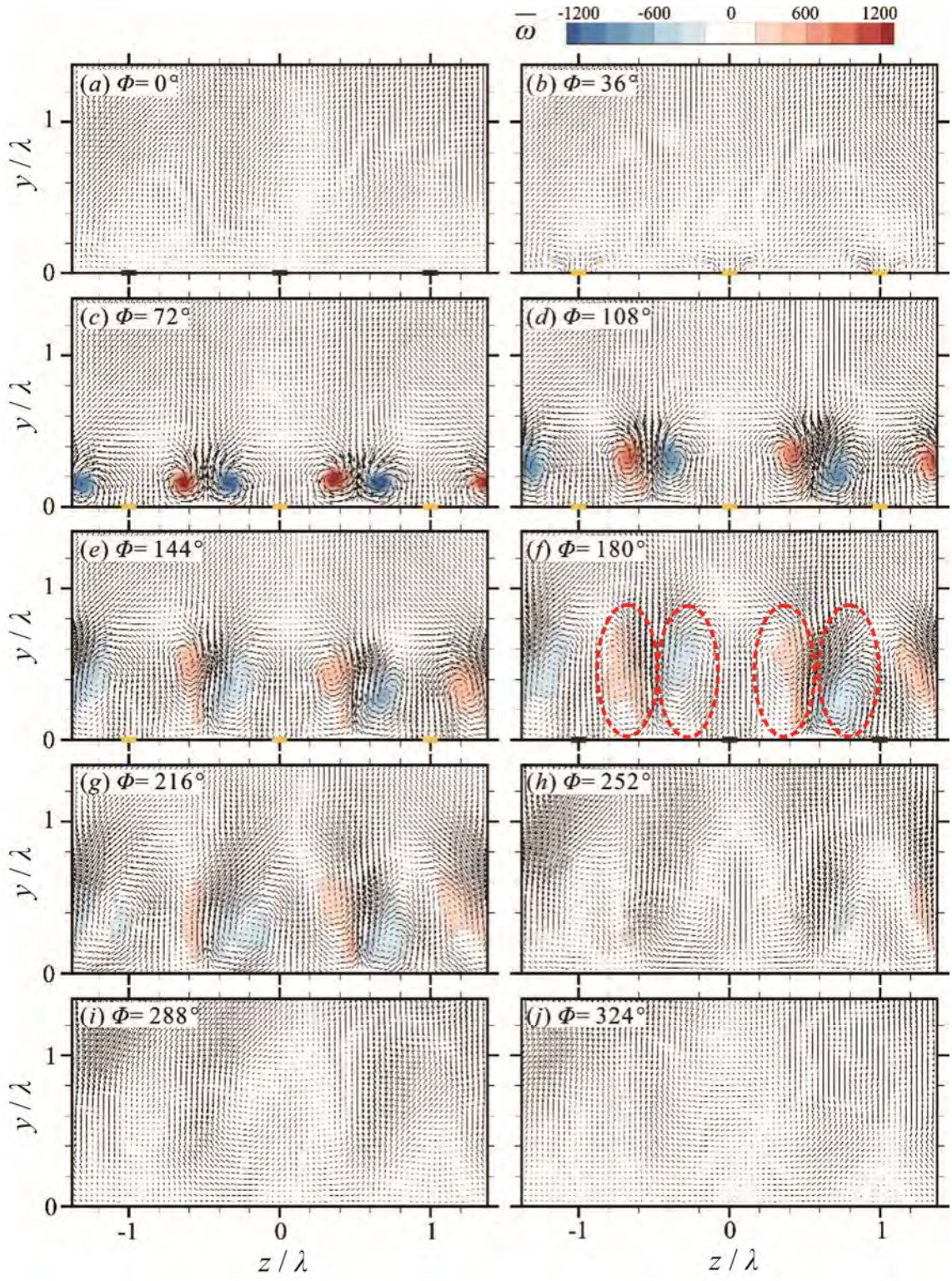

Figure 4-12. Phase-averaged vorticity contour with the velocity vector of the induced flow caused by the PSVGs 5, V_{pp} = 12 kV and DC = 50% and f_m = 10 Hz.

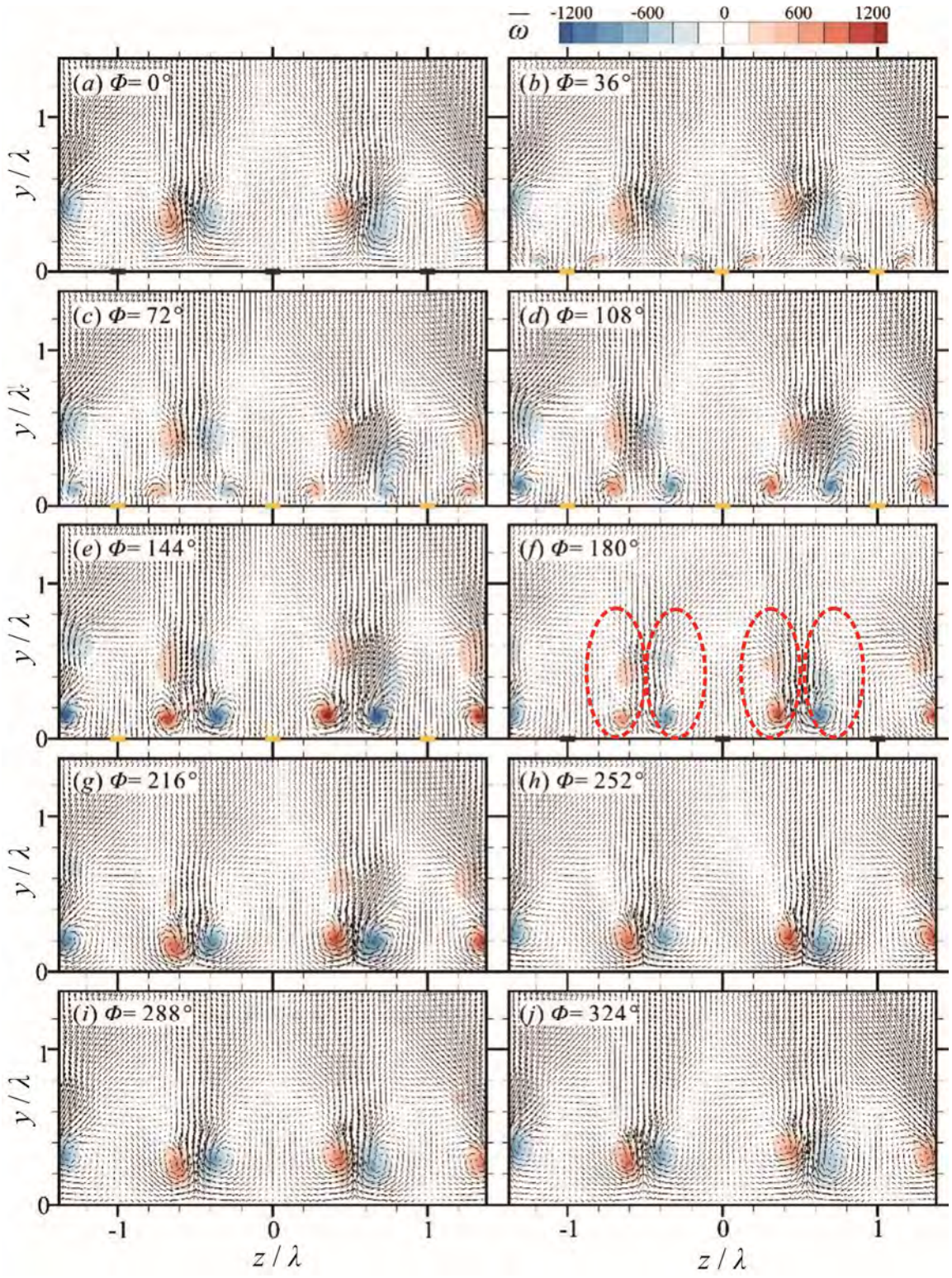

Figure 4-13. Phase-averaged vorticity contour with the velocity vector of the induced flow caused by the PSVGs 5, V_{pp} = 12 kV and DC = 50% and f_m= 50 Hz.

4.3. Characteristic of a nanosecond DBD plasma actuator (NSDBD)

To comprehensively investigate the thermal effects of NSDBD, the energy input and discharge features in detail are studied first. Then, temperature measurements using IR thermography on the

surface are conducted in quiescent air to estimate heat deposition on and conduction to the dielectric surface. The surface temperature increase is characterized by various parameters, such as the applied voltage, frequency, and air pressure and the underlying physical mechanisms are carefully analyzed. The dynamics and strength of the induced shock and the evolution of the heated fluid are presented. At last, the efficiency of surface heating is discussed.

4.3.1. Energy input at different air pressures

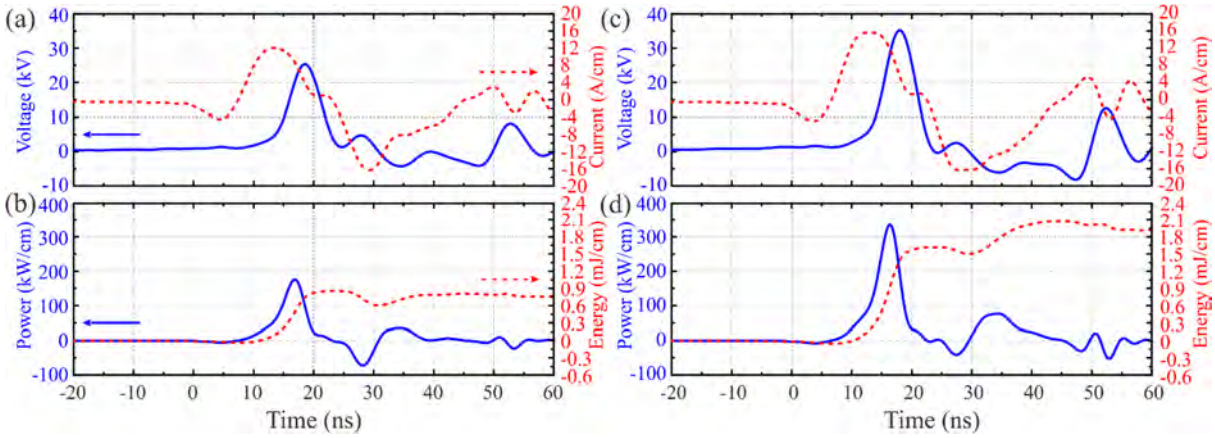

Figure 4-14. Electrical aspects of a positive pulse discharge: voltage and current at (a) 25 kV and (c) 35 kV, power and energy at (b) 25 kV and (d) 35 kV at P = 0.1 bar.

First, the electrical properties of discharge in this study are investigated. Figure 4-14(a) and Figure 4-14(c) show typical waveforms of the applied voltage and the current of unit length for a positive polarity discharge at 0.1 bar. The measured peak voltage amplitudes are 25 kV (Figure 4-14(a)) and 35 kV (Figure 4-14(b)), respectively, with a duration time of approximately 10 ns. The results are averaged by 5 times repeated measurements. Also, the measurement uncertainties are listed in Table 4-2, and the confidence coefficient is 3. Both cases share a short rise time of 4 ns. A shorter rise time leads to an increase in the current amplitude and a rapid energy deposition from the pulsed generator to the plasma actuator.

Table 4-2. Parameters uncertainty under 0.1 bar at 25 and 35 kV in Figure 4-14.

Case (0.1 bar)	Voltage (V)	Current (A/cm)	Power (kW/cm)	Energy (mJ/cm)
25 kV	200(0.8%)	0.41(3.4%)	10.5(3.5%)	0.0164(3.5%)
35 kV	315(0.9%)	0.47(2.9%)	17.2(3.1%)	0.0269(3.1%)

The maximum currents are approximately 12 A/cm and 16 A/cm for the peak voltage cases of 25 kV and 35 kV, respectively, during the voltage rise time. This current peak is caused by charge deposition resulting from discharge near the exposed electrode when the electric field is sufficient to initiate air breakdown. Following the first peak, there is no obvious silent period due to an extremely short duration time. The subsequent negative current trough occurs during the fall time of the voltage,

where a new discharge occurs with a sufficient potential difference. These current peaks and troughs manifest an asymmetry associated with the completely different discharge regimes[31]. Typical waveforms of the electric power and energy are shown in Figure 4-14(b) and Figure 4-14(d). The power peak results from the power transfer through the supply to the actuator. The energy input of each pulse, integrated by the instantaneous power, reaches an asymptotic quantity of approximately 0.75 mJ/cm at 25 kV and 1.95 mJ/cm at 35 kV at the end of the voltage pulse.

Figure 4-15 plots the energy inputs as a function of the gas pressure for the cases of 25 kV and 35 kV. The energy inputs are approximately 7.5 mJ/pulse at 25 kV and 20 mJ/pulse at 35 kV with the 100-mm spanwise length of the actuator. The energy input increases with the applied voltage and depends on the gas pressure only marginally, which is coincident with Nudnova's observation[41]. The PRF used in measurements of the electrical properties of discharge is fixed at 1 kHz. According to Zhang's work[30], the PRF does not affect the electrical parameters.

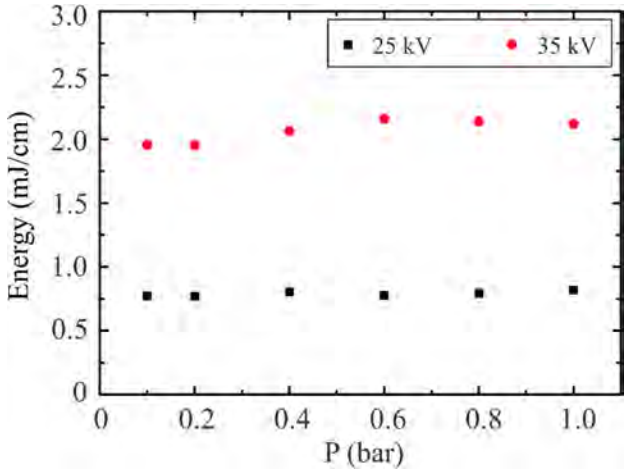

Figure 4-15. Energy input per unit length versus pressure at 25 kV and 35 kV.

4.3.2. Discharge characteristics

In this section, the effects of the air pressure, voltage amplitude and PRFs on discharge streamers are examined. The transformation between two discharge modes – diffuse mode and filamentary mode – is captured using CCD images.

4.3.2.1. Effects of air pressure

Figure 4-16 shows images of a repetitive nanosecond pulse discharge taken with a CCD camera under different air pressures and PRFs. The camera exposure time was adjusted to keep 10 discharge pulses during the exposure to each PRF case. All images are acquired after 10000 pulses to ensure the same energy input. The images indicated that there is no significant discharge difference between 10000 pulses. The locations of the exposed and insulated electrodes are marked by the gray strip and dashed line, respectively, in the upper-left image (35 kV, PRF of 1 kHz and 1 bar). Considering the higher voltage case of 35 kV at 1 kHz as an example at atmospheric pressure (the first column in Figure 4-16(a)), the discharge is composed of many streamers distributed along the length of the

exposed electrode. The discharge streamers propagate in a filamentary structure in the direction of the insulated electrode and form a plume-like shape at the streamer end. These branching structures occur in the decaying period of the positive voltage pulse, and there is a lower density of charges and a reduced number of streamer channels compared to the process in the rising period[37]. The location, shape and intensity of individual filaments are fairly random due to a series of orderless discharge channels[107]. When the discharge is sufficiently strong, these distinct channels are distributed discretely. Although some filaments tend to form at nearly the same positions, they are not caused by defects on the electrodes. These inhomogeneous and separated channels characteristic of the discharge are summarized as the filamentary mode[108]. This mode is believed to be a contractive state of the discharge channel caused by the instability of radial perturbations[109]. For the lower voltage case of 25 kV at 3 kHz (the first column in Figure 4-16(d)), the surface discharge is less intense but also keeps the filamentary features.

When the air pressure decreases to 0.8 bar (the second column in Figure 4-16(a)), the discharge channel width decreases and becomes dispersive. This change makes the filaments distribute more uniformly, prompting the transformation to diffuse mode. With the decrease in air pressure to 0.6 bar, the filaments disappear, and the plasma luminosity descends significantly, as shown in Figure 4-16(a) third column. The plasma distributes quasi-homogeneity along the electrode edge, presenting as the filamentary/diffuse mixed mode. Several discharge streamers with a higher luminosity can still be observed in this mode, which indicates that the surface discharge supplied by a repetitive nanosecond pulse was a microfilament discharge, which primarily consisted of a series of discharge channels. At 25 kV, the transformation will be delayed to a lower air pressure condition of 0.4 bar, even at a high PRF of 3 kHz. In addition, the discharge remains nearly constant when the air pressure drops from 1 bar to 0.8 bar, which can be attributed to the relatively lower applied voltage inducing a marginally weaker discharge, which is less susceptible to air density, particularly in the relatively high range of air pressure.

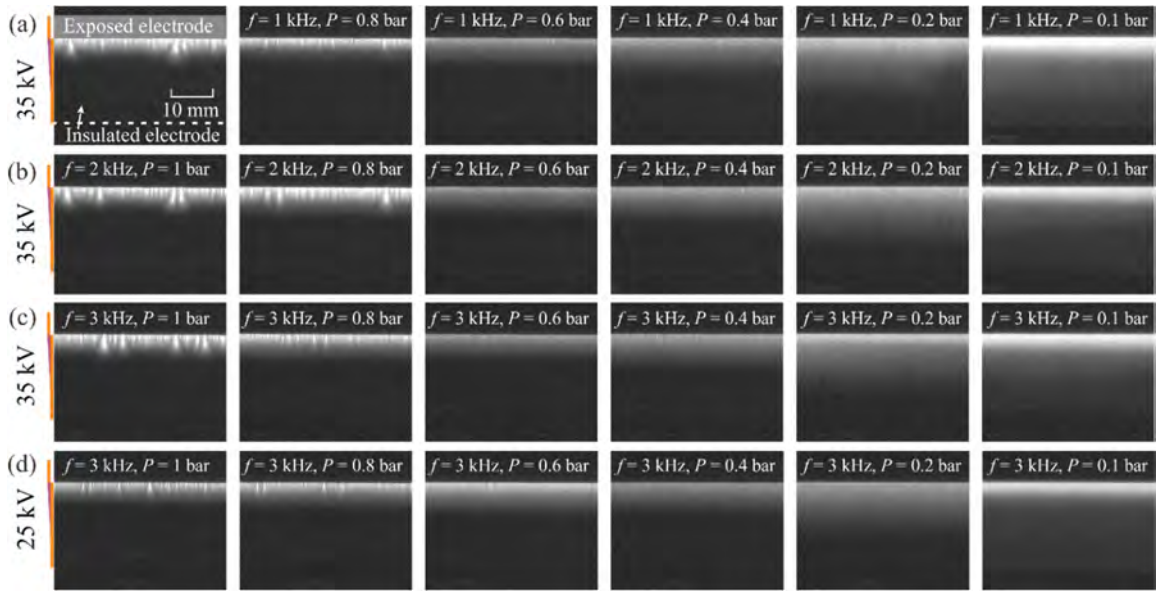

Figure 4-16. Images of the discharge at different gas pressures at PRF of (a) 1 kHz, (b) 2 kHz, (c) 3 kHz at 35 kV and (d) 3 kHz at 25 kV. The exposure time is set as ten pulses after the 10000th pulse.

As the air pressure drops further from 0.4 bar to 0.2 bar (the fifth column in Figure 4-16(a)), the discharge gradually becomes a diffuse mode presented as a glow-like discharge. This result should be distinguished from the glow discharge, which has a distinct discharge formation mechanism. In this condition, plasma length and thickness increase with the descending air pressure. The expansion of discharge channels lends to a more stable state toward the radial direction, which accounts for the absence of microfilaments. This trend is manifested at the lowest air pressure of 0.1 bar.

As the air pressure drops from 1 bar to 0.1 bar, the discharge undergoes the transition from the filamentary mode to the mixed mode and the diffuse mode. The filamentary streamers extend along the radius direction, forming a larger yet more stable and uniform plasma region. The current for a diffuse discharge mode (in Figure 4-14) also occurs earlier than that for a filamentary discharge (not shown here, see Ref.110 FIG.3(a)[110]), indicating that rapid heat is faster in the former discharge mode. The plasma luminosity reduces to the minimum in the mixed mode and increases again in the diffuse mode for both cases of 25 kV and 35 kV (Figure 4-17). Due to the plasma volume increase in the diffuse mode, the plasma region tends to have a larger luminosity. Figure 4-18 shows the plasma length and thickness, which are estimated from the position with a 5% maximum normalized luminous intensity captured by CCD images, and the exposure time is set as one pulse in this study. As shown in Figure 4-18(c) and Figure 4-18(d), both plasma length and thickness increase with the descending air pressure because the ionized volume should be increased due to the sparse air to maintain the high values of the reduced electric field (E/N). In filamentary mode, the plasma length and thickness barely change, particularly for the 35 kV case. When the discharge transforms to the diffuse mode, they increase exponentially with decreasing air density. In general, an increase in the voltage amplitude

results in a growth of plasma volume. The voltage increase will increase the longitudinal and transverse components of the local electric fields. The increase in the transverse electric field causes a thicker plasma layer. In contrast, the longitudinal electric field increase leads to a larger ionization wave speed, leading to a plasma layer length growth[41]. However, the two voltage cases examined in this study share little difference in the plasma volume. When the applied voltage reaches 25 kV, the discharge becomes saturated in the plasma volume. The persistent increase in voltage causes a radius growth of filamentary channels, forming a plume-like structure instead of the plasma volume growth. The filament to diffuse transition is a common feature as a function of the amplitude and polarity of the applied voltage, the gas pressure and the gas mixture composition[42].

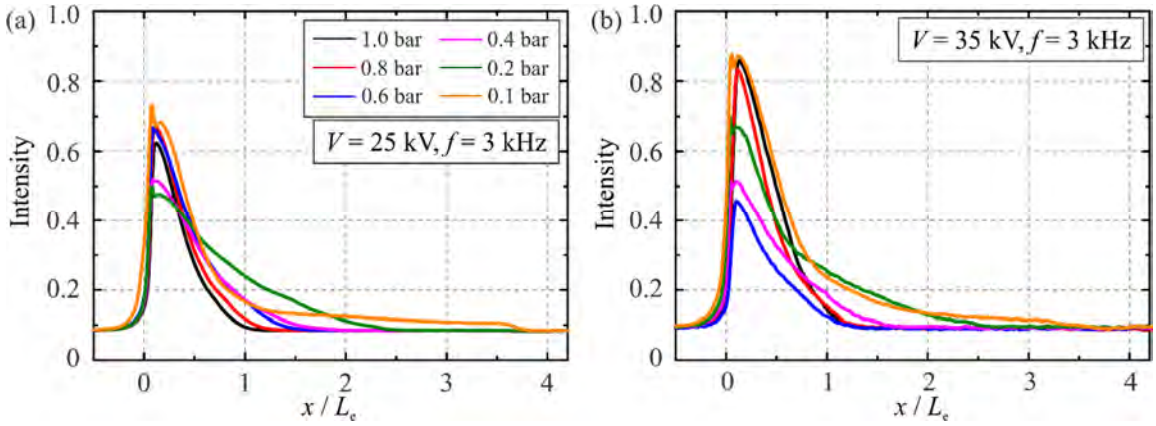

Figure 4-17. Normalized luminous intensity versus dimensionless length along the *x*-direction at (a) 25 kV and (b) 35 kV of 3 kHz PRF.

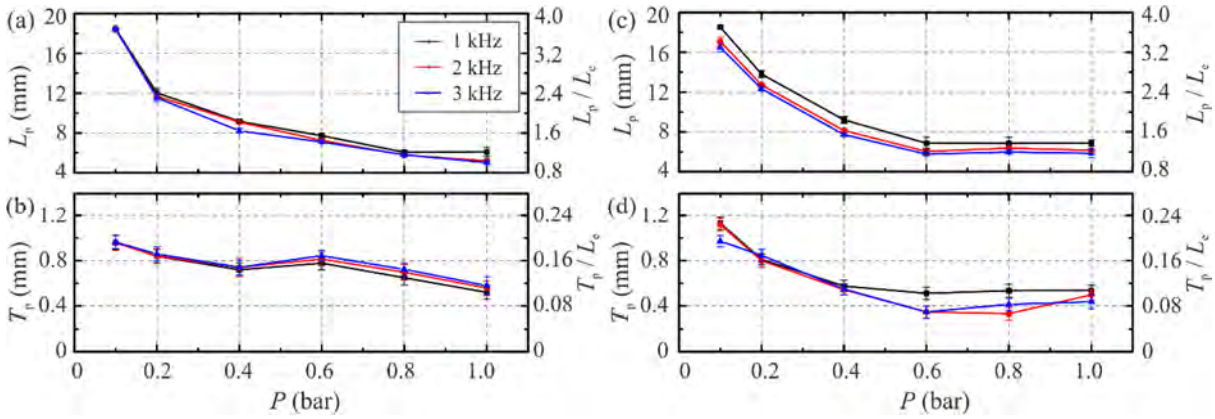

Figure 4-18. Plasma length and thickness at (a)(b) 25 kV and (c)(d) 35 kV versus air pressure.

4.3.2.2. Effects of PRF

Each column of Figure 4-16(a)–(c) shows discharge images of 35 kV at different PRFs with the same air pressure. Results indicate that the PRF does weakly affects the streamer distribution, luminosity and discharge mode transition within the current air pressure range. These results imply that although the plasma accumulation grows in a fixed time interval, the discharge formation mechanism is nearly unchanged. The discharge intensity weakens at an air pressure of 0.1 bar and a

PRF of 2 kHz and 3 kHz (the sixth column in Figure 4-16(b) and (c)). At high voltage and low air density, the air in the vicinity of the exposed electrode cannot maintain an intense discharge. The discharge intensity will attenuate to accommodate the increased PRF, which can strongly influence the residual heat deposition. Similar observations can be made for the plasma length and thickness (Figure 4-18(c) and (d)), which tend to diminish with increasing PRF. In addition, the PRF rarely affects the discharge properties in a lower voltage amplitude case of 25 kV. However, the PRF plays an important role in flow control because the interrelation between the residual heat accumulation and the characteristic time in flow can strongly improve the control efficiency, as discussed in the following section.

4.3.3. Heat transfer on the dielectric layer surface

The gas heating process of an NSDBD plasma actuator is primarily caused by the complex collisions, reactions, and interactions between energetic electrons, ions, and excited molecules generated in the plasma region[30]. Driven by the intense electrical field, energetic electrons impact N_2 and O_2 molecules, which will be excited to high electronic states from the ground state. Then, these excited molecules can be dissociated by electron impact. The dissociation leads to the transfer of the excess energy into the translational degrees of freedom of the produced oxygen atoms. The energy released in collisions of thermalized oxygen atoms is expended on the rotational excitation of molecules and gas heating, and the rotational energy relaxes into the translational energy during multiple collisons[111]. The kinetic energy in this quenching process is rapidly transferred into the surrounding gas.

In addition to the collisional quenching of excited electronic states of N_2 molecules by O_2, the excited oxygen atoms $O(^1D)$ quenched primarily by O_2 and N_2 molecules also provide excitation energy to the gas heating. The quenching process of the excited oxygen atoms $O(^1D)$, which are generated in O_2 dissociation, proceeds through the formation of an intermediate complex[112]. These two quenching processes dominate the heat transfer on gas heating at $E/N \leq 200$ Td, while at $E/N > 400$ Td, the dissociation reactions of N_2 molecules by electron impact and the processes involving charged particles make the primary contribution[113]. Another important contribution to gas heating when the degree of dissociation of O_2 molecules is sufficiently high is the reaction of the vibrational-translational relaxation of the vibrational levels $N_2(v)$ by excited oxygen atoms $O(^3P)$. This process is considered to provide slow heating that occurs on a time scale of approximately 200 μs[114].

4.3.3.1. Surface heating behaviors in long-term activation

A longer-duration case of 250 s in standard air pressure was investigated first to gain the global characteristics of surface heat transfer. In this study, 10 Kapton film layers each with a thickness of 0.5 mm and an applied voltage of 22 kV were used to avoid surface material failure caused by residual heat. All data were averaged along the spanwise direction. Figure 4-19(a) plots the time variation of temperature rise at $x/L_e = 0.2$ with different PRFs. The entire temperature increase can be divided into two stages: a rapid temperature increase in the initial 10 s and then slow growth until a steady-state

value at long times. A high PRF strongly increases the heat accumulation in the same period. The surface temperature increases with the operation time, analogous to the exponential curves. Figure 4-19(b) shows the heat flux variations at x/L_e = 0.2 calculated by the one-dimensional semi-infinite model. In the rapid increase stage, the heat flux rises quickly and reaches a peak value, which indicates that the heat in the discharge transfers to the surface of the dielectric layer in a short time. Then, the heat flux decreases to a steady value, which implies that the temperature increase slows down gradually, and heat transfer achieves a balance when the heat increment from the gas equals the heat dissipation in the dielectric substrate. This process can also be observed in spanwise-averaged temperature changes at different times, as shown in Figure 4-19(d). The streamwise (x-direction) variation in the temperature increase at t = 60 s with different PRFs is shown in Figure 4-19(c). The highest temperature occurs near the edge of the electrode (x/L_e = 0.2) and gradually reduces downstream in the insulated electrode direction, attaining a value near room temperature. No noteworthy changes are observed between the PRF cases in terms of the tendency to increase the temperature increment distribution.

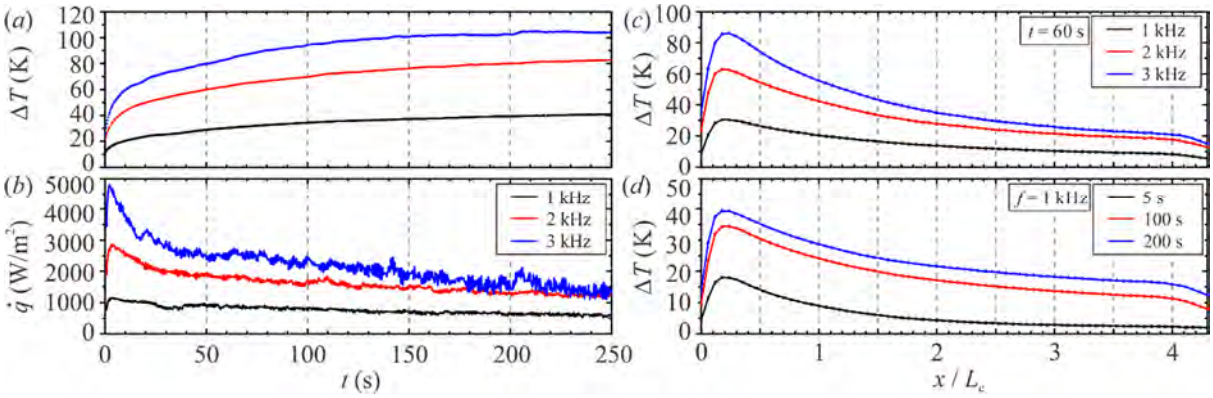

Figure 4-19. (a) Temperature increase with time at x/L_e = 0.2; (b) heat flux variation with time at x/L_e = 0.2; (c) temperature increase along the x direction at t = 60 s with different PRFs; (d) temperature increase along the x direction at PRF f = 1 kHz at different times.

The corresponding spatiotemporal variations in the spanwise-averaged temperature increment at PRFs of 1, 2, and 3 kHz are plotted in Figure 4-20 as contour fields. The horizontal axis is the dimensional length in x distance, and the vertical axis is the time. The dashed lines mark the edge of the insulated electrode. According to the spatiotemporal temperature increment distribution, the dielectric surface can be divided into three typical regions in the streamwise direction distinguished by two inflection points (red dots in Figure 4-20): the plasma region, the insulated electrode region, and the far-field region[26]. Large temperature increases are observed near the exposed electrode corresponding to the plasma region ($0 \le x/L_e \le 1$). At 1 kHz, the temperature increment reached 40 K at t = 220 s but only takes several seconds to approach 40 K in the 3 kHz case. The denser isotherms near the exposed electrode during the early period after activation also indicate this rapid increase stage, particularly in the high PRF case. Because the plasma is the dominant heating source, the spanwise averaged surface

temperature is much higher than that in the other two regions. Due to the absence of plasma, the surface temperature in the insulated electrode region is low. Although the temperature continues to grow in this region, the growth rate has become moderate. The first inflection point in the isotherms also highlights this change. The temperature increase in the dielectric surface is caused by the heat generated by the dielectric losses and the heat transfer from the residual heat in plasma. This process exchanges the thermal energy from the induced flow, although it is small for an NSDBD plasma actuator. Part of the thermal energy in the dielectric layer is transferred to the far-field region through internal thermal conduction. In the far-field region, the surface temperature drops considerably near the edge of the insulated electrode, which is indicated by the second inflection point in the isotherms. The local heating in this region is provided by thermal convection with the ambient air and internal thermal conduction from the upstream areas. The thermal conduction inside the dielectric layer is slow due to the small thermal conductivity of the dielectric material of only 0.12 W/m·K, compared to that of the copper electrodes, which was approximately 400 W/m·K.

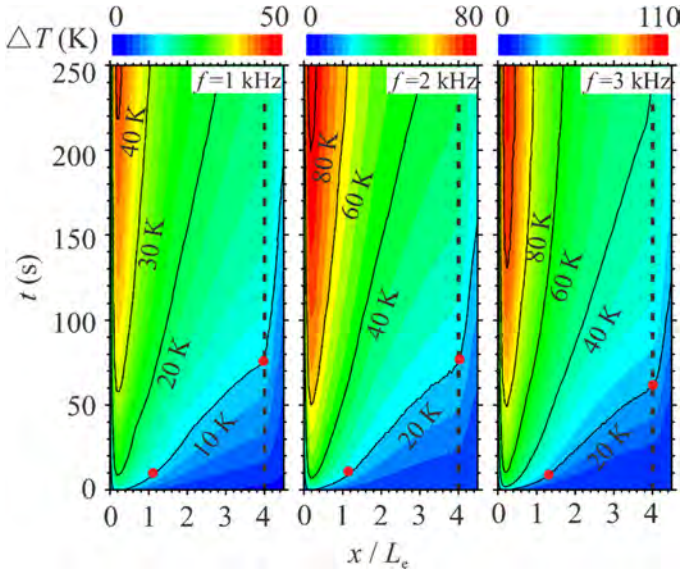

Figure 4-20. Spanwise-averaged spatiotemporal temperature increment distribution of the NSDBD plasma actuator at different PRFs.

4.3.3.2. Surface heating behaviors at different air pressures

In this section, the rapid temperature increase stage around the first 10 s is chosen to investigate the thermal characteristics of varying air pressures. Examples of instantaneous surface temperature increases at 35 kV are plotted in a top view of the plasma actuator in Figure 4-21. Three different air pressure conditions of 0.2, 0.6, and 1 bar are selected to represent three typical discharge modes for comparison. The isotherms of 2 K, 5 K, 10 K, 20 K, and 40 K are marked with solid black lines. As shown in Figure 4-21(c1)(c2)(c3), in a standard atmosphere, the discharge leads to an inhomogeneous temperature increment in the spanwise direction near the exposed electrode ($0 \le x/L_e \le 1$). In all three PRF cases, the high-temperature spots concentrate from $x/L_e = 0$ to 0.5 (Figure 4-20), where the

maximum temperature rise is more than twice that in the streamer head of x/L_e = 1.4. Babaeva[115] indicates that the predicted ionization occurs primarily in the streamer head and propagates downstream under a high electric field in a positive nanosecond pulse discharge. The electrical field reduces quickly on the dielectric surface, leading to an attenuated ionization source and the deceleration of the ionization wave. Because gas heating is generated in the quenching process of excited molecules, the local strength of the electron impact ionization source strongly affects the temperature rise in the gas. The weakened gas heating along with the streamer channel direction is a result of the ionization attenuation starting from the streamer head propagating downstream. Most gas heating concentrates on the upstream side of discharge streamers. In the mixed mode at 0.6 bar, as shown in Figure 4-21(b1)(b2)(b3), the increase in temperature becomes uniform along the spanwise direction. The high-temperature spots corresponding to the filamentary streamers disappear gradually. Considering PRF of 2 kHz as an example, the isotherm of 2 K is located on average at x/L_e = 2.1(Figure 4-21(b2)), which is the smallest among the cases of x/L_e = 2.6 (Figure 4-21(a2)) at 0.2 bar and x/L_e = 3.1(Figure 4-21(c2)) at 1 bar. This result indicates that the heating region decreases streamwise when the filaments shrink with decreasing air pressure and increases again due to the plasma volume growth at a lower air density at 0.2 bar. Although PRFs rarely affect discharge features, the heating region and the maximum temperature rise increase markedly with increasing PRF in all pressure cases of the same energy input after 10000 pulses. While a more homogeneous surface temperature along the streamwise direction is observed at 0.2 bar (Figure 4-21(a1)(a2)(a3)), the temperature rise in the upstream side of the plasma is also much more evident, which is consistent with the observation of the most intense discharge (see the sixth column in Figure 4-16(b)).

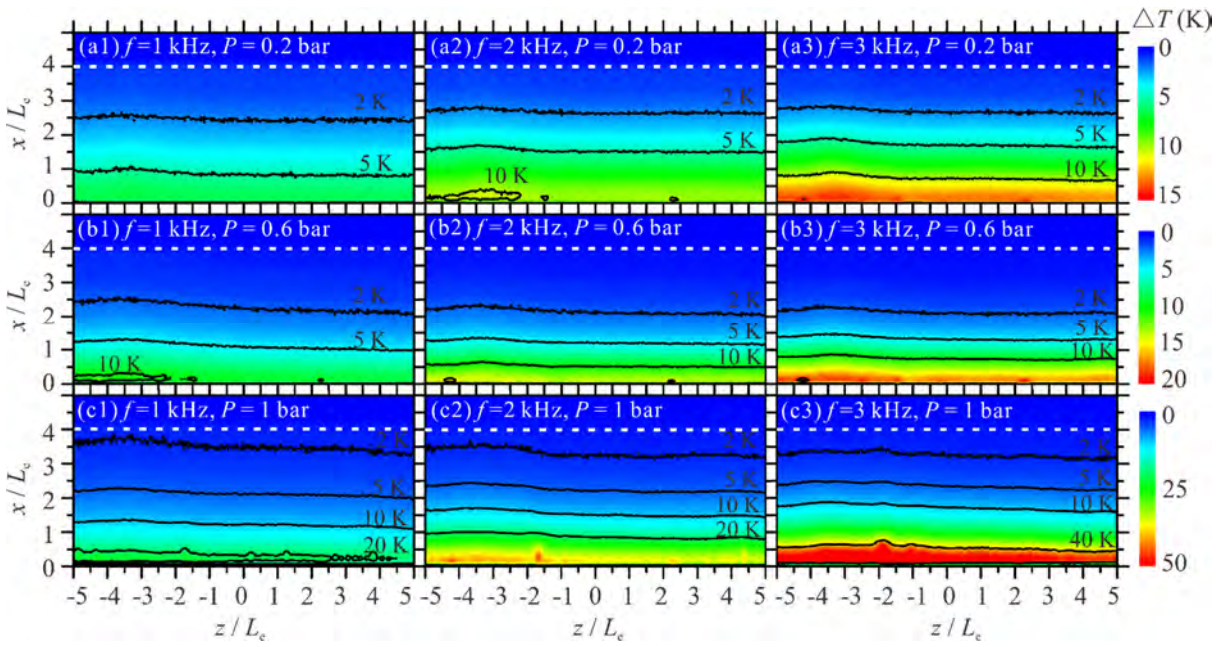

Figure 4-21. Instantaneous surface temperature increment distributions after the 10000th pulse at 35 kV in the cases of (a1) 1 kHz, (a2)2 kHz, (a3) 3 kHz at 0.2 bar; (b1) 1 kHz, (b2) 2 kHz, (b3) 3 kHz at 0.6 bar; and (c1) 1 kHz, (c2) 2 kHz, (c3) 3 kHz at 1 bar.

Based on the measured surface temperature increase distribution, the spanwise-averaged spatiotemporal profiles at the different air pressures and PRFs in the rapid increase stage are plotted in Figure 4-22. Isotherms at 2 K, 5 K, 10 K, 20 K, and 30 K are extracted with solid lines. The three typical regions can still be distinguished by the isotherm at a low temperature (marked by the black dashed line), which pervades all spatiotemporal ranges. In the far-field region divided by the edge of the insulated electrode, the temperature is nearly unchanged in the rapid temperature increase stage in all cases. This result is likely caused by slow thermal conduction inside the dielectric layer and the long distance from the upstream heated gas. The steep slope of this isotherm in the far-field region also suggests a tenuous temperature change, particularly in low air pressure cases. In contrast, the subdued slope implies that the temperature rises nearly synchronously in this region, which can present the plasma region's heating features well. In addition, the intensive isotherms indicate a more significant temperature growth rate. In the plasma region, the temperature growth rate decreases with more tenuous air, independent of the discharge mode. The maximum temperature markedly decreases from the filamentary mode to the diffuse mode but only marginally decreases from 0.4 bar to 0.2 bar in the diffuse mode.

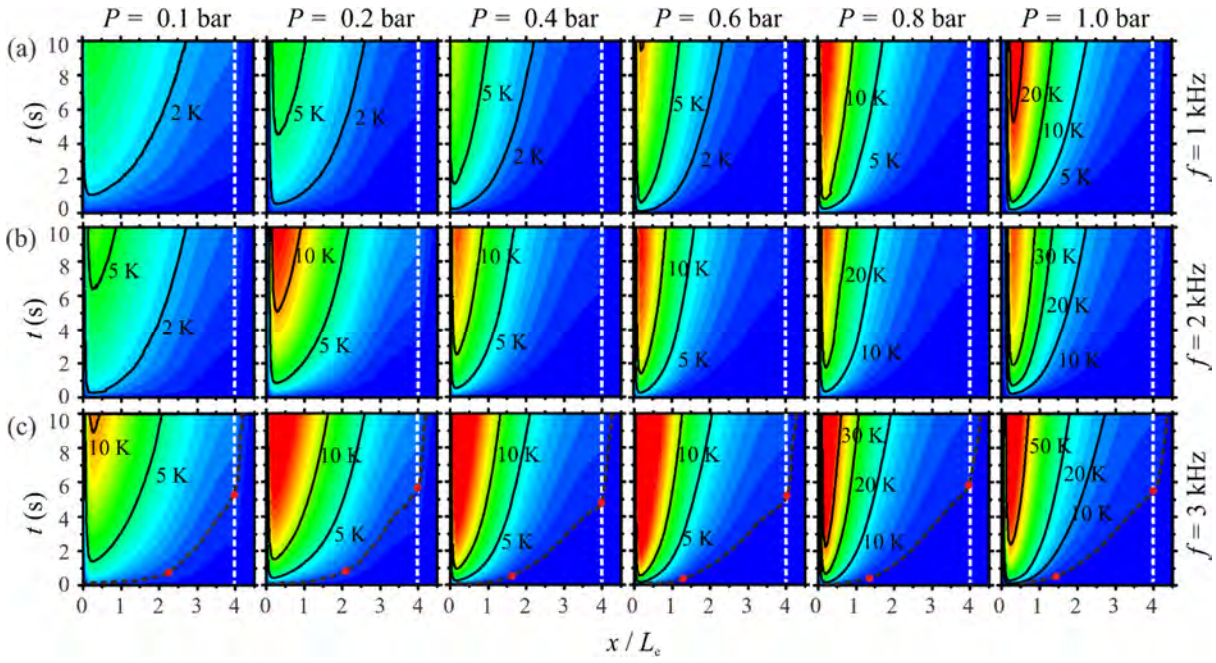

Figure 4-22. Spanwise-averaged spatiotemporal temperature increment distributions of the NSDBD plasma actuator at PRF = (a) 1 kHz, (b) 2 kHz, and (c) 3 kHz with different air pressures at 35 kV. The dashed line indicates the edge of the insulated electrode.

To evaluate the heating process on the surface in more detail, the heat flux is calculated using the one-dimensional semi-infinite model, as shown in Figure 4-23. The residual heat power on the dielectric layer above the insulated electrode region (from x/L_e = 0 to 4) is integrated and plotted in Figure 4-24. The heat flux distribution indicates that the maximum occurs around x/L_e = 0.2 (x = 1 mm), independent of the applied voltage and PRF, which is consistent with the observation by Correale *et al.*[40]. On the dielectric surface from x/L_e = 0.2 to 4, the heat flux curve decreases smoothly. Dielectric heating occurs in the dielectric layer, in addition to the convective heat transfer of the heating gas. The total heat transfer on the surface typically increases within 1 s, reaching a constant value.

At a relatively high air pressure (filamentary mode), the trends of heat flux density with air pressure are different for the two applied voltages. At 25 kV and 1 kHz (Figure 4-23(a)), the heat flux remains at a similar level (approximately 1500 W/m^2 at the peak value) for air pressures ranging from 1 bar to 0.4 bar. Comparatively, at 35 kV and 1 kHz (Figure 4-23(d)), the maximum heat flux decreases markedly from 2400 W/m^2 to 500 W/m^2 when the air pressure drops from 1 bar to 0.2 bar. At 25 kV, 0.6 bar, and 1 kHz, the residual heat power is 0.12 W (Figure 4-24(a)), even larger than the same air pressure case of 35 kV at 0.085 W (Figure 4-24(d)). This phenomenon, which agrees with the observation of discharge characteristics shown in Figure 4-16, is stronger at high PRF, which indicates that the discharge intensity of a relatively high voltage heavily depends on the air density. Comparing Figure 4-23(c) and Figure 4-23(f) suggests that increasing the applied voltage may not increase the heat flux at moderate air pressures ranging from 0.6 to 0.8 bar. When PRF rises, the residual heat

increases monotonically in both cases. Also, at 25 kV and 1 kHz, a low air pressure case at 0.4 bar retains a high residual heat value, while at 2 kHz and 3 kHz, the residual heats decrease, indicating that there is a critical air density for different PRFs corresponding to the transition from the filamentary mode to the diffuse mode.

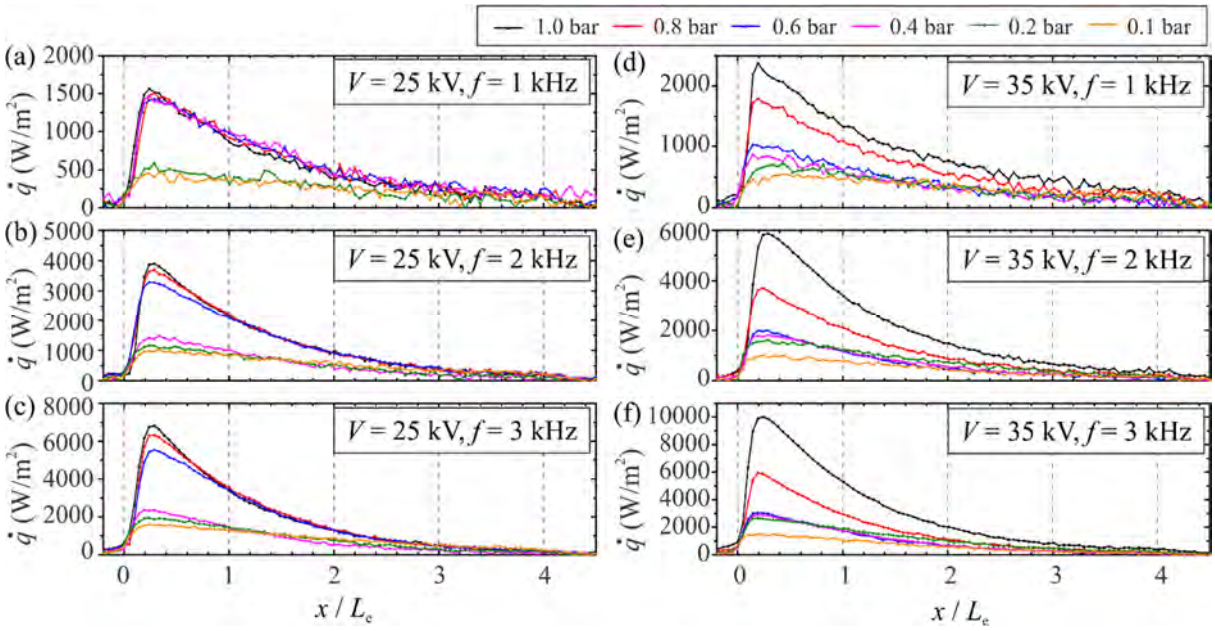

Figure 4-23. Spanwise-averaged heat fluxes after the 10000th pulse at 25 kV in the cases of (a) 1 kHz, (b) 2 kHz, and (c) 3 kHz and at 35 kV of (d) 1 kHz, (e) 2 kHz, and (f) 3 kHz.

With the low air pressure at 0.4 bar in a diffuse discharge, the residual heat power suddenly drops to a lower level at 25 kV and PRF of 2 or 3 kHz but maintains this level when the air pressure further drops to 0.1 bar in both voltage cases. The maximum heat flux in the plasma region marginally decreases with pressure from 0.4 bar to 0.1 bar, but the heat flux in the original insulated region increases due to a longer plasma, leading to an irregular variation in the total heat (Figure 4-24(a)–(c)). The residual heat power still increases monotonically with PRF. The heat increment caused by increasing voltage marginally reduces for the diffuse mode compared to the filamentary mode. A large residual heat drop occurs at 0.1 bar at 35 kV and PRFs of 2 kHz and 3 kHz, which may be caused by insufficient air for discharge under a high voltage and frequency power supply. These results imply that the applied voltage amplitude and PRF are not decisive factors in heat generation in diffuse mode and are even counterproductive under high voltage and high frequency activation. Thus, heat transfer is strongly associated with the discharge mode. Compared to the diffuse mode, the gas heating process is more acute in the filamentary mode. At 25 kV, when the air pressure drops below a critical value, the heat transfer will jump from a high value to a low value. However, at a higher voltage of 35 kV, the surface heat transfer decreases with the air pressure drop accompanied by the attenuation of filaments and then remains at a constant value approximately in the diffuse mode (0.6 bar to 0.2 bar).

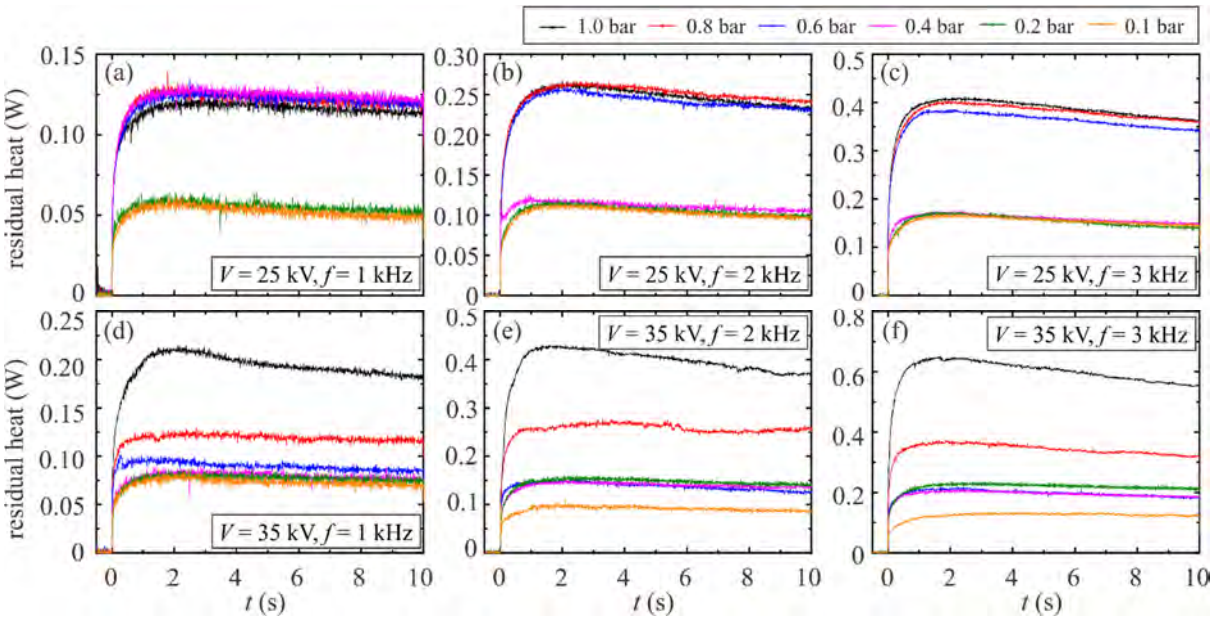

Figure 4-24. Residual heat on the dielectric surface above the insulated electrode area in the rapid temperature increase stage in the cases of (a) 1 kHz, (b) 2 kHz, (c) 3 kHz at 25 kV, and (d) 1 kHz, (e) 2 kHz, (f) 3 kHz at 35 kV.

4.3.4. Induced shock wave dynamics and evolution of heated fluid

4.3.4.1. Induced shock structures and overpressure

The Schlieren images acquired at four typical times are shown in Figure 4-25(a), where the frames show the shockwaves from the 1st, 100th, 1000th, and 10000th pulses of 35 kV at 1 kHz. The induced shock wavefront consists of a semicylindrical shock and a planar shock. The semicylindrical shock expands from the alignment line of the exposed and insulated electrodes. Planar shock propagates upward parallel to the discharge streamers, which corresponds to the most gas heating in the discharge region. The shock structures are the same as those observed by Zhou *et al*.[29] and are produced through a quick pressure increase caused by the intense energy density in the discharge. Due to the residual heat near the surface, the shock wave propagation velocity reduces in subsequent pulses after a long time (e.g., the 10000th pulse, or after 10 s). This reduction in shock wave velocity is also substantiated in the overpressure measurements, presenting a longer time for the peak pressure to arrive at the sensor.

The overpressure of the induced shock can be captured as an abrupt pressure rise by the dynamic pressure sensor that remains at zero until the shock wave arrives at the monitoring points (Figure 4-25(c)). After the overpressure peak, there is a quick pressure drop, which is attributed to the rarefaction wave following the shock. This rarefaction wave is then reflected from the surface and catches up to the induced shock wavefront. Finally, the induced shock wave is weakened and decelerates to a sonic wave due to the interaction with the rarefaction waves[110]. The second peak at approximately 210 μs that is shown in Figure 4-25(c) is the reflection of the first shock wave between the copper shield over the sensor and the dielectric surface. To estimate the shock wave propagation

velocity, the curve fitting was used by a displacement–time diagram. Figure 4-25(b) shows the wave propagation velocity through the Schlieren images, and the points indicate the shock front vertical positions above the anode-cathode edge, which are same as the measurement points of the pressure sensor. The darkest point with a local maximum intensity along the semicylindrical shock is identified as the shock front. The induced shock wave propagates at approximately 390 m/s (*Ma* = 1.13) at the beginning and rapidly attenuates to a sonic wave at 345 m/s under the interaction of the reflected rarefaction wave. The lower applied voltage amplitude of 25 kV leads to a lower initial velocity of 374 m/s (*Ma* = 1.08), which agrees with the observation of peak overpressure measurements. Due to the intense electromagnetic interference (EMI), the overpressure in the vicinity of the plasma region has rarely been reported in detail. The pressure profile can provide more information on the shock wave strength and further imply the interaction of shock and the surrounding gas. Due to the protection provided by the copper shield, the minimum distance of the pressure sensor from the NSDBD actuator can be set to 5 mm in this study. However, a large negative signal remains in the measurement at the beginning of the activation and is likely caused by EMI noise that lasts approximately 5 μs. Figure 4-25(d) shows the peak pressure of the induced shock wave created by the NSDBD plasma actuator versus the propagation time at a standard atmosphere, implying that the overpressure drops in an exponential fashion approximately as the shock propagates. Here, the values are the average peak overpressure for all pulses over the first 4 s. The pressure measurement for each case was repeated five times to fit the experimental repeatability. The peak pressure values are averaged over 1000 pulses at 1 kHz, and the error bars are marked in the figure. The maximum value of the pressure peak is approximately 11000 Pa at 35 kV with Kapton as the dielectric material and drops to 7000 Pa at a lower voltage amplitude. Another dielectric material of PMMA with the same thickness was used, and results showed that the different dielectric properties strongly affect the overpressure but with the same trend. Zhao *et al.*[29] believed that the shock wave generated by the NSDBD plasma actuator is fundamentally a blast wave, the strength and attenuation of which are strongly dependent on the voltage amplitude of the applied pulse. The time evolution of the shock pressure profile follows the Friedlander equation fairly well, as shown by the red curve in Figure 4-25(c). This good fit indicates that the NSDBD plasma discharge actually exhibits a microblast wave.

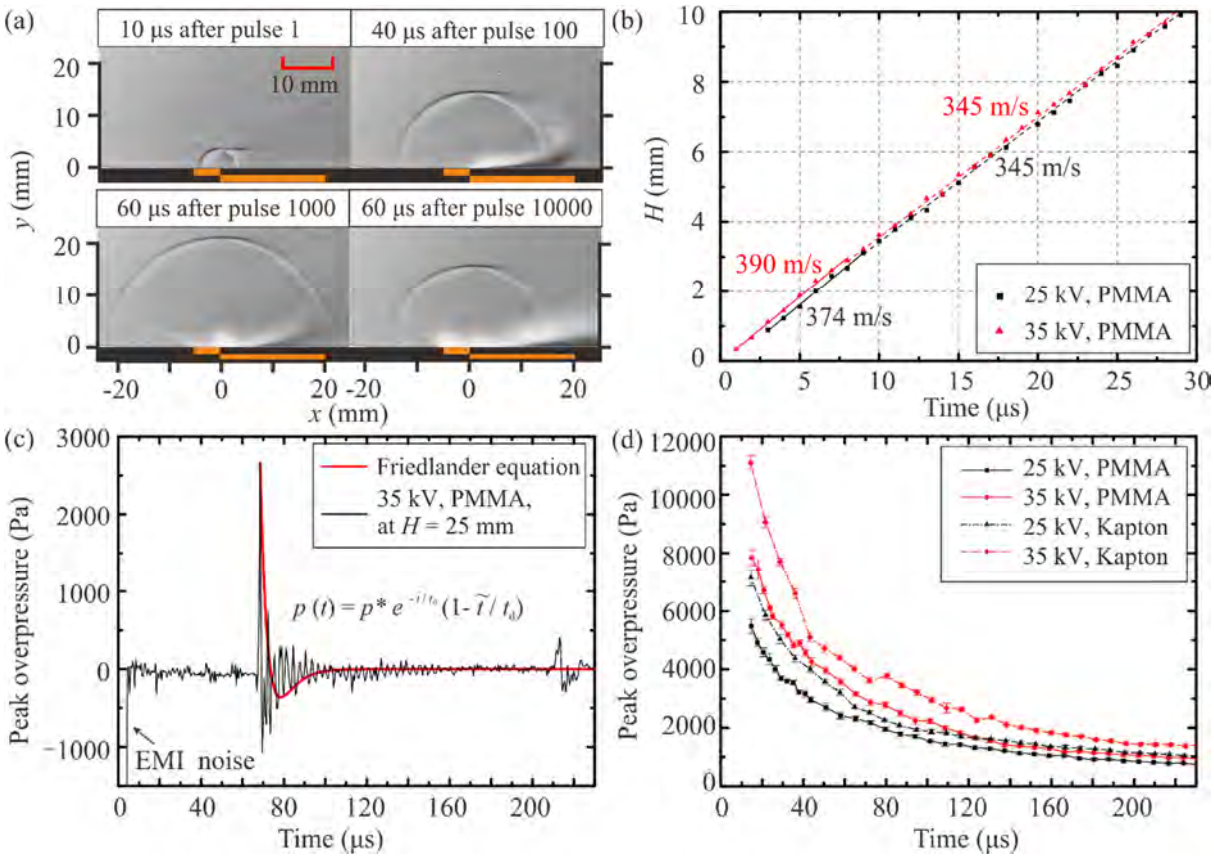

Figure 4-25. (a) Schlieren images showing the induced shock structures and the residual heat in a repetitive case of 35 kV, 1 kHz; (b) the displacement versus time diagram of the peak overpressure with a curve fitting of shock velocity in Schlieren images; (c) the overpressure at *H* = 25 mm, *V* = 35 kV with curve fitting of Friedlander equation; (d) the peak overpressure as a function of the propagation time under a standard atmosphere

Figure 4-26 shows the attenuation of the peak overpressure with time at different air pressures. The properties of varying air pressure shown in overpressures are consistent with the thermal performance associated with the discharge mode. First, in filamentary mode, the strength of the induced shock wave scarcely changes with air pressure under a lower voltage amplitude of 25 kV (see black, red and blue lines in Figure 4-26(a)(b)(c)) but deviates markedly at 35 kV. Second, in the transition mode, the peak overpressure quickly decreases, accompanied by a larger fluctuation that indicates an unsteady discharge state. Third, in the diffuse mode at 0.1 bar pressure, the strength of the induced shock wave drops below 1000 Pa, which is only one-eighth of that at standard pressure, at both voltages. This similarity to thermal features also indicates that the induced shock wave is generated by the fast-heating process; the PRF does little work on the strength of overpressure.

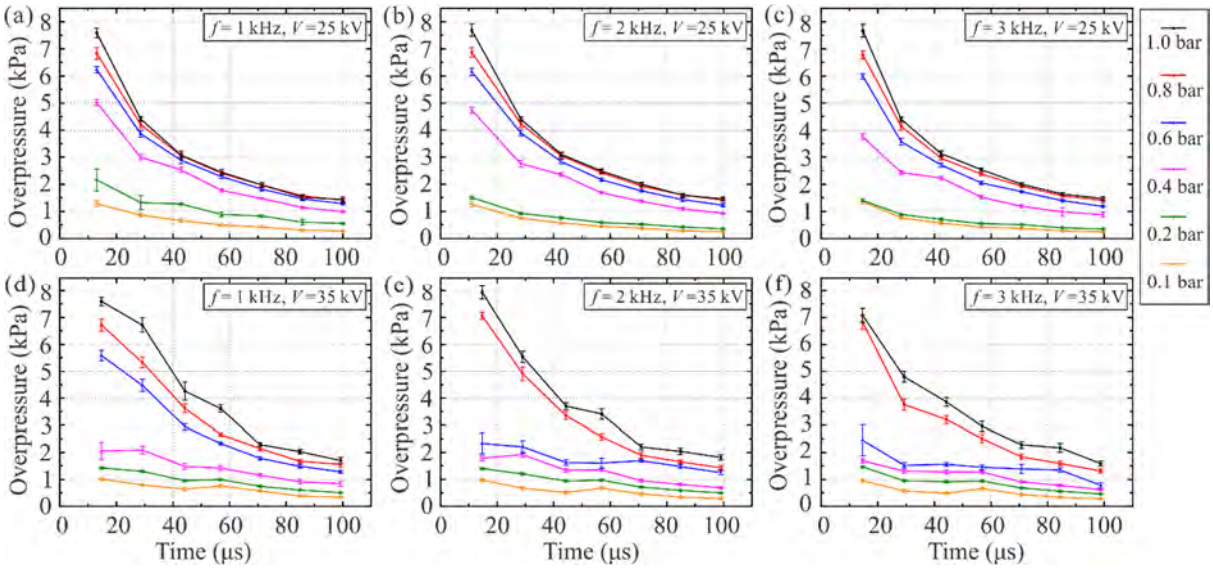

Figure 4-26. Time-averaged peak overpressure under different air pressures of the 25 kV cases at (a) 1 kHz, (b) 2 kHz, and (c) 3 kHz and the 35 kV cases at (d) 1 kHz, (e) 2 kHz, and (f) 3 kHz.

4.3.4.2. Development of the heated fluid

The starting vortex is also an important characteristic of the induced flow caused by the plasma actuator. The development of the starting vortex is described in Figure 4-27. When the plasma is generated, the residual heat is deposited rapidly in the discharge region. As shown in Figure 4-27(b1), the heat transfers to the surrounding air and forms a hotspot area that is completely decoupled from the induced compression waves. Each single pulse intensifies the heating in this region and expands thermally to the vicinity. The hotspot area is concentrated upstream of the discharge streamer, which is consistent with the regions of the maximum luminosity and fastest temperature increase. The ionized particles move toward the dielectric surface under the body force produced by the strong electric field. Due to the short effect time of the electric field (nanosecond scale for each pulse), the movement of thermal fluid is more sluggish than the deposition of heat. To replenish the fluid that was ejected downstream, the fluid upstream of the plasma region is entrained and rolls up to form a starting vortex in the jet front, as shown in Figure 4-27(a2). The vorticity originates at the transient front, which is similar to a wedge of vorticity intruding into an inviscid region[116]. The vorticity fronts form in a shear flow as the result of fast patches of fluid catching up with slower ones. The front of the nose steepens and propagates later, 'backward' wave breaking occurs, and outer irrotational fluid is entrained[116]. Due to the velocity gradient near the wall, negative vorticity was observed at the wall. Brain *et al.*[117] believed that the wall will cause a bias to the initial shear layer where the circulation associated with the positive vorticity will be greater than that associated with the negative vorticity. The initially quiescent domain exerts its influence on the relative amounts of positive and negative vorticities through the proximity of the jet to the boundary. Due to the growth of the secondary vorticity and the interaction between positive and negative vorticities, the positive vortex will be pushed into the outer irrotational ambient flow[118]. The vortex generation in the vorticity front and

separation of the jet from the wall arise, not from vorticity diffusing in from the boundary or from a Kelvin-Helmholtz instability, such as occurs for a steady wall jet[117]. Because the high-temperature fluid will move downstream to form a vortex and cause a change in the density gradient, the formation of the starting vortex can be captured by the Schlieren images in Figure 4-27(b2) and (b3). Estimated from the Schlieren images, the vortex structure propagates with a velocity of approximately 0.3 m/s and remains for a period longer than 80 ms. To preserve the no-slip boundary condition, secondary vorticity is generated at the wall and wraps around the starting vortex to steer the trajectory away from the wall[119], as shown in Figure 4-27(b3). The starting vortex becomes weaker and repeatedly breaks down under the impact of the induced shock waves. Finally, a steady wall jet with a high temperature is formed, similar to an ACDBD plasma actuator. Zhao *et al*.[29] measured the transient flow behind the moving shock wave at a speed of up to 35 m/s. The induced jet becomes turbulent, which can be attributed to the combined effects of the impact of induced flow moving with the shock wave, the localized convection caused by the heated actuator surface, and the pulsed energy thermalization in the discharge filaments[91]. The maximum velocity of the induced jet is typically no more than 1 m/s, which is markedly smaller than that generated by the ACDBD plasma actuator of 8 m/s. The additional momentum caused by the induced jet no longer plays the dominant role in the flow control using the NSBDB plasma actuator.

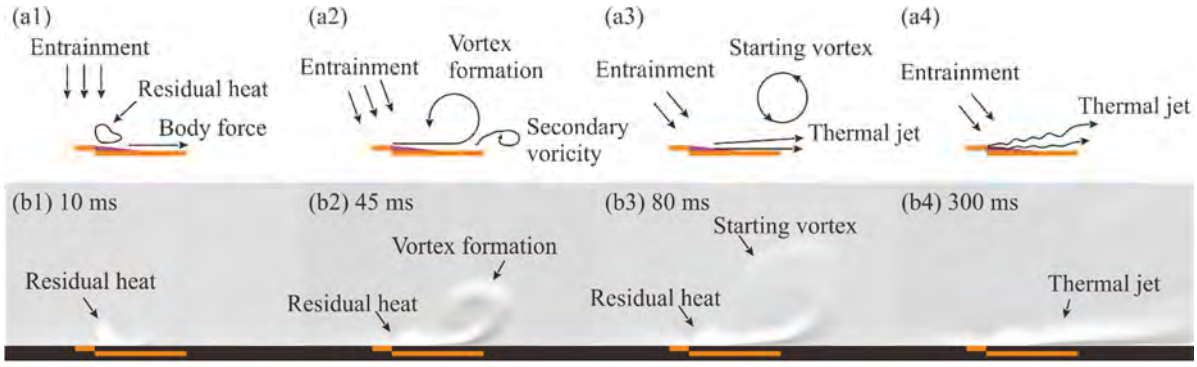

Figure 4-27. (a) Schematic of the development of the starting vortex and thermal jet and (b) Schlieren images in the case of 35 kV and 3 kHz at standard atmosphere.

The evolution of residual heat with different PRFs is plotted in Figure 4-28 at a standard atmosphere. Increasing PRF results in a quicker fluid movement downstream, a larger residual heat region, and heat convection reduction to the upstream fluid. A more extended thermal jet, which is markedly longer than the insulated electrode length, can be observed with a high PRF (Figure 4-28(a5)(b5)(c5)). A large portion of the heat is convected downstream under the ionized wind. The lower applied voltage case with the same PRF shares a similar evolution but has an marked contractible residual heat region. The case of 25 kV at 3 kHz is considered to demonstrate the evolution of residual heat at the different air pressures, as shown in Figure 4-29. When the discharge is shifted to the diffuse mode at 0.4 bar, the residual heat prefers to convect vertically from the surface

(larger residual heat region) due to a thicker plasma region, which also explains the reduction in heat convection on the dielectric surface. The thermal jet lifts off from the wall surface because the fluid in the discharge region has a lower density through the fast-heating process and then accelerates under the electric field. Therefore, the heat convection in the far-field region on the wall surface plays a relatively minor role in the surface temperature increase. However, because the Schlieren images measure the density gradient normal to the knife direction, the low air density will directly affect the measurement sensitivity. Therefore, the changes under 0.1 bar are debatable. However, the discharge is strongly weakened at a lower air density.

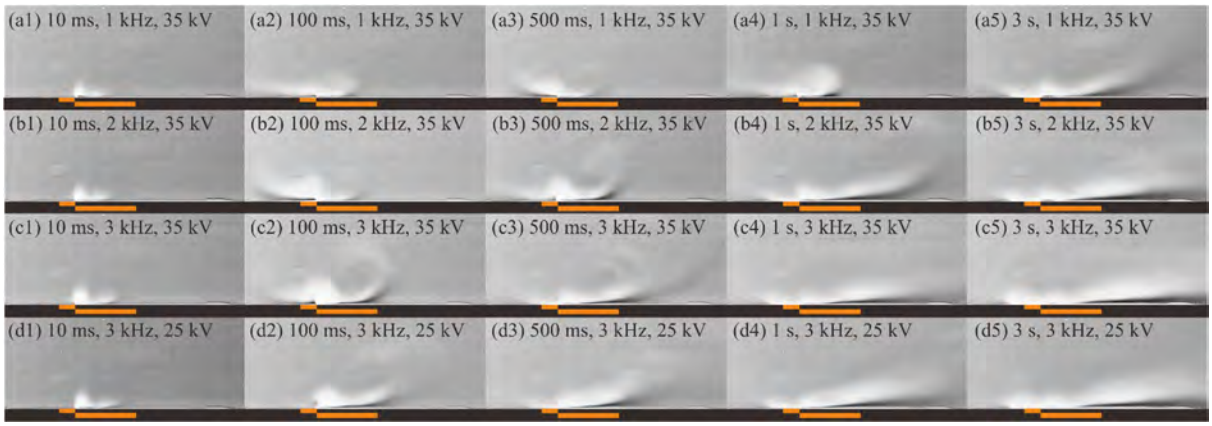

Figure 4-28. Evolution of residual heat of the NSDBD of 35 kV at (a1) to (a5) 1 kHz, (b1) to (b5) 2 kHz, (c1) to (c5) 3 kHz, and (d1) to (d5) 3 kHz of 25 kV at a standard atmosphere.

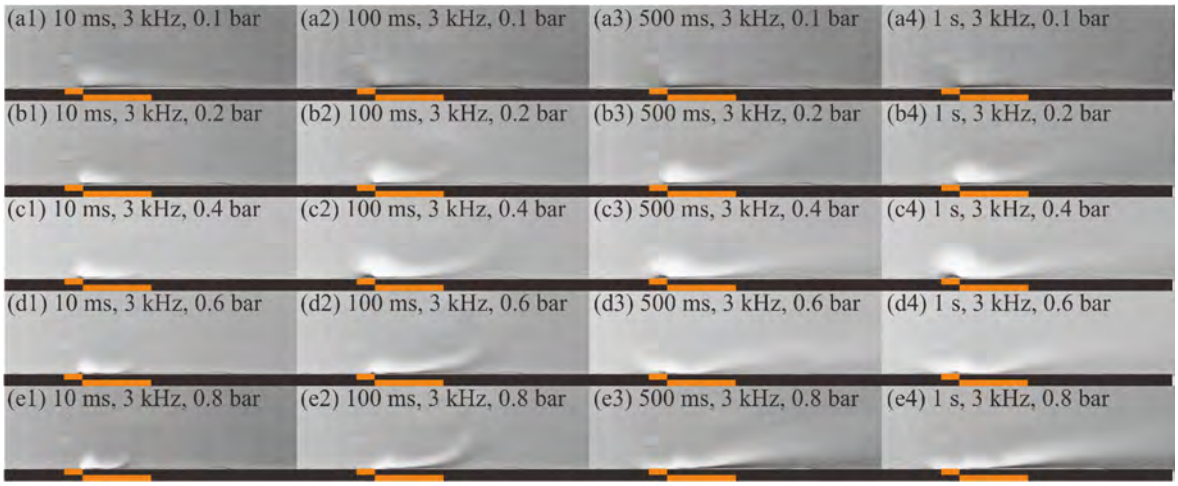

Figure 4-29. Evolution of residual heat generated by the NSDBD plasma actuator, which is operated at 3 kHz of 25 kV under ambient pressures of (a1) to (a4) 0.1 bar, (b1) to (b4) 0.2 bar, (c1) to (c4) 0.4 bar, (d1) to (d4) 0.6 bar, and (e1) to (e4) 0.8 bar.

4.3.5. Heat efficiency

The definition of the energy stages was clarified by Kriegseis *et al.*[120] and improved by Liu *et al.*[35], as shown in Figure 4-30. The efficiency of the first operational stage is defined as the ratio between the discharge energy E_A and the electrical input energy E_{in}[40]. The efficiency of the second

stage is defined as the ratio between the output energy (kinetic and thermal energy) and discharge energy. Because the control mechanism of an NSDBD plasma actuator is based on a thermal effect, this study aims to estimate the thermal energy efficiency, which is necessary for engineering such as anti-icing. The heating efficiency is defined as the ratio of thermal energy on the dielectric surface E_{heat} and total energy input E_{in}, as shown in Eq.4-4. In this study, E_{heat} includes the heat convection from the gas to the surface (E_S) and heat generation by the dielectric losses:

$$\eta_{heat} = \frac{E_{heat}}{E_{in}} \tag{4-4}$$

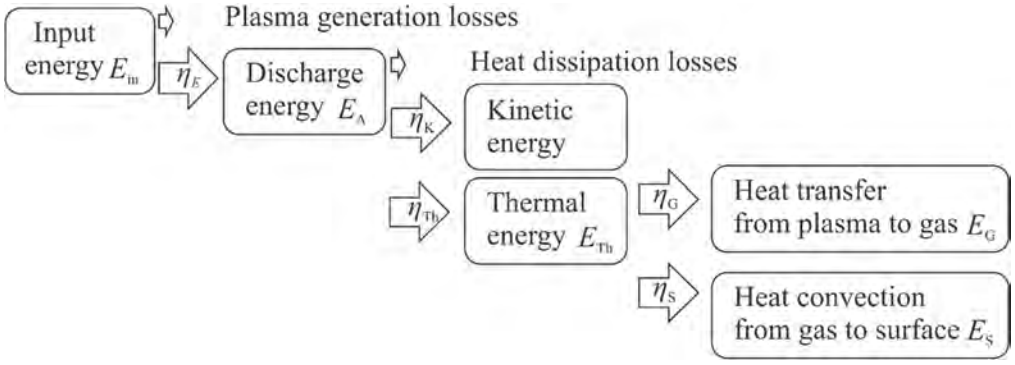

Figure 4-30. Schematic of the energy budget of an NSDBD plasma actuator

The surface heating efficiency was calculated by Eq.4-4 using the integration of heat flux on the dielectric surface. η_{heat} is small, ranging from 0.5% to 2%, similar to the observation of Liu *et al.*[35]. As shown in Figure 4-31, the reduction in air pressure would heavily affect the heating efficiency, with the heating process being more efficient at high air pressure. Under a relatively low voltage, the figure shows two states that are relevant to the discharge mode. The air pressure change in the respective discharge mode would not influence the heating efficiency. However, at high voltage, the heating efficiency decreases with thinner air in filamentary mode due to the weaker discharge filaments. PRF rarely affects the heating efficiency, although the absolute heat strongly increases with a high PRF. In the diffuse mode at 35 kV, a high PRF marginally decreases the heating efficiency. Aleksandrov[121] reported that most of the thermal energy generated in the plasma is stored in the gas layer near the surface. The thermal energy efficiency η_{Th} from the discharge is relatively higher and varies from 40% to 90%[24, 40, 122]. In this study, the large fluctuation range of η_{Th} is caused by the uncertainties in measuring the thermal energy of hot gas by different authors. Due to the low heating efficiency on the surface, it remains a challenge in real applications of NSDBD plasma actuators, such as icing mitigation on aircraft.

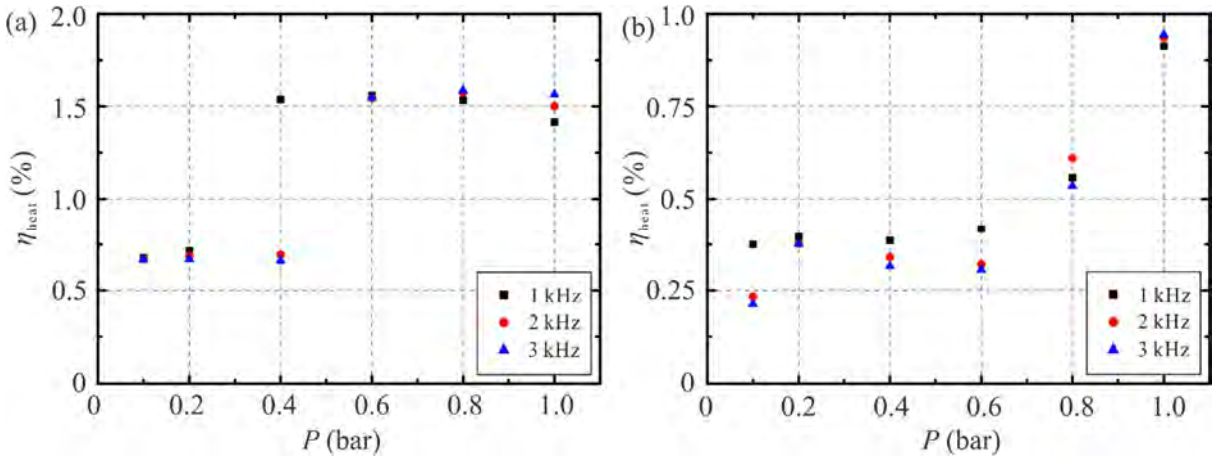

Figure 4-31. Surface heating efficiency η_{heat} under different air pressures at (a) 25 kV and (b) 35 kV.

4.4. Remark

In this Chapter, the characteristics of the ACDBD, PSVGs, and NSDBD plasma actuator were examined experimentally. Because the ACDBD and PSVGs have been widely studied, this study mainly focuses on the validation before installing them on the models. The main results are concluded in the relative sections. For the NSDBD, as a new technology, its thermal effects were investigated detailly and the main findings are summarized as followings:

i. By measuring the applied voltage and current, results show that energy input increases with the applied voltage and only slightly depends on the gas pressure. By observing discharge features, the transition from a filamentary mode to a diffuse mode with decreasing air pressure is described. The filamentary streamers extend along the radius direction, forming a more stable, uniform, thicker plasma region because the ionized volume should be increased due to the sparse air to maintain the high values of the reduced electric field. Although the PRF plays an important role in flow control, it only slightly affects the streamer distribution, luminosity and discharge mode transition with changes in air pressure.

ii. The spatiotemporal temperature distribution on the surface indicates that the heated surface can be divided into three typical regions in the streamwise direction: the plasma region, the insulated electrode region, and the far-field region distinguished by two inflection points. Because gas heating is generated during quenching of the excited molecules, the maximum temperature increase on the surface occurs in the plasma region and attenuates downstream. The surface temperature increase is primarily caused by heat convection from the residual heat in plasma and the heat generated by the dielectric losses. The thermal effects are strongly associated with the discharge mode. Compared to the diffuse mode, the gas heating process is more acute in a filamentary mode. At 25 kV, when the air pressure drops below a critical value, the heat transfer will jump from a high to low value. However, at a higher

voltage of 35 kV, the surface heat transfer decreases with the air pressure drop accompanied by the attenuation of filaments and then remains at a value in the diffuse mode. Choosing the most appropriate applied voltage and PRF based on discharge characteristics will strongly increase the control efficiency.

iii. The hydrodynamics of the induced shock wave and its strength are also investigated. Results show that the overpressure drops approximately exponentially with the shock spread. The induced shock wave propagates at approximately 390 m/s (Ma = 1.13) at the beginning and rapidly attenuates to a sonic wave at 345 m/s under the interaction of the reflected rarefaction wave. The time evolution of the shock pressure profile generally follows the Friedlander equation and indicates that the NSDBD plasma discharge actually achieves a microblast wave characteristic. The similarity between the overpressure strength and thermal features also shows that the induced shock wave is generated from the fast heating process. The evolution of a starting vortex and a steady wall jet is similar to that of an ACDBD plasma actuator. In diffuse mode at 0.4 bar, the residual heat prefers to convect vertically from the surface with a larger residual heat region due to a thicker plasma region. Eventually, the thermal jet lifts off from the wall surface because the expanded thermal fluid accelerates under the electric field. The heating efficiency on the surface ranges from 0.5 to 2%. The low heating efficiency on the surface suggests that there is still a challenge for the application of NSDBD plasma actuators.

The results in this study can also help establish a more exact thermodynamic model of NSDBD plasma actuation, particularly in the extreme cases of high voltage and PRFs. The results of this study also provide references for the mechanism detection of icing mitigation and flow control based on NSDBD plasma actuators. In future work, the variation characteristics of the spatial temperature field should be investigated in more detail to quantitatively evaluate the heat in the gas.

CHAPTER 5 Flow control over a D-shaped bluff body in the incompressible flow

The control performance of a streamwise-oriented dielectric barrier discharge (DBD) plasma actuator, a set of plasma streamwise vortex generators (PSVGs), and a hybrid actuator of the plasma actuator and PSVGs on the reduction in bluff body flow separation, vortex-induced vibration (VIV), and wake fluctuation is experimentally investigated. Experiments are conducted in a low-speed and low-turbulence wind tunnel with a Reynolds number between 3×10^3 and 1.2×10^4 based on the diameter of a half circular cylinder. Particle image velocimetry (PIV) is used to obtain details on the flow fields over a short D-shaped bluff body. Force measurement is conducted to compare the reduction in drag and vibration oscillations using these three types of plasma actuators. The PIV flow fields show that all of the plasma actuators suppress the flow separation on the bluff body, narrow the size of the wake, and decrease the turbulence kinetic energy (TKE) level in the wake. This stable controlled vortex shedding system can reduce the effect of the natural frequency of the bending stiffness-dominated cylinder structure system, thus avoiding the occurrence of resonance in advance. The reduction in drag and lateral lift oscillation are studied by mapping the changes in force coefficients and fluctuations as a function of Reynolds number. A comparison of these plasma actuators shows that the hybrid actuator achieves best drag reduction, suppression of lift oscillation, and Kármán vortex shedding in the wake at low speed, because three-dimensional flow structures are generated on the surface of the bluff body that consequently enhance the mixing. The results suggest that PSVGs and ameliorative actuators are promising for wake flow control in bluff bodies at low speeds.

5.1. The natural case without control on a D-shaped bluff body

To investigate the control effects of the different actuators, the natural flow around the short bluff body without control was characterized. Figure 5-1 summarizes the mean velocity fields at different tested freestream velocities. In the case of a low *Re* (see Figure 5-1(a)), the boundary layer, which starts at the stagnation point x/D = -1.5, separates upstream from the junction of the round nose and square body. Here, D is the diameter of the circular nose. The vortex streets form in the bluff body's far downstream wake by interacting with the two separated shear layers via entrainment. For this type of flow, the wake is initiated by a separation at the body front and is referred to as the WI flow regime[123]. In the near wake, the mean bubble length, an important wake flow characteristic, is defined as the distance from the corresponding saddle point (reattachment point) to the back surface of the bluff body[64]. When the freestream velocity (and the corresponding *Re*) increases to a certain extent, the detached boundary layer reattaches at the trailing edge (at Re_D = 13333 and C/D = 1.5; see Figure 5-1(c)). The wake is initiated from a separation at the rear salient edges (referred to as the WII flow

regime). The WI and WII regimes have very different bluffness[123]. A similar flow reattachment phenomenon was reported in a prior study by Vladimir *et al.*[53] when Re_D = 13000 and C/D = 2. The mean bubble length gradually decreases as the freestream velocity increases due to the flow reattachment on the side surface. Yamagata *et al.*[50] found that the chord length to diameter ratio (C/D) significantly affects the flow field around a bluff body at the same freestream velocity (Re), which indicates that the reattachment is related to the Reynolds number based on the chord length. In an elongated bluff body, separation at the leading edge and reattachment before separating again at the trailing edge can be observed, forming a separation bubble. The flow separation at the trailing edge is a significant departure from the relatively thin layers typical of separated shear layers in shorter bluff bodies[51]. In this study, to avoid the complicated effects of flow reattachment on wake formation and to consider all the control cases under the same WI flow regime, the Re will be limited between 3300 and 12000 (before the transition to WII) hereinafter. The actuator controls all have the same flow separation conditions without flow reattachment on the model surface.

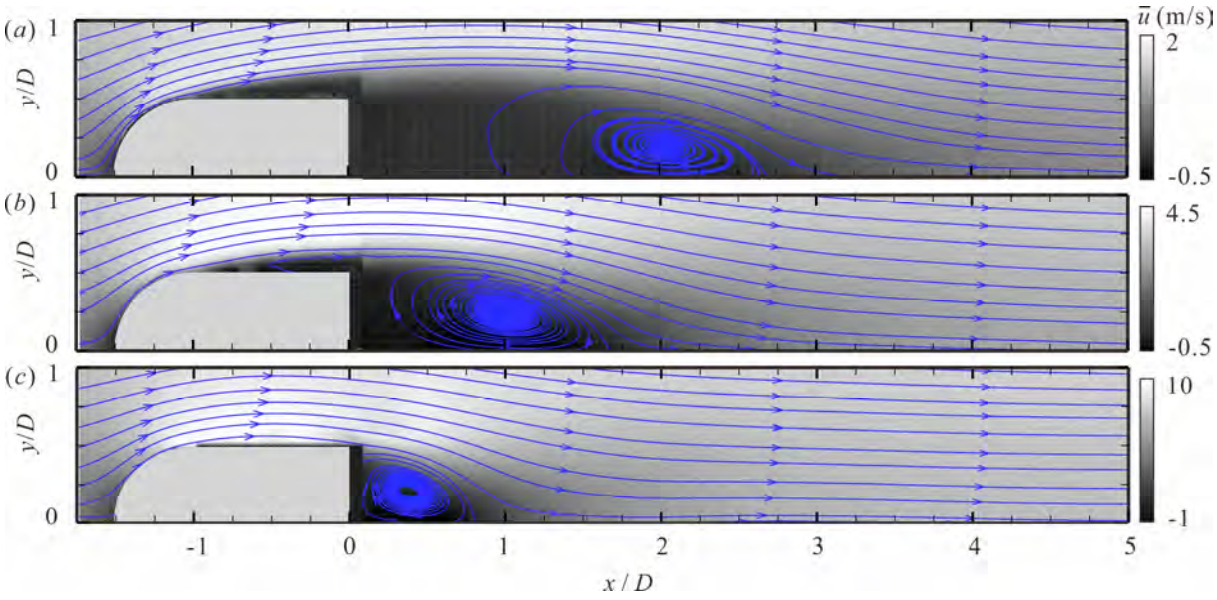

Figure 5-1. The natural flow field around the bluff body (without control) at U_∞ = (a) 1.67 m/s, (b) 3.33 m/s, and (c) 6.67 m/s. The corresponding Re_D are 3.33 × 10^3, 6.67 × 10^3 and 1.33 × 10^4, respectively. The time-averaged streamwise velocity and streamlines are presented in gray contours and in blue lines, respectively.

Zdravkovich[48] subdivided a flow regime over a circular cylinder into 15 typical states based on the boundary layer characteristics on the cylinder surface and the separated shear layer. In a global flow structure of a short bluff body, the flow properties may share the same features as a circular cylinder. Nevertheless, the shape of the afterbody and the near wake region of a short bluff body downstream from its separation points strongly affect the flow structures[49]. The flow physics is also determined by the state of the free shears just after separation. However, due to the current limitation of experimental methods, we focus on the control effect on the wake initiated from the separation at

the body front (WI) of the baseline case by actuators in this study. In the future, the transition in free shear layers to boundary layers, especially after the reattachment point, and the control effect on the wake initiated from the separation at the trailing edge (WII) of the baseline case on a D-shaped bluff body will be studied.

Three different configurations of DBD plasma actuators are studied: a typical DBD plasma actuator (DBD; see Figure 2-4(a)), plasma streamwise vortex generators (PSVGs; see Figure 2-4(b)), and a combination of DBD actuators and PSVGs (Hybrid; see Figure 2-4(c)). The key parameters, such as exposed electrode width and gaps between exposed electrodes and insulated electrodes, were optimized according to Wicks's work. They indicated that the optimum spanwise interelectrode spacing does not scale with the approach boundary-layer thickness. Instead, optimum λ_z is governed solely by the local plasma dynamics[16]. For fixed applied voltage, if the interelectrode spacing is too small, the spanwise extent of the plasma forming region is artificially constrained, which reduces the body force and hence the ability to produce streamwise vorticity. For too large a spacing, the local upwelling produced by colliding spanwise wall jets is negatively affected, which in turn reduces the velocity gradient in z direction required for effective actuator performance[16]. The optimization of vortex flow caused by interactions between induced vortex and freestream velocity will be further studied. The main purpose of this study is to find out the underlying control mechanisms of PSVGs on the short D-shaped body and to increase its control performance, such as drag reduction and periodic vibrations, by changing the electrode configurations. Thus, other parameters, such as applied voltage and frequency, were fixed at 11 kV and 20 kHz, respectively. Moreover, the control effectiveness of afterbody size which strongly affect the natural flow regimes, will be verified in the future. The following sections show the details of the control performance of these three kinds of configurations.

5.2. Characteristics of the vortex-induced vibration

To investigate the effects of the VIV control, the dynamic vibration responses in the transverse lift and streamwise drag directions are studied in this section. First, the natural frequency of the cantilevered model was measured using the free decay test. The corresponding power spectra in the lift and drag directions are shown in Figure 5-2(a) and (b), respectively. The power spectra indicate that there are several dominant frequencies in the oscillation of the bending stiffness-dominated cylinder structure. In the lift direction, the first peak at 5.6 Hz corresponds to the natural frequency of the first mode with the maximum amplitude occurring at the cylinder's free end. The second and third peaks at 47.8 Hz and 51.9 Hz represent the second and third modes' frequencies, respectively. The third peak is very close to the second peak because the third vibration mode may couple with the second mode due to the model's peculiarity. Harmonics of these coupling peaks appear close to 100 Hz and 150 Hz. A similar phenomenon can be observed in the drag direction. To be noted, the natural frequency in the drag direction is slightly higher than in the lift direction because the bending rigidity is higher in the drag direction.

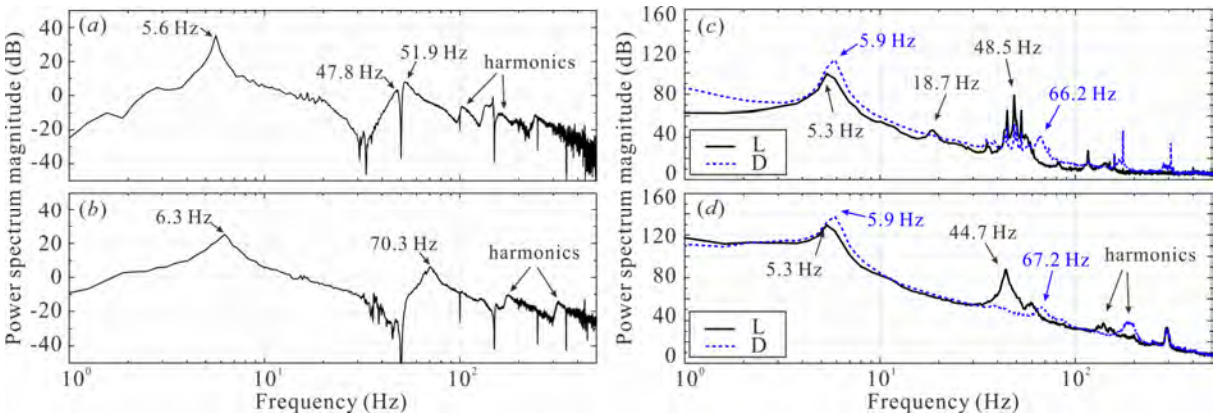

Figure 5-2. The power spectra of the vibration amplitude with the excitation force without flow in the (a) lift (y) and (b) drag directions (x). The power spectrum of the transverse lift and drag at (c) U_∞ = 3 m/s and (d) 5 m/s ($Re_D = 6 \times 10^3$ and 1×10^4, respectively).

In the subcritical Reynolds numbers' range, the VIV is dominated by two different frequency responses in the selected D-shape cylinder structure. Figure 5-2(c) and (d) present the frequency responses of the two aforementioned representative characteristics at two different freestream velocities. As previously mentioned, in the lift direction shown in Figure 5-2(c), peaks at 5.3 Hz and 48.5 Hz represent the first and second modes' frequencies, respectively. Notably, in proximity to the second natural frequency, peaks with prominent contributions may also appear in addition to the dominant peak. Because of vibration mode coupling, the second natural frequency presented in a rather broad band with several peaks. Between the first and second modes' two peaks, a peak at 18.7 Hz is clearly observed, which represents the VIV response frequency. In this condition (called the VIV-dominated region), the dynamic frequency response is characterized only by the vortex shedding process. However, at a higher Reynolds number as shown in Figure 5-2(d), a strong peak at 44.7 Hz (instead of the original two peaks at 18.7 Hz and 48.5 Hz) appears with a slightly lower frequency than the second natural frequency. This result suggests that VIV is characterized by the synchronization of the forcing frequency and second natural frequency under this condition (called the motion-dominated region). This synchronization can also be observed as a lock-in region in lift oscillation as shown Figure 5-3(a). These two regions are marked and separated by the dotted line in Figure 5-4. In the drag direction shown as blue dotted lines in Figure 5-2(c), peaks at 5.9 Hz and 66.2 Hz represent the first and second natural frequencies along the drag direction, slightly higher than those in the lift direction due to the higher bending rigidity. To be noted, the second frequency peak in Figure 5-2(d) moves slightly to 67.2 Hz because of the frequency synchronization.

To study the control effect of the force oscillation, the dynamic vibration responses in the transverse lift and drag directions are assessed using the force oscillation magnitude and corresponding frequency domain. Figure 5-3 shows the force coefficient variations as a function of the reduced velocity $U_r = U_\infty/f_n D$, where f_n (= 5.6 ± 0.1 Hz) is the first natural frequency in the y direction (lift direction) in air. A significant difference can be observed between the VIV- and motion-

dominated regions. In the VIV-dominated region, the force oscillation is low and slightly increases after controls due to induced flow excitation. The lift oscillation considerably increases and gradually decreases in the lock-in region. Although this trend is not completely changed after controls, the bandwidth and pick value of lock-in region decrease considerably. Delays in the increasing phases in both the lift and drag coefficients can be also observed. The drag oscillation obviously increases in the DBD case, but this adverse effect improves after the PSVGs and hybrid controls are applied. This might be caused by the thrust force generated by induced jet of DBD actuator along the drag direction.

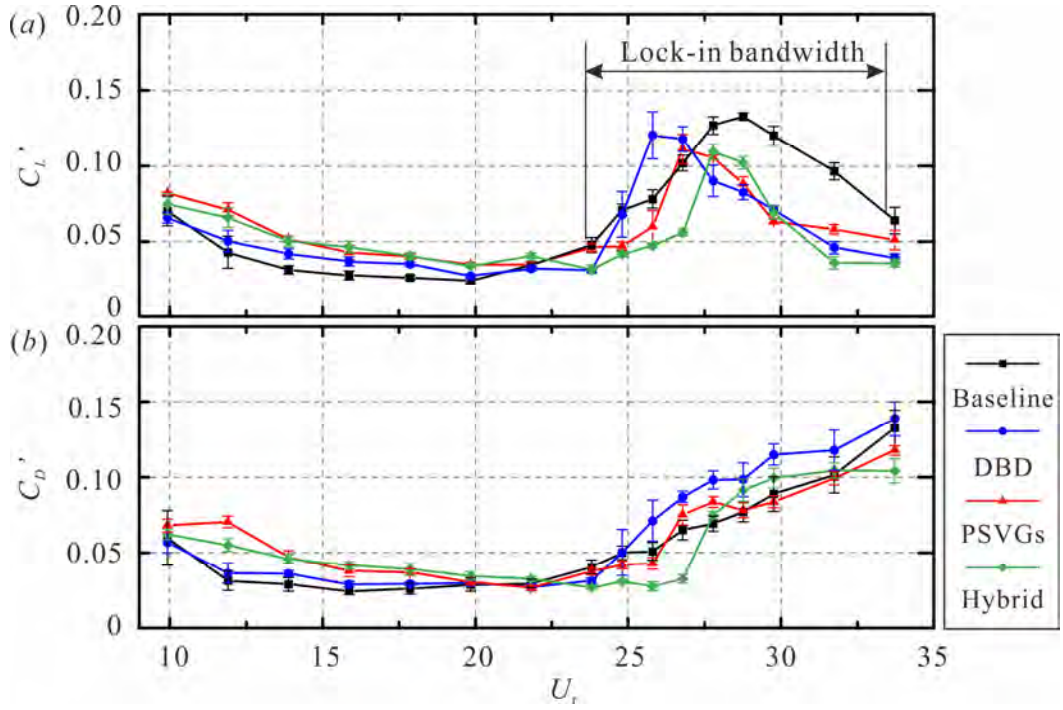

Figure 5-3. Variations in the lift and drag coefficients as a function of the reduced velocity.

The dominant oscillation frequency responses (f_o) were further acquired through fast Fourier transform (FFT) analysis of the force measurements. Figure 5-4 presents the power spectral density (PSD) contours (on a logarithmic scale) of the transverse lift (f_y^*) and drag force (f_x^*) in all of the cases as a function of the reduced velocity and normalized frequency (marked with the superscript "*") based on f_n. In the baseline case's transverse lift frequency response, an obvious feature of the continuous increase in the dominant oscillation frequency is shown in Figure 5-4(a1). The dominant oscillation frequency follows the trend of the vortex shedding frequency in the low reduced velocity region, and a significant VIV response is observed. Following this continuous increase in the dominant frequency, there is a distinct jump of f_y^* at a point where the transverse lift amplitude sharply increases (see Figure 5-3(a)) due to the switch to its subsequent mode, that is, the lock-in mode. The vertical dashed line in each plot demonstrates the occurrence of this saltation, which is a special feature of flow transformation to the lock-in region. Because the structural motion controls the vortex shedding process, the vortex shedding frequency will adapt the cylinder's natural frequency[124, 125]. This occurs quite prominently in bending stiffness-dominated structures such as clamped-free

slender cylinders. The sharp transitions between the vibration modes also occur after controlling using different actuators (see Figure 5-4(b1), (c1), and (d1)). In the DBD case, in the VIV-dominated region, the VIV frequency decreases, which means that the vortex shedding has changed. Limited variations can be observed in the corresponding reduced velocity where the frequency jump occurs. However, when controlled by the PSVGs and hybrid actuator, not only the bandwidths of the dominant oscillation frequency in the VIV-dominated region shrink, but also saltation is delayed due to higher reduced velocities. This behavior indicates more stable vortex shedding that can reduce the effect of the natural frequency and thus avoids the occurrence of resonance in advance. However, this abrupt jump did not occur in the drag fore direction (see Figure 5-4(a2)) because the VIV signal is eliminated in the VIV-dominated region after control. Conversely, the lock-in response persists in the drag direction in the motion-dominated region. It is relevant to note, the PSD strength obviously decreases in the hybrid case (see Figure 5-4(d2)).

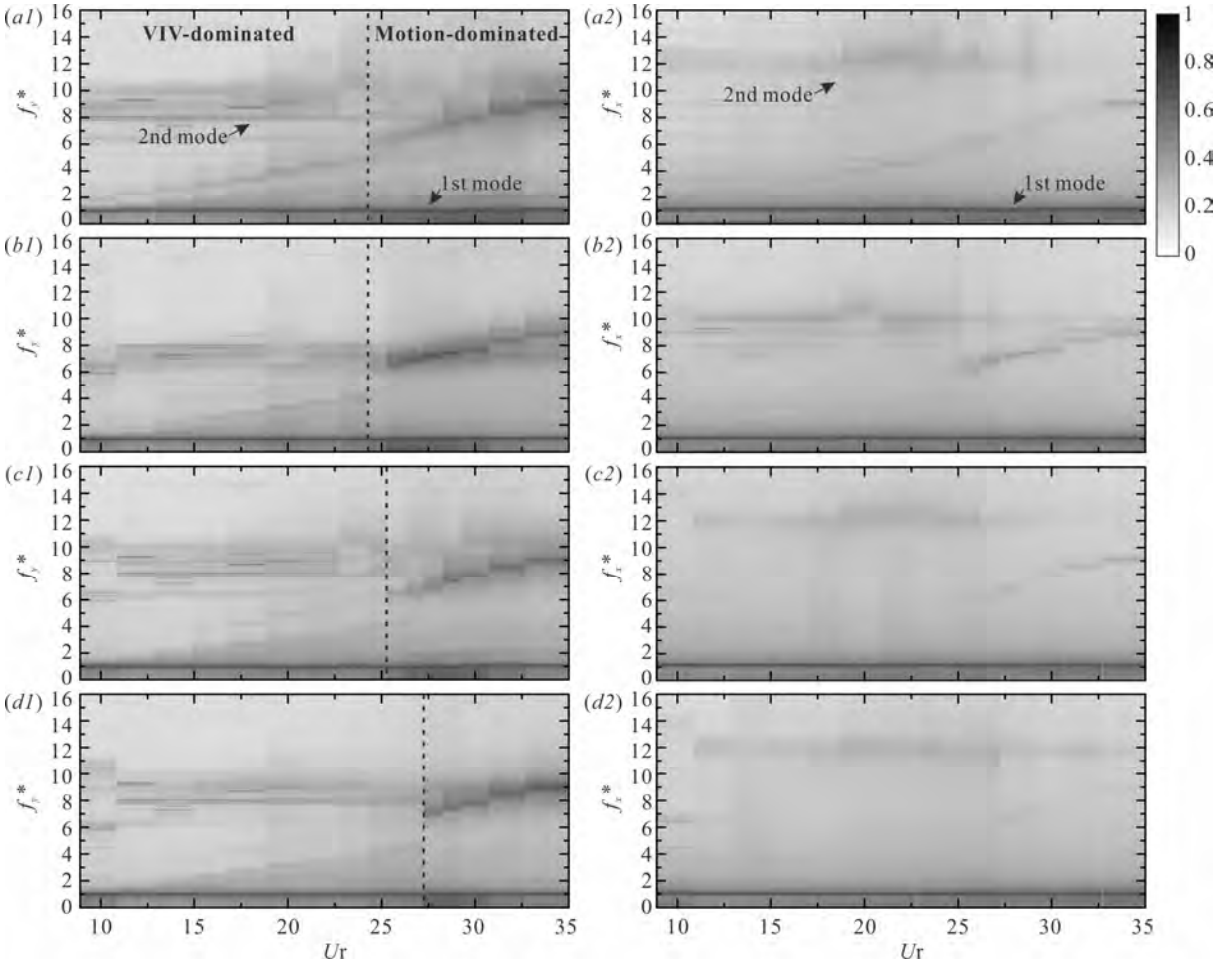

Figure 5-4. The power spectral density contours in the logarithmic scale versus the normalized frequency and reduced velocity in all of the cases. f^*_y and f^*_x are the normalized transverse lift frequency and the normalized drag force frequency based on f_n, respectively. The left column represents the transverse lift data under (a1) baseline, (b1) DBD, (c1) PSVGs, (d1) and hybrid actuator conditions. The right column denotes the drag force data under (a2) baseline, (b2) DBD,

(c2) PSVGs, (d2) and hybrid actuator conditions. The VIV-dominated region and motion-dominated region are distinguished by the dotted line in the left column.

The Strouhal number is defined as $St = f_{st}D/U_\infty$, where f_{st} is the vortex shedding frequency. It was 0.216 in the baseline at Re_D = 3333[64], which is in good agreement with prior studies, for example, St = 0.221 at Re_D = 1.3 × 10^4 and C/D = 2[53], and St = 0.238 at Re_D =3.6 × 10^4 and C/D = 1.92[52] (see Table 5-1). To further investigate the model oscillation frequency that is strongly associated with the periodic oscillating wake in the different cases, the dimensionless analysis of $St_{oD} = f_oD/U_\infty$ and Ro_{oD} (Roshko number) = $St_{oD}Re_D$ as a function of the Reynolds number is studied based on f_o. A linear relationship can be observed between Re_D and Ro_{oD} in Figure 5-5, which is in good agreement with the wake oscillating characteristics of blunt trailing edge profiled bodies by Naghib-Lahouti *et al.* [126]. In the VIV-dominated region, St_{oD} in the baseline case is approximately 0.224, very close to the Strouhal number found in prior studies. After controls, the slope of Re_D versus Ro_{oD} decreased to 0.183, 0.171, and 0.167, respectively. Naghib-Lahouti *et al.*[126] found that the reduction in this slope in the wake is an indicator of the boundary layer's transition from laminar to turbulent. Thus, after controls, the vortex shedding process changes, which strongly affects the vibration induced by vortex shedding. However, in the motion-dominated region, the controls have limited influence on the oscillation frequency due to the resonance between the model and vortex shedding.

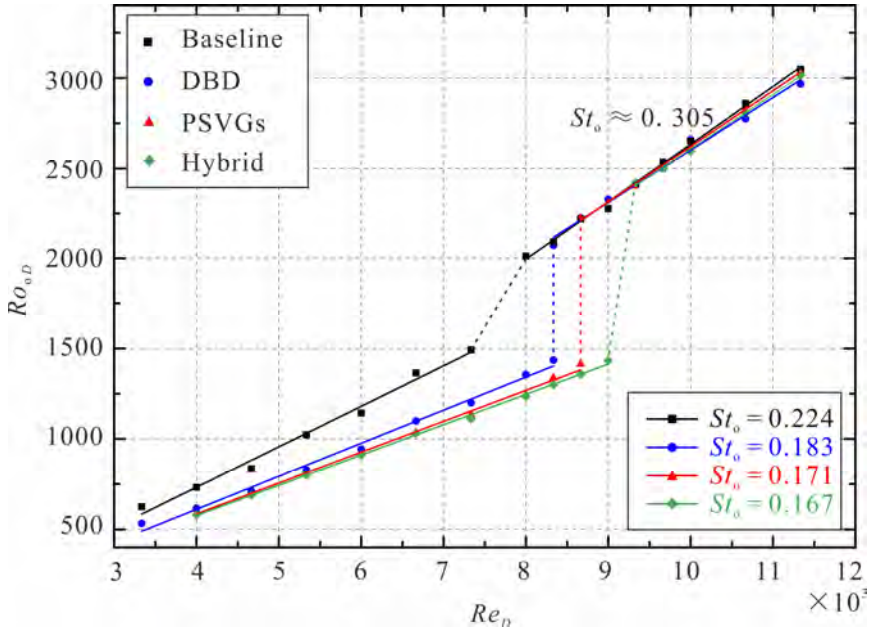

Figure 5-5. Variations in the oscillation frequency as a function of the Reynolds number.

Table 5-1. Comparison of experimental parameters given in literature of a D-shaped bluff body.

Authors	C/D	Re_D	St	C_D
Parezanović and Cadot, 2012	2	1.3 × 10^4	0.221	0.74

Thiria *et al.*, 2009	1.92	3.6×10^4	0.238	-
Yamagata *et al.*, 2017	1	3.0×10^4	-	0.78±0.13
This study	1.5	3.3×10^3	0.216	0.78

5.3. Drag reduction and control efficiency

Flow control with different plasma actuator configurations may affect aerodynamic forces on the bluff body. Figure 5-6 presents the differences in drag reduction using the three control layouts. As shown in Figure 5-6(a), although the arrangement of active electrodes is distinct, the exposed electrodes' effect on the drag coefficient is rather insignificant when the plasma actuation is off. The exposed electrodes do not cause a significant increase in the drag in the plasma-off cases. In prior studies, the drag coefficient was 0.74 measured experimentally at $Re_D = 1.3 \times 10^4$ and $C/D = 2$[53] and 0.78 ± 0.13 at $Re_D = 3 \times 10^4$ and $C/D = 1$[50]. In this study, the drag coefficient in the baseline case (no control) is approximately 0.78 at low Reynolds numbers. Notably, the drag coefficient increases to 0.82 when the Reynolds number is 7000. Then, as the Reynolds number increases, the drag coefficient remains a transitory invariant and eventually decreases rapidly. The inherent three-dimensionality at the onset of the boundary layer transition disturbs the near wake, resulting in an initial decrease in the drag coefficient[48]. As the separation region shrinks, the separated flow more strongly interacts with the sharp trailing edge of a short bluff body. After controls, the drag coefficients decrease significantly (see Figure 5-6(a)), due to formation of a separation-reattachment (see Figure 5-8(a) in Section 5.4) which reinvigorates the boundary layer[123] and allows the final separation occurs at the rear salient edges (WII regime), yielding greatly reduced wakes (see Figures 5-9, 5-10, 5-11 in Section 5.5) and drag, consequently.

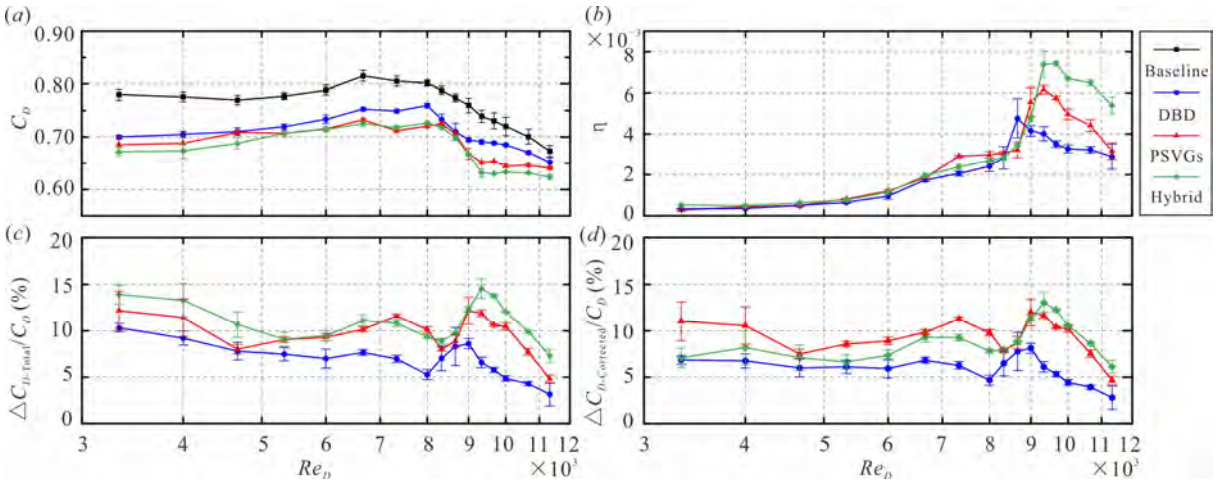

Figure 5-6. (a) Drag coefficients, (b) actuator efficiencies, (c) total reduced drag percentages, and (d) corrected reduced drag percentage under the baseline and three control configurations in an *Re* range between 3.3×10^3 and 1.2×10^4.

The actuator efficiency can be defined as the mechanical power saved by drag reduction divided by the electric power provided to the actuator as shown in Eq. (5-1):

$$\eta = \frac{P_{saved}}{P_{electrical}} = \frac{\Delta F_D \cdot U_\infty / L}{f_{ac} \int E_{ac} I_{ac} d\tau / l} \quad \textbf{(5-1)}$$

where ΔF_D is the reduced drag after control, L is the model's total spanwise length, l is the actuators' discharge length, and E_{ac}, I_{ac}, and f_{ac} is the voltage, current, and frequency of the AC power delivered to the plasma actuators, respectively. Note that, the power saved by reducing the transverse lift fluctuation is not considered in the total saved power. This economization depends on the different control systems and can be more important than the drag reduction[127]. Figure 5-6(b) plots the efficiency as a function of Re_D. The maximum value is 0.75% in the case, which is the same order of magnitude as the results of Jukes *et al.*[15]. The efficiency increases significantly at higher Reynolds numbers because the actuators continue reducing the drag with a similar electrical energy input, saving considerable mechanical power. Nevertheless, the efficiency decreases again due to the weakened drag reduction. Actually, the body force generated by an AC-DBD plasma actuator is quite small, usually of several mN/m[128], and the electromechanical efficiency is very low. Most of the power consumption by an AC-DBD plasma actuator releases into the surrounding environment as heat, mainly due to the plasma heating mechanism[26].

The total drag reduction percentage ($\Delta C_{D,Total}/C_{D,plasma\text{-}off}$) is plotted in Figure 5-6(c) for each case. At $Re_D = 3.3 \times 10^3$ ($U_\infty = 1.67$ m/s), the total drag reduction is approximately 10.3% when controlled by the DBD actuator, while the drag reduction increases slightly to 12.1% and 13.9% when controlled by the PSVGs and hybrid actuator, respectively. At higher Re_D (freestream velocities), the results indicate that the total drag reduction efficiency declines slightly in all three cases. Then, it sharply increases again, followed by a rapid decreasing trend. In summary, the performance of total drag reduction by the hybrid actuator is superior to the other two actuators and the PSVG is better than the DBD actuator. Further, to consider the propulsive effect on the total drag reduction of actuated flows, the thrust T generated by actuators in the quiescent air were characterized. The corresponding corrected drag reduction percentage ($\Delta C_{D,Corrected}$ / $C_{D,plasma\text{-}off}$) were investigated and plotted in Figure 5-6(d) for each case, in comparison with Figure 5-6(c). Here, the $\Delta C_{D,Corrected}$ is defined as $(\Delta F_D - Th)/(0.5\rho_\infty U^2_\infty DL)$. As seen, corrected by the propulsive force, the drag reduction percentages reduce to 6.8%, 11.0%, 7.0% at $Re_D = 3.3 \times 10^3$ for the DBD actuator, PSVGs and the hybrid actuator, respectively. Because the propulsive force is mainly contributed by the spanwise parts of exposed electrodes, the thrust Th is significant, especially in the DBD and hybrid cases where Th contributes about 33% and 49% of total drag reduction, respectively. However, this contribution by thrust declines gradually with increasing Re_D and is less than 10% at last. It indicates that the propulsive force cannot be ignored especially at a low Re_D, but its effect is gradually weakened when Re_D increases. Comparatively, for PSVGs, the ratio of Th to total drag force reduction never exceeds 10% for all Re_D studied. For all control cases, the corrected drag reduction percentage increases again, followed by a

rapid decreasing trend, similar to the total drag reduction percentage. The measured thrust, which forces on the model with plasma actuators switch-on on both sides in the quiescent air, is listed in Table 5-2 for reference. Notably, the effect of the free stream flow on the body force may be another important factor but not considered in this study.

Table 5-2. Thrust of different plasma actuators in the quiescent air.

Actuator type	DBD	PSVG	Hybrid
Th (N) at $U_\infty = 0$	8.61×10^{-4}	2.26×10^{-4}	1.182×10^{-3}

5.4. Cross-flow over the surface

To investigate the control mechanism of the different actuator configurations, the induced flow was studied first. In a traditional DBD plasma actuator, air around the exposed electrodes ionizes when high-voltage AC power is applied[129, 130]. The electrical field exerts a physical force on the ionized air that accelerates the charged particles from the exposed electrodes to the insulated electrodes. An ionic wind is generated that transfers momentum to the surrounding air (through collisions by ionized air molecules). In PSVGs in quiescent air, wall jet-like flows can be observed on the model surface, suctioning from the top of the exposed electrodes toward the insulated electrodes. Pairs of opposite induced flows meet in the middle of the insulated electrodes and become strong shear flows moving upward. These shear flows then roll into pairs of counter-rotating vortices along the streamwise direction. Figure 5-7(a1) to 5-7(e1) and 5-7(a2) to 5-7(e2) show the flow topology induced by the PSVGs and hybrid actuator at a velocity of 1.67 m/s (Re_D = 3333) from $x/D = -0.67$ to $x/D = 0.67$, respectively. In the PSVGs, at $x/D = -0.67$ (the actuator's front edge; see Figure 5-7(a)), streamwise vortices do not form. At $x/D = -0.33$, pairs of vorticity concentrations are observed very close to the model's surface. As the downstream develops, the height of vortices core increases, as clearly observed at the bluff body's trailing edge ($x = 0$). Both the induced vorticity magnitude and their influenced region simultaneously increase significantly. After the trailing edge ($x > 0$), the strength of streamwise vorticities rapidly decreases because of the lack of plasma actuation. These vortices then break down in the wake. In the hybrid case, the flow structure is similar to the PSVGs before the trailing edge ($x < 0$), but different when the flow propagates downstream. Compared with the PSVGs, the vorticity's intensity generated by the hybrid actuator significantly increases because the jet induced by the front exposed electrode along the spanwise direction (see Figure 2-4(c)) injects momentum into the induced vortex pair. Therefore, these vortices remain intact with enough intensity for a longer streamwise distance. Notably, the vortex core height and the spacing between two counter-rotating vortex cores in the hybrid actuator changes compared with that in the PSVGs due to the acceleration process resulting from the jet induced by the front exposed electrode along the spanwise direction. The hybrid actuator generates stronger and clingier vortex pairs than the PSVGs.

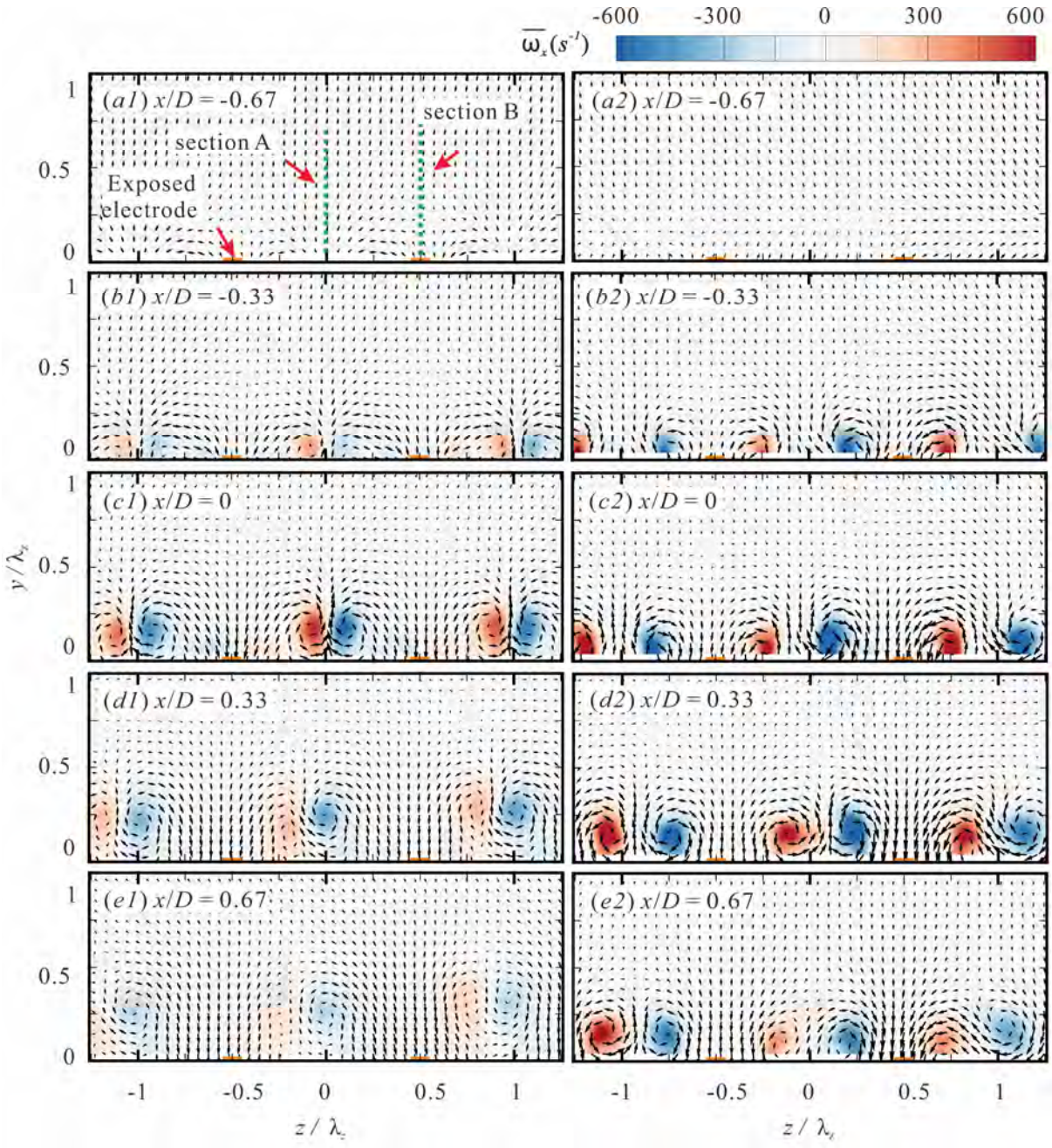

Figure 5-7. Flow visualization of the induced velocity field and vorticity in the *y*-*z* planes by PIV measurement in the PSVGs (left column) and hybrid case (right column) with U_∞= 1.67 m/s (Re_D=3333) at (a1) and (a2) *x*/*D* = -0.67, (b1) and (b2) *x*/*D* = -0.33, (c1) and (c2) *x*/*D* = 0, (d1) and (d2) *x*/*D* = 0.33, and (e1) and (e2) *x*/*D* = 0.67.

Flow separation on the surface of the bluff body was investigated to understand the underlying control mechanisms. To observe the fluid interaction more clearly, the low *Re* case (Re_D = 3333, U_∞ = 1.67 m/s) with the maximum separation and recirculation regions was chosen. The flow structures on the top surface are shown in Figure 5-8, where u(represented by contours) and *v* are the average incoming flow speed components in the *x* and *y* directions. Without plasma actuation (Figure 5-8(a)), the flow separates on the round surface, creating a recirculation region with velocity defects on the

upper surface. Notably, because the chord is insufficiently long, the separated shear flows do not reattach to the surfaces. As shown in Figure 5-8(b), the actuation of the DBD plasma actuator suppresses the separation. In the PSVGs and hybrid, the suppression of separations are observed in both sections A (Figure 5-8(c) and (e)) and B (Figure 5-8(d) and (f)). Compared with the PSVGs, in section A, the flow separation is totally suppressed by the hybrid actuator and no velocity defects are observed near the trailing edge due to the additional momentum injection by the exposed electrode along the spanwise direction. All three actuators successfully suppress the separation because the induced flows by the actuators transfers the momentum into the downstream boundary layer of the original separation point with no control and consequently increase the resistance from separation[54]. In the PSVGs and hybrid actuators, an up-wash flow moves up fluid with lower u momentum from the wall in section A and a downwash flow brings fluid with higher *u* momentum from the incoming flow toward the wall in section B (see Figs. 5-7 and 5-8). However, the hybrid actuator results in more effective momentum mixing and more significant shrinkage of the recirculation zone than the other two.

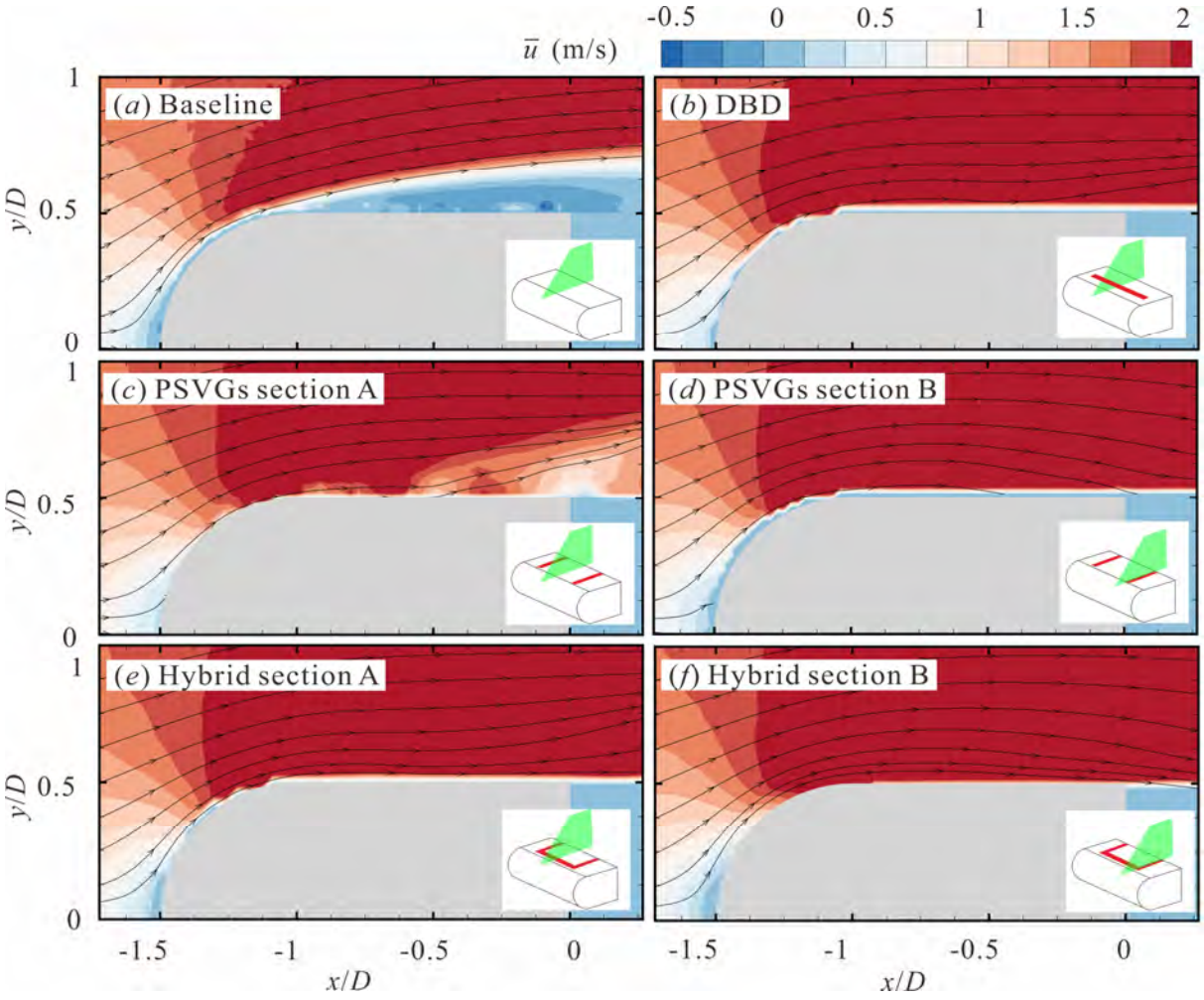

Figure 5-8. Time-averaged flow structure on the bluff body's top surface in the *x*-*y* planes at 1.67 m/s (Re_D=3333): (a) no control, (b) DBD, (c) PSVGs section A, (d) PSVGs section B, (e) hybrid section A, and (f) hybrid section B.

5.5. Effect of control on the wake characteristics

The plasma actuators' control effectiveness, which is reflected by drag reduction and attenuation of the Kármán vortex shedding, can also be confirmed by the wake region's characteristics. The control effect on these characteristics is investigated in this section.

A typical mean wake recirculation region of a half-cylindrical head cylinder[131] is represented by the streamlines in Figure 5-9. The recirculation bubble region is quite large when the bluff body flow is not controlled (see Figure 5-9(a)), and shear flows reattach at x/D = 2.8. When controlled by a traditional DBD actuator (see Figure 5-9(b)), the recirculation bubble size shrinks, and the reattachment point moves upstream to x/D = 1.75. In the PSVGs, reductions in the recirculation bubble region are also observed in both sections A (Figure 5-9(c)) and B (Figure 5-9(d)), and the corresponding reattached point advances to x/D = 1.2 and x/D = 1.0, respectively. Similar to the PSVGs, when controlled by the hybrid actuator, the reattached point moves forward to x/D = 1.1 and

x/D = 1.2 in sections A and B, respectively. This result implies that both the PSVGs and hybrid actuator can significantly advance the reattached point and decrease the recirculation bubble region due to the strong three-dimensional effect induced on the flow field.

In Figure 5-9, the gray contours represent the different levels of turbulence kinetic energy (TKE) per unit mass. The TKE per unit mass is defined as:

$$\frac{k}{m} = \frac{3}{2}(\bar{u}I)^2 \tag{5-2}$$

$$I = \frac{\sqrt{(u'^2 + v'^2 + w'^2)/3}}{\bar{u}} \tag{5-3}$$

where $\bar{u}$ is the average velocity, I is the turbulence intensity in percentage, and $u' = u - \bar{u}$. The contour displays approximate symmetry about the centerline in each case. For the baseline (Figure 5-9(a)), the TKE is very large, and the maximum region is at approximately x/D = 3. After control by the DBD actuator (Figure 5-9(b)), the turbulence kinetic energy declines by more than 50% in the baseline case, and the streamwise position of the maximum TKE moves forward to x/D = 2.75. In the PSVGs, this position's advancement is also observed in both sections A and B at x/D = 1.2 and x/D = 1.4, respectively. The corresponding peak TKE value decreases to approximately 55% of the baseline. Controlled by the hybrid actuator, the TKE is again significantly suppressed, and the peak value declines to 40% of the baseline (control-off) in both sections. This observation suggests that flow control by plasma actuators impairs vortex shedding, and this impairment is more significant combining the DBD actuators and PSVGs instead of a single actuator.

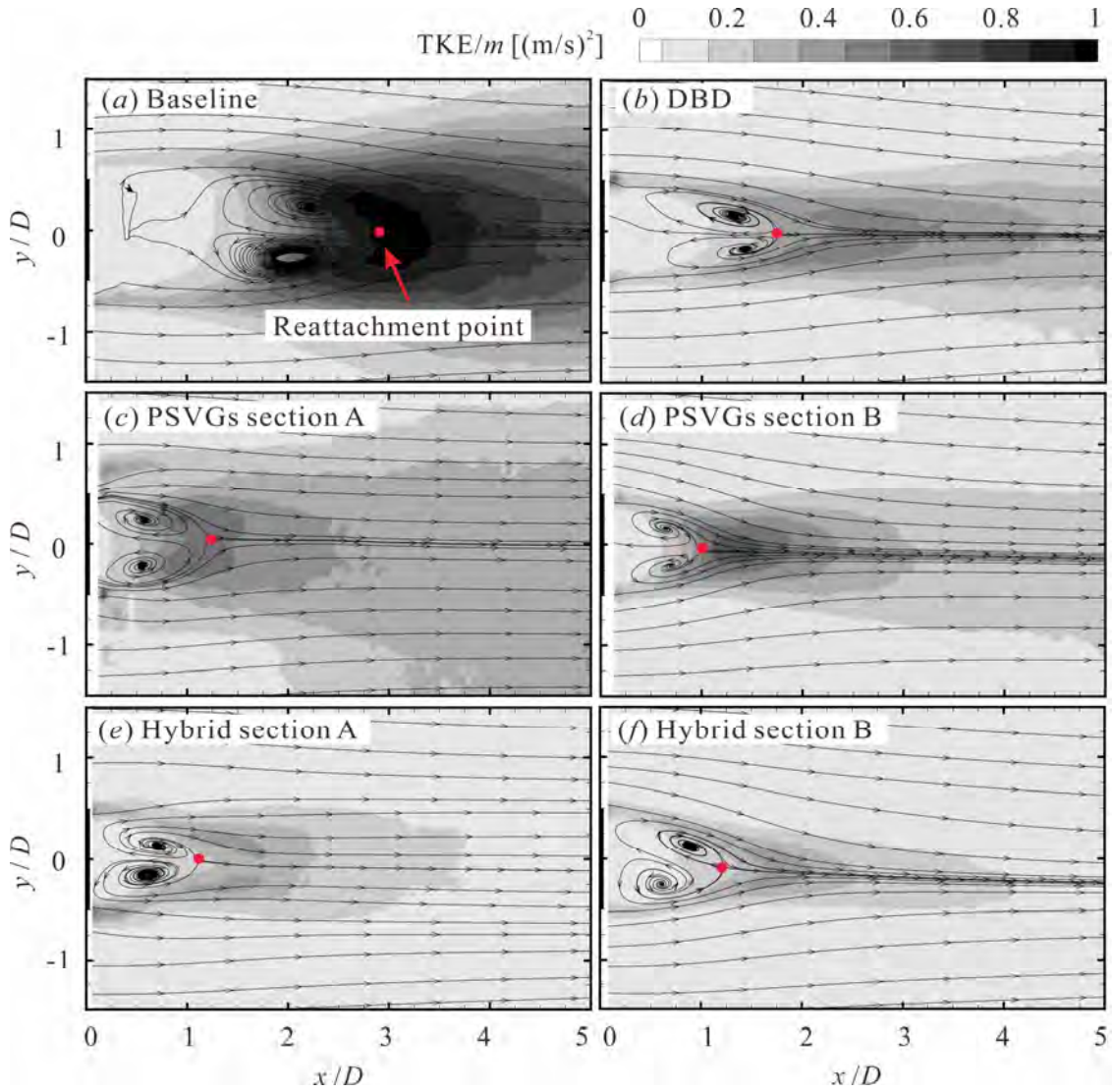

Figure 5-9. Time-averaged wake structures and TKE contours in the *x*-*y* planes at 1.67 m/s (Re_D=3333): (a) no control, (b) DBD, (c) PSVGs section A, (d) PSVGs section B, (e) hybrid section A, and (f) hybrid section B. (Obtained by PIV results)

The length of the recirculation bubble is defined, therefore, by the distance from the corresponding saddle point to the back surface of the bluff body. Meanwhile, the width of the recirculation bubble normalized by D is defined by the maximum lateral distance between two separation streamlines from the model. The width of the recirculation bubble is about 1.5 for the plasma-off cases. The experiment for each case was repeated three times, as shown in Figure 5-10. Good experimental repeatability is observed. The decrease of the recirculation bubble length is significant when compared with that in the DBD case. Also, a noticeable difference in the width of the recirculation bubble between the DBD case and the PSVGs case can be seen in Figure 5-10. The width of the recirculation bubble reduces to 0.9 for section A and 1.0 for section B, respectively. This result implies that the PSVGs have a strong three-dimensional effect on the flow field.

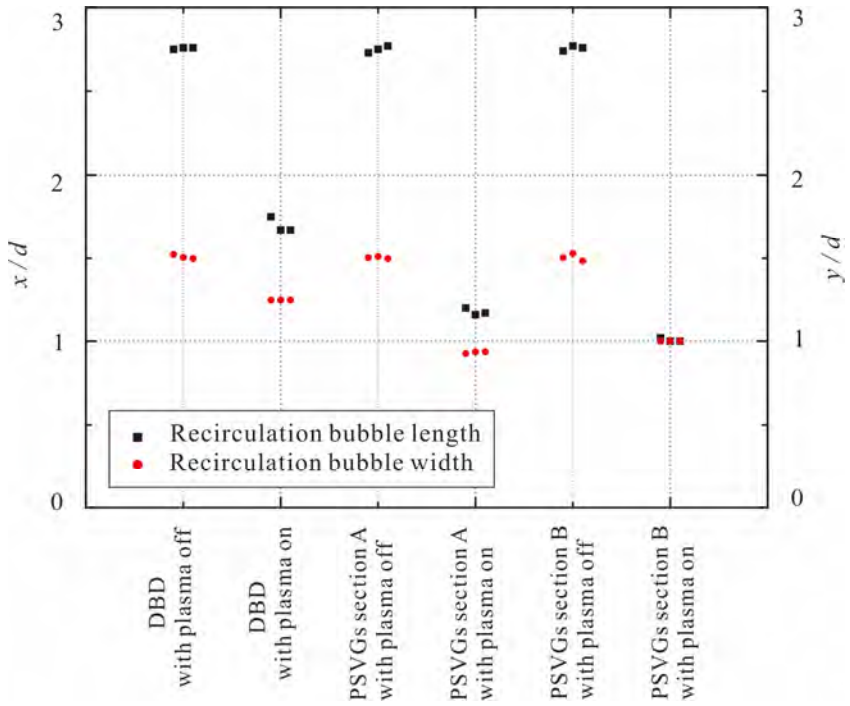

Figure 5-10. Length (*x*/*D*) and width (*y*/*D*) of the recirculation bubble for different cases.

The temporal velocity fluctuations in the wake (x/D = 4, and y/D = 1) were acquired using hot-wire measurements. A fast Fourier transform analysis was conducted to obtain the frequency power spectra. The results of the plasma-off case, the DBD case, and PSVGs case are shown in Figure 5-11. In the plasma-off case, the dominant spectra peak at f_{st} = 11.7 Hz represents the natural frequency of the Kármán vortex shedding from the separated flow region. With the traditional DBD control, the dominant spectra peak increases to f_{st} = 20.5 Hz, and the overall power spectrum decreases dramatically. For the PSVG controls, the power spectra of the dominant peak are significantly lower than those of the DBD control at lower frequencies (f_{st} = 17.6 Hz). Hence, both the DBD and PSVG actuators affect the vortex shedding frequency and suppress the fluctuation level in the bluff body wake[132, 133]. The increase of the dominant vortex shedding frequency is due to the different degree of flow acceleration over the bluff body by the DBD and PSVG actuators[44].

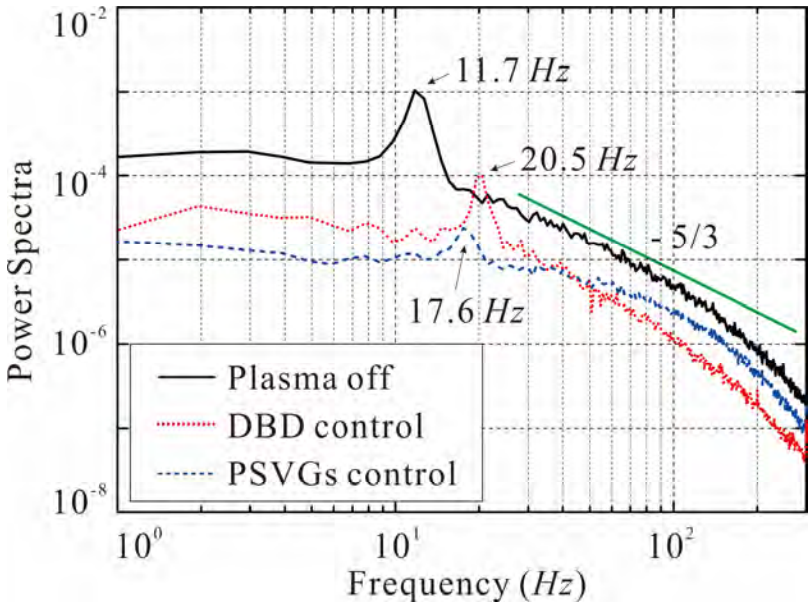

Figure 5-11. Power spectra of the velocity fluctuations in the wake.

The magnitudes of the mean normalized streamwise velocity profile along the y direction in all of the cases are shown in Figure 5-12(a) and (b). The profiles are selected at positions $x/D \in [1,2,3,4]$. Narrowing wakes with lower momentum deficits can be observed after different controls that are caused by the suppressed flow separation and accelerations of the upstream shear layer. This is consistent with the previously described shrinkage of the recirculation bubble region. To be highlighted, a narrower profile is observed in section B than section A in both the PSVGs and hybrid cases because of the downwash flow generated in section B and the upwash flow in section A. Figure 5-12 (c) and (d) show the normalized root mean square (rms) profiles of the streamwise velocity fluctuations. In the baseline case, a double peak profile can be observed symmetric to the centerline, where a vortex pair rolls up. After different controls, the maximal fluctuating region moves upstream because of the surface separation attenuation. Notably, compared to the PSVGs, the hybrid case has a smaller and narrower streamwise fluctuating distribution.

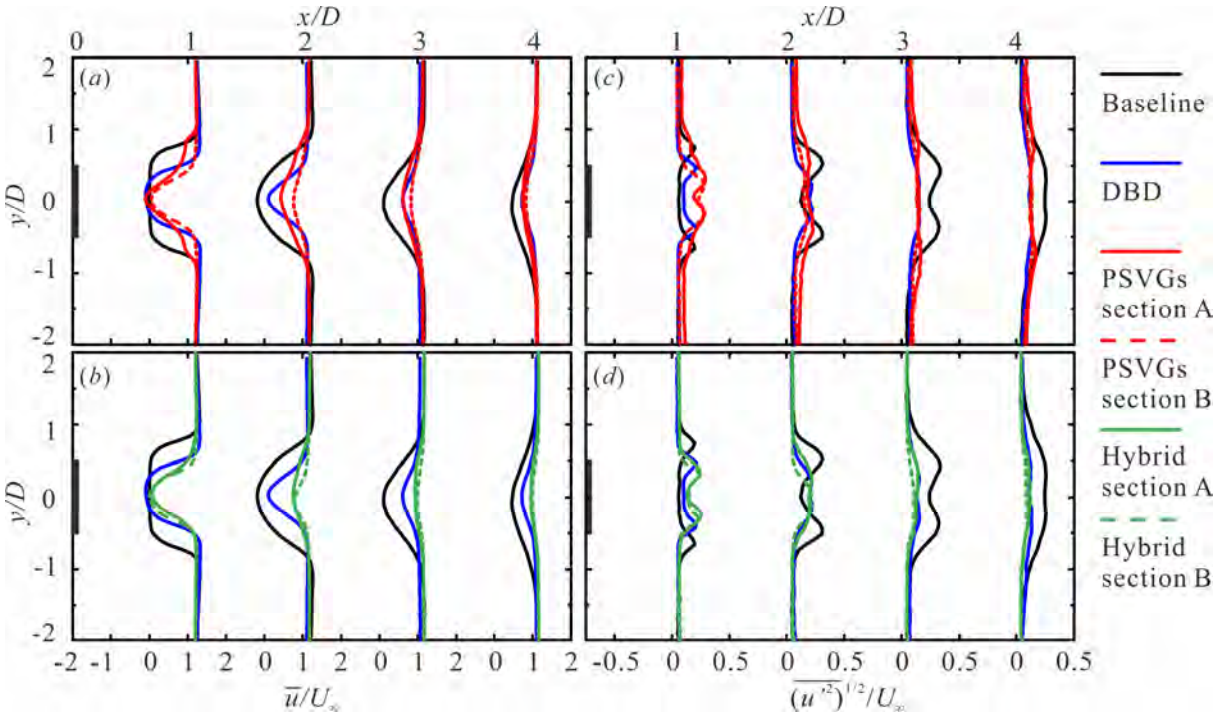

Figure 5-12. Profiles of normalized (a) and (b) time-averaged streamwise velocity and (c) and (d) rms streamwise velocity fluctuation in the baseline, DBD, PSVGs, and hybrid cases (U_∞= 1.67 m/s and Re_D=3333), respectively.

To further investigate the wake dynamics in the vortex formation region, the mean vorticity field and Reynolds stress components $\overline{u'v'}$ and $\overline{v'^2}$ captured from PIV measurements are studied. For the no control case (see Figure 5-13(a1)), the separated shear layers extend in the wake region, roll up, and meet together, yielding vortex shedding with a selected frequency. In the DBD case (see Figure 5-13(b1)), the shear layers are closer to the centerline due to the suppression of separation. In section A of the PSVGs (see Figure 5-13(c1)), the shear layer is split by the spanwise counter-rotating vortex caused by the control. The main part of the shear layer deviates from the trailing edge with a larger deflection angle inward and the other expands slightly outward compared to the original trajectory due to the upwash flow. Instead of the split of the shear layer, a slightly broad shear region can be observed in section A in the hybrid case (see Figure 5-13(e1)) due to the acceleration of the straight component in the exposed electrode configuration. In section B in both the PSVGs and hybrid cases (see Figure 5-13(d1) and (f1)), the shear layer only deviates inward from the trailing edge due to the downwash flow. The hybrid case has a longer vortex formation region than the PSVGs because of the acceleration, but it is still shorter than the DBD case. The counter-rotating vortex induced by the PSVGs not only diminishes the separation, but also changes the shear layer direction and features, resulting in the reduction in the vortex formation length.

Significant changes can also be observed in the mean Reynolds stress components. The maximum streamwise locations of the Reynolds stress $X_{\overline{u'v'}max}$ and $X_{\overline{v'^2}max}$ are defined in Figure

5-13. The extrema of $\overline{u'v'}$ moves upstream after controls to a maximum of $\overline{v'^2}$. In the DBD case, the fluctuations shrink in the zonary region, but in the PSVGs, the high fluctuation region moves closer to the trailing edge in elliptical structures. In the hybrid case, the Reynolds stress fluctuation distribution features are similar to that of the PSVGs, but the amplitude is drastically reduced. These results confirm that the turbulent wake is significantly suppressed after controls, and the PSVGs and hybrid actuators can aggregate the high fluctuation wake field in more restrained regions with a lower fluctuation amplitude. This reduction in the Reynolds stress components is indicative of the changes to Kármán vortex shedding, which will be studied in detail in the next section.

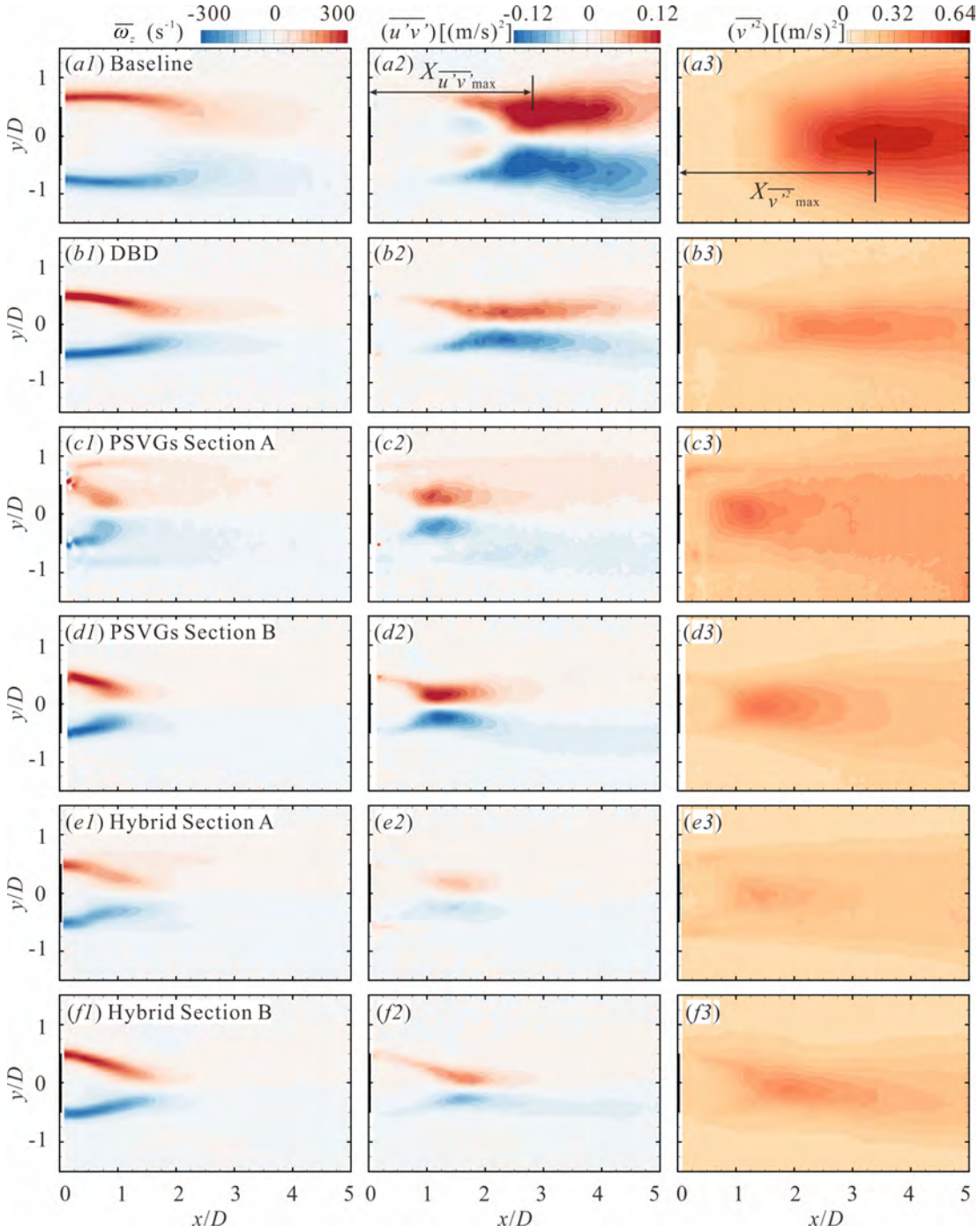

Figure 5-13. Mean vorticity field (left column) and mean Reynolds stress components $\overline{u'v'}$ (middle column) and $\overline{v'^2}$ (right column) at U_∞= 1.67 m/s (Re_D=3333) in cases of (a) no control, (b) DBD, (c) PSVGs section A, (d) PSVGs section B, (e) hybrid section A, and (f) hybrid section B.

5.6. POD analysis of wake flow structures

The proper orthogonal decomposition (POD) technique was adopted to study the complex spatiotemporal flow behind the bluff body. It is a useful method of extracting coherent structures from turbulent flow fields[80, 82]. It indicates that global variations in the Kármán vortex street dynamics can

be represented by first few POD modes of velocity field. This is because the first few POD modes summarize the large-scale coherent components that include most of the energy, while higher modes capture regions where small-scale structures appear in the turbulent wake[81]. The POD analysis of the velocity field acquired from 1000 snapshots of PIV measurements was applied to present the effect of vortex shedding control on the wake by the three different plasma actuators. The eigenvalue λ_i represents the amount of kinetic energy contained by the ith POD mode. The eigenmode contribution of the total kinetic energy is given by $\lambda_i / \sum_{n=1}^{N} \lambda_n$, where N is the total number of modes. Figure 5-14(a) shows the relative energy of the first 10 POD modes and indicates that the first two eigenmodes of the baseline case corresponding to the Kármán vortex shedding account for 27% and 22% of the total fluctuation energy. After controls, the combined contributions of the first two eigenmodes declined to 18%, 13%, and 12% of the total fluctuation energy (from 49 % in the baseline case), respectively, using the DBD, PSVGs, and hybrid plasma actuators. The DBD plasma actuators reduced the fluctuating structures' total kinetic energy by approximately 60% compared to the baseline, while the hybrid actuator decreased their kinetic energy by up to 75%. Moreover, in the control cases of the DBD and PSVGs' section A, the contribution of eigenmodes higher than 4 increases slightly compared to the baseline. This is because increased smaller vortical structures are generated in these two cases, but all the energy increases are less than 1% that of the baseline counterpart. All of the eigenmodes' cumulative energy is shown in Figure 5-14(b), which indicates that the first few eigenmodes contain most of the kinetic energy in the natural case because large-scale coherent structures represented by the first several eigenmodes dominate the global wake region. However, in the plasma actuation cases, a considerable reduction in the energy of the first two eigenmodes can be observed, especially the hybrid case. This result suggests the suppression in the dominance of the Kármán vortex compared to other dynamic properties in the wake, which can be regarded as the attenuation of vortex shedding of this flow system after control. In section A in the hybrid case, the energy significantly declines compared to the PSVGs, which benefits from the acceleration of the straight part of the exposed electrodes.

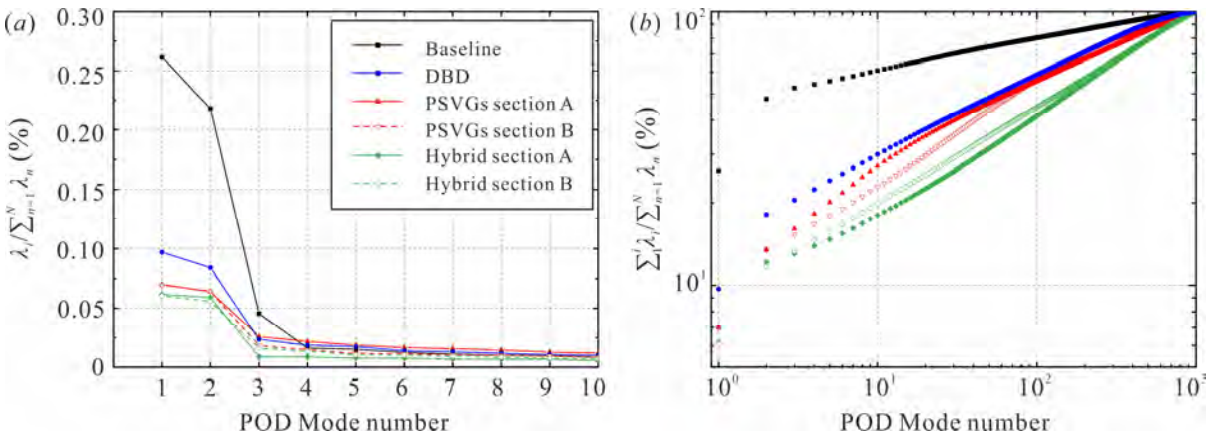

Figure 5-14. (a) POD mode contribution to the total energy. (b) Cumulative contribution of the POD mode energy to the flow field inside $0 \leq x/D \leq 5$ and $-1.5 \leq y/D \leq 1.5$ in the natural and different control cases at 1.67 m/s (Re_D=3333).

The spatial POD modes $\varphi_i(x)$, which can capture the regions where flow fluctuations occur in the wake, were used to investigate fluctuation distribution features of the Kármán vortex street. The POD analyses of the streamwise and vertical velocity are shown in Figure 5-15 and Figure 5-16, respectively. Because the first several modes take up most of the kinetic energy, the flow field representation focuses on the first few POD modes[134, 135]. As shown by Ma *et al.*[136], the first two eigenmodes correctly capture the Kármán vortex street's large-scale coherent structures, which means that the first two modes' characteristics can be regarded as a reliable barometer of Kármán vortex dominance compared with other wake features. The first four POD streamwise velocity modes are shown in Figure 5-15. In modes 1 and 2 (first two columns) in the baseline case (see Figure 5-15(a)), the large-scale boomerang-like structures are antisymmetric near the wake region's centerline, corresponding to the Kármán vortex shedding asymmetry. After control by the DBD plasma actuator (see Figure 5-15(b)), these antisymmetric structures alternately propagating in the downstream direction become small and compact. In the PSVGs in both sections A (see Figure 5-15(c)) and B (see Figure 5-15(d)), the high-intensity antisymmetric elliptical structures are closer to the trailing edge and their intensities rapidly attenuate downstream. The vortex shedding process occurs earlier and concentrates in the near wakes compared to the DBD. The hybrid actuator has the advantages of both DBD and PSVGs actuators and generates a more slender and agminate distribution. Notably, the hybrid actuator has the lowest kinetic energy in the first two modes at the same time (Figure 5-14). For all the actuation cases, there are still antisymmetric structures in the wake, although their distribution features are quite different. This behavior illustrates that Kármán vortex shedding persists after the control, but the shedding schema has changed significantly. In the baseline case, modes 3 and 4 are symmetric around the centerline, which might represent symmetric spatial small-scale vortex structures in the wake[137]. After the control, the symmetric distribution changes to a periodic

antisymmetric schema, especially in the DBD case. This indicates the probable appearance of small-scale antisymmetric shedding modes although it is not noticeable in the PSVGs and hybrid cases.

Figure 5-16 presents the POD analysis results of the vertical velocity (v). In the baseline case, modes 1 and 2 show the symmetry of a large-scale alternating elliptical structure around the centerline, while the last two modes have antisymmetric structures. This result is opposite to the phenomenon observed in the streamwise velocity analysis, which indicates that using only one velocity component to conduct the POD analysis is appropriate. In the control cases, the general mode distribution features are similar to the streamwise velocity POD results, except the symmetry. It is interesting to highlight, some smaller structures that might be related to the shear layer branching appear in section A in the PSVGs and hybrid cases (see Figure 5-16(c) and (e)).

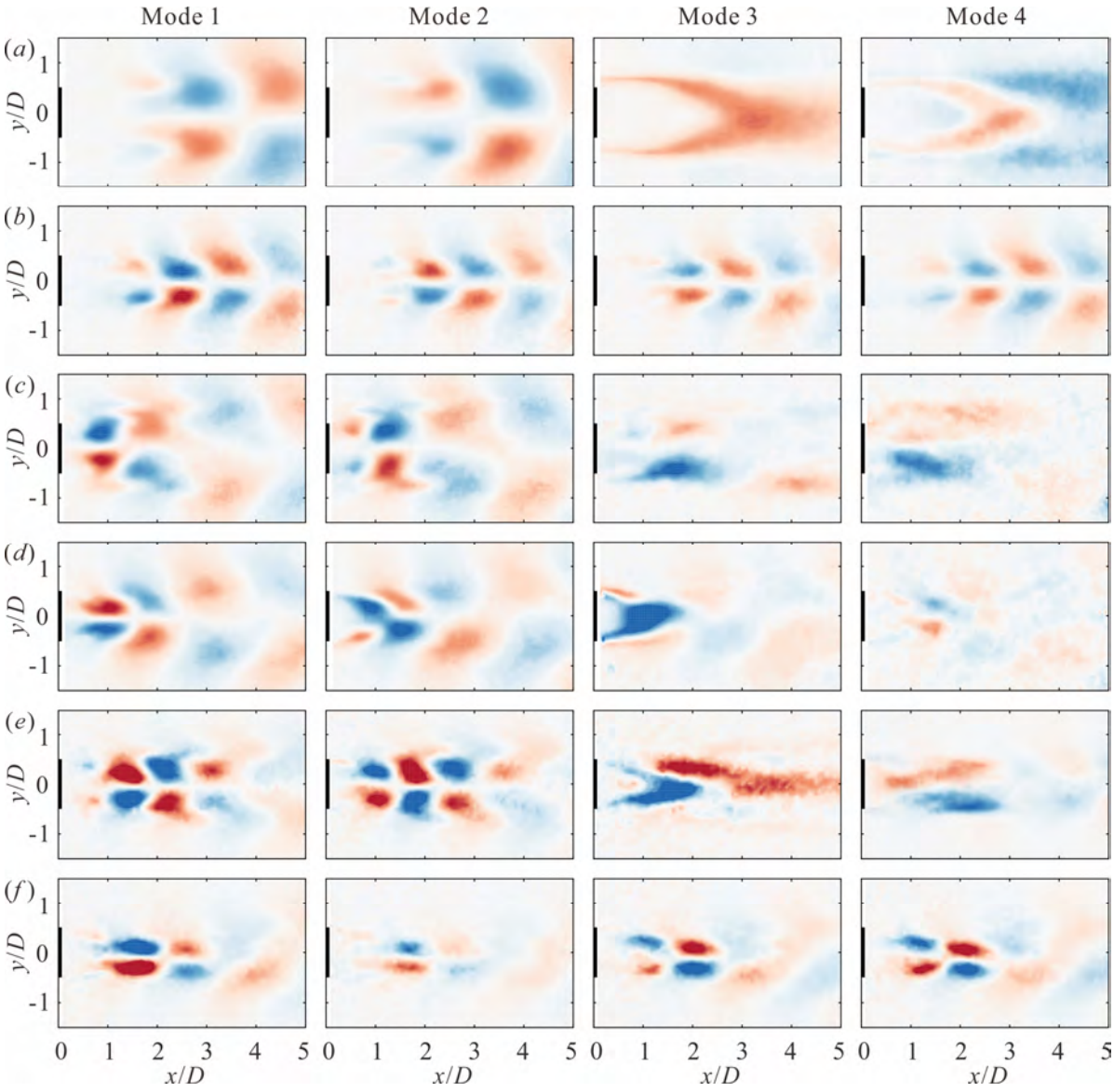

Figure 5-15. First four dominant POD streamwise velocity modes in the natural (baseline) and different control cases at 1.67 m/s (Re_D=3333): (a) no control, (b) DBD, (c) PSVGs section A, (d) PSVGs section B, (e) hybrid section A, and (f) hybrid section B.

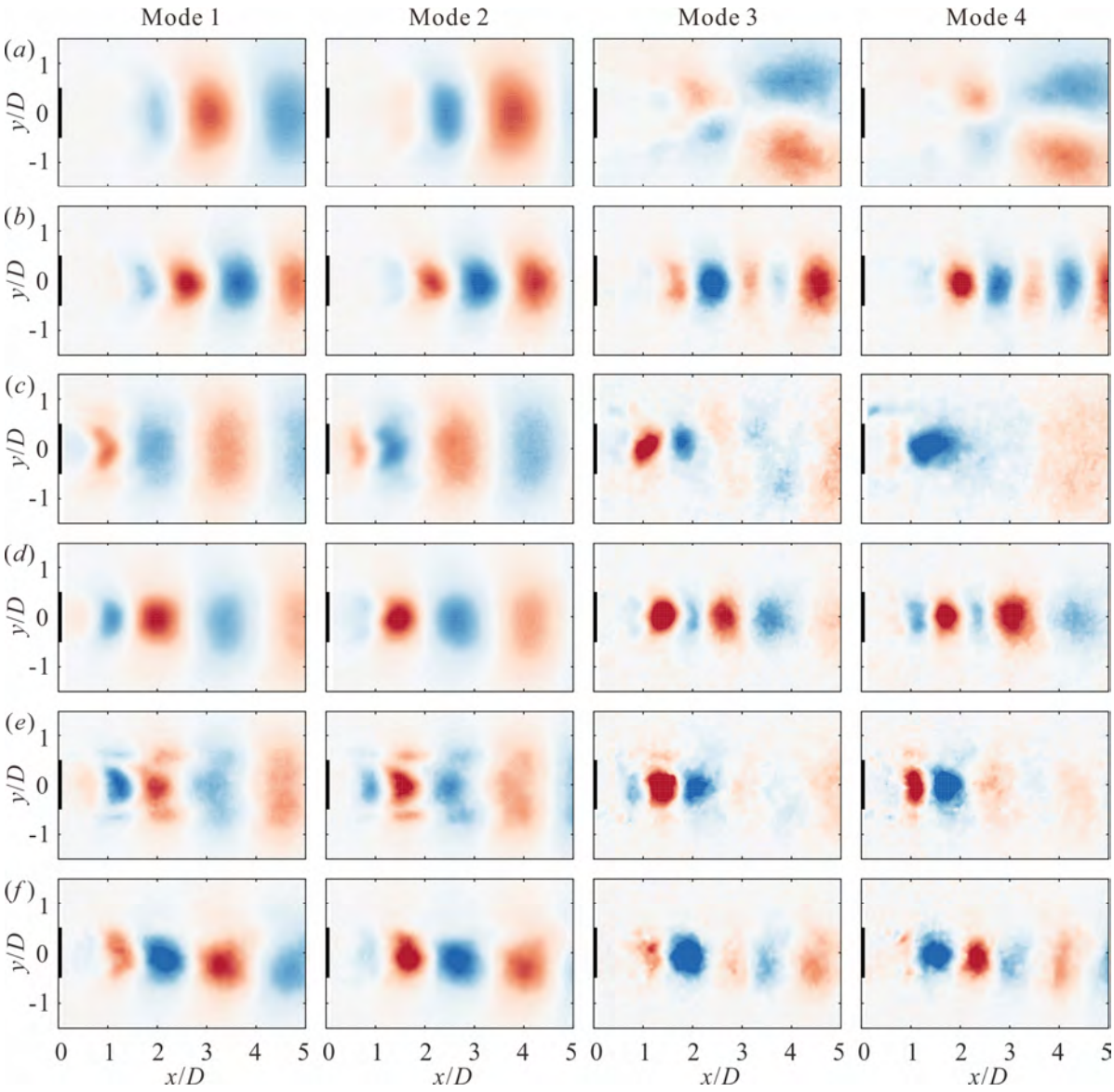

Figure 5-16. First four dominant vertical velocity POD modes for natural (baseline) and different control cases at 1.67 m/s (Re_D=3333): (a) no control, (b) DBD, (c) PSVGs section A, (d) PSVGs section B, (e) hybrid section A, and (f) hybrid section B.

To further investigate the control effect on the Kármán vortex shedding in this flow system using the different plasma actuators, the time history of the first two POD modes' coefficients that are associated with the Kármán vortex street are studied. The POD coefficients are determined by projecting the velocity field's fluctuating section onto the POD modes. The cross-plot using the first two modes' POD coefficients should be illustrated as a circular cycle if the Kármán vortex is the dominant component in the wake. As shown in Figure 5-17(a), this is represented by a circle within the a_1 and a_2 plane for the natural case, which confirms this relationship. The aggregate data distribute in a scattered annulus, which can be an indicator of the periodic vortex shedding process. Because small-scale fluctuations or turbulence in the shedding vortices change the amplitudes and phases of the POD coefficients, the distribution appears as an annulus instead of a perfect circle. The POD

coefficients' amplitude corresponding to the radius of the annulus indicates the coherent mode's identified strength. After actuation, the annulus region shrinks due to the wake's decreasing kinetic energy, especially in the hybrid case. It is important to realize that the scatters have a more discrete distribution instead of an annulus after controls, indicating that plasma actuation can disorganize the Kármán vortex street in the wake.

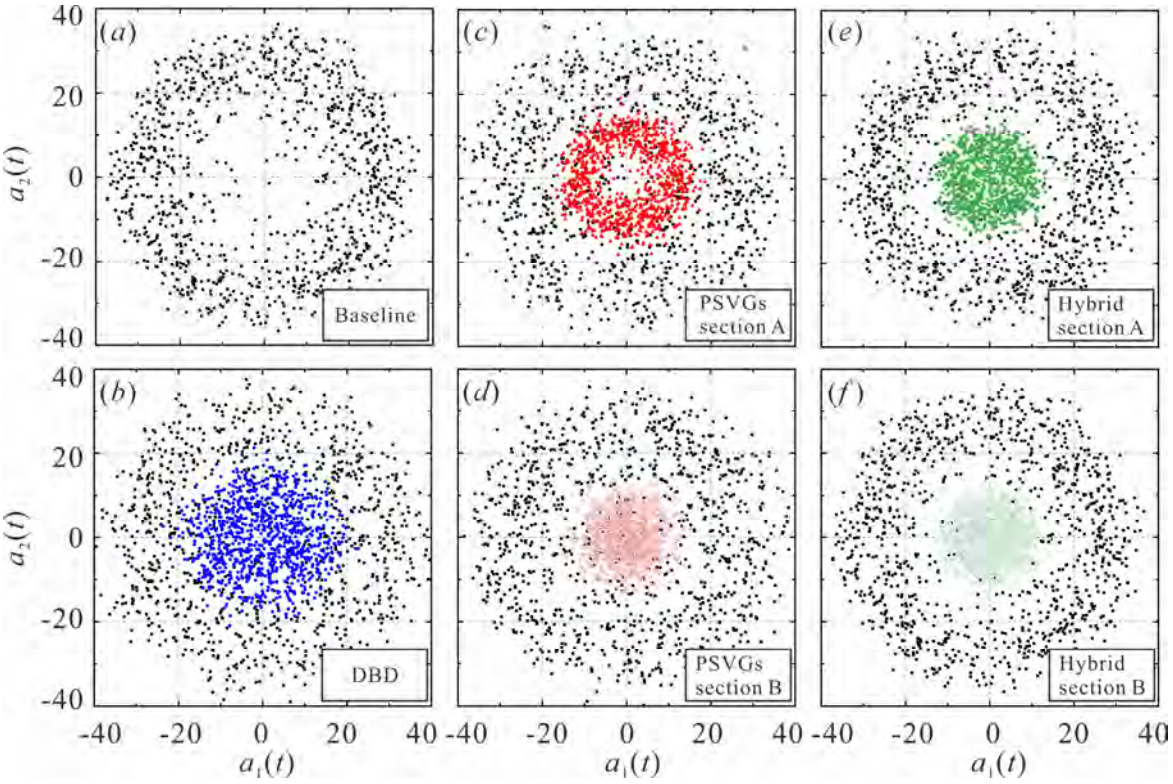

Figure 5-17. Phase portrait of the first two POD coefficients in different control cases compared to the natural case at 1.67 m/s (Re_D=3333): (a) no control (solid black scatters), (b) DBD (solid blue scatters), (c) PSVGs section A (solid red scatters), (d) PSVGs section B (hollow red scatters), (e) hybrid section A (solid green scatters), and (f) hybrid section B (hollow green scatters).

5.7. Remark

The objective of this article was to illustrate the control mechanism of global flow features at an intermediate Reynolds number when DBD plasma actuators are arranged on the top and bottom surfaces of a short D-shaped bluff body. A novel hybrid actuator was proposed and compared to a traditional DBD actuator and PSVGs to improve the control efficiency of plasma actuators.

A global survey of the flow field and drag coefficient in a natural case (no control) was studied. In the tested Reynolds number range, the short D-shaped bluff body had leading edge flow separation and a vortex generated from the interaction of the two separated shear layers via entrainment. To further study the drag reduction and actuator efficiency based on the saved and consumed electrical power, the results indicated that the PSVGs' performance was slightly better than the DBD actuator, and the hybrid actuator was superior to the two other actuators.

The transverse and streamwise VIV dynamic responses were experimentally studied. A more stable vortex shedding system was generated by the actuators to reduce the natural frequency's effect, thus avoiding the occurrence of resonance in advance. The dominant oscillation frequency's bandwidths in the VIV-dominated region shrank and saltation was delayed due to higher reduced velocities controlled by the PSVGs and hybrid actuator.

The cross-flow results on the model's surface showed that all of the plasma actuators successfully suppressed the leading edge separation because the actuators' induced flows transferred the momentum into the boundary layer downstream from the original separation point, consequently increasing the resistance from separation. Compared to the PSVGs, the hybrid actuator generated a stronger and clingier vortex pair that maintained enough intensity for a longer streamwise distance. The control's effects on the wake were pronounced in the different observed planes. The recirculation region significantly shrank downstream due to the suppression of the leading edge separation. In the PSVGs and hybrid actuator cases, because of the three-dimensional counter-rotating vortex pair, the separated shear layer mixed more sufficiently with the fluid near the trailing edge, resulting in a shorter recirculation bubble length than in the DBD case. The peak TKE values declined to approximately 55% and 40% of the baseline case after controlling via the PSVGs and hybrid actuators, respectively. The fluctuating wake's attenuation was also confirmed through the marked decreases in the first two eigenvalues in the POD analysis that represented the periodic shedding's kinetic energy. The POD modes' distribution in both the PSVGs and hybrid actuators indicated that the vortex shedding process occurred earlier and concentrated in the near wake compared to the DBD case. The hybrid actuator had the advantages of both the DBD and PSVGs actuators and the lowest kinetic energy in the first two modes simultaneously. Although the Kármán vortex shedding persisted after the control, the shedding schema changed significantly; the small-scale antisymmetric shedding mode may have appeared based on the observation of the higher POD modes.

The comparison of the different plasma actuators' control performance indicated that the hybrid actuator achieved the best suppression of leading edge separation, Kármán vortex shedding, and VIV. This was because the hybrid actuator generated strong three-dimensional flow structures near the streamwise exposed electrodes; the front spanwise exposed electrode injected more momentum and hindered the flow separation. In the exposed electrodes' downstream regions, streamwise vortices were induced to impede the formation of the recirculation region behind the bluff body. Thus, the recirculation bubbles behind the bluff body decreased significantly, and the vortex shedding's turbulence kinetic energy in the wake was suppressed. This study suggests that the amelioration of the traditional DBD plasma actuator using PSVGs or the hybrid actuator is a feasible and promising method for flow control in bluff body wakes. As for the low electromechanical efficiency of this type of flow control technology, more fundamental studies on the actuator design, and how to reduce plasma heating from the electrical power used and convert it into the electromechanical work should

be pursued. In the future, periodic control of these actuators will be applied to explore the influence of the actuation frequencies on the control performance.

CHAPTER 6 Flow control over a supersonic compression corner

In this chapter, the control performance of a pulsed nanosecond dielectric barrier discharge (NSDBD) plasma actuator with varying pulse voltages and locations on a supersonic compression corner is studied using experiments and numerical simulations. The compression corner with a flat plate length of 60 mm and a ramp angle of 10° under laminar flow separation is experimentally investigated in a Ludwieg wind tunnel under a unit Reynolds number of 7.8 $\times 10^6$ m^{-1} and Mach number of 4. The plasma actuators are placed either upstream or downstream of the separation point, extending in the spanwise direction. The Schlieren technique is used to visualize the shock wave interaction and estimate the propagation speed of the induced shock by the plasma actuator. For the numerical simulations, a one-zone inhomogeneous phenomenological plasma model is adopted to predict key discharge parameters and simulate the fast-heating region. The evolution of the flow structures is examined to reveal the underlying control mechanism.

6.1. SWBLIs on the compression corner

The compression corner comprises a flat plate with a sharp leading edge followed by a ramp. Supersonic flow over a compression ramp is a canonical case of SWBLIs and has been of great interest for more than half a century. Under certain conditions, the ramp-induced pressure rise leads the boundary layer to separate ahead of the corner, forming a separation bubble and a complex shock system[63]. And the presence of streamwise streaks occurs in the vicinity of flow reattachment. The streamwise streaks manifest themselves in variations of surface heat flux, wall pressure, skin friction, etc., and they can usually persist for a certain distance post-reattachment until transition to turbulence happens. Recently, utilising an input–output analysis, Dwivedi *et al.*[138] were able to analyze the formation of streamwise streaks as a result of the amplification of external disturbances in a compression ramp flow. It was shown that baroclinic effects arising from the interactions of base-flow density gradients with spanwise gradients of pressure perturbations play a dominant role in triggering the streamwise streaks. Therefore, baroclinic effects and centrifugal effects are two potential mechanisms that can amplify upstream disturbances, leading to vortical structures[139]. The effects of plasma actuators on streaks will be studied in the future. This research first focuses on the effects on the SWBLIs and separations bubbles.

Figure 6-1 schematically depicts the main details of a separated supersonic flow over the compression corner. As shown in Schlieren images (see Figure 6-2(a) numerical; Figure 6-2(b) experimental), the light curves near the surface, which begin at the leading edge and extend downstream, indicate the development of the boundary layer. The numerical and experimental results agree well with each other. The flat plate boundary layer separates from the surface, caused by the sufficiently large pressure increase due to the ramp. Then, it reattaches at the downstream ramp,

causing a reattachment shock (RS). An expansion wave (EW) emanates from the triple point (TP) where the separation shock (SS) caused by the separated boundary layer and reattachment shocks intersect. Below the separated shear layer, between the separation point (SP) and reattachment point (RP), a recirculation bubble forms. The size of the recirculation bubble is strongly affected by the deflection angle, Mach number, and Reynolds number of the incoming flow[140]. In this study, the separation bubble is narrow with a small separation shock angle, which represents a stable laminar separated flow. Note that a secondary eddy will appear in the recirculation region under a large deflection angle, and multiple eddies will form as the deflection angle further increases. According to the global instability analysis of Hao *et al.*, the prediction of the stability boundary in terms of a scaled ramp angle is $\alpha^* = 4.59$ for the current flow conditions, under which the secondary eddy begins to emerge. In this study, the scaled ramp angle α^* is 4.2, which is less than the above critical value of 4.59.

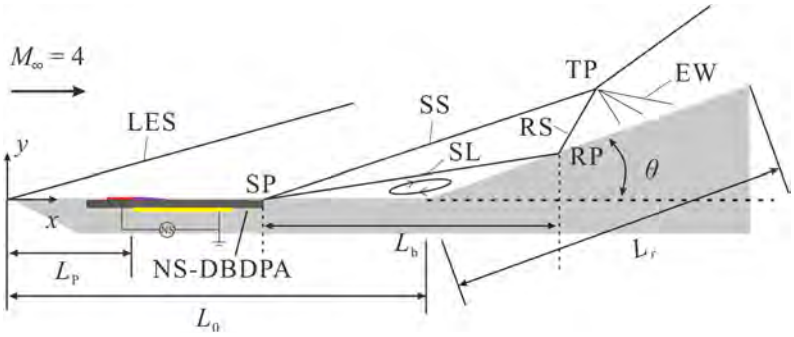

Figure 6-1. The schematic of the flow structures on the compression corner in a supersonic flow. LES: leading edge shock; SS: separation shock; RS: reattachment shock; EW: expansion wave; SL: separated shear layer; SP: separation point; RP: reattachment point; TP: triple point.

The time-averaged Schlieren images are shown in Figure 6-2(c)(d) to investigate the shock system after control, taking case C2 as an example. Note that the field of view of Schlieren did not include the expansion wave and the triple point. It should be pointed out that although the height of the exposed electrode is only 0.02 mm, this small embossment also generates a weak shock wave in the experiment (see Figure 6-3(b)). Chuvakhov[141] indicated that the small height of roughness elements (in their case, less than 0.6 mm) does not affect the separated flow much and only results in a shock wave. This is further proven by the fact that the separated shock angle does not have an obvious change in both the simulation and experiment, calculated by the linear regression of the sampling points in the Schlieren images. In addition, the accumulation of residual heat can not be observed in experimental Schlieren images because the activated frequency of the plasma actuator is too low compared to the characteristic frequency (L_0/U_∞). The residual heat has been totally convected downstream of the separation region and the separated flow has restored to the uncontrolled state before the next pulse. The repetition frequency of plasma actuator, which may play a significant role in the control, will be studied in the future.

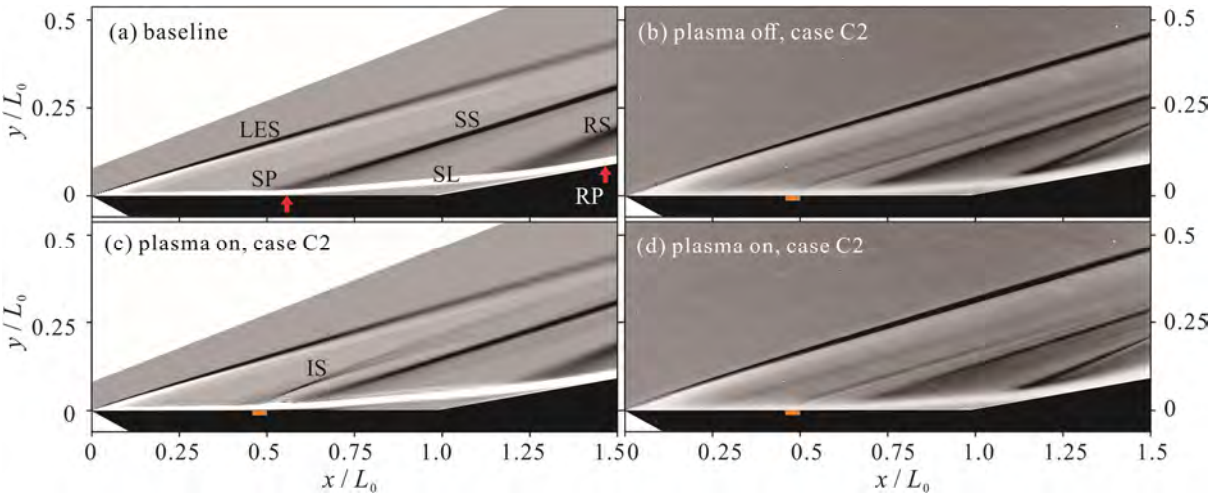

Figure 6-2. (a) Numerical Schlieren image of the baseline case (steady); (b) time-averaged experimental Schlieren image of the plasma-off case within one period of case C2; (c) time-averaged numerical Schlieren image of the plasma-on case within the first 0.2 period (t^* = 2.25) of case C2; and (d) time-averaged experimental Schlieren image of the plasma-on case within the first 0.2 period (t^* = 2.25) of case C2.

Figure 6-3 shows the Schlieren images at t^* = 0.1 and 0.2 when the NSDBD plasma actuator is installed at L_p/L_0 = 0.5 (case C2). The induced shock (IS) moves downstream and interacts with the separated shock wave. Sweeping by the induced shock wave, the strength of the separated shock seems to be locally perturbed and decreased. Because the experiments were conducted at a low applied voltage, the separation bubble showed little change, which can also be observed in the simulation results. The simulated and experimental Schlieren images rarely show obvious changes for other actuation position cases, which are not shown here to save space. To determine the control mechanism, more details are analyzed in the simulation study.

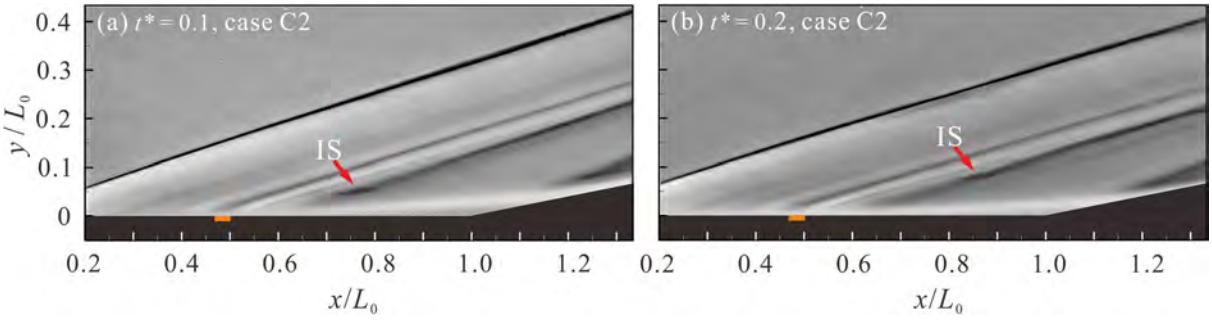

Figure 6-3. Shock propagation from NSDBD in the case of C2 at t^* = (a) 0.1 and (b) 0.2.

6.2. Control effects on the separation region for a single pulse activation

Hereinafter, all results were acquired from numerical simulations. To compare the control effects on the size of the separation region, the time-averaged flow field for a single pulse case was studied. Regarding the underlying control mechanism, the evolution of flow after one discharge pulse is

investigated in the next section. The averaged time slot was set within $t^* = 2.25$ when the flow has recovered to be steady. A typical separation flow field over a supersonic compression corner is presented by the streamlines in Figure 6-4. The separation points (SP), reattachment points (RP), and locations of plasma actuators are marked by closed circles and squares, respectively. The contours of the dimensional streamwise velocity $\bar{u}/U_\infty$ are plotted in Figure 6-4(a), where $\bar{u}$ is the local streamwise velocity of steady flow. The separation bubble region is relatively large when the flow is not controlled (see Figure 6-4(a)). The shear flow separates at $x/L_0 = 0.58$ and reattaches at $x/L_0 = 1.42$ with a separation bubble length of $L_b/L_0 = 0.84$. When the actuator is activated at $L_p/L_0 = 0.33$ in the case of C4 (see Figure 6-4(b)), the bubble size slightly shrinks, and the SP moves downstream to $x/L_0 = 0.62$. In the case of C5, where the location of plasma is close and upstream of the initial SP, reductions in the main separation bubble region are also observed (see Figure 6-4(c)), and the corresponding SP retards to $x/L_0 = 0.72$. Similar to case C5, when the actuator is arranged close to but downstream of the initial SP at $L_p/L_0 = 0.67$, the SP moves downstream to $x/L_0 = 0.89$, but the RP advances to $x/L_0 = 1.35$, resulting in significant suppression of L_b/L_0 to 0.46. In general, the reduction of separation bubble length is obvious in the cases of C5 and C6 (up to 17% and 45%, respectively). Actually, an initial induced separation exists upstream of the excitation position, which will be discussed in the next chapter.

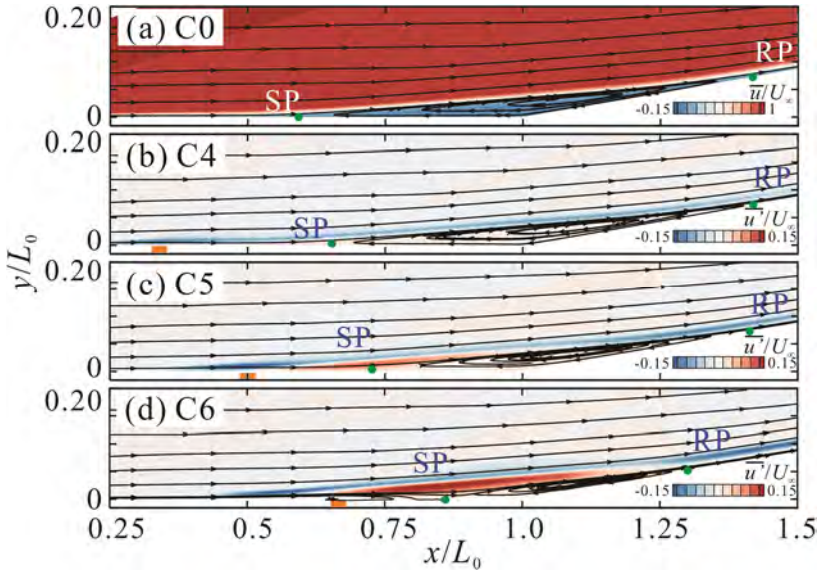

Figure 6-4. Time-averaged contours of (a) normalized streamwise velocity ($\bar{u}/U_\infty$) for case C0 and normalized streamwise velocity fluctuation ($\overline{u'}/U_\infty$) for cases (b) C4; (c) C5; and (d) C6 with streamlines superimposed.

The contours of the time-averaged dimensionless streamwise velocity fluctuation $\overline{u'}/U_\infty$ are plotted in Figure 6-5(b)–(d), where $\overline{u'}$ is defined as $\overline{u\text{-}u_0}$. After control, the streamwise velocity component decreases upstream of the initial shear layer and then obviously increases downstream, especially in the case of C6. This result implies momentum exchange upstream and downstream of the

initial shear layer. The high-speed fluid with more momentum is transferred to the separation region. This enhances the flow capability to withstand an adverse pressure gradient, resulting in the shrinkage of the separation bubble. To further demonstrate this, profiles of streamwise velocity at $x/L_0 = 0.8$ are plotted in Figure 6-5(a). A prominent velocity defect with a negative value is observed in the baseline case, which represents a typical separation flow. After control, the velocity increases near the wall, which benefits from the momentum supplement by the upper high-speed fluid. It can be seen in Figure 6-5(b) that the most momentum supplement from the upper flow at the selected position is observed in the C6 case. However, the time-averaged momentum increase is not obvious in the boundary layer because of the low-density region caused by the gas heating process and the short period when the separation is totally suppressed. Therefore, the prediction of the potential control authority of the NSDBD here should be made with caution. The control mechanism may be linked to the actuation position and its local specific fluid characteristics. A more appropriate excitation position may lead to a better control effect under the same energy input. Analyses of surface pressure and skin friction are helpful to understand the local fluid status after control and elucidate the control mechanism.

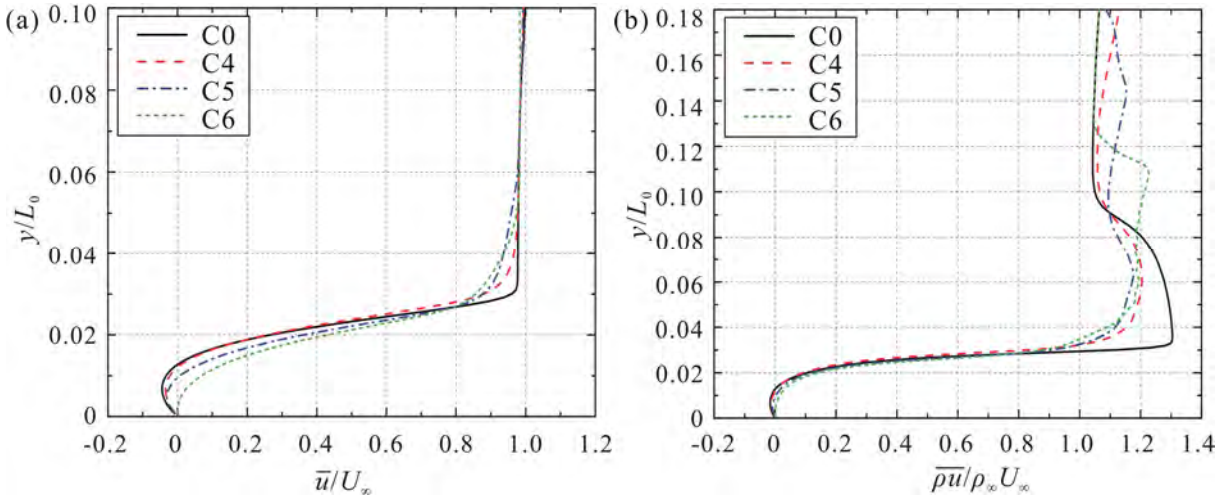

Figure 6-5. Profiles of (a) normalized time-averaged velocity $\bar{u}/U_\infty$ and (b) normalized time-averaged mass flux $\overline{\rho u}/\rho_\infty U_\infty$ streamwise at $x/L_0 = 0.8$.

Figure 6-6 shows the distributions of the skin friction coefficient for different actuator locations and applied voltages. The SP and RP of the main separation bubble are indicated by solid open circles. Inside the separation region, there are two local minima of C_f and a local skin friction peak between these two minima near the corner. Downstream of the reattachment point, the skin friction rises to another peak value and then decreases gradually. A sharp valley, marked in a dotted circle, can be seen clearly in all controlled cases. This is caused by the heat impulse originating from the fast heating of pulsed discharge. The actuation drops the surface friction upstream of the heating region and subsequently results in a rebound downstream of it, which is consistent with the process of initial separation and reattachment due to the induced vortex. For the cases of applied voltage at 25 kV (see Figure 6-6(a)), the separation bubble sizes show limited changes. However, with the higher applied

voltage at 50 kV, the separation bubble strongly shrinks. As the excitation position moves close to the corner, the process becomes more complicated. Inside the separation bubble, the downstream local minimum increases after control. It is indicated that the effects of the NSDBD diminish the accelerated process caused by the favorable pressure in the recirculation boundary layer. After control, the local peak near the corner (see the enlarged region in Figure 6-6) becomes positive except in case C1, indicating the emergence of vortices in the separation region. The fluctuating positive peaks illustrate the vortices' time evolution.

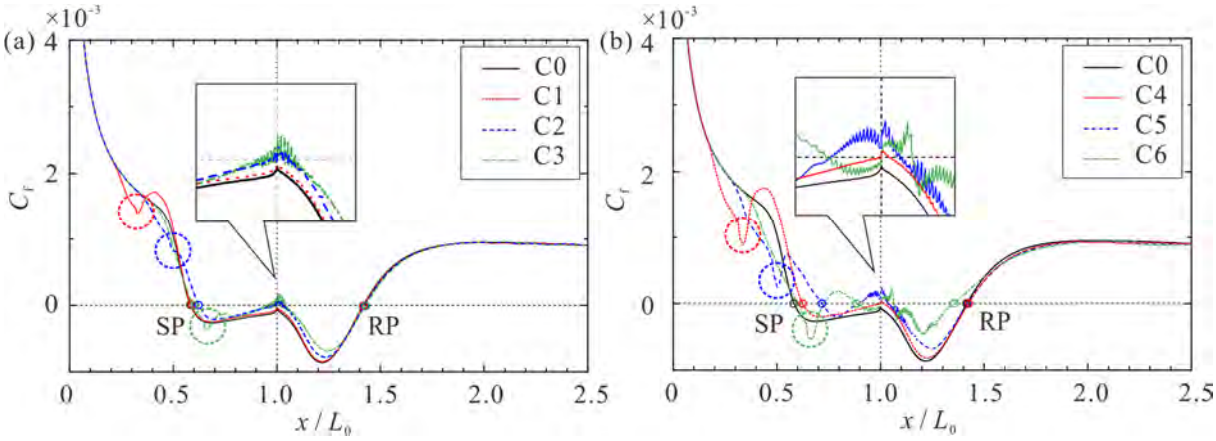

Figure 6-6. Distributions of the time-averaged skin friction coefficient for different actuator locations at (a) 25 kV and (b) 50 kV.

The distributions of the surface pressure coefficient for different actuator locations and voltages are shown in Figure 6-7. The surface pressure begins to increase upstream of the SP controlled by the free-interaction process[142]. The flow expansion caused by the fast heating process increases the local C_p, resulting in the SP moving downstream. Notably, when the upstream actuation is far from the SP, C_p will drop slightly before it rises again. The rise is followed by a plateau region, the value of which increases slightly after control. The pressure rises again near the reattachment point and reaches its peak value mainly determined by the oblique shock theory.

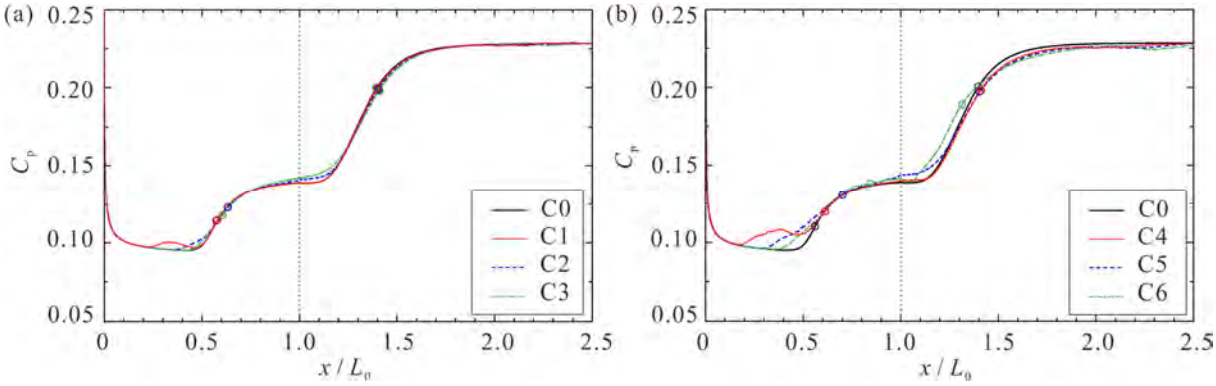

Figure 6-7. Distributions of the time-averaged surface pressure coefficient for different actuator locations at (a) 25 kV and (b) 50 kV.

6.3. Effects of PRF on the separation region

Furthermore, different PRFs depending on flow characteristic time were studied to compare the control performance of periodic activation. Eq. 6-1 defines the dimensionless frequency F^+. Here, the flow field variables are nondimensionalized by L_0, which is considered the characteristic length of the flow and where U_∞ is the velocity of the free stream. Three different F^+ of 1, 10, and 20 were simulated. For case $F^+ = 1$, the actual PRF is 11233 Hz. To compare the control effects on the size of the separation region, the key characteristics of the time-averaged flow field were studied first in this section. Regarding the underlying control mechanism, the evolution of flow after one discharge pulse is investigated in the next section. The averaged time slot was set within $t^* = 3$, which means the free stream can pass through the model length three times.

$$F^+ = \frac{PRF \cdot L_0}{U_\infty} \tag{6-1}$$

6.3.1. L_p/L_0 = 0.33 (case C1, C4)

The time-averaged separation flow structures of cases C1 and C4 are presented by the streamlines in Figure 6-8. The contours of the dimensional streamwise velocity increment $\overline{u'}/U_\infty$ are also plotted. The separation bubble sizes after periodic control are summarized in Table 6-1. For baseline case C0, the shear flow separates at $x/L_0 = 0.58$ and reattaches at $x/L_0 = 1.42$ with a separation bubble length of $L_b/L_0 = 0.84$. When the actuator is activated at $L_p/L_0 = 0.33$ in the case of C1 and C4 at $F^+ = 1$ (see Figure 6-8(a) and (d)), the bubble size slightly shrinks, and there is no obvious induced separation bubble. This also can be observed in Figure 6-9(a) and (c) red lines without negative values. The SP moves downstream to $x/L_0 = 0.59$ and 0.67, respectively. The bubble length L_b reduces by 0.83% and 9.2%. Compared to the single pulse control with the same location (0% for C1 and 5% for C4), the efficiency slightly increases. Figure 6-9 shows the skin friction coefficient. Compared to single pulse control, continuous activation causes a more significant local decrease in C_f. At higher F^+ of 10 and 20, the negative values in C_f upstream of the actuator location indicate the induced vortex region. Downstream peak is a rebound in C_f related to the entrained high-speed flow. Figure 6-10 shows the surface pressure coefficient. The pressure peak near the activation location indicates that the induced shock by the fast heating process impacts the surface and reflects the upward side. The asymmetry of the peak illustrates its distortion under the interaction with freestream. In the cases C4 at $F^+ = 1$ (red lines in Figure 6-9(d)), the positive local skin friction peak near the corner implies a secondary vortex occurs beneath the primary bubble.

Table 6-1. The reduction of separation bubble length of simulated cases.

Case	C0	C1			C2			C3		
F^+	-	1	10	20	1	10	20	1	10	20

SP	0.58	0.59	0.66	0.69	0.66	0.8	0.83	0.78	0.98	1.20
RP	1.42	1.42	1.45	1.45	1.43	1.46	1.48	1.44	1.46	1.40
L_b/L_0	0.84	0.83	0.79	0.76	0.77	0.66	0.65	0.66	0.48	0.20
Reduction(%)	-	0.8	6.3	9.9	12.7	21.4	22.6	21.7	42.6	76.2
Case	C0	C4			C5			C6		
F^+	-	1	10	20	1	10	20	1	10	20
SP	0.58	0.67	0.98	1.04	0.78	-	-	0.94	-	-
RP	1.42	1.43	1.48	1.46	1.43	-	-	1.34	-	-
L_b/L_0	0.84	0.76	0.50	0.42	0.65	-	-	0.40	-	-
Reduction(%)	-	9.2	40.5	49.6	22.6	-	-	52.6	-	-

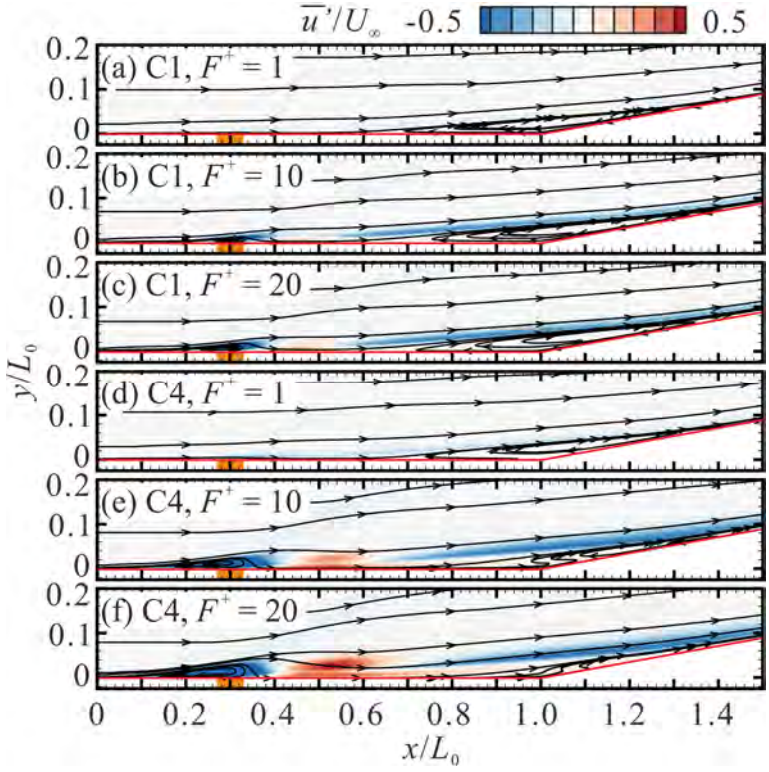

Figure 6-8. Time-averaged contours of normalized streamwise velocity fluctuation ($\overline{u}'/U_\infty$) for cases C1 at (a) $F^+ = 1$; (b) $F^+ = 10$; (c) $F^+ = 20$; and case C4 at (d) $F^+ = 1$; (e) $F^+ = 10$; (f) $F^+ = 20$ with streamlines superimposed.

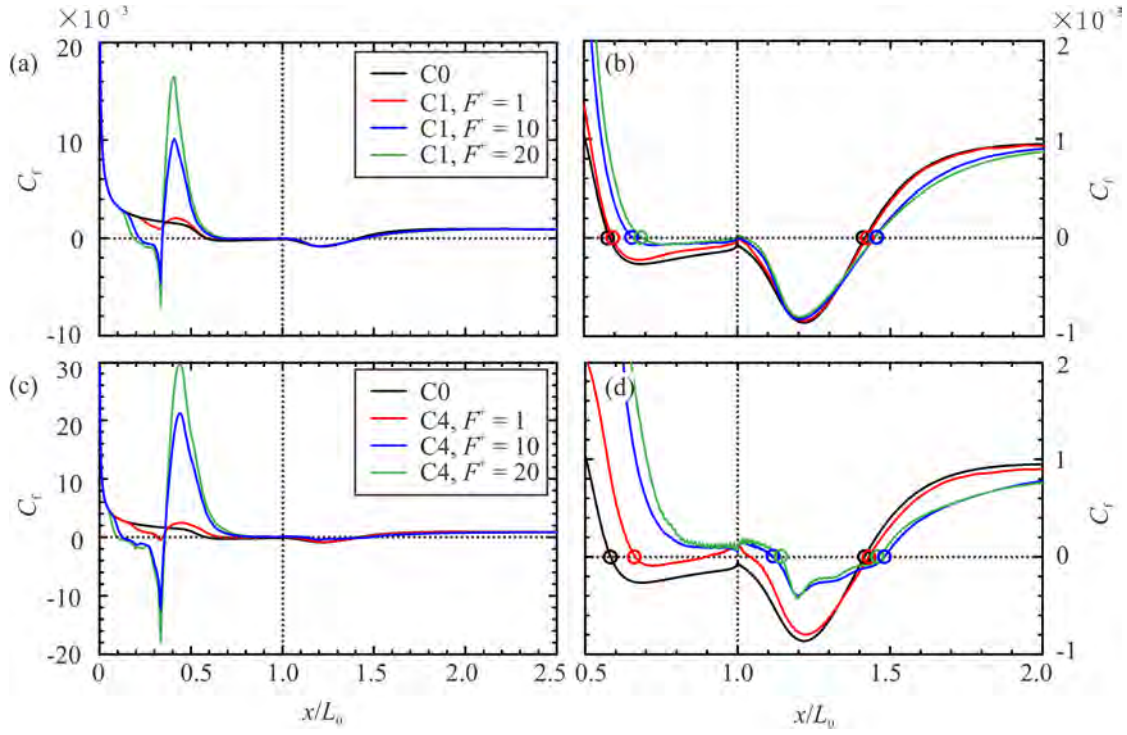

Figure 6-9. Distributions of the time-averaged skin friction coefficient for cases (a)(b) C1 (25 kV) and (c)(d) C4 (50 kV) at L_p/L_0 = 0.33 with different F^+. Open circles: separation and reattachment points.

In the case of C1 at F^+ = 10 and 20 (see Figure 6-8(b), (c) and Table 6-1), the main bubble length L_b reduces by 6.3% and 9.9%, and an induced separation bubble appears upstream of the activation location. The velocity upside the separation bubble decreases significantly, leading to the reduction of skin friction and surface pressure in the vicinity of RP on the ramp. This also can be observed in Figure 6-10(b) with blue and green lines. The separation region is pushed downstream with a slight shrinkage. But from skin friction distribution, the separation bubble seems to keep the same state. Compared to case C4 of F^+ = 1, the suppression of the main separation bubble size is approximate to case C1 of F^+ = 20, but the energy consumption is quite different. Take the case C1 (F^+ = 1) as a reference. The energy input of case C4 (F^+ = 1) is 5.1 times, but which is 20 times in the case of C1 (F^+ = 20). It implies that when the activation location is far away upstream from the SP, improving the applied voltage is more effective than increasing the PRF. Depending on the secondary vortex appearance in the case of C4 (F^+ = 1), at the higher applied voltage, the high-speed external fluid will affect the separation region. However, the SP is pushed downstream by increasing the PRF because the pressure increases significantly upstream of the original SP.

For case C4 at F^+ = 10 and 20 (see Figure 6-8(e), (f) and Table 6-1), the main bubble length L_b reduces by 40.5% and 49.6%, and the induced separation bubble further expands due to a high activation frequency upstream of the activation location. Meanwhile, the main separation occurs on

the ramp, and the bubble on the flat plate section is restrained. The pressure and skin friction reduce significantly.

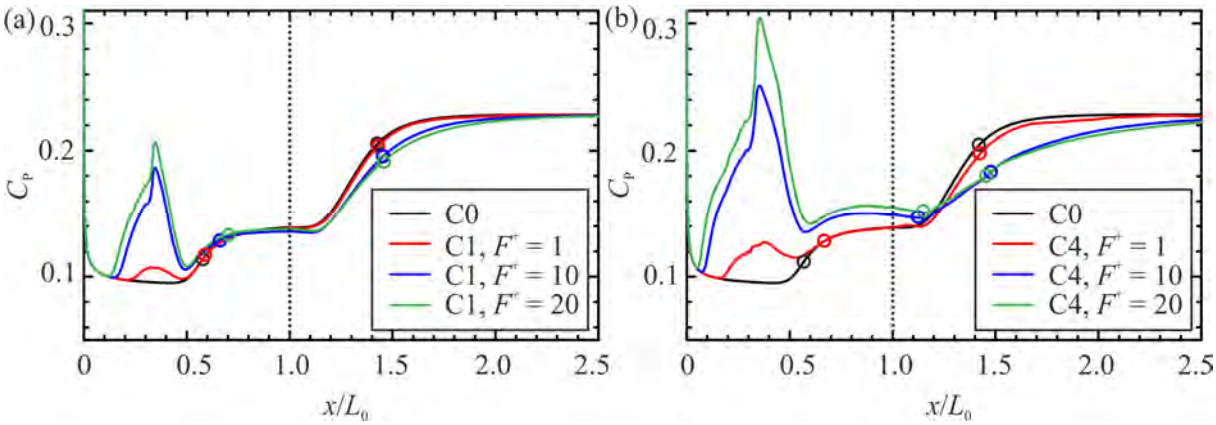

Figure 6-10. Distributions of the time-averaged surface pressure coefficient for different actuator locations at (a) C1 25 kV and (b) C4 50 kV at L_p/L_0 = 0.33 with different F^+. Open circles: separation and reattachment points.

6.3.2. L_p/L_0 = 0.5 (case C2, C5)

The time-averaged separation flow structures of cases C2 and C5 are presented by the streamlines in Figure 6-11. The activation location is at L_p/L_0 = 0.5 where upstream of the original SP. The contours of the dimensional streamwise velocity increment $\overline{u'}/U_\infty$ are also plotted. The suppression efficiency in this activation location is markedly higher than L_p/L_0 = 0.33 with corresponding cases. In the case of C5 at F^+ = 10 and 20 (see Figure 6-11(e) and (f)), the main separation bubble is totally eliminated. It can be seen clearly that the velocity in the boundary layer grows significantly in these two cases. In Figure 6-13(b)(blue and green lines), the surface pressure arises upstream of the corner and has a smaller adverse pressure gradient on the ramp, which favors separation suppression. This simulation results indicate that it is possible to eliminate the flow separation on the supersonic compression corner totally. Improving the F^+ from 10 to 20, the skin friction increases due to a larger entrained velocity, but it is limited. And, the efficiency only increases by 1.2% (case C2). However, the induced vortex grows to a larger induced separation bubble upstream of the activation location(same in cases C2 and C5). It elucidates there is a critical F^+ that can eliminate the main separation and have a minimum side-effect of the induced bubble. Similar to cases C1 (F^+ = 20) and C4 (F^+ = 1), the case C2 (F^+ = 20) and case C5 (F^+ = 1) share the same efficiency of 22.6%. This implies improving the applied voltage is also more effective than increasing the PRF at L_p/L_0 = 0.5.

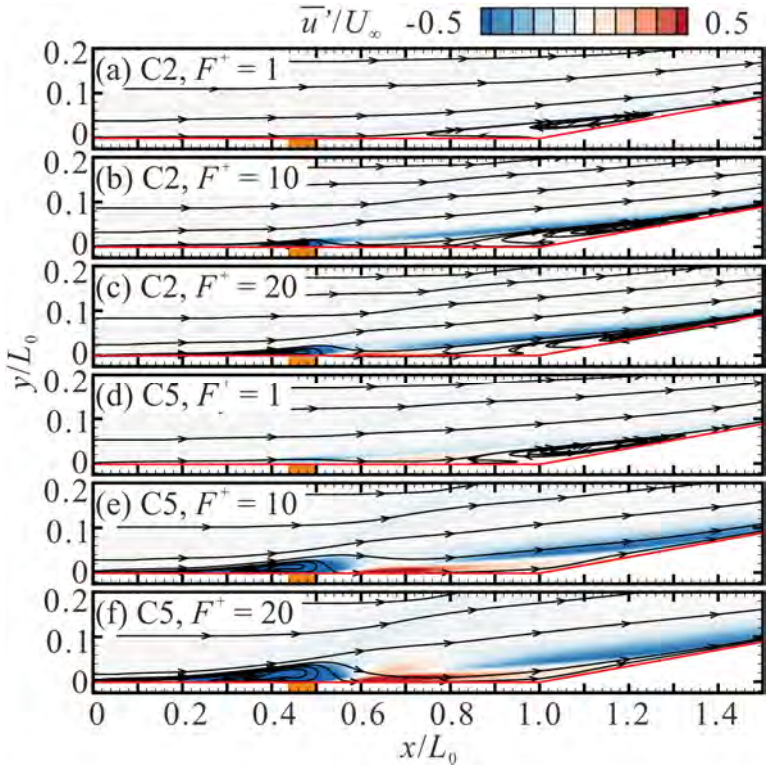

Figure 6-11. Time-averaged contours of normalized streamwise velocity fluctuation ($\overline{u}'/U_\infty$) for cases C2 at (a) $F^+ = 1$; (b) $F^+ = 10$; (c) $F^+ = 20$; and case C5 at (d) $F^+ = 1$; (e) $F^+ = 10$; (f) $F^+ = 20$ with streamlines superimposed.

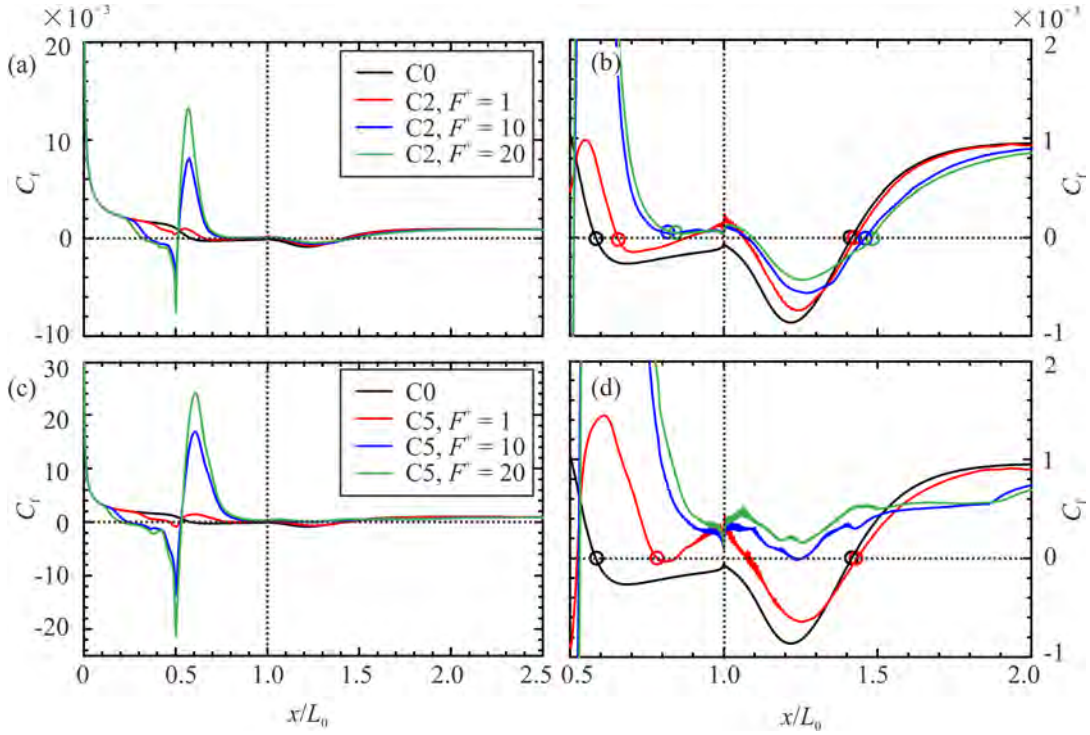

Figure 6-12. Distributions of the time-averaged skin friction coefficient for cases (a)(b) C2 (25 kV) and (c)(d) C5 (50 kV) at L_p/L_0 = 0.5 and different F^+. Open circles: separation and reattachment points.

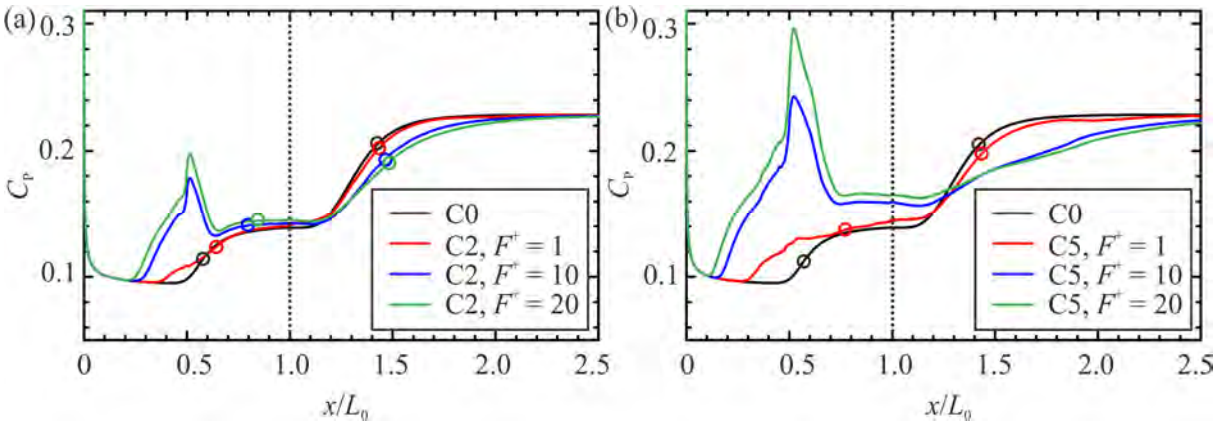

Figure 6-13. Distributions of the time-averaged surface pressure coefficient for different actuator locations at (a) C2 25 kV and (b) C5 50 kV at L_p/L_0 = 0.5 with different F^+. Open circles: separation and reattachment points.

6.3.3. L_p/L_0 = 0.67 (case C3, C6)

Figure 6-14 shows the time-averaged separation flow structures of cases C3 and C6 by the streamlines. The activation location is at L_p/L_0 = 0.67 downstream of the original SP. The contours of the dimensional streamwise velocity increment $\overline{u'}/U_\infty$ are also plotted. The control efficiency in this activation location shows the best performance compared to the last two cases at the corresponding F^+. Similar to case C5, case C6 at F^+ = 10 and 20 will totally eliminate the separation. But the induced bubble seems to enlarge It should be noted that case C3 of F^+ = 20 also almost represses the main bubble. Only a small separation on the ramp from 1.2 to 1.4 which can be neglected (see Figure 6-14(c) and Figure 6-15(b) green line). This indicates that applying a lower voltage but with a high activation frequency also can eliminate the bubble. However, the choice of activation location becomes the key factor. Compared to case C2 (F^+ = 20) at L_p/L_0 = 0.50, the efficiency increases from 22.6% to 76.2% in case C3 (F^+ = 20) at L_p/L_0 = 0.67. Similarly, take the case of 25 kV and F^+ = 1 as the reference, the power consumption of case C3 (F^+ = 20) is 20 times. But in case C5 (F^+ = 10), it is around 50 times. This result again implies that the activation location plays an important role in supersonic corner flow control.

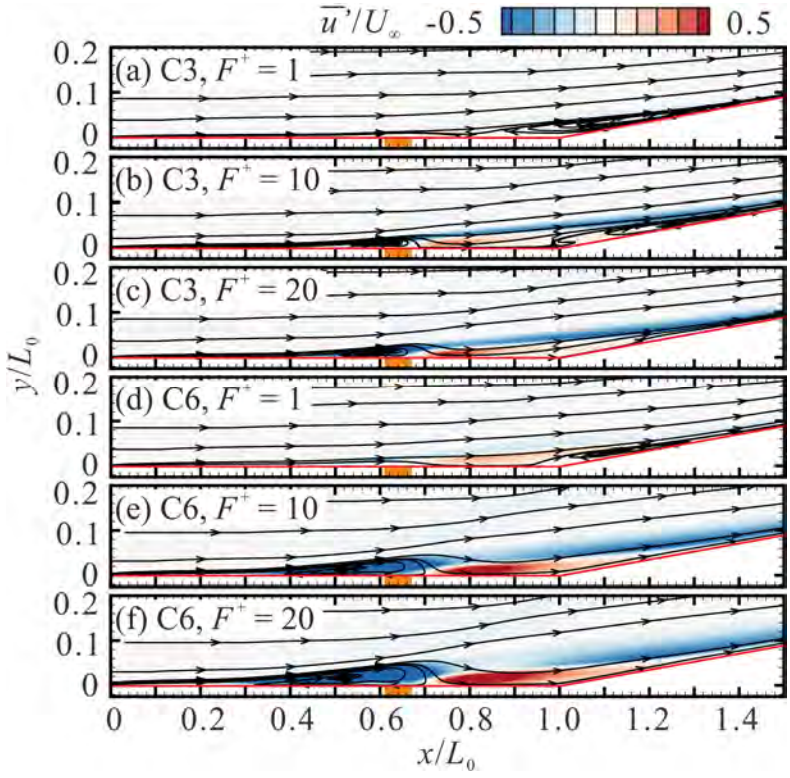

Figure 6-14. Time-averaged contours of normalized streamwise velocity fluctuation ($\overline{u}'/U_\infty$) for cases C3 at (a) $F^+ = 1$; (b) $F^+ = 10$; (c) $F^+ = 20$; and case C6 at (d) $F^+ = 1$; (e) $F^+ = 10$; (f) $F^+ = 20$ with streamlines superimposed.

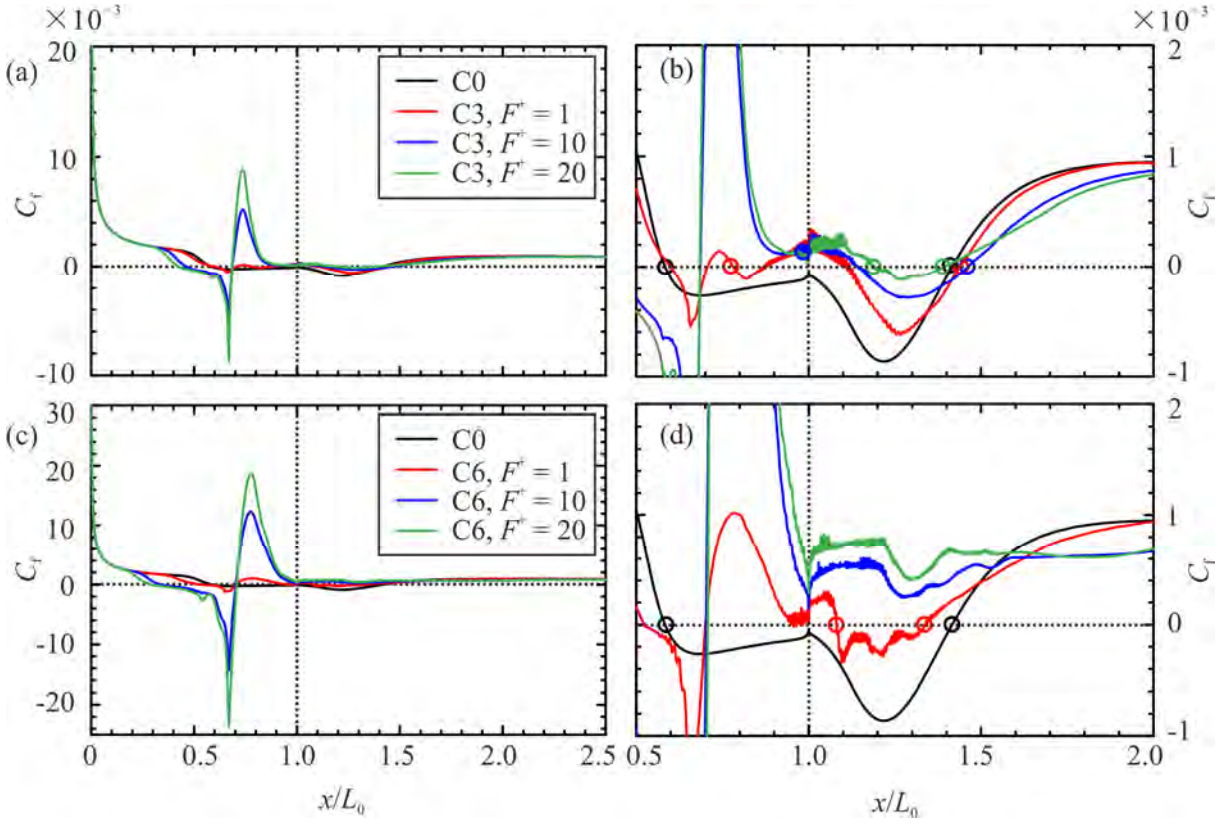

Figure 6-15. Distributions of the time-averaged skin friction coefficient for cases (a)(b) C3 (25 kV) and (c)(d) C6 (50 kV) at L_p/L_0 = 0.67 and different F^+. Open circles: separation and reattachment points.

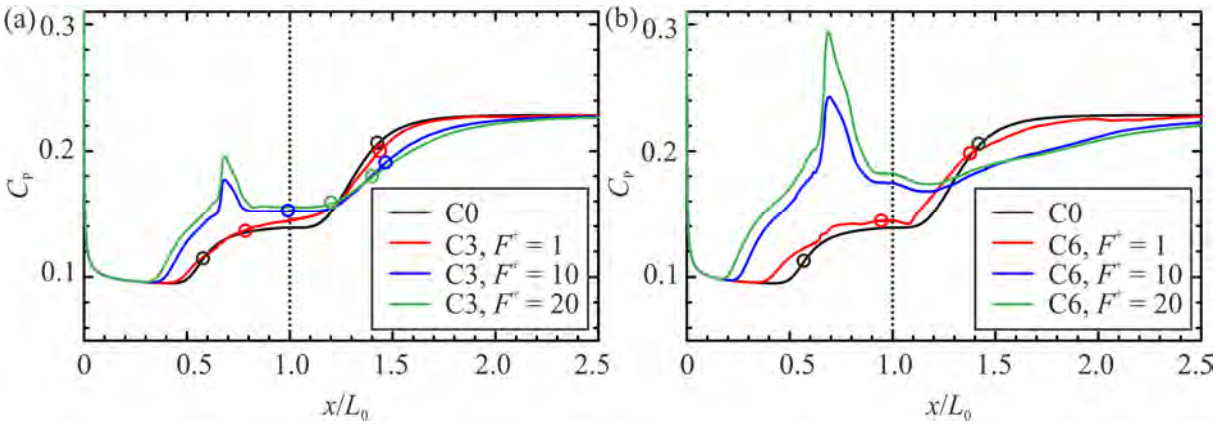

Figure 6-16. Distributions of the time-averaged surface pressure coefficient for different actuator locations at (a) C3 25 kV and (b) C6 50 kV at L_p/L_0 = 0.67 with different F^+. Open circles: separation and reattachment points.

6.4. Discussion of the control mechanism

6.4.1. Single pulse activation

To gain the underlying control mechanism, the instantaneous flow field after the first pulse discharge is investigated in all cases. Taking the example of case C5 first, the normalized streamwise velocity contours overlaid with the streamlines are visualized in Figure 6-17. At t^* = 0.1, 9 μs after the beginning of the discharge, the induced vortices form the initial separation bubble near the original separation point of the boundary layer, which is observed clearly in Figure 6-17(a). Its formation is attributed to the interaction between the freestream and the local flow expansion caused by the fast heating process. Downstream of the bubble, the high-speed external fluid is entrained into the original separation region, resulting in flow reattachment upstream of the corner. The entrained fluid with high momentum compels the main separation to move downstream, accompanied by the fragmentation of the original shear layer. Note that, at this time, the flow field on the ramp, e.g., the RP, is not affected because the perturbed fluid has not propagated downstream to the corner. Subsequently, at t^* = 0.5 (see Figure 6-17(b)) when the entrained fluid passes through the corner, the original shear layer is destroyed, and multiple vortices emanate in the original separation region caused by the impact between the entrained high-speed fluid and the reverse flow coming from the reattachment point. The reattachment point is pushed downstream transitorily and then fluctuates on the ramp surface near the original reattachment point in the form of small vortices fragmented in the separation region (see Figure 6-17(c)). At the same time, the original induced separation bubble is elongated, flattened, and moves downstream to coalesce with fragmented vortices. At t^* = 2 (see Figure 6-17(d)), the main

separation bubble forms again. At this time, the bubble length is still shorter than that in the steady case and recovers to its original size gradually. Case C2, which has a lower energy input but the same excitation position, shares similar control authority with weaker effects.

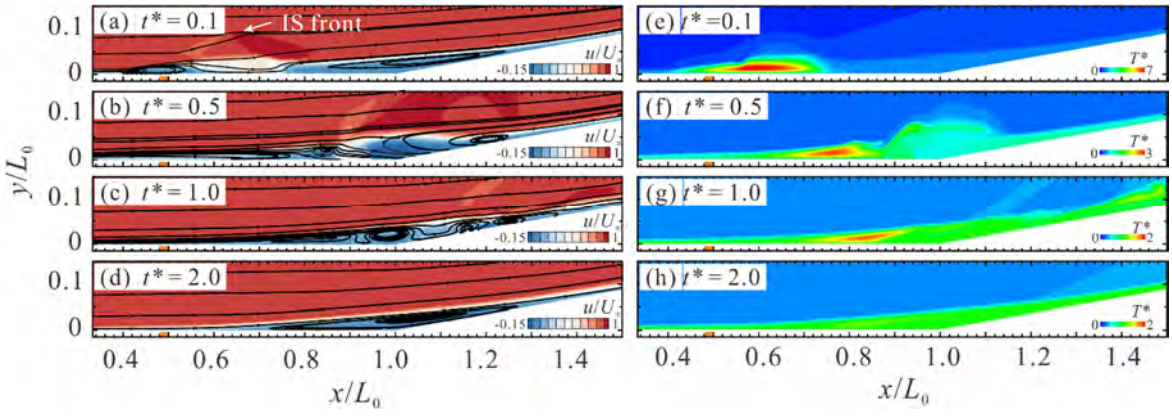

Figure 6-17. Contours of instantaneous normalized streamwise velocity u/U_∞ (left column) with streamlines superimposed and nondimensional temperature T^* (right column) at t^* = (a)(e) 0.1; (b)(f) 0.5; (c)(g) 1.0; and (d)(h) 2.0. The actuator location is at L_p/L_0 = 0.5 and V= 50 kV (case C5).

Correspondingly, Figure 6-17(e)(f)(g)(h) show the "moving heat" evolution at different t^*. Here, the dimensionless temperature T^* is defined as T/T_w. It can be seen in Figure 6-17(a) and Figure 6-17 (e) that the high momentum fluid is brought into the separation region with the heated fluid traveling downstream of the separation point. Under a sufficient mixture with the downstream fluid, the heat dissipates in the shear flow very quickly. The process of destruction and reattachment of the shear layer seems to be in accordance with the evolution of the heated fluid transmitted downstream. These results indicate that thermal perturbation may have the greatest contribution. The energy deposition during the discharge poses a significant change in temperature, which also changes the local density and viscosity. This drastic thermal perturbation, such as the temperature gradient, may excite inherent flow instability, such as Kelvin-Helmholtz instability of the shear layer, and eventually induce the generation of vortices[143]. Meanwhile, the induced shock during the fast heating process may make little contribution to the induced vortices in the initial separation bubble. First, the perturbation to flow properties caused by the induced shock is limited in a narrow region behind the shock front. Second, the induced shock will decay very quickly. It can be seen in Figure 6-17(a) that at t^* = 0.1, the induced shock wave front has moved to y/L_0 = 0.1 and is outside the separation region. The streamlines are deformed across the induced shock. At t^* = 0.5, after the induced shock decays rapidly, the flow field swept by the induced shock wave has returned almost to its steady state. The heated fluid propagates into the shear layer while the induced wavefront has traveled far away from the separation region. This is due to the appreciable velocity difference between the external and separated regions. Apparently, the perturbated flow field highly depends on both the freestream velocity and induced shock intensity. These results imply that the influence on the separation region by the induced shock is

transient and limited. The lasting effects may be caused by momentum entrainment into the separation region due to residual heat-induced vortices.

For cases C1 and C4, in which the excitation position is far upstream of the main separation region, the control effects are limited. In the beginning, the entrained high momentum fluid is brought into the boundary layer before the main separation bubble. Then, it has a weak impact on the separation region and finally dissipates in the shear layer. Although the main separation bubble is broken, the crushed structures are recombined quickly with little effect on the separation point (see Figure 6-18(b)). In this case, the heat dissipates in the boundary layer, and high momentum fluid is hardly transferred into the separated region, which only leads to a weak impact on the main separation bubble.

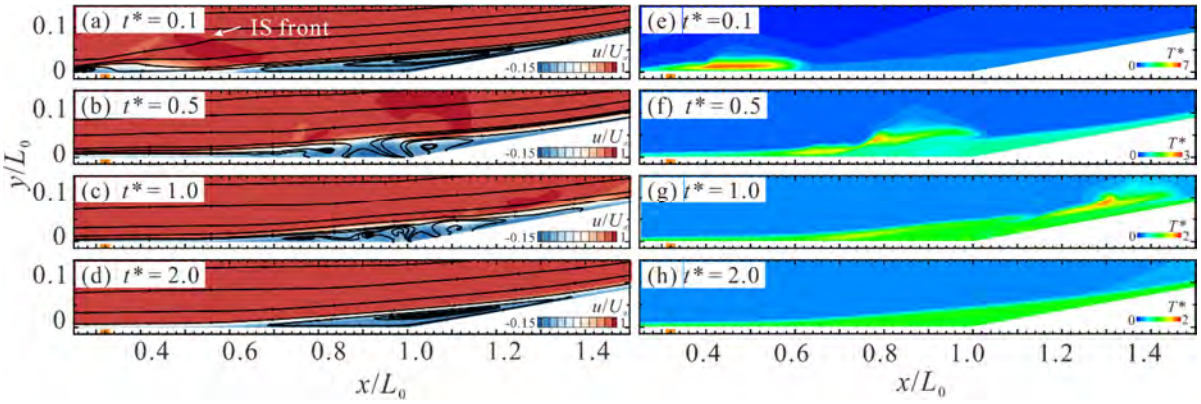

Figure 6-18. Contours of instantaneous normalized streamwise velocity u/U_∞ (left column) with streamlines superimposed and nondimensional temperature T^* (right column) at t^* = (a)(e) 0.1; (b)(f) 0.5; (c)(g) 1.0 and (d)(h) 2.0. The actuator location is at L_p/L_0 = 0.33 and V=50 kV (case C4).

Compared to these four cases hereinbefore, the actuators in cases C3 and C6, which are installed downstream of the original separation point, may function in a different way. When the energy input is low in the case of C3, only a small amount of upper high-speed fluid is brought into the separation region, and the attached flow cannot be sustained for a long time. Moreover, the shear layer cannot be totally destroyed. The separation bubble grows due to the heating effects in the separation region for a short time at the beginning of activation (see Figure 6-19(b)). That is why there is a larger time-averaged L_b in the case of C3 compared to C2 (see Figure 6-7(a)). However, in the case of C6, the drastic discharge at a higher voltage than C3 causes a more lasting and stronger momentum input in the separation region (see the contours in Figure 6-4(d)), resulting in a more complicated perturbation in the shear layer. In Figure 6-19(e), the high momentum fluid impacts the reversed flow and totally breaks the original separated shear layer. More high momentum fluid is brought into the separation region to withstand the adverse pressure gradient. Note that, caused by the coaction of both the adverse pressure gradient and heating effects, the induced separation bubble is larger than in other cases. In a time-averaged result, the original separation region seems to be divided into two parts, an induced separation bubble and the main separation, which is significantly shrunken.

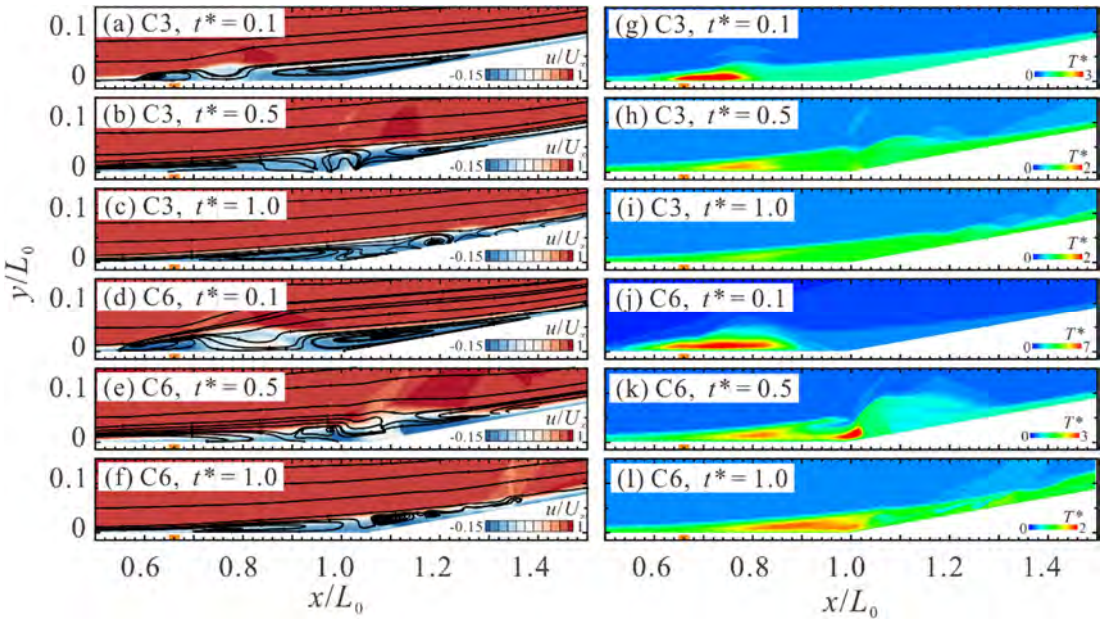

Figure 6-19. Contours of instantaneous normalized streamwise velocity u/U_∞ (left column) with streamlines superimposed and nondimensional temperature T^* (right column), at t^* = (a)(g) 0.1; (b)(h) 0.5; (c)(i) 1.0 of case C3 and (d)(j) 0.1; (e)(k) 0.5; (f)(l) 1.0 of case C6. The actuator location is at L_p/L_0 = 0.67 (cases C3 and C6).

It is concluded that sufficient momentum exchange in the separation region caused by the induced vortex is the control mechanism. The excitation location is a dominant parameter depending on the specific flow system and its local fluid characteristics. In addition, Zheng *et al.*[143] proposed that the residual heat can be considered a remarkable "moving perturbation source" whose influence region can be extended with advection. A new perturbation in the boundary layer is generated downstream of the initially induced vortices with the advection of residual heat. In this study, a similar perturbation is also observed in the simulation on a plat plate under supersonic flow conditions. The results indicate that the residual heat triggers the initial vortices and plays a dominant role in the control of a separated flow. Moreover, the supersonic flow manifests a more resilient characteristic to the thermal impact, and the shear layer breakup procedure is more complex. A more appropriate excitation near the separation point strongly increases the control efficiency.

6.4.2. Periodic activation

To further study the evolution of flow structures, the instantaneous flow field with a periodic discharge is investigated in all cases which can suppress the bubble efficiently. Taking the example of case C5 of F^+ = 10 first, the normalized streamwise velocity contours overlaid with the streamlines are visualized in Figure 6-20. At t^* = 0.1, at the beginning of the first discharge, the induced vortices form the initial separation bubble near the original separation point of the boundary layer and downstream of the bubble, the high-speed external fluid is entrained into the original separation region. This is the same as one pulse activation, detailed in the last section. Subsequently, at t^* = 0.5 (see Figure 6-20(b),

after the fifth pulse), when the entrained fluid passes through the corner, the flow structure is quite different from the single pulse case. It can be seen clearly that the separation bubble is pushed downstream due to the continuous entrained fluid. Subsequently, the high-speed fluid impacts the ramp and further compresses the bubble. Although the original shear layer is totally destroyed, the adverse pressure region still occurs near the corner where the surface pressure increases rapidly, leading to the fractured recirculation flow above the surface. Until the influenced flow by the first pulse passes through the main bubble region, the flow structures above the corner converge, as shown in Figure 6-20(e) at $t^* = 2.5$. At the same time, the original induced separation bubble is locked upstream of the activation points. In the converged flow, under the impact of entrained high momentum fluid, the main bubble is suppressed, but some fragmentary recirculation regions still exist near the corner. Case C5 at $F^+ = 20$, which has a higher PRF but the same excitation position, shares similar control authority with higher effects. Correspondingly, Figure 6-20(f)(g)(h)(i)(j) show the "moving heat" evolution at different t^*. Compared to the single activation case, the heat can be transferred farther downstream of the activation point. But it still dissipates in the shear flow very quickly. The process of destruction and reattachment of the shear layer keeps in accordance with the evolution of the heated fluid transmitted downstream. At $t^* = 0.5$, with the continuous activation, the heating region expands downstream, but the highest temperature core locks subsequently upstream of the corner which is highly related to the applied PRF. In the converge stage, the original separation region is heated and the maximum temperature location is still on the upstream part of the main bubble. The lasting effects are caused by momentum entrainment into the separation region due to continuous pulses.

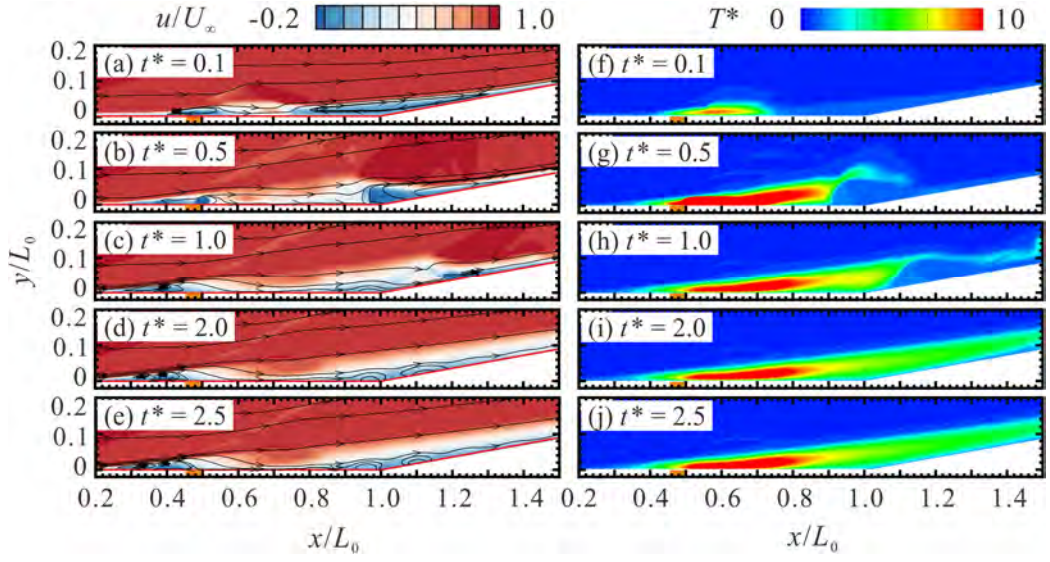

Figure 6-20. Contours of instantaneous normalized streamwise velocity u/U_∞ (left column) with streamlines superimposed and nondimensional temperature T^* (right column), at t^* = (a)(f) 0.1; (b)(g) 0.5; (c)(h) 1.0 (d)(i) 2.0; (e)(j) 2.5 of case C5 at $F^+ = 10$. The actuator location is at L_p/L_0 = 0.50.

Compared to case C5, the actuators in case C6, which are installed downstream of the original separation point, may function more effectively. In case C6 at F^+ = 10, the strong entrained momentum gives a shove toward the bubble, shown in Figure 6-21(b). The high momentum fluid impacts the reversed flow and totally breaks the original separated shear layer. The suppression of the main bubble is more effective than case C5. There is almost no adverse pressure region above the surface. More high momentum fluid is brought into the separation region to withstand the adverse pressure gradient. Note that, caused by the coaction of both the adverse pressure gradient and heating effects, the induced separation bubble is larger than in other cases. The results in the periodic control suggest that increasing the PRF is an effective way to suppress the separation region. The three-dimensional effects of NSDBD will be studied in future work.

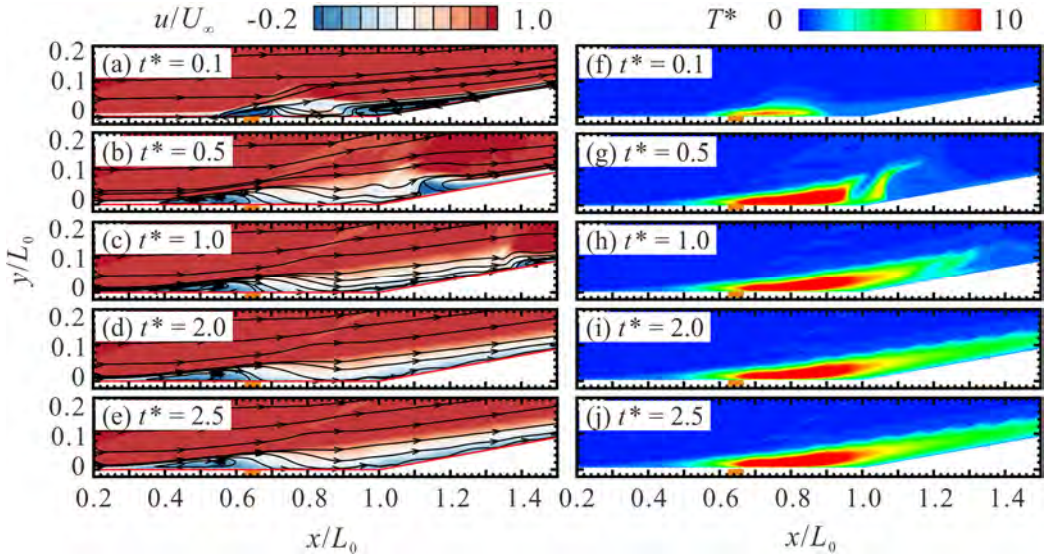

Figure 6-21. Contours of instantaneous normalized streamwise velocity u/U_∞ (left column) with streamlines superimposed and nondimensional temperature T^* (right column), at t^* = (a)(f) 0.1; (b)(g) 0.5; (c)(h) 1.0 (d)(i) 2.0; (e)(j) 2.5 of case C6 at F^+ = 10. The actuator location is at L_p/L_0 = 0.50.

6.5. Remark

In this section, the flow control of an NSDBD on a laminar supersonic compression corner is investigated in detail to explore the probable control mechanism. First, conventional high-speed Schlieren imaging was used to visualize the shock wave systems. A one-zone inhomogeneous phenomenological plasma model was adopted to simulate the fast-heating process of discharge. The flat plate simulation demonstrated that there exists a momentum exchange between the upper external flow and the boundary layer. The high-momentum fluid is entrained through the induced vortex caused by the discharge. A similar acceleration was observed in the ramp cases, which can increase the ability to resist the adverse pressure gradient in the separation region. Moreover, the separated shear layer is broken under the collision of high-speed fluid upstream, which can bring more kinetic

energy into the separation region. Hence, choosing the most appropriate position based on its local fluid characteristics will strongly increase the control efficiency. For a supersonic compression corner, excitation near the separation point achieves higher efficiency in suppressing the separation bubble. For the periodic control, the results suggest that improving the applied voltage is more effective than increasing the PRF if considering the energy consumption. It is possible to totally eliminate the flow separation on the supersonic compression corner. Improving the F^+ from 10 to 20, the performance is better but limited, and the choice of activation location is the key factor. The results of case C3 at F^+ = 20 indicate that applying a lower voltage but with a high activation frequency also can eliminate the bubble. It elucidates there is a critical F^+ that can eliminate the main separation and have a minimum side-effect of the induced bubble. The control efficiency in the activation location downstream of the SP shows the best performance at the corresponding F^+. In the current study, the case at L_p/L_0 = 0.50, F^+ = 10, V = 50 kV shows the best suppression on the separation region.

This study suggests that the NSDBD plasma actuator is a feasible and promising method for separation control in a laminar supersonic flow. It is expected that this study can provide some guidance for further investigation on the heat flux on the surface and inspire more ideas on the application of this control technology.

CHAPTER 7 Conclusions

This thesis mainly focuses on the application of DBD plasma actuators on the D-shaped bluff body and the laminar supersonic compression corner. Experimental investigations were conducted in a low-speed closed-loop wind tunnel and a Ludwig tube at *Ma* 4. Simulation studies were executed in PHAROS with an inhomogeneous phenomenological plasma model. First, the characteristic of the AC, NSDBD plasma actuators, and PSVGs on a flat plate were studied, especially the thermal effects of the NSDBD under low air pressure. The discharge mode transition from diffuse mode to filamentary was observed. Second, the vortex shedding over a D-shaped bluff body in the low Reynolds numbers with/without DBD plasma actuators was measured and analyzed. The aerodynamics and vibration of the bluff body were measured, and the control mechanisms were proposed. Third, the SWBLIs over a supersonic compression corner with/without a plasma actuator were observed first by the Schlieren system. The control effects on the flow structures were studied in detail using numerical simulation, and the control mechanism was discussed. Finally, the periodic control was applied and compared to the single pulse control. The major conclusions of this study were drawn as follows:

For characteristics of NSDBD:

i. By observing the discharge features with a CCD camera, the transition from a filamentary discharge mode to a diffuse mode with decreasing air pressure is demonstrated. The filamentary streamers extend along the radius direction, forming a thicker, yet more stable and uniform plasma region due to the increasing ionized volume yielded by the decreasing air pressure in order to maintain the high values of the reduced electric field. The spatiotemporal temperature distribution on the surface is captured by an infrared camera, indicating the heated surface can be divided into three typical regions with different features. Because the gas heating is generated in the quenching process of excited molecules, the maximum temperature increase on the surface occurs in the plasma region and attenuates downstream. The surface temperature increase is mainly caused by heat convection from the residual heat in plasma and the heat generated by the dielectric losses. The results of heat flux on the surface suggest that the blindly rising applied voltage may not increase the heat flux in a moderate air pressure ranging from 0.6 to 0.8 bar. Different discharge modes and discharge parameters show quite different thermal performance. Furthermore, the Schlieren technique and the pressure sensor are used to visualize the induced shock wave, estimate the thermal expansion region, and measure the overpressure strength. The results of the overpressure strength in different air pressure share a similarity to thermal features, which further proves the significant influence of discharge mode on the thermal effect of NSDBD plasma actuators.

For flow control on a D-shaped bluff body:

i. A global survey of the flow field and drag coefficient in a natural case (no control) was studied. In the tested Reynolds number range, the short D-shaped bluff body had leading edge flow

separation and a vortex generated from the interaction of the two separated shear layers via entrainment. To further study the drag reduction and actuator efficiency based on the saved and consumed electrical power, the results indicated that the PSVGs' performance was slightly better than the DBD actuator, and the hybrid actuator was superior to the two other actuators.

ii. The transverse and streamwise VIV dynamic responses were experimentally studied. A more stable vortex shedding system was generated by the actuators to reduce the natural frequency's effect, thus avoiding the occurrence of resonance in advance. The dominant oscillation frequency's bandwidths in the VIV-dominated region shrank and saltation was delayed due to higher reduced velocities controlled by the PSVGs and hybrid actuator.

iii. The cross-flow results on the model's surface showed that all of the plasma actuators successfully suppressed the leading edge separation because the actuators' induced flows transferred the momentum into the boundary layer downstream from the original separation point, consequently increasing the resistance from separation. Compared to the PSVGs, the hybrid actuator generated a stronger and clingier vortex pair that maintained enough intensity for a longer streamwise distance. The control's effects on the wake were pronounced in the different observed planes. The recirculation region significantly shrank downstream due to the suppression of the leading edge separation. In the PSVGs and hybrid actuator cases, because of the three-dimensional counter-rotating vortex pair, the separated shear layer mixed more sufficiently with the fluid near the trailing edge, resulting in a shorter recirculation bubble length than in the DBD case. The peak TKE values declined to approximately 55% and 40% of the baseline case after controlling via the PSVGs and hybrid actuators, respectively. The fluctuating wake's attenuation was also confirmed through the marked decreases in the first two eigenvalues in the POD analysis that represented the periodic shedding's kinetic energy. The POD modes' distribution in both the PSVGs and hybrid actuators indicated that the vortex shedding process occurred earlier and concentrated in the near wake compared to the DBD case. The hybrid actuator had the advantages of both the DBD and PSVGs actuators and the lowest kinetic energy in the first two modes simultaneously. Although the Kármán vortex shedding persisted after the control, the shedding schema changed significantly; the small-scale antisymmetric shedding mode may have appeared based on the observation of the higher POD modes.

iv. The comparison of the different plasma actuators' control performance indicated that the hybrid actuator achieved the best suppression of leading edge separation, Kármán vortex shedding, and VIV. This was because the hybrid actuator generated strong three-dimensional flow structures near the streamwise exposed electrodes; the front spanwise exposed electrode injected more momentum and hindered the flow separation. In the exposed electrodes' downstream regions, streamwise vortices were induced to impede the formation of the recirculation region behind the bluff body. Thus, the recirculation bubbles behind the bluff

body decreased significantly, and the vortex shedding's turbulence kinetic energy in the wake was suppressed. This study suggests that the amelioration of the traditional DBD plasma actuator using PSVGs or the hybrid actuator is a feasible and promising method for flow control in bluff body wakes. As for the low electromechanical efficiency of this type of flow control technology, more fundamental studies on the actuator design, and how to reduce plasma heating from the electrical power used and convert it into the electromechanical work should be pursued. In the future, periodic control of these actuators will be applied to explore the influence of the actuation frequencies on the control performance.

For flow control on a supersonic compression corner:

i. The flow control of an NSDBD on a laminar supersonic compression corner is investigated in detail to explore the probable control mechanism. First, conventional high-speed Schlieren imaging was used to visualize the shock wave systems. A one-zone inhomogeneous phenomenological plasma model was adopted to simulate the fast-heating process of discharge. The flat plate simulation demonstrated that there exists a momentum exchange between the upper external flow and the boundary layer. The high-momentum fluid is entrained through the induced vortex caused by the discharge. A similar acceleration was observed in the ramp cases, which can increase the ability to resist the adverse pressure gradient in the separation region. Moreover, the separated shear layer is broken under the collision of high-speed fluid upstream, which can bring more kinetic energy into the separation region. Hence, choosing the most appropriate position based on its local fluid characteristics will strongly increase the control efficiency. For a supersonic compression corner, excitation near the separation point achieves a higher efficiency in suppressing the separation bubble.

ii. For the periodic control, the results suggest that improving the applied voltage is more effective than increasing the PRF if considering the energy consumption. It is possible to totally eliminate the flow separation on the supersonic compression corner. Improving the F^+ from 10 to 20, the performance is better but limited, and the choice of activation location is the key factor. The results of case C3 at $F^+ = 20$ indicate that applying a lower voltage but with a high activation frequency also can eliminate the bubble. It elucidates there is a critical F^+ that can eliminate the main separation and have a minimum side-effect of the induced bubble. The control efficiency in the activation location downstream of the SP shows the best performance at the corresponding F^+.

iii. This study suggests that the NSDBD plasma actuator is a feasible and promising method for separation control in a laminar supersonic flow. It is expected that this study can provide some guidance for further investigation on the control efficiency and inspire more ideas on the application of this control technology. In the future, the effects on the heat flux on the surface will be studied.

References

[1] L. Prandtl, "Über Flussigkeitsbewegung Bei Sehr Kleiner Reibung," presented at the Verhandl. III, Internat. Math.-Kong., Heidelberg, Teubner, Leipzig, 1904.

[2] L. N. Cattafesta III and M. Sheplak, "Actuators for Active Flow Control," *Annual Review of Fluid Mechanics,* vol. 43, pp. 247-272, 2011.

[3] A. Glezer and M. Amitay, "Synthetic Jets," *Annual review of fluid mechanics,* vol. 34, no. 1, pp. 503-529, 2002.

[4] R. G. Crittenden, P. Natarajan, U.-L. Pen, and T. Theuns, "Spin-Induced Galaxy Alignments and Their Implications for Weak-Lensing Measurements," *The Astrophysical Journal,* vol. 559, no. 2, p. 552, 2001.

[5] A. Alvi, T. Doherty, and G. Lewen, "Facial Fractures and Concomitant Injuries in Trauma Patients," *The laryngoscope,* vol. 113, no. 1, pp. 102-106, 2003.

[6] E. Moreau, "Airflow Control by Non-Thermal Plasma Actuators," *ournal of physics D: applied physics,* vol. 40, no. 3, p. 605, 2007.

[7] Y. Li, M. Nahon, and I. Sharf, "Airship Dynamics Modeling: A Literature Review," *Progress in Aerospace Sciences,* vol. 47, no. 3, pp. 217-239, 2011.

[8] L. Dalla Longa, A. S. Morgans, and J. A. Dahan, "Reducing the Pressure Drag of a D-Shaped Bluff Body Using Linear Feedback Control," *Theoretical and Computational Fluid Dynamics,* vol. 31, no. 5-6, pp. 567-577, 2017.

[9] T. C. Corke, M. L. Post, and D. M. Orlov, "Sdbd Plasma Enhanced Aerodynamics: Concepts, Optimization and Applications," *Progress in Aerospace Sciences,* vol. 43, no. 7-8, pp. 193-217, 2007.

[10] L. Shen, C.-Y. Wen, and H.-A. Chen, "Asymmetric Flow Control on a Delta Wing with Dielectric Barrier Discharge Actuators," *AIAA Journal,* vol. 54, no. 2, pp. 652-658, 2016.

[11] C. L. Enloe, T. E. McLaughlin, R. D. VanDyken, K. D. Kachner, E. J. Jumper, and T. C. Corke, "Mechanisms and Responses of a Single Dielectric Barrier Plasma Actuator: Plasma Morphology," *AIAA Journal,* vol. 42, no. 3, pp. 589-594, 2004.

[12] C. L. Enloe, T. E. McLaughlin, R. D. VanDyken, K. D. Kachner, E. J. Jumper, T. C. Corke, M. Post, and O. Haddad, "Mechanisms and Responses of a Dielectric Barrier Plasma Actuator: Geometric Effects," *AIAA Journal,* vol. 42, no. 3, pp. 595-604, 2004.

[13] T. C. Corke, C. L. Enloe, and S. P. Wilkinson, "Dielectric Barrier Discharge Plasma Actuators for Flow Control," *Annual Review of Fluid Mechanics,* vol. 42, no. 1, pp. 505-529, 2010.

[14] E. Moreau, "Airflow Control by Non-Thermal Plasma Actuators," *Journal of Physics D: Applied Physics,* vol. 40, no. 3, pp. 605-636, 2007.

[15] T. N. Jukes, T. Segawa, and H. Furutani, "Flow Control on a Naca 4418 Using Dielectric-Barrier-Discharge Vortex Generators," *AIAA Journal,* vol. 51, no. 2, pp. 452-464, 2013.

[16] M. Wicks, F. O. Thomas, T. C. Corke, M. Patel, and A. B. Cain, "Mechanism of Vorticity Generation in Plasma Streamwise Vortex Generators," *AIAA Journal,* vol. 53, no. 11, pp. 3404-3413, 2015.

[17] C. L. Kelley, T. C. Corke, F. O. Thomas, M. Patel, and A. B. Cain, "Design and Scaling of Plasma Streamwise Vortex Generators for Flow Separation Control," *AIAA Journal,* vol. 54, no. 11, pp. 3397-3408, 2016.

[18] M. Belan and F. Messanelli, "Compared Ionic Wind Measurements on Multi-Tip Corona and Dbd Plasma Actuators," *Journal of Electrostatics,* vol. 76, pp. 278-287, 2015.

[19] M. Tang, Y. Wu, H. Wang, S. Guo, Z. Sun, and J. Sheng, "Characterization of Transverse Plasma Jet and Its Effects on Ramp Induced Separation," *Experimental Thermal and Fluid Science,* vol. 99, pp. 584-594, 2018.

[20] F. Liu, H. Yan, W. Zhan, and Y. Xue, "Effects of Steady and Pulsed Discharge Arcs on Shock Wave Control in Mach 2.5 Flow," *Aerospace Science and Technology,* vol. 93, 2019.

[21] H. Ayan, G. Fridman, A. F. Gutsol, V. N. Vasilets, A. Fridman, and G. Friedman, "Nanosecond-Pulsed Uniform Dielectric-Barrier Discharge," *IEEE Transactions on Plasma Science,* vol. 36, no. 2, pp. 504-508, 2008.

[22] L. Shen, Z. N. Chen, and C.-Y. Wen, "Experimental Investigation of the Flow Structure over a Delta Wing Via Flow Visualization Methods," *J Vis Exp,* no. 134, Apr 23 2018.

[23] M. Nudnova, S. Kindusheva, and N. Aleksahdrov, "Rate of Plasma Thermalization of Pulsed Nanosecond Surface Dielectric Barrier Discharge," presented at the 8th AIAA Aerospace Sciences Meeting Including the New Horizons Forum and Aerospace Exposition, Orlando, Florida, 2010.

[24] G. Correale, R. Winkel, and M. Kotsonis, "Energy Deposition Characteristics of Nanosecond Dielectric Barrier Discharge Plasma Actuators: Influence of Dielectric Material," *Journal of Applied Physics,* vol. 118, no. 8, 2015.

[25] Z. J. Z. Y.D. Cui, Y. Bouremel, J. Li, J.G. Zheng, F.G. Hu and B.C. Khoo, "Studies on the Configurations of Nanosecond Dbd Pulse Plasma Actuators," presented at the 19th Australasian Fluid Mechanics Conference, Melbourne, Australia, 8-11 December 2014, 2014.

[26] L. Shen, Z. N. Chen, and C.-Y. Wen, "Thermal Effect on the Performance of an Alternating-Current Dielectric-Barrier-Discharge Plasma Actuator," *AIAA Journal,* vol. 58, no. 8, pp. 3368-3377, 2020.

[27] W. Hui, H. Zhang, J. Wang, X. Meng, and H. Li, "Heat Transfer Characteristics of Plasma Actuation in Different Boundary-Layer Flows," *Physics of Fluids,* vol. 34, no. 3, 2022.

[28] X. Zhang, Y. D. Cui, C.-M. J. Tay, and B. C. Khoo, "Ultrasound Generated by Alternating Current Dielectric Barrier Discharge Plasma in Quiescent Air," *Plasma Sources Science and Technology,* vol. 29, no. 1, 2020.

[29] Z. Zhao, J.-M. Li, J. Zheng, Y. D. Cui, and B. C. Khoo, "Study of Shock and Induced Flow Dynamics by Nanosecond Dielectric-Barrier-Discharge Plasma Actuators," *AIAA Journal,* vol. 53, no. 5, pp. 1336-1348, 2015.

[30] C. Zhang, B. Huang, Z. Luo, X. Che, P. Yan, and T. Shao, "Atmospheric-Pressure Pulsed Plasma Actuators for Flow Control: Shock Wave and Vortex Characteristics," *Plasma Sources Science and Technology,* vol. 28, no. 6, 2019.

[31] A. C. A. a. Ndong, N. Zouzou, N. Benard, and E. Moreau, "Geometrical Optimization of a Surface Dbd Powered by a Nanosecond Pulsed High Voltage," *Journal of Electrostatics,* vol. 71, no. 3, pp. 246-253, 2013.
[32] C. Kolbakir, Y. Liu, H. Hu, A. Starikovskiy, and R. B. Miles, "An Experimental Investigation on the Thermal Effects of Ns-Dbd and Ac-Dbd Plasma Actuators for Aircraft Icing Mitigation," presented at the 2018 AIAA Aerospace Sciences Meeting, 2018.
[33] Y. Liu, C. Kolbakir, H. Hu, X. Meng, and H. Hu, "An Experimental Study on the Thermal Effects of Duty-Cycled Plasma Actuation Pertinent to Aircraft Icing Mitigation," *International Journal of Heat and Mass Transfer,* vol. 136, pp. 864-876, 2019.
[34] B. Wei, Y. Wu, H. Liang , J. Chen, G. Zhao, M. Tian, and H. Xu, "Performance and Mechanism Analysis of Nanosecond Pulsed Surface Dielectric Barrier Discharge Based Plasma Deicer," *Physics of Fluids,* vol. 31, no. 9, 2019.
[35] Y. Liu, C. Kolbakir, A. Y. Starikovskiy, R. Miles, and H. Hu, "An Experimental Study on the Thermal Characteristics of Ns-Dbd Plasma Actuation and Application for Aircraft Icing Mitigation," *Plasma Sources Science and Technology,* vol. 28, no. 1, 2019.
[36] D. V. Roupassov, A. A. Nikipelov, M. M. Nudnova, and A. Y. Starikovskii, "Flow Separation Control by Plasma Actuator with Nanosecond Pulsed-Periodic Discharge," *AIAA Journal,* vol. 47, no. 1, pp. 168-185, 2009.
[37] A. Y. Starikovskii, A. A. Nikipelov, M. M. Nudnova, and D. V. Roupassov, "Sdbd Plasma Actuator with Nanosecond Pulse-Periodic Discharge," *Plasma Sources Science and Technology,* vol. 18, no. 3, 2009.
[38] K. Takashima, Y. Zuzeek, W. R. Lempert, and I. V. Adamovich, "Characterization of a Surface Dielectric Barrier Discharge Plasma Sustained by Repetitive Nanosecond Pulses," *Plasma Sources Science and Technology,* vol. 20, no. 5, 2011.
[39] J. Little, K. Takashima, M. Nishihara, I. Adamovich, and M. Samimy, "Separation Control with Nanosecond-Pulse-Driven Dielectric Barrier Discharge Plasma Actuators," *AIAA Journal,* vol. 50, no. 2, pp. 350-365, 2012.
[40] G. Correale, F. Avallone, and A. Y. Starikovskiy, "Experimental Method to Quantify the Efficiency of the First Two Operational Stages of Nanosecond Dielectric Barrier Discharge Plasma Actuators," *Journal of Physics D: Applied Physics,* vol. 49, no. 50, 2016.
[41] M. M. Nudnova, S. V. Kindysheva, N. L. Aleksandrov, and A. Y. Starikovskii, "Fast Gas Heating in N2/O2 Mixtures under Nanosecond Surface Dielectric Barrier Discharge: The Effects of Gas Pressure and Composition," *Philos Trans A Math Phys Eng Sci,* vol. 373, no. 2048, Aug 13 2015.
[42] C. Ding, A. Y. Khomenko, S. A. Shcherbanev, and S. M. Starikovskaia, "Filamentary Nanosecond Surface Dielectric Barrier Discharge. Experimental Comparison of the Streamer-to-Filament Transition for Positive and Negative Polarities," *Plasma Sources Science and Technology,* vol. 28, no. 8, 2019.
[43] J. H. Gerrard, "The Mechanics of the Formation Region of Vortices Behind Bluff Bodies," *Journal of Fuild Mechanics,* vol. 25, pp. 401-413, 1966.
[44] O. M. Griffin and S. E. Ramberg, "The Vortex-Street Wakes of Vibrating Cylinders," *J. Fluid Mech,* vol. 66, pp. 553-576, 1974.
[45] P. W. Bearman, "Vortex Shedding from Oscillating Bluff Bodies," *Ann. Rev. Fluid Mech,* vol. 16, pp. 195-222, 1984.
[46] Á. A. Rodríguez-Sevillano, M. Á. Barcala-Montejano, R. Bardera-Mora, and J. Batuecas-Fuejo, "Flow Study over Bluff Bodies Based on Visualization Technique," *American Journal of Science and Technology* vol. 4, pp. 97-104, 2018.
[47] A. W. Marris, "A Review on Vortex Streets, Periodic Wakes," *Journal of Basic Engineering,* vol. 96, 1964.
[48] M. M. Zdravkovich, *Flow around Circular Cylinders Volume 1: Fundamentals*. Oxford Science Publications, 1997.
[49] J. Zhao, K. Hourigan, and M. C. Thompson, "Flow-Induced Vibration of D-Section Cylinders: An afterbody Is Not Essential for Vortex-Induced Vibration," *Journal of Fluid Mechanics,* vol. 851, pp. 317-343, 2018.
[50] T. Yamagata, N. Saito, and N. Fujisawa, "Experimental and Numerical Studies on Aeolian Tone from D-Shaped Cylinder," *Proceedings of the Institution of Mechanical Engineers, Part C: Journal of Mechanical Engineering Science,* vol. 232, no. 22, pp. 4007-4018, 2017.
[51] Z. J. Taylor, E. Palombi, R. Gurka, and G. A. Kopp, "Features of the Turbulent Flow around Symmetric Elongated Bluff Bodies," *Journal of Fluids and Structures,* vol. 27, no. 2, pp. 250-265, 2011.
[52] B. Thiria, O. Cadot, and J. F. Beaudoin, "Passive Drag Control of a Blunt Trailing Edge Cylinder," *Journal of Fluids and Structures,* vol. 25, no. 5, pp. 766-776, 2009.
[53] V. Parezanović and O. Cadot, "Experimental Sensitivity Analysis of the Global Properties of a Two-Dimensional Turbulent Wake," *Journal of Fluid Mechanics,* vol. 693, pp. 115-149, 2012.
[54] W. K. H. Do , M. G. Mungal and M. A. Cappelli "Bluff Body Flow Separation Control Using Surface Dielectric Barrier Discharges," presented at the 45th AIAA Aerospace Sciences Meeting and Exhibit, Reno, Nevada, 8 – 11 January 2007, 2007.
[55] S. Bhattacharya and J. W. Gregory, "Optimum-Wavelength Forcing of a Bluff Body Wake," *Physics of Fluids,* vol. 30, no. 1, 2018.
[56] A. V. Kozlov and F. O. Thomas, "Bluff-Body Flow Control Via Two Types of Dielectric Barrier Discharge Plasma Actuation," *AIAA Journal,* vol. 49, no. 9, pp. 1919-1931, 2011.
[57] A. Naghib-Lahouti, H. Hangan, and P. Lavoie, "Distributed Forcing Flow Control in the Wake of a Blunt Trailing Edge Profiled Body Using Plasma Actuators," *Physics of Fluids,* vol. 27, no. 3, 2015.
[58] L. A. AL-Sadawi, "Vortex Shedding-Induced Noise Reduction Using (Dbd) Plasma Actuator," Doctor of Philosophy, Department of Mechanical Aerospace and Civil Engineering, Brunel University, 2018.
[59] J. A. Vernet, R. Örlü, and P. H. Alfredsson, "Flow Separation Control Behind a Cylindrical Bump Using Dielectric-Barrier-Discharge Vortex Generator Plasma Actuators," *Journal of Fluid Mechanics,* vol. 835, pp. 852-879, 2017.
[60] V. Theofilis, "On the Origins of Unsteadiness and Three-Dimensionality in a Laminar Separation Bubble," *Philosophical Transactions of the Royal Society of London. Series A: Mathematical, Physical and Engineering Sciences,* vol. 358, pp. 3229-3246, 2000, Art. no. 1777.

[61] V. Theofilis, "Global Linear Instability," *Annual Review of Fluid Mechanics,* vol. 43, no. 1, pp. 319-352, 2011.
[62] J. C. Robinet, "Bifurcations in Shock-Wave/Laminar-Boundary-Layer Interaction: Global Instability Approach," *Journal of Fluid Mechanics,* vol. 579, pp. 85-112, 2007.
[63] S. Cao, J. Hao, I. Klioutchnikov, H. Olivier, and C.-Y. Wen, "Unsteady Effects in a Hypersonic Compression Ramp Flow with Laminar Separation," *Journal of Fluid Mechanics,* vol. 912, 2021.
[64] Z. Chen, L. Shen, and C.-Y. Wen, "Flow Control on a Bluff Body Using Dielectric Barrier Discharge Plasma Actuators," *AIAA Journal,* vol. 57, no. 7, pp. 2670-2674, 2019.
[65] Z. Chen and C.-Y. Wen, "Flow Control of a D-Shaped Bluff Body Using Different Dbd Plasma Actuators," *Journal of Fluids and Structures,* vol. 103, 2021, Art. no. 103292.
[66] Y. Wang, H. Zhang, Y. Wu, Y. Li, and Y. Zhu, "Supersonic Compressor Cascade Flow Control Using Plasma Actuation at Low Reynolds Number," *Physics of Fluids,* vol. 34, no. 2, 2022.
[67] A. Belinger, N. Naudé, J. P. Cambronne, and D. Caruana, "Plasma Synthetic Jet Actuator: Electrical and Optical Analysis of the Discharge," *Journal of Physics D: Applied Physics,* vol. 47, no. 34, 2014.
[68] C. A. Brown, "Scalability of the Localized Arc Filament Plasma Actuators," presented at the 29th AIAA Aeroacoustics Conference, Vancouver, British Columbia Canada, 5 - 7 May 2008, 2008.
[69] Y. D. Cui, Z. J. Zhao, J. Li, J. G. Zheng, and B. C. Khoo, "Flow Separation Control over a Ramp with Nanosecond-Pulsed Plasma Actuators," presented at the Proceedings of 30th International Symposium on Shock Waves 2, 2017.
[70] Z.-J. Zhao, Y. D. Cui, J.-M. Li, J.-G. Zheng, and B. C. Khoo, "On the Boundary Flow Using Pulsed Nanosecond Dbd Plasma Actuators," *Modern Physics Letters B,* vol. 32, no. 12n13, 2018, Art. no. 1840035
[71] M. Nishihara, K. Takashima, J. W. Rich, and I. V. Adamovich, "Mach 5 Bow Shock Control by a Nanosecond Pulse Surface Dielectric Barrier Discharge," *Physics of Fluids,* vol. 23, no. 6, 2011, Art. no. 066101.
[72] N. J. Bisek, J. Poggie, M. Nishihara, and I. Adamovich, "Hypersonic Flow over a Cylinder with a Nanosecond Pulse Electrical Discharge," *Journal of Thermophysics and Heat Transfer,* vol. 28, no. 1, pp. 18-26, 2014.
[73] J. G. Zheng, Y. D. Cui, J. Li, and B. C. Khoo, "A Note on Supersonic Flow Control with Nanosecond Plasma Actuator," *Physics of Fluids,* vol. 30, no. 4, 2018, Art. no. 040907.
[74] K. Kinefuchi, A. Y. Starikovskiy, and R. B. Miles, "Control of Shock-Wave/Boundary-Layer Interaction Using Nanosecond-Pulsed Plasma Actuators," *Journal of Propulsion and Power,* vol. 34, no. 4, pp. 909-919, 2018.
[75] K. Kinefuchi, A. Y. Starikovskiy, and R. B. Miles, "Numerical Investigation of Nanosecond Pulsed Plasma Actuators for Control of Shock-Wave/Boundary-Layer Separation," *Physics of Fluids,* vol. 30, no. 10, 2018, Art. no. 106105.
[76] M. Forte, J. Jolibois, J. Pons, E. Moreau, G. Touchard, and M. Cazalens, "Optimization of a Dielectric Barrier Discharge Actuator by Stationary and Non-Stationary Measurements of the Induced Flow Velocity: Application to Airflow Control," *Experiments in Fluids,* vol. 43, no. 6, pp. 917-928, 2007.
[77] D. Ashpis, M. Laun, and E. Griebeler, "Progress toward Accurate Measurements of Power Consumption of Dbd Plasma Actuators," presented at the 50th AIAA Aerospace Sciences Meeting including the New Horizons Forum and Aerospace Exposition, 2012.
[78] L. Shen, Z. N. Chen, and C.-Y. Wen, "Experimental Investigation of the Flow Structure over a Delta Wing Via Flow Visualization Methods," *Journal of Visualized Experiments,* no. 134, Apr 23 2018.
[79] A. Sciacchitano and B. Wieneke, "Piv Uncertainty Propagation," *Measurement Science and Technology,* vol. 27, no. 8, p. 084006, 2016.
[80] G.Berkooz, P. Holmes, and J. L. Lumley, "The Proper Orthggonal Decomposition in the Analysis of Turbulent Flows," *Annu. Rev. Fluid Mech,* vol. 25, pp. 539-575, 1993.
[81] L.-H. Feng, J.-J. Wang, and C. Pan, "Proper Orthogonal Decomposition Analysis of Vortex Dynamics of a Circular Cylinder under Synthetic Jet Control," *Physics of Fluids,* vol. 23, no. 1, 2011.
[82] K. E. Meyer, J. M. Pedersen, and O. ÖZcan, "A Turbulent Jet in Crossflow Analysed with Proper Orthogonal Decomposition," *Journal of Fluid Mechanics,* vol. 583, pp. 199-227, 2007.
[83] Y. Zhu, D. Gu, W. Zhu, S. Chen, C. Lee, and E. S. Oran, "Dilatational-Wave-Induced Aerodynamic Cooling in Transitional Hypersonic Boundary Layers," *Journal of Fluid Mechanics,* vol. 911, 2021.
[84] H. Jiaao, "Modeling of Thermochemical Nonequilibrium Coupling Effects in Hypersonic Flows," Ph.D, Aeronautic Science and Engineering, Beihang University, Beijing, China, 10006BY1305173, 2017.
[85] A. Starikovskiy and N. Aleksandrov, *Nonequilibrium Plasma Aerodynamics*. INTECH Open Access Publisher Rijeka, 2011.
[86] Z. Chen, L. Hao, and B. Zhang, "A Model for Nanosecond Pulsed Dielectric Barrier Discharge (Nsdbd) Actuator and Its Investigation on the Mechanisms of Separation Control over an Airfoil " *SCIENCE CHINA Technological Sciences,* vol. 56, pp. 1055–1065, 2013.
[87] G.-Y. Zhao, Y.-H. Li, H. Liang, W.-Z. Hua, and M.-H. Han, "Phenomenological Modeling of Nanosecond Pulsed Surface Dielectric Barrier Discharge Plasma Actuation for Flow Control," *Acta Physica Sinica,* vol. 64, no. 1, 2015.
[88] J. G. Zheng, Z. J. Zhao, J. Li, Y. D. Cui, and B. C. Khoo, "Numerical Simulation of Nanosecond Pulsed Dielectric Barrier Discharge Actuator in a Quiescent Flow," *Physics of Fluids,* vol. 26, no. 3, 2014, Art. no. 036102.
[89] T. Unfer and J. P. Boeuf, "Modelling of a Nanosecond Surface Discharge Actuator," *Journal of Physics D: Applied Physics,* vol. 42, no. 19, 2009.
[90] C.-C. Wang and S. Roy, "Energy and Force Prediction for a Nanosecond Pulsed Dielectric Barrier Discharge Actuator," *Journal of Applied Physics,* vol. 111, no. 10, 2012.
[91] A. Montello, D. Burnette, M. Nishihara, W. R. Lempert, and I. V. Adamovich, "Dynamics of Rapid Localized Heating in Nanosecond Pulse Discharges for High Speed Flow Control," *Journal of Fluid Science and Technology,* vol. 8, no. 2, pp. 147-159, 2013.
[92] K. Takashima, Z. Yin, and I. Adamovich, "Measurements and Kinetic Modeling Analysis of Energy Coupling in Nanosecond Pulse Dielectric Barrier Discharges," presented at the 43rd AIAA Plasmadynamics and Lasers Conference, 2012.

[93] A. N. Lagarkov, and Rutkevich, I.M., *Ionization Waves in Electric Breakdown of Gases*. Springer, New York, 1994.
[94] J. Hao and C.-Y. Wen, "Effects of Vibrational Nonequilibrium on Hypersonic Shock-Wave/Laminar Boundary-Layer Interactions," *International Communications in Heat and Mass Transfer,* vol. 97, pp. 136-142, 2018.
[95] J. Hao, C.-Y. Wen, and J. Wang, "Numerical Investigation of Hypervelocity Shock-Wave/Boundary-Layer Interactions over a Double-Wedge Configuration," *International Journal of Heat and Mass Transfer,* vol. 138, pp. 277-292, 2019.
[96] J. Hao and C.-Y. Wen, "Hypersonic Flow over Spherically Blunted Double Cones," *Journal of Fluid Mechanics,* vol. 896, 2020.
[97] B. V. Leer, "Towards the Ultimate Conservative Difference Scheme," *Journal of computational physics,* vol. 32, pp. 101-136, 1979.
[98] M. J. Wright, G. V. Candler, and D. Bose, "Data-Parallel Line Relaxation Method for the Navier-Stokes Equations," *AIAA Journal,* vol. 36, no. 9, pp. 1603-1609, 1998.
[99] J.-C. Laurentie, J. Jolibois, and E. Moreau, "Surface Dielectric Barrier Discharge: Effect of Encapsulation of the Grounded Electrode on the Electromechanical Characteristics of the Plasma Actuator," *Journal of Electrostatics,* vol. 67, no. 2-3, pp. 93-98, 2009.
[100] J. Kriegseis, B. Möller, S. Grundmann, and C. Tropea, "Capacitance and Power Consumption Quantification of Dielectric Barrier Discharge (Dbd) Plasma Actuators," *Journal of Electrostatics,* vol. 69, no. 4, pp. 302-312, 2011.
[101] A. V. Pipa, J. Koskulics, R. Brandenburg, and T. Hoder, "The Simplest Equivalent Circuit of a Pulsed Dielectric Barrier Discharge and the Determination of the Gas Gap Charge Transfer," *Rev Sci Instrum,* vol. 83, no. 11, p. 115112, Nov 2012.
[102] Z. F. a. J. J. Coogan, "Microdischarge Behaviour in the Silent Discharge of Nitrogen - Oxygen and Water - Air Mixtures," *J. Phys. D: Appl. Phys,* vol. 30, 1997.
[103] M. Cheong, A. Greig, B. Gibson, and M. Arjomandi, "An Investigation into the Effect of Electric Field on the Performance of Dielectric Barrier Discharge Plasma Actuators," *Experimental Thermal and Fluid Science,* vol. 35, no. 8, pp. 1600-1607, 2011.
[104] L. Wang, C. W. Wong, Z. Lu, Z. Wu, and Y. Zhou, "Novel Sawtooth Dielectric Barrier Discharge Plasma Actuator for Flow Separation Control," *AIAA Journal,* vol. 55, no. 4, pp. 1405-1416, 2017.
[105] F. P. a. T. Butterworth, "Electrical Diagnostics of Dielectric Barrier Discharges."
[106] L. Shen, "Application of Dielectric Barrier Discharge Plasma Actuacors on a Highly Swept Delta Wing," PhD, Mechanical Engineering, The Hong Kong Polytechnic University, Pao Yue-kong Library, The Hong Kong Polytechnic University, Hung Hom, Kowloon, Hong Kong 2018.
[107] Valentin I Gibalov and G. J. Pietsch, "The Development of Dielectric Barrier Discharges in Gas Gaps and on Surfaces," *Journal of Applied Physics,* vol. 33, pp. 2618–2636, 2000, Art. no. 20.
[108] M. Simeni Simeni, Y. Tang, K. Frederickson, and I. V. Adamovich, "Electric Field Distribution in a Surface Plasma Flow Actuator Powered by Ns Discharge Pulse Trains," *Plasma Sources Science and Technology,* vol. 27, no. 10, 2018.
[109] C.-W. Yao, Z.-S. Chang, H. Ma, G. Xu, H. Mu, and G.-J. Zhang, "Experimental Research on Mode Transitions of Atmospheric Pressure Helium Dielectric Barrier Discharge," *IEEE Transactions on Plasma Science,* vol. 44, no. 11, pp. 2576-2588, 2016.
[110] Z. Chen, J. Hao, and C.-Y. Wen, "Control of Supersonic Compression Corner Flow Using a Plasma Actuator," *Physics of Fluids,* vol. 34, no. 7, 2022.
[111] N. A. Popov, "Investigation of the Mechanism for Rapid Heating of Nitrogen and Air in Gas Discharges," *Plasma Physics Reports,* vol. 37, pp. 886–896, 2001, Art. no. 10.
[112] J. C. Tully, "Reactions of O(1d) with Atmospheric Molecules," *The Journal of Chemical Physics,* vol. 62, no. 5, pp. 1893-1898, 1975.
[113] N. A. Popov, "Fast Gas Heating in a Nitrogen–Oxygen Discharge Plasma: I. Kinetic Mechanism," *Journal of Physics D: Applied Physics,* vol. 44, no. 28, 2011.
[114] S. Lanier, I. Shkurenkov, I. V. Adamovich, and W. R. Lempert, "Two-Stage Energy Thermalization Mechanism in Nanosecond Pulse Discharges in Air and Hydrogen–Air Mixtures," *Plasma Sources Science and Technology,* vol. 24, no. 2, 2015.
[115] N. Y. Babaeva, D. V. Tereshonok, and G. V. Naidis, "Fluid and Hybrid Modeling of Nanosecond Surface Discharges: Effect of Polarity and Secondary Electrons Emission," *Plasma Sources Science and Technology,* vol. 25, no. 4, 2016.
[116] M. E. Stern and L. J. Pratt, "Dynamics of Vorticity Fronts," *Journal of Fluid Mechanics,* vol. 161, no. -1, 1985.
[117] B. P. Conlon and S. Lichter, "Dipole Formation in the Transient Planar Wall Jet," *Physics of Fluids,* vol. 7, no. 5, pp. 999-1014, 1995.
[118] F. B. Hsiao and S. S. Sheu, "Double Row Vortical Structures in the near Region of a Plane Wall Jet," *Experiments in Fluids,* vol. 17, pp. 291-301, 1994.
[119] R. D. Whalley and K.-S. Choi, "The Starting Vortex in Quiescent Air Induced by Dielectric-Barrier-Discharge Plasma," *Journal of Fluid Mechanics,* vol. 703, pp. 192-203, 2012.
[120] J. Kriegseis, A. Duchmann, C. Tropea, and S. Grundmann, "On the Classification of Dielectric Barrier Discharge Plasma Actuators: A Comprehensive Performance Evaluation Study," *Journal of Applied Physics,* vol. 114, no. 5, 2013.
[121] N. L. Aleksandrov, S. V. Kindysheva, M. M. Nudnova, and A. Y. Starikovskiy, "Mechanism of Ultra-Fast Heating in a Non-Equilibrium Weakly Ionized Air Discharge Plasma in High Electric Fields," *Journal of Physics D: Applied Physics,* vol. 43, no. 25, 2010.
[122] J. V. d. Broecke, "De-Icing Using Ns-Dbd Plasma Actuators," master, Faculty of Aerospace Engineering, Delft University of Technology, 2016.
[123] A. Roshko, "Perspectives on Bluff Body Aerodynamics," *Journal of Wind Engineering and Industrial Aerodynamic,* vol. 49, pp. 79-100, 1993.
[124] L. Lee and D. Allen, "Vibration Frequency and Lock-in Bandwidth of Tensioned, Flexible Cylinders Experiencing Vortex Shedding," *Journal of Fluids and Structures,* vol. 26, no. 4, pp. 602-610, 2010.

[125] B. Sanaati and N. Kato, "A Study on the Effects of Axial Stiffness and Pre-Tension on Viv Dynamics of a Flexible Cylinder in Uniform Cross-Flow," *Applied Ocean Research,* vol. 37, pp. 198-210, 2012.
[126] A. Naghib-Lahouti, P. Lavoie, and H. Hangan, "Wake Instabilities of a Blunt Trailing Edge Profiled Body at Intermediate Reynolds Numbers," *Experiments in Fluids,* vol. 55, no. 7, 2014.
[127] T. N. Jukes and K.-S. Choi, "Flow Control around a Circular Cylinder Using Pulsed Dielectric Barrier Discharge Surface Plasma," *Physics of Fluids,* vol. 21, no. 8, 2009.
[128] M. Kotsonis, S. Ghaemi, L. Veldhuis, and F. Scarano, "Measurement of the Body Force Field of Plasma Actuators," *Journal of Physics D: Applied Physics,* vol. 44, no. 4, 2011.
[129] L. Shen and C.-Y. Wen, "Leading Edge Vortex Control on a Delta Wing with Dielectric Barrier Discharge Plasma Actuators," *Applied Physics Letters,* vol. 110, no. 25, 2017, Art. no. 251904.
[130] L. Shen and C.-Y. Wen, "Oscillations of Leading-Edge Vortex Breakdown Locations over a Delta Wing," *AIAA Journal,* vol. 56, no. 6, pp. 2113-2118, 2018.
[131] B. Balachandar, R. Mittal, and F. M. Najjar, "Properties of the Mean Recirculation Region in the Wakes of Twodimensional Bluff Bodies," *journal of Fluid Mechanics,* vol. 351, pp. 167-199, 1997.
[132] A. K. a. T. C. C. Flint O. Thomas, "Plasma Actuators for Bluff Body Flow Control," presented at the 3rd AIAA Flow Control Conference, San Francisco, California, 5 - 8 June 2006, 2006.
[133] F. O. Thomas, A. Kozlov, and T. C. Corke, "Plasma Actuators for Cylinder Flow Control and Noise Reduction," *AIAA Journal,* vol. 46, no. 8, pp. 1921-1931, 2008.
[134] K. Taira, S. L. Brunton, S. T. M. Dawson, C. W. Rowley, T. Colonius, B. J. McKeon, O. T. Schmidt, S. Gordeyev, V. Theofilis, and L. S. Ukeiley, "Modal Analysis of Fluid Flows: An Overview," *AIAA Journal,* vol. 55, no. 12, pp. 4013-4041, 2017.
[135] K. Taira, M. S. Hemati, S. L. Brunton, Y. Sun, K. Duraisamy, S. Bagheri, S. T. M. Dawson, and C.-A. Yeh, "Modal Analysis of Fluid Flows: Applications and Outlook," *AIAA Journal,* vol. 58, no. 3, pp. 998-1022, 2020.
[136] X. Ma, G. S. Karamanos, and G. E. Karniadakis, "Dynamics and Low-Dimensionality of a Turbulent near Wake," *Journal of Fluid Mechanics,* vol. 410, pp. 29-65, 2000.
[137] L.-H. Feng and J.-J. Wang, "Modification of a Circular Cylinder Wake with Synthetic Jet: Vortex Shedding Modes and Mechanism," *European Journal of Mechanics - B/Fluids,* vol. 43, pp. 14-32, 2014.
[138] A. Dwivedi, G. S. Sidharth, J. W. Nichols, G. V. Candler, and M. R. Jovanović, "Reattachment Streaks in Hypersonic Compression Ramp Flow: An Input–Output Analysis," *Journal of Fluid Mechanics,* vol. 880, pp. 113-135, 2019.
[139] P. Reijasse, V. I. Zapryagaev, I. N. Kavun, I. I. Lipatov, D. Knight, M. Ivanov, and I. Lipatov, "Supersonic Laminar Separated Flow Structure at a Ramp for a Free-Stream Mach Number of 6," presented at the Progress in Flight Physics, 2013.
[140] M. Bleilebens and H. Olivier, "On the Influence of Elevated Surface Temperatures on Hypersonic Shock Wave/Boundary Layer Interaction at a Heated Ramp Model," *Shock Waves,* vol. 15, no. 5, pp. 301-312, 2006.
[141] P. V. Chuvakhov and V. N. Radchenko, "Effect of Görtler-Like Vortices of Various Intensity on Heat Transfer in Supersonic Compression Corner Flows," *International Journal of Heat and Mass Transfer,* vol. 150, 2020.
[142] J. Hao, S. Cao, C.-Y. Wen, and H. Olivier, "Occurrence of Global Instability in Hypersonic Compression Corner Flow," *Journal of Fluid Mechanics,* vol. 919, 2021.
[143] J. G. Zheng, Y. D. Cui, Z. J. Zhao, J. Li, and B. C. Khoo, "Investigation of Airfoil Leading Edge Separation Control with Nanosecond Plasma Actuator," *Physical Review Fluids,* vol. 1, no. 7, 2016.